UNIVERSIDAD DE GRANADA

PROGRAMA DE DOCTORADO EN MEDICINA CLÍNICA Y SALUD PÚBLICA

TESIS DOCTORAL

Diseño y Evaluación *in vitro* de Nanopartículas Poliméricas Funcionalizadas con un Antagonista de GSK-3β para Mejorar las Propiedades de la Interfase Resina-Dentina

Doctorando

José Enrique Fernández Romero

Directores

Prof. Dr. D Manuel Toledano Pérez

Profa. Dra. Dña Raquel Osorio Ruiz

Granada 2024

Editor: Universidad de Granada. Tesis Doctorales
Autor: José Enrique Fernández Romero
ISBN: 978-84-1195-736-6
URI: https://hdl.handle.net/10481/102873

Agradecimientos

Durante la elaboración de mi Tesis Doctoral, muchos compañeros, amigos y familiares me han ayudado, animado o contribuido de alguna forma a que esto fuera posible. Mi más sincero agradecimiento a todos. Además, me gustaría que quedaran grabadas unas palabras de especial gratitud a aquellas personas que han sido determinantes en este trabajo.

En mi primer lugar me gustaría agradecer a mis directores, el Prof. Manuel Toledano y la Profa. Raquel Osorio. Ellos me han guiado en mis primeros pasos en el mundo académico y me han brindado oportunidades con las que cualquier estudiante soñaría. Gracias a su confianza desde el primer momento, he tenido las puertas abiertas a un grupo de investigación de excelencia, tanto profesional como humana. Su disponibilidad y ayuda infinita durante la Tesis han sido inestimables. Conocerlos ha supuesto un antes y un después en mi trayectoria profesional y académica. Gracias de todo corazón.

A la Profa. Fátima Sánchez y Profa. Estrella Osorio, mis mentoras en este proceso. Quiero agradeceros por ser una fuente inagotable de ánimos. Siempre habéis mostrado vuestro cariño y habéis sabido levantarme y sacarme una sonrisa en los momentos más difíciles. Sin vosotras, esto no habría sido posible. Fátima, tú me has enseñado y guiado en la práctica de la investigación básica en materiales dentales, no podría haber tenido mejor maestra, gracias.

A María Gertrudis Gómez, por su conocimiento, compañía y ayuda. Gracias por tu paciencia enseñándome las diferentes técnicas de laboratorio. Poder aprender de ti ha sido un privilegio.

A la Dra. Marta Vallecillo y Dra. Cristina Vallecillo, que habéis estado a mi lado desde el primer momento, apoyándome, guiándome y enseñándome. Teneros como compañeras ha sido un regalo que el mundo académico me ha dado. Sois una fuente de inspiración para mí a nivel clínico, investigador y humano. Nunca podré agradeceros lo suficiente todo lo que habéis hecho por mí.

Quisiera expresar también mi agradecimiento a mis compañeros y profesores del Máster de Cirugía Bucal e Implantología de la Universidad de Granada por sus mensajes de apoyo y ánimos. Aprender de vosotros me acerca al profesional que quiero ser.

A Valerie, por tu apoyo incondicional, cariño, paciencia y comprensión al tener que sacrificar nuestro tiempo juntos para dedicárselo a la Tesis. Tenerte a mi lado en este proceso ha sido una suerte; tú lo has hecho todo un poco más fácil.

A mis hermanas, Andrea y Natalia, por valorar siempre el esfuerzo y trabajo que hago. Vuestra comprensión durante todo este tiempo ha sido fundamental para mí. Sé que mi dedicación a este trabajo me ha impedido estar más presente como hermano mayor en vuestro día a día, y os agradezco de corazón vuestra paciencia y apoyo incondicional. Vuestro optimismo y madurez me han reconfortado en este camino. Estoy orgulloso de las personas que sois.

Y, por último, y no menos importante, sino más bien todo lo contrario, quisiera expresar mi agradecimiento de forma especial a mis padres.

Papá y mamá, vosotros sois mi verdadera referencia y ejemplo a seguir. Vuestro amor, dedicación y sacrificio han sido el cimiento sobre el cuál he construido mi camino A pesar de las adversidades, me habéis dado la oportunidad de conseguir todo cuanto me propusiera. Me habéis apoyado en mis decisiones en todo momento y habéis confiado siempre en mí, incluso cuando yo mismo dudaba. Gracias por motivarme, animarme y empujarme hacia mis sueños.

Esta tesis es tanto vuestra como mía, y os la dedico con todo mi corazón. Gracias por ser los mejores padres que podría haber pedido, y por enseñarme que, con esfuerzo, determinación y pasión, todo es posible.

Normativa Universidad de Granada

La presente memoria sigue la estructura que dicta la normativa del Programa de Doctorado de Medicina Clínica y Salud Pública de la Universidad de Granada (https://doctorados.ugr.es/medicinaysalud/pages/organizacion_programa/doctorandos) para las Tesis presentadas como agrupación de trabajos de investigación publicados, que dice textualmente:

"Aunque no existe una única forma de presentar una tesis por agrupación de artículo, en general se presentará una memoria con una introducción e hipótesis común para los 3 o más artículos presentados y unos objetivos generales u específicos que podría pertenecer a diferentes artículos; los resultados podrían ser los 3 o más artículos presentados, insertándolos en el propio documento de la Tesis, con o sin un resumen general de los mismos; finalmente un apartado de discusión que trate de justificar la unidad temática y que resuma la idea global de la Tesis Doctoral y las conclusiones, donde se debería responder a cada uno de los objetivos planteados previamente." ....

Resumen

Uno de los principales retos de la odontología adhesiva actual es desarrollar un biomaterial para adhesión a dentina, capaz de producir una remineralización funcional de la base de la capa híbrida, considerada la parte más débil de la unión resina-dentina. A pesar de las diferentes propuestas hasta el momento, ninguna de ellas satisface las exigencias actuales del biomaterial ideal para la adhesión a este sustrato. Entre estas propiedades que se exigen a un biomaterial destacan la capacidad de ejercer un efecto prolongado en el tiempo, la capacidad de devolver las propiedades mecánicas a la dentina desmineralizada y una baja toxicidad. En este sentido, la ingeniería tisular ha supuesto un avance para la odontología adhesiva, acelerando el desarrollo de biomateriales que reúnen unas condiciones más próximas a las ideales. Entre estas opciones se encuentran las nanopartículas poliméricas, previamente desarrolladas por nuestro grupo de investigación. Estas nanopartículas son capaces de ser funcionalizadas con diferentes medicamentos que pueden promover la remineralización dentinaria o desarrollar un efecto antibacteriano, y ser transportados hasta el lugar deseado para liberarlos de forma controlada y mantenida en el tiempo.

En la presente tesis doctoral, hemos utilizado estas nanopartículas para transportar un inhibidor de GSK3-β, el tideglusib. El tideglusib es un material orgánico biodegradable, actualmente en ensayo para la enfermedad de Alzheimer, que ha demostrado ser capaz de inducir la reparación dentinaria mediante la activación de la vía canónica Wnt en modelos animales. Además, debido a su estructura química, podría ser capaz de actuar como quelante de diferentes iones, promoviendo la nucleación mineral *de novo.* Sin embargo, se ha comprobado que uno de los principales problemas del tideglusib es su inestabilidad, lo que justifica la funcionalización de las nanopartículas poliméricas con este fármaco. En un estudio previo realizado por nuestro grupo de investigación, estas nanopartículas funcionalizadas con tideglusib han conseguido mejorar los valores de resistencia a la microtensión de las interfases resina-dentina. En esta línea de investigación, se crean interfases resina-dentina, en las que se infiltra este biomaterial previo a la aplicación del adhesivo y tras el acondicionamiento con ácido ortofosfórico. Además, las interfases resina-dentina se someten a diferentes desafíos que simulan las condiciones ambientales que se producen en la cavidad oral, como el estrés térmico y mecánico.

En este trabajo de investigación se realizan múltiples pruebas a diferentes niveles, tales como mecánico, histológico, morfológico, cristalográfico, bioquímico, físico y ultraestructural, con el fin de evaluar detalladamente las propiedades remineralizadoras y mecánicas de este nuevo biomaterial. Destacamos también que las publicaciones que sustentan esta tesis combinan tanto pruebas mecánicas como *tests* que evalúan la remineralización dentinaria producida con el objetivo de determinar el tipo de remineralización obtenida, extrafibrilar o intrafibrilar.

En general, las interfases resina-dentina tratadas con nanopartículas poliméricas funcionalizadas con tideglusib han conseguido los mayores valores en las distintas pruebas de remineralización y *tests* de resistencia mecánica. Además, los resultados obtenidos muestran que los cristales formados con este nuevo biomaterial son de hidroxiapatita de alta madurez. Finalmente, los valores de las diferentes pruebas mecánicas que presentaron las nanopartículas funcionalizadas con tideglusib denotan que la remineralización producida fue de tipo intrafibrilar.

Nakabayashi, N., Nakamura, M., & Yasuda, N. (1991). Hybrid layer as a dentin-bonding mechanism. Journal of esthetic dentistry, 3(4), 133–138. https://doi.org/10.1111/j.1708-8240.1991.tb00985.x

Gungormus, M., & Tulumbaci, F. (2021). Peptide-assisted pre-bonding remineralization of dentin to improve bonding. Journal of the mechanical behavior of biomedical materials, 113, 104119. https://doi.org/10.1016/j.jmbbm.2020.104119

Osorio, R., Osorio, E., Medina-Castillo, A. L., & Toledano, M. (2014). Polymer nanocarriers for dentin adhesion. Journal of dental research, 93(12), 1258–1263. https://doi.org/10.1177/0022034514551608

Neves, V. C., Babb, R., Chandrasekaran, D., & Sharpe, P. T. (2017). Promotion of natural tooth repair by small molecule GSK3 antagonists. Scientific reports, 7, 39654. https://doi.org/10.1038/srep39654

Carvalho, R. G., Patekoski, L. F., Puppin-Rontani, R. M., Nakaie, C. R., Nascimento, F. D., & Tersariol, I. L. S. (2023). Self-assembled peptide P11-4 interacts with the type I collagen C-terminal telopeptide domain and calcium ions. Dental materials : official publication of the Academy of Dental Materials, 39(8), 708. https://doi.org/10.1016/j.dental.2023.06.004

Toledano, M., Aguilera, F. S., Fernández-Romero, E., Lagos, A. J., Bonilla, M., Lynch, C. D., & Osorio, R. (2024). Dentin remineralization using a stimuli-responsive engineered small

molecule GSK3 antagonists-functionalized adhesive. Dental materials : official publication of the Academy of Dental Materials, 40(3), 393–406. https://doi.org/10.1016/j.dental.2023.12.010

Bertassoni, L. E., Habelitz, S., Kinney, J. H., Marshall, S. J., & Marshall, G. W., Jr (2009). Biomechanical perspective on the remineralization of dentin. Caries research, 43(1), 70–77. https://doi.org/10.1159/000201593

Índice

1. Introducción

1.1. Concepto de odontología adhesiva.

En la caries dental se produce la desmineralización de la dentina, lo que lleva a una pérdida de minerales del diente que progresa hasta formar una cavidad que necesita ser restaurada [1]. A menudo, la restauración de estas cavidades se realiza mediante el uso de resinas compuestas. El proceso de unión adhesiva resina-dentina también constituye una causa importante de desmineralización, ya que implica la utilización de ácidos o adhesivos ácidos, que llevan a cabo el acondicionamiento de la dentina. Esta pérdida de minerales produce la exposición de la red de colágeno que conforma el componente orgánico dentinario [2].

La unión adhesiva resina-dentina implica una adhesión física, pero también química, donde el adhesivo debe difundir y envolver las fibras de colágeno expuestas, formando la capa híbrida. La capa híbrida y sus propiedades determinarán el éxito de la unión adhesiva a medio y largo plazo [2,3].

1.2. Problemas asociados a la odontología adhesiva actual.

El problema actual es que, en condiciones clínicas reales, los adhesivos no son capaces de envolver todo el colágeno expuesto, dando lugar a un gradiente de concentración decreciente, dejando como consecuencia colágeno desprotegido en la base de la capa híbrida. Este colágeno es susceptible a la degradación proteolítica mediada por metaloproteinasas de la matriz dentinaria y colagenasas bacterianas, lo que lleva a microfiltraciones y, en última instancia, a caries secundaria [4]. Esto convierte a la base de la capa híbrida en el talón de Aquiles de las restauraciones de composite [5].

Actualmente, las restauraciones de composite presentan una vida media de tan solo 5 años, y la caries recurrente es responsable del 60-70% de todas las restauraciones que se reemplazan, lo que resulta en importantes costes económicos y humanos [6].

1.3. Biomateriales remineralizadores para adhesión a dentina.

Se han propuesto diferentes alternativas para solucionar esta situación de alto impacto clínico. Entre ellas, la remineralización de la base de la capa híbrida mediante biomateriales. La utilización de biomateriales remineralizadores durante el protocolo adhesivo podría promover la protección de la interfase resina-dentina, a pesar de las

condiciones severas del entorno oral [7], como la fatiga mecánica y el estrés térmico [8]. Algunos de los biomateriales remineralizadores que han sido estudiados son adhesivos que liberan flúor o que han sido funcionalizados con agregados minerales, los cuáles generarán nuevos depósitos minerales, así como la inactivación de las metaloproteinasas presentes en la matriz dentinaria [9]. Otro tipo de abordaje se centra en elaborar materiales que tengan la capacidad de entrecruzar el colágeno expuesto para hacerlo más resistente a la degradación proteolítica [10]. A pesar de las diversas propuestas, ninguno de estos materiales ha mostrado resultados funcionales a largo plazo debido a su cinética de degradación, a su toxicidad o a que dejan parte del colágeno desprotegido en la interfase resina-dentina [11,12].

1.4. Nanopartículas poliméricas para adhesión a dentina.

Para el tratamiento de la dentina, es importante que los biomateriales empleados sean capaces de liberarse de forma controlada [13]. De esta forma, estos medicamentos serían capaces de ejercer una acción farmacológica prolongada en el tiempo, disponiendo de una dosis estable y segura, maximizando los beneficios de una menor frecuencia de aplicación y reduciendo la toxicidad y los efectos secundarios relacionados con dichos fármacos [14]. Actualmente, esto es posible gracias a los rápidos avances que ha experimentado la nanotecnología aplicada a la odontología. La nanotecnología permite elaborar materiales de escala nanométrica y aplicarlos de forma localizada y dirigida [15,16].

Un claro ejemplo de estos materiales son las nanopartículas poliméricas (NPs), las cuales han sido ya utilizadas anteriormente como *carriers* para liberar de forma controlada y prolongada diferentes agentes remineralizadores o antibacterianos [17,18]. Estas NPs son biomateriales biocompatibles y no reabsorbibles, fabricados a partir de ácido metacrílico, dimetacrilato de etilenglicol y metacrilato de 2-hidroxietilo, conectados covalentemente [19,20]. A lo largo de la columna de estas NPs poliméricas, hay cadenas de grupos carboxilato aniónicos (es decir, COO-) que facilitan la funcionalización con cationes y sustancias que presentan en su composición química grupos carboxílicos (COOH) o grupos amino (NH_2) [19]. Además, estas NPs están cargadas negativamente, por lo que tienen una alta afinidad por el colágeno desmineralizado, que se encuentra cargado positivamente [21].

Estas NPs sin funcionalizar no han sido capaces de mejorar las propiedades de la interfase resina-dentina *per se* en anteriores estudios *in vitro* [22]. Se ha propuesto, en anteriores investigaciones, la funcionalización de estos nanopolímeros con zinc [20], dexametasona [23], melatonina [24], doxiciclina [17] y otros agentes, con el fin de remineralizar la dentina o ejercer poder antibacteriano. La infiltración de NPs funcionalizadas con Zn en la dentina ha demostrado tener efectos antibacterianos y remineralizadores combinados [22]. Sin embargo, el efecto antimicrobiano del Zn^{2+} es limitado, ya que se basa en su propiedad bacteriostática, afectando de forma reversible sobre diversos procesos celulares (glucólisis, F-ATPasa, etc) [25]. Por otro lado, las NPs funcionalizadas con doxiciclina no han sido capaces de remineralizar la interfase adhesiva, aunque ejercieron un destacado papel antibacteriano [22]. Además, el uso repetido de antibióticos, probablemente, induzca la aparición de cepas resistentes locales, limitando la capacidad para erradicar los patógenos que conforman el *biofilm*, lo que llevaría eventualmente al fracaso del tratamiento [26,27].

1.5. Tideglusib como agente remineralizador.

Recientemente, Neves y cols. (2017) han propuesto un método biológico para la reparación y remineralización de la dentina, describiendo el papel del péptido glucógeno-sintasa-quinasa 3 (GSK-3). Mediante la inhibición del péptido GSK-3, se logra la activación de la vía de señalización Wnt/β-catenina, que está relacionada con procesos de reparación tisular temprana [28]. Varias moléculas antagonistas de GSK-3 han demostrado ser fármacos efectivos promoviendo los procesos naturales de formación de dentina reparativa, mediante la movilización de células madre residentes en la pulpa dental [28]. Además, el calcio es capaz de unirse a diferentes ligandos, como los del oxígeno de los grupos carboxilo, los grupos carboxamida o los grupos hidroxilo, lo que podría promover la formación de nuevos depósitos de calcio [29]. Los depósitos minerales formados por estas pequeñas moléculas han mostrado tener relaciones de carbonato/fosfato y de mineral/matriz iguales a las de la dentina nativa, e incluso una mayor cristalinidad y madurez de la apatita que la de la dentina natural [30,31].

El tideglusib (TDg) (NP-12, NPO3112) es una molécula inhibidora selectiva e irreversible de la glucógeno sintasa quinasa-3β (GSK-3β), no competitiva con ATP [30], y agonista de la vía canónica Wnt [32]. TDg es un material orgánico biodegradable, actualmente en ensayo para la enfermedad de Alzheimer, que promueve la reparación de

caries dentales y el nuevo crecimiento de minerales [30]. Esta molécula ha sido capaz de influir significativamente en los valores de expresión de diferentes proteínas relacionadas con la formación de nuevo mineral como son, la fosfatasa alcalina (ALP), la proteína morfogenética ósea, la osteocalcina o el colágeno tipo 1 [33].

Uno de los principales inconvenientes de estas proteínas agonistas de Wnt es su inestabilidad, así como el transporte hasta el lugar de acción farmacológica [32]. Previamente, se ha incorporado TDg a esponjas de colágeno marino biodegradable para desencadenar una liberación rápida del fármaco; sin embargo, un método capaz de mantener una cinética prolongada debería ser más efectivo [28].

Debido a las propiedades previamente mencionadas, las NPs podrían servir como portadores de TDg, para conseguir un efecto remineralizador prolongado y estable. La funcionalización de las NPs es posible mediante su inmersión en una solución con el TDg y posterior agitación durante dos horas a temperatura ambiente. Durante este proceso, el grupo COO^- de las NPs facilitará la unión del grupo funcional del tideglusib, NH_2. Hasta el presente trabajo de investigación, las NPs funcionalizadas con TDg (NPs-TDg) no han sido estudiadas para su aplicación en la remineralización de la interfase resina-dentina.

1.6. Propuesta de un nuevo biomaterial para la remineralización dentinaria.

En la presente tesis doctoral se utilizan partículas nanoestructuradas poliméricas hidrofílicas como transportadores, para evaluar la eficacia clínica *in vitro* del TDg en la interfase resina-dentina. Aprovechando la capacidad de las nanopartículas para ser funcionalizadas y el potente efecto remineralizador del TDg, se propone la utilización de este nuevo biomaterial para su aplicación en la remineralización de la dentina. Este material experimental se utilizará previo a la aplicación del adhesivo (*prebonding)* a modo de *primer,* con el objetivo de promover la reparación dentinaria, intentando devolver a la dentina sus propiedades biológicas, mecánicas y estructurales.

1.7. Evaluación de TDg-NPs como agente remineralizador

Nuestro grupo de investigación ha demostrado, en un estudio previo, la capacidad de las NPs-TDg para mejorar la fuerza de adhesión a dentina mediante un *test* de resistencia a la microtensión. Además, en dicho estudio, se ha visualizado con microscopía láser confocal la difusión del adhesivo dentro de los túbulos dentinarios, así como la capacidad de generar nuevos depósitos de calcio en la capa híbrida [34]. Esta

tesis doctoral supone la continuación de esta línea de investigación, y enfocará sus objetivos en evaluar la capacidad de TDg para devolver a la dentina sus propiedades mecánicas, mediante el aumento de la nanodureza de la capa híbrida [20]. Otro objetivo consistirá en usar la tinción tricrómica de Masson para observar cualitativamente la encapsulación del colágeno en la interfase resina-dentina. Se realizará también un análisis de espectroscopía RAMAN, que permitirá conocer las características bioquímicas de la interfase adhesiva. Se evaluarán, de una forma más precisa, los cambios morfológicos, microestructurales y mecánicos de la dentina mediante el uso de microscopía de fuerzas atómicas (AFM), análisis dinámico nanomecánico (nano-DMA) y módulo de Young, respectivamente. Y finalmente, se observarán los cambios producidos en los cristales de hidroxiapatita (HAp) a nivel físico y ultraestructural mediante el uso combinado de técnicas de difracción de rayos X (XRD) y microscopía electrónica de transmisión (TEM).

Todas estas pruebas se realizarán en interfases de resina-dentina que serán sometidas a desafíos de: 1) inmersión durante 24h en una solución de fluido corporal simulado (SBFS), 2) ciclado mecánico y 3) ciclado térmico, que simularán las condiciones orales. Esto es importante. ya que se ha demostrado que la durabilidad a largo plazo de la adhesión resina-dentina puede verse comprometida debido a diferentes tipos de estrés, como la masticación, la deglución o los hábitos parafuncionales [35,36].

2. Hipótesis

La hipótesis del presente trabajo es que la funcionalización de nanopartículas poliméricas con tideglusib mejora la remineralización y la cristalinidad de los depósitos minerales producidos, así como las propiedades mecánicas, estáticas y dinámicas, a lo largo de la interfase resina-dentina.

3. Objetivos

3.1. Objetivo general

Determinar si la infiltración de nanopartículas poliméricas funcionalizadas con tideglusib en dentina acondicionada con ácido fosfórico y previa a la aplicación del adhesivo, mejora la remineralización y las propiedades mecánicas de la interfase resina-dentina.

3.2. Objetivos específicos

- Objetivo específico 1**:** Valorar cualitativamente la encapsulación del colágeno por la resina adhesiva y la remineralización efectuada; evaluar la recuperación mecánica mediante un *test* de nanoindentación, y realizar un análisis de la composición químico-molecular de las interfases tratadas con nanopartículas funcionalizadas con tideglusib y sometidas a desafíos térmico-mecánicos.

- Objetivo específico 2: Evaluar las propiedades viscoelásticas, la capacidad para disipar energía y la morfología de las interfases resina-dentina tratadas con nanopartículas funcionalizadas con tideglusib y sometidas a diferentes tipos de estrés que simulan los de la cavidad oral.

- Objetivo específico 3: Realizar un análisis físico-cristalográfico de la madurez de la hidroxiapatita formada y de la elasticidad de las interfases resina-dentina infiltradas con nanopartículas funcionalizadas con tideglusib tras ser sometidas a diferentes desafíos.

4. Metodología

Para alcanzar los objetivos propuestos, la metodología de la presente tesis doctoral ha sido la siguiente:

- Actividad 1: Realizar un estudio *in vitro* donde se evalúe la capacidad de recuperación mecánica de la capa híbrida mediante un *test* de nanoindentación que calcule la nanodureza. Determinar, cualitativamente, la capacidad de encapsulación del colágeno mediante la tinción de tricrómico de Masson y llevar a cabo un análisis de espectroscopía Raman y de *clusters* para conocer la composición molecular de las interfases resina-dentina tratadas con NPs-TDg y sometidas a desafíos térmicos y mecánicos.

- Actividad 2: Analizar el comportamiento viscoelástico y la capacidad de disipar energía, acompañado de un análisis morfológico mediante microscopía de fuerzas atómicas de las interfases resina dentina tratadas con NPs-TDg bajo diferentes tipos de estrés.

- Actividad 3: Investigar el efecto que tiene la infiltración de NPs-TDg en la formación de hidroxiapatita, cristalinidad y elasticidad en interfases de resina-dentina sometidas desafíos térmicos y mecánicos.

5. Resultados

Siguiendo la normativa del Programa de Doctorado de Medicina Clínica y Salud Pública de la Universidad de Granada para las Tesis presentadas con la modalidad de agrupación de trabajos de investigación publicados, se incluyen en el apartado de resultados los tres artículos publicados:

- Toledano, M., **Fernández-Romero, E**., Aguilera, F. S., Osorio, E., Rodríguez-Santana, J. A., Garrido, M., Solís, P. A., García-Godoy, F., & Osorio, R. (2024). Tunable polymer-peptide hybrids for dentin tissue repair. Journal of dentistry, 148, 105027. https://doi.org/10.1016/j.jdent.2024.105027.

- Toledano, M., **Fernández-Romero, E**., Osorio, E., Aguilera, F. S., Lynch, C. D., Osorio, M. T., Toledano, R., & Osorio, R. (2024). Effect of the anti-Alzheimer drug GSK-3β antagonist on numerical modeling of the energy dissipation through the resin-dentin interface. Dental materials: official publication of the Academy of Dental Materials, S0109-5641(24)00271-9. Advance online publication. https://doi.org/10.1016/j.dental.2024.09.005.

- Toledano, M., **Fernández-Romero, E**., Osorio, M. T., Osorio, E., Aguilera, F. S., Toledano, R., & Osorio, R. (2024). Investigation of the effect of Tideglusib on the hydroxyapatite formation, crystallinity and elasticity of conditioned resin-dentin interfaces. Journal of dentistry, 150, 105334. Advance online publication. https://doi.org/10.1016/j.jdent.2024.105334.

Los artículos completos se pueden consultar en el Anexo, adjunto al final de la Memoria, desde la página 65.

6. Discusión

Las publicaciones que conforman esta tesis doctoral presentan algunas similitudes metodológicas entre sí, ya que recurren al mismo protocolo adhesivo (mismos grupos) y a un procedimiento similar para obtener las muestras de interfase resina-dentina. Además, en los tres manuscritos, los grupos se someten a los mismos métodos de almacenamiento/desafíos (mismos subgrupos). El biomaterial experimental consiste en nanopartículas poliméricas funcionalizadas con tideglusib. Las NPs utilizadas para transportar el TDg son capaces de actuar como biomateriales quelantes de fosfato y calcio [37], promoviendo la nucleación de minerales [38]. Estas NPs poliméricas no se disuelven ni reabsorben y se ha observado que son capaces de propiciar depósitos de fosfato cálcico amorfo en su superficie. Además, tienen la habilidad de adherirse a las fibrillas de colágeno e incorporarse al tejido remineralizado [18]. El crecimiento del fosfato de calcio puede ser modelado por los grupos COOH que contiene, como se ha demostrado previamente en otros polímeros sintéticos [39,40]. En esta investigación, se han llevado a cabo técnicas a diferentes niveles (histológico, morfológico, cristalográfico, químico, físico, ultraestructural y mecánico) con el objetivo de evaluar si la infiltración de NPs-TDg es efectiva promoviendo la remineralización y mejorando las propiedades mecánicas de interfases adhesivas resina-dentina. Existe una íntima relación entre la remineralización intrafibrilar o funcional y una mejora en las propiedades mecánicas de la interfase resina-dentina [41]. Por esto, en cada uno de los estudios publicados se combinan técnicas que analizan ambas propiedades, remineralización y capacidad de mejora mecánica. Para una mayor claridad, la discusión de los artículos presentados se realizará de forma conjunta.

En este estudio, para los valores de nanodureza, los especímenes del grupo *test* obtuvieron los resultados más altos, tanto en la capa híbrida como en la base de la capa híbrida en los diferentes subgrupos (Figura 2 del Artículo 1), siendo los más elevados en las interfases resina-dentina después de 24 h de almacenamiento en SBFS. Este aumento de los valores de propiedades mecánicas no solo se obtuvo para la nanodureza, sino que cuando se midió el módulo de Young, los grupos control y de NPs sin funcionalizar registraron las propiedades más bajas (Figura 2 del Artículo 3), en comparación con el grupo de las NPs-TDg. El módulo de Young aporta información sobre el comportamiento elástico de un material. Este aumento de las propiedades mecánicas del colágeno

previamente desmineralizado sugiere, de forma indirecta, una precipitación de depósitos minerales en la interfase resina-dentina [39]. Los valores obtenidos en nanodureza y módulo de Young también se correlacionan con los valores de resistencia a la microtensión obtenidos por Toledano y cols (2024) [34]. Además, el tipo de fallo en este *test* fue mayoritariamente mixto, probablemente debido a los depósitos de minerales en la capa híbrida y en la base de la capa híbrida [34], desde donde ocurrieron la mayoría de las líneas de fractura, tal y como revelan las imágenes de microscopía electrónica de barrido de emisión de campo (FESEM) en dicho estudio. En las imágenes de FESEM publicadas por Toledano y cols (2024) también puede observarse cómo las NPs-TDg permiten la formación de *tags* de resina y la precipitación de minerales alrededor de la dentina peritubular e intertubular, propiciando la oclusión de los túbulos dentinarios [34].

En la presente investigación, dicha precipitación de minerales puede observarse de forma cualitativa en los cortes histológicos obtenidos con la tinción de tricrómico de Masson. Este método colorimétrico muestra de color verde el colágeno mineralizado (dentina), de color rojo el colágeno desmineralizado y de color beige la resina adhesiva. Como resultado, el colágeno desmineralizado infiltrado por la resina adhesiva aparecerá con tonalidades anaranjadas. En las muestras tratadas con las NPs-TDg después de 24 h de almacenamiento en SBFS se puede visualizar una discontinuidad del color rojo a lo largo de las interfases resina-dentina (Figura 3C del Artículo 1), indicando un avance relativo del frente de remineralización [20]. Además, el desarrollo de los túbulos dentinarios en este subgrupo fue notable, prolongándose dicha remineralización hasta el colágeno desmineralizado, indicando ganancia de mineral tanto de la dentina peritubular como intertubular. Cabe destacar que la formación de nuevos depósitos minerales no se limitó a la capa híbrida, sino que se extendió a las primeras 5-20 μm de los túbulos dentinarios [7,42]. Estos resultados son comparables a los obtenidos por Toledano y cols (2024) en el análisis de microscopía láser confocal, donde se utilizó la fluoresceína para revelar en color verde la permeabilidad de los túbulos dentinarios y la rodamina para observar en color rojo la distribución del adhesivo [34]. Por otro lado, cuando se utilizaron NPs no funcionalizadas, se visualizó una clara presencia de dentina desmineralizada sin proteger a lo largo de la interfase resina-dentina (banda de color rojo) (Figuras 3B, 3E, 3H del Artículo 1). La mayor remineralización observada fue en el grupo de las NPs-TDg después del ciclado mecánico. Esto podría deberse a que el ciclado mecánico ha demostrado mejorar la resistencia del colágeno a la degradación enzimática [43]. En las

muestras sometidas al desafío de termociclado, también pudo visualizarse en el grupo de TDg-NPs un mayor número de franjas de colágeno remineralizado cubriendo las paredes tubulares e incluso en la dentina intertubular (Figura 3I del Artículo 1), en comparación con los grupos control y de NPs no funcionalizadas (Figura 3G y 3H del Artículo 1, respectivamente), que presentaron trazadas teñidas de color rojo en mayor medida. Estos hallazgos sugieren un mayor grado de dentina descalcificada y sin infiltrado adhesivo en estos dos grupos, que se confirma mediante la visualización del menor grado de penetración [1453/1667] y de conversión del adhesivo [1637/1608] en el análisis de espectroscopía Raman (Tabla 4 del Artículo 1). El termociclado, además de permitirnos simular de una forma más acertada las condiciones orales reales, ha demostrado *in vivo* e *in vitro* ser capaz de aumentar la actividad de la ALP, así como la estimulación de otras proteínas de la matriz dentinaria [34,44], lo que podría resultar en una mayor remineralización en comparación al almacenamiento durante 24h en SBFS. Las NPs-TDg son capaces de penetrar en los túbulos dentinarios formando parte de los *tags* de resina, así como de infiltrar la dentina intertubular y generar frentes activos de remineralización. Estos resultados refuerzan los hallazgos que revelaron el análisis histológico y morfológico de Toledano y cols (2024), mediante microscopía láser confocal y FESEM [34]. Los presentes datos muestran que al utilizar NPs-TDg se favorece una mayor protección de la capa híbrida y de la base de la capa híbrida a lo largo de toda la interfase resina-dentina. Hasta el momento, la mejora en las propiedades mecánicas, unida a los datos cualitativos observados, sugiere que la precipitación mineral podría tener lugar en la sección intrafibrilar del colágeno [41,45].

Para analizar cuantitativamente la remineralización producida, así como la madurez cristalográfica, se llevó a cabo un análisis bioquímico y físico de la cristalinidad del precipitado mineral formado, mediante espectroscopía Raman y difracción de rayos X, respectivamente. El análisis bioquímico con espectroscopía Raman reveló que las interfases tratadas con NPs-TDg obtuvieron el mayor grado mineralización (Tabla 1 del Artículo 1), tal y como muestran los valores de intensidad de los picos fosfato (PO_4) (961 cm^{-1}) y picos carbonato (CO_3^{2-}) (1070 cm^{-1}) en la Figura 4 del Artículo 1. Monitorizar la intensidad del pico 961 cm^{-1} nos permite detectar diferencias en el contenido de fosfato [46]. Además, en este estudio se han representado y analizado los valores de intensidad del pico fosfato con un mapa micro-Raman en 2D (Figura 6 del Artículo 1). Cuando las muestras fueron tratadas con NPs-TDg, la mayor presencia relativa de minerales pudo observarse en toda la interfase resina-dentina, pero específicamente en la base de la capa

híbrida, que reflejó los picos de máxima intensidad en todos los subgrupos (Tabla 1 del Artículo 1). Desde el punto de vista físico, los minerales formados también mostraron el mayor tamaño de cristal y grano, textura (R_{hkl}) más cercana al valor 1 y la menor microdeformación en los planos de difracción 002 y 310 en el análisis de XRD, cuando los especímenes eran infiltrados con NPs-TDg después del ciclado mecánico (Tabla 1 del Artículo 3). Estos minerales se trataban principalmente de prismas de morfología hexagonal y de tamaño submicrométrico, que seguían una alineación bien definida, confirmando así una mineralización biomimética (Figura 5 del Artículo 3). Además, cabe destacar, que en las muestras tratadas con NPs-TDg, los patrones de XRD indicaron que los cristales formados están constituidos principalmente por HAp de una alta cristalinidad, es decir, con la anchura máxima a media altura (FWHM) más baja (Tabla 1 del Artículo 3).

Bioquímicamente, el análisis de espectroscopia Raman de un solo punto específico en la dentina resulta insuficiente para caracterizar con precisión la composición general de la interfase resina-dentina. Es por esto, que se incorporaron técnicas de análisis de datos 2D con información espacial [47,48]. El análisis micro-Raman 2D unido a un análisis jerárquico de clústers (HCA), nos permite visualizar la distribución espacial de los principales espectros y compuestos químicos. En este caso, el HCA muestra cinco grupos de clústeres diferenciables que reunían características similares [49]. Cada clúster fue representado con un color diferente [50] (Figura 5 del Artículo 1). En la interfase adhesiva de los especímenes tratados con NPs-TDg y sometidos a ciclos mecánicos, los resultados de HCA Raman mostraron un aumento general del pico fosfato (Figura 4F y 6F del Artículo 1), en comparación con las muestras tratadas con NPs no funcionalizadas (Figura 4E y 6E del Artículo 1). El clúster correspondiente a la capa híbrida (HCA_4) (Figura 5F del Artículo 1), que aparece en el gráfico de color púrpura, muestra en la Figura 4F del Artículo 1, una ligera disminución en el área de la capa híbrida (de 11 a 8 unidades de intensidad) después del ciclado mecánico en las muestras tratadas con NPs-TDg, cuando son comparadas con los especímenes infiltrados con NPs no funcionalizadas (Figura 4E del Artículo 1). La ganancia mineral que ocurrió en el colágeno desmineralizado hizo que disminuyera el porcentaje de varianza en la dentina tratada con NPs-TDg. Esta tendencia se invirtió en la base de la capa híbrida (HCA_3), donde las varianzas cambiaron del 11 % en muestras infiltradas con NPs no funcionalizadas, al 21% cuando los especímenes infiltrados con NPs-TDg se sometieron a ciclado mecánico. Este hecho indica una remineralización que va desde la base de la capa híbrida, hacia la parte

más superior de la misma, cuando se usa el inhibidor de GSK3, es decir una remineralización controlada y biomimética [3].

Por otro lado, la capa híbrida formada cuando las muestras son tratadas con NPs-TDg y sometidas a termociclado aumentó su porcentaje de varianza (27%) (Figura 4I del Artículo 1) de área púrpura (clúster en la Figura 5I del Artículo 1), en comparación con el resto de grupos. Una posible explicación a este aumento de área de la capa híbrida es un incremento del mineral extrafibrilar, considerando que este grupo no aumentó sus valores de nanodureza después del termociclado [45] (Figura 2 del Artículo 1). Los picos a 1340 cm^{-1} asociados con α-hélices también se incrementaron en las muestras tratadas con TDg (Figura 4 del Artículo 1), lo que indica una mayor capacidad de orientación molecular que podría facilitar la mayor cristalización [51] (Tabla 3 del Artículo 1) observada en el análisis de XRD (Tabla 1 del Artículo 3). En cuanto al gradiente en contenido mineral (GMC) en la capa híbrida, las interfases resina-dentina tratadas con NPs-TDg termocicladas alcanzaron los valores más altos (0,29) (Tabla 2 del Artículo 1). El incremento relativo de mineral en la capa híbrida fue de naturaleza amorfa, pero cristalina en la base de la capa híbrida, donde se obtuvieron valores más bajos de GMC junto con valores altos de nanodureza. El GMC más alto se obtuvo en la base de la capa híbrida en las interfases adhesivas creadas después de la infiltración con NPs-TDg a las 24 h (0,17) (Tabla 2 del Artículo 1). Esto se correlaciona también con el valor máximo obtenido de nanodureza (0,64 GPa) (Figura 2 del Artículo 1). Los resultados de GMC nos indican por tanto, desde un punto de vista bioquímico, que hay una menor sustitución de carbonato por fosfato, y por consiguiente denota una mayor madurez y cristalinidad en comparación con el grupo control [52,53].

El análisis químico demuestra un proceso de amorfización en todos los subgrupos de estudios, después de infiltrar la dentina con NPs-TDg (Tabla 2 del Artículo 1), ya que la FWHM aumentó tanto en la capa híbrida como en la base de la capa híbrida, excepto cuando se evaluó el carbonato en las muestras sometidas a ciclado mecánico (Tabla 2 del Artículo 1). Por otro lado, el análisis de XRD muestra que el termociclado de las interfases resina-dentina produjo una amorfización de cristales, asociada a mayores grados de impurezas de los cristalitos en toda la interfase resina-dentina [54] en ambos planos, 002 y 310 (Tabla 1 del Artículo 3), junto con una apariencia de apatita poliédrica (Figura S4A del Artículo 3) y un ensanchamiento de los picos de difracción (Figura 3A inserciones A y B del Artículo 3). Esta amorfización probablemente está asociada a la incorporación de

CO_3 como sustituto del PO_4^{3-} en la red de apatita [51]. Cuando los grupos OH son sustituidos, ocurre el efecto opuesto [55]. Sin embargo, el mayor aumento observado en el pico de carbonato (1070 cm^{-1}) en las muestras tratadas con NPs-TDg (Tabla 1 del Artículo 1) indica una mayor presencia de apatita carbonatada en estas muestras, en comparación con el resto de los grupos. La apatita carbonatada se considera un precursor de la HAp [51]. La capa híbrida en las interfases infiltradas con NPs-TDg sometidas a ciclado mecánico mostró los valores de intensidad más bajos (22.48) (cristalinidad) y, por el contrario, la base de la capa híbrida obtuvo los valores más altos (22.48) (amorfización). La presencia de fosfato de calcio amorfo supone un entorno local rico en iones, proporcionando condiciones favorables para la formación *in situ* de nucleación mineral en la base de la capa híbrida (Figura S4J del Artículo 3) [56]. Por el contrario, si lo que se forman son fosfatos de calcio cristalinos, los tiempos de degradación serán más largos, y la liberación de iones será menor [57], lo cual representa también una gran ventaja desde un punto de vista clínico, pues la mejora obtenida en propiedades mecánicas y ópticas será más mantenida en el tiempo. En la interpretación de los resultados obtenidos con XRD es necesario tener en cuenta que picos más estrechos (Figura 3A del Artículo 3) significan menos variación estructural en los ángulos y distancias de la red cristalina, y que a su vez una FWHM más baja indica un mejor orden relativo cristalográfico de átomos [53] mostrando alta pureza cristalográfica [58]. Los resultados obtenidos van en consonancia a los que mostraron el estudio de espectroscopía Raman. La morfología de los minerales formados en el grupo experimental sometido a ciclado mecánico se correspondía con cristales ensamblados, tal y como muestra el análisis de difracción de electrones en área seleccionada (SAED) (Figuras 5A, 6A del Artículo 3). El grupo de Deng y cols (2021) [59] obtuvo resultados similares en su análisis de XRD. Se visualizaron altas intensidades de difracción en las muestras tratadas con las NPs-TDg después del ciclado mecánico en los planos 112 y 211, donde los contornos de difracción revelan la existencia de HAp (barras rojas) con picos cristalinos nítidos y estrechos (Figura 3A del Artículo 3). De igual forma, la evaluación de la difracción reflejó anillos más brillantes en este grupo (Figura 3C del Artículo 3), lo que significa un mayor estrechamiento de los picos.

En la Tabla 1 del Artículo 3 se muestra el tamaño del cristalito, donde el grupo experimental logró el mayor aumento de tamaño medio, junto con una dirección paralela (H, altura de los cristalitos) [plano 002(H)] y perpendicular (L, diagonal base más larga)

al eje c [plano 310(L)]. La ecuación de Scherrer revela anchuras similares en el grupo control (6,74 nm) (Tabla 1 del Artículo 3) a las obtenidas por Kinney y cols [60], que indicaron un grosor de ~5,0 nm. En cuanto a los patrones de difractografía mostrados en el grupo experimental, estos van desde picos amplios y difusos a las 24 horas, a picos más cristalinos después de los ciclos mecánicos (Figuras 3A, 3B, 3C del Artículo 3), garantizando que la amorfización es un proceso dinámico [55]. Después de analizar estos resultados de XRD, es posible (i) relacionar la mayor cristalinidad y el crecimiento a lo largo de la dirección ortogonal al eje c; y (ii) aceptar que el mayor grosor de cristalitos en este grupo (22,20 y 10,89 nm en los planos 002 y 310, respectivamente) (Tabla 1 del Artículo 3) se ajusta a una mayor mineralización y madurez dentinaria.

Estos datos se vieron reforzados tras el análisis de TEM-SAED y el mapeo elemental de la espectroscopía por difracción de energía (EDS), que permitió definir la estructura cristalina de los depósitos minerales. El grupo experimental después del ciclado mecánico reveló una alta presencia de P y Ca (Figuras 6D, 6E y 6F del Artículo 3). De igual manera, el análisis de SAED (Figura 5B del Artículo 3) coincidía con los anillos más brillantes formados en los planos 002, 211 y 112, mostrados por el análisis de XRD (dobles flechas en la Figura 3C del Artículo 3) en comparación con el subgrupo sometido a 24 h en SBFS (Figura 3B del Artículo 3) o a termociclado (Figura 3D del Artículo 3), indicando un menor ensanchamiento de las líneas de los picos. El SAED simulado correspondiente a la dirección 002 de las Figuras 4C y 5B del Artículo 3 fue coherente con la imagen de la Transformada Rápida de Fourier (FFT) de la Figura 8C del Artículo 3, indicando que los nanobastones observados se trataban de HAp [61]. Además, los contenidos de P y Ca revelaron también, indirectamente, la formación de HAp [62] (Figura 6C del Artículo 3). Las intensidades relativas más altas después del análisis TEM en el plano 002 a 0,352 nm (alta intensidad) [31% (Tabla S1 del Artículo 3)] y en el plano 004 a 0,171 nm (baja intensidad) [74% (Tabla S1 del Artículo 3)] confirman el mayor contenido de HAp en las formaciones minerales en el grupo experimental sometido a ciclado mecánico. Esta HAp se manifestó mediante agrupaciones de cristales delgados y largos (Figuras 5C, S3C del Artículo 3). Se observaron nanocristales en forma de varilla con una longitud de 22,20 nm y un ancho de 11,56 nm (Tabla 1 y Figura 5C del Artículo 3). Las imágenes de alta resolución de TEM revelaron que las nanovarillas poseen la estructura monocristalina mencionada. Por lo tanto, se puede concluir la presencia de una

fase de apatita [63]. Además, el análisis de FFT reveló también una naturaleza cristalina de los minerales (Figura 8C del Artículo 3).

Según el análisis de FFT, las interfases resina-dentina del grupo experimental consiguieron altos niveles de átomos de calcio y fosfato (Figuras 8D·I, 8D·II del Artículo 3) en comparación al resto de grupos. El tamaño de grano medido por la ecuación aplicada de Scherrer-Wilson ha mostrado en el plano 002 que los cristales de HAp se volvían más pequeños (~1,14 veces) en interfases resina-dentina tratadas con NPs sin funcionalizar (18,97 nm) que en muestras tratadas con NPs-TDg (21,65 nm) (Tabla 1 del Artículo 3) después del ciclado mecánico. En las reflexiones observadas en el plano 310 esta diferencia aumentó ~1,65 veces (Tabla 1 del Artículo 3). El desplazamiento de átomos respecto a su posición de referencia dentro de una red perfecta provoca microdeformaciones. El aumento de microdeformaciones es dependiente del orden de la red, mientras que el aumento de tamaño es independiente del orden de la misma [64]. En ambos planos 002 y 310, las interfases resina-dentina infiltrada con NPs-TDg y sometidas a ciclado mecánico lograron los valores más bajos de microdeformaciones ($1{,}09 \times 10^{-6}$ y $0{,}4 \times 10^{-5}$ respectivamente) (Tabla 1 del Artículo 3). La sustitución del carbonato por el fosfato (tipo β) en la HAp causa lo que se conoce como "desorden de la red", que está correlacionado con la distorsión del tetraedro de fosfato [65] y en este estudio ocurrió cuando los especímenes se trataron con NPs no funcionalizadas. Se ha establecido en este estudio una asociación entre altos valores de microdeformaciones en interfases resina-dentina tratadas con NPs no funcionalizadas, amorfización y un aumento notable de polielectrolitos o iones [64] (Figuras 7C y 7D del Artículo 3), mientras que en las muestras tratadas con NPs-TDg (Figuras 8D·I, 8D·II del Artículo 3) la composición de la apatita del análisis elemental mostró los niveles más altos de átomos de calcio y fosfato.

También se analizaron los índices de textura (R_{hkl}) de estructuras policristalinas según la Eq. 2) del Artículo 3. Los valores de R mayores o menores que 1.0 determinan la orientación preferida del grano o la textura [66,67]. La textura influye en la resistencia a la fractura y además, regula los cambios microestructurales [68]. Las muestras tratadas con NPs-TDg después de ciclado mecánico, alcanzaron los valores más cercanos a este número en los planos 002 y 310 (0,778 y 1,134 respectivamente) (Tabla 1 del Artículo 3), relacionando así la orientación con una alta estabilidad química [69]. Los cristales producidos en el grupo experimental mostraron menos espacio entre los ángulos de co-alineación (Figuras 5A, 5C, 6 del Artículo 3) que en el resto de grupos (Figura 4 del

Artículo 3). Además, el análisis de TEM evidenció la formación de nanocristales planos de 15-30 nm de longitud (Figura 6 del Artículo 3) desarrollados a lo largo del eje c y de morfología hexagonal (Figuras 5, S3 del Artículo 3). Por otro lado, las imágenes TEM del grupo control tras el ciclado mecánico exhibieron cristales de apatita polimórfica de ~30-160 nm (Figuras S5A, S5B del Artículo 3). Además, este grupo también mostró intensidades intermedias en ambos anillos de Debye (inserción de la Figura 5SB del Artículo 3) en 310 (0,238 nm) y en 330 (0,156 nm), probablemente debido al papel que juegan los distintos componentes del fosfato de calcio amorfo (ACP), como el fosfato de calcio octacálcico y el fosfato tricálcico beta (Tabla S1 del Artículo 3). A día de hoy, no se conoce el método a través del cual se produce la maduración de ACP a HAp [70].

El aumento en el contenido mineral se vio acompañado de una mejora en el componente orgánico. El pico del grupo fenilo (1003 cm^{-1}) mostró los valores más altos en el grupo experimental, indicando mejoras en la naturaleza y estructura secundaria del colágeno (Tabla 3 del Artículo 1). En cambio, las muestras no tratadas con la molécula inhibidora de GSK-3 contenían una matriz de colágeno con calidad deficiente, caracterizada por una falta de conformación y organización [71,72]. La medición del grupo fenilo es importante, ya que antes de la aparición de cristales de HAp, suele haber un aumento en la señal espectral de proteínas en la fenilalanina [51]. Por otro lado, el máximo entrecruzamiento del colágeno fue observado en las muestras tratadas con NPs-TDg (Tabla 3 del Artículo 1). Normalmente, después de la precipitación mineral, tiene lugar un aumento del entrecruzamiento del colágeno [73,74], lo cual puede considerarse como la base para la mejora del rendimiento mecánico observado en estas interfases resina-dentina [75]. En general, la aplicación de NPs-TDg junto con el ciclado mecánico alcanzó el pico más alto de glicación avanzada (AGEs)-pentosidina, a 1550 cm^{-1} (Tabla 3 del Artículo 1). La pentosidina es considerada el componente principal de los productos finales de AGEs [76]. Estos resultados pueden deberse a que el ciclado mecánico haya desencadenado la conversión de cetoaminas (entrecruzamientos inmaduros), dando lugar a un pico más pronunciado en 1550 cm^{-1}, tanto en la capa híbrida como en la base de la capa híbrida. Generalmente, esto se asocia a la formación de entrecruzamientos no reducibles, reforzando los resultados obtenidos en los anteriores análisis y denotando que el proceso inicial de remineralización es intrafibrilar, acompañado de una mejora de las propiedades mecánicas [75]. De esta forma, el colágeno puede servir de andamio activo

promoviendo la formación de la HAp cristalina orientada dentro de las fibrillas [77,78], tal y como ha sido observado en el análisis de XRD.

Se describió también el comportamiento viscoelástico de las interfases resina-dentina de los diferentes grupos mediante un análisis DMA. El análisis DMA reveló que tanto las NPs no funcionalizadas, como las NPs-TDg facilitaron la formación de grietas en la dentina; sin embargo, solo la presencia del TDg favoreció la remineralización de las zonas de fractura. La capacidad de almacenar energía de un material durante un ciclo de carga viene definida por el módulo de almacenamiento (elástico), mientras que la capacidad de un material para disipar energía está caracterizada por el módulo de pérdida (viscoso). Ambos pueden medirse mediante el análisis mecánico dinámico [79].

Como tanto el módulo de almacenamiento, como el módulo de pérdida están implicados en la definición del módulo complejo (E*) y de tan delta (δ), solo estos dos últimos se discutirán en detalle. Tan (δ) se define como la relación de la energía disipada con la energía almacenada y permite conocer la recuperación elástica de un material, mientras que el módulo complejo se define como la resistencia de un material a ser deformado [80]. Los valores más altos del módulo complejo en la capa híbrida y en la base de la capa híbrida se obtuvieron cuando las muestras tratadas con NPs no funcionalizadas o las NPs-TDg se sometieron a ciclado mecánico (Tabla 1 del Artículo 2). Esta mayor resistencia a la deformación dinámica que mostraron estos dos grupos refuerza la teoría de que ha tenido lugar una precipitación mineral intrafibrilar [81]. Los valores más altos en el subgrupo de ciclado mecánico pueden deberse a una estimulación de la actividad de la ALP presente en la matriz dentinaria. La ALP tisular, existente en todas los tejidos mineralizados, es una metaloenzima del zinc capaz de proteger al colágeno [82]. Además, hidroliza un amplio espectro de monoésteres de fosfato [83] que promueve la supersaturación de apatita [84], lo que facilita la penetración del fosfato de calcio amorfo en el colágeno.

Por otro lado, la dentina peritubular ha mostrado valores de módulo complejo significativamente más altos que la dentina intertubular (~1,5 veces) cuando se utilizaron NPs no funcionalizadas y se ciclaron mecánicamente las muestras (134,49 vs 87,62 GPa) (Tabla 1 del Artículo 2). Por lo tanto, los resultados de nano-DMA revelan una heterogeneidad en la distribución de las propiedades mecánicas entre la dentina peritubular e intertubular (Figura 1 del Artículo 2) en este grupo. Cuando se presentan

propiedades viscoelásticas discrepantes en las distintas estructuras dentro de la dentina, aumenta el riesgo de fractura, ya que la energía se concentra en exceso en las regiones de bajo módulo elástico [85]. Las propiedades viscoelásticas de la dentina intertubular y peritubular son de vital importancia en la prevención y propagación de *cracks* de dentina [86]. De acuerdo con Misra y cols. (2004) [87], según los mapeos obtenidos con nano-DMA, las fracturas pueden darse en tres ubicaciones diferentes de la interfase resina-dentina, dependiendo donde se concentran las tensiones (Figura S1 del Artículo 2): i) en la interfase entre los *tags* de resina y la dentina peritubular; ii) en los *tags* de resina adhesiva próximos a la capa híbrida; o iii) cerca de la base de la capa híbrida. Además, si la unión entre la dentina peritubular y los *tags* de resina no es perfecta como en la Figura 3B del Artículo 2, entonces dentro de la capa híbrida es muy probable que se concentren tensiones y la integridad de la interfase resina-dentina peligre a medio plazo [88].

Por el contrario, cuando se utilizaron NPs-TDg tras el ciclado mecánico, el módulo complejo en la dentina peritubular fue ~1,1 veces mayor que en la dentina intertubular, pero sin diferencias significativas (Tabla 1 del Artículo 2), revelando homogeneidad en la distribución de propiedades mecánicas entre la dentina intertubular y peritubular. Este hecho facilita la disipación de energía a lo largo de la estructura [89]. En estas mismas muestras, los valores de tan (δ) en la dentina intertubular fueron significativamente más altos (~2,9 veces) que en la dentina peritubular. El mapa 3D de la distribución de tan (δ) (Figura 2C del Artículo 2) para los especímenes tratados con NPs-TDg, muestra este mismo comportamiento viscoelástico opuesto entre dentina peritubular e intertubular. Unos valores bajos de tan (δ) significan que la proporción de energía que absorbe un sistema será mayor [90]. Se observa también como el grupo experimental fue capaz de promover la oclusión total de los túbulos dentinarios, creando plataformas gruesas de mineral en el estudio de AFM (Figura 4B del Artículo 2) tal y como se observó también en las imágenes de FESEM en Toledano y cols (2024) [34]. Este hallazgo tiene repercusiones en el comportamiento mecánico de la dentina, pues una semioclusión de los túbulos causaría un mayor riesgo de microfracturas en la interfase resina-dentina que aquellos túbulos que se encuentran completamente ocluidos (Figuras 3A y S4B del Artículo 2) [91,92]. El análisis de AFM también mostró que la dentina infiltrada con NPs-TDg después del ciclado mecánico (Figura S5B del Artículo 2) y térmico (Figura S5C del Artículo 2) promovía un aumento significativo del diámetro de las fibrillas de colágeno (Figura 5 del Artículo 2), lo cual sugiere un entrecruzamiento del colágeno o de

mineralización intrafibrilar tal y como se confirmó anteriormente [85,93] en el análisis de microscopía Raman. Estos resultados obtenidos se relacionan con los publicados por otros autores, quienes afirman la capacidad que tiene el TDg de promover la formación de puentes dentinarios [32]. La remineralización producida se mostró en forma de varillas o arbotantes (Figura 4 del Artículo 2) que podrían prevenir la propagación de grietas y de fracturas [92]. Se han propuesto diversas teorías para explicar el papel del TDg en la mineralización de tejidos duros: i) la presencia de péptidos podría inducir la atracción electrostática de iones solubles, generando zonas locales de supersaturación que promueven la nucleación en la interfase resina-dentina [11]; ii) distintos ligandos presentes en los péptidos, como grupos hidroxilo, carboxilo o carboxamida podrían unirse al calcio y provocar su precipitación controlada [29]; iii) el TDg podría ser capaz de provocar un aumento de la rigidez de las fibras de colágeno, causando así una mayor resistencia a la proteólisis de las fibras de colágeno tipo I [34]; o iv) la dentina peritubular puede absorber preferentemente algunos péptidos, donde existe una importante actividad remineralizadora [6]. En la capa híbrida, las interfases tratadas con NPs-TDg y sometidas a termociclado mostraron un módulo complejo más alto que las tratadas con NPs no funcionalizadas. En general, el ciclado mecánico promovió un módulo complejo más alto que el termociclado (Tabla 1 y Figuras 1B, 1C, 4C, 4B del Artículo 2), tal y como se observó en las otras pruebas mecánicas. Este suceso confirma que el ciclado mecánico facilita un grado relativo de remineralización biomimética tal y como sugieren Kinney y cols [81]. Los resultados obtenidos por el grupo control en esta serie de estudios podrían deberse a la alta hidrofilicidad que presenta el adhesivo Single Bond cuando se aplica a dentina grabada con ácido ortofosfórico, dando lugar a una absorción excesiva de agua y a la ulterior degradación de la interfase resina-dentina [94]. Debido a este fenómeno, aunque la resina adhesiva haya sido capaz de infiltrar la dentina intertubular, ha podido producirse una escasa formación de *tags* de resina, derivando en nanofiltración y degradación de la interfase adhesiva a medio plazo [95]. Estos datos pueden visualizarse también en los resultados de microscopía confocal presentados por Toledano y cols (2024) [34].

De acuerdo con los resultados obtenidos, se ha podido demostrar el papel que desempeña el uso de NPs-TDg en la interfase resina-dentina, siendo capaz de promover la remineralización, especialmente en los especímenes sometidos a ciclado mecánico. Además, según los datos de las diferentes pruebas mecánicas, podemos confirmar que la

remineralización producida es de tipo biomimética o funcional. A pesar de la variedad de técnicas empleadas en la presente tesis doctoral para la evaluación de este biomaterial, sería conveniente completar estos hallazgos con la utilización de microtomografía computarizada o estudios que evalúen la actividad enzimática. Otra limitación del presente estudio puede ser la utilización especímenes *ex vivo*. Realizar estudios *in vivo* que valoren la remineralización en superficie dentinaria coronal, aclararía el método a través del cual el tideglusib ejerce su actividad biológica.

7. Conclusiones

1º El estrés mecánico en las interfases resina-dentina tratadas con nanopartículas poliméricas funcionalizadas con tideglusib induce la remineralización de la dentina peritubular e intertubular con una mayor madurez química cristalográfica. Además, el tideglusib produjo una mayor calidad del colágeno de las interfases resina-dentina, favoreciendo una organización adecuada de la matriz para promover la nucleación de apatita.

2º La infiltración de nanopartículas funcionalizadas con tideglusib facilita un módulo complejo similar entre la dentina peritubular e intertubular y una disipación homogénea de la energía. El tan delta en la dentina intertubular es mayor que en la dentina peritubular cuando se usa el biomaterial experimental en interfases sometidas a ciclado mecánico. Las nanopartículas funcionalizadas con tideglusib generan una mayor anchura de las fibrillas de colágeno y promueve la formación de estructuras minerales en forma de puente que aceleran la reparación de la dentina. Este hallazgo ha sido especialmente evidente en regiones histológicas próximas con comportamiento viscoelástico discrepante, donde la remineralización de las líneas de fractura provocadas ha ayudado a consolidar las estructuras dentinarias afectadas. El termociclado disminuye la mineralización producida por las nanopartículas funcionalizadas con tideglusib, pero con limitadas zonas de fractura en la interfase resina-dentina.

3º El tideglusib promueve la precipitación de hidroxiapatita, como fase cristalina principal, en la sección intrafibrilar de las fibrillas de colágeno, permitiendo la mineralización funcional. Las nanopartículas funcionalizadas con tideglusib facilitan la nucleación de cristales y mejoran la madurez de los mismos. Los nanocristales producidos por las nanopartículas funcionalizadas con tideglusib son prismas hexagonales de tamaño submicrónico. El estrés térmico de las interfases tratadas con nanopartículas funcionalizadas con tideglusib provoca una disminución de la mineralización funcional y la cristalinidad, lo que se asocia a una hidroxiapatita de menor madurez.

8. Financiación

El trabajo presentado ha sido realizado gracias a la financiación recibida del Proyecto PID2020–114694RB-I00, que fue subvencionada por el programa MCIN/AEI 10.13039/501100011033.

9. Indicios de calidad objetivos de la Tesis Doctoral

9.1. Trabajos presentados a congresos

9.1.1. Comunicación tipo Póster presentada en el IV Simposio de Terapias Avanzadas y Tecnologías Biomédicas: Tideglusib doped nanoparticles improve static nanomechanical properties in resin-dentin interfaces. Granada. 15/12/23.

9.1.2. Comunicación Oral presentada en el 53º Congreso Anual de la Sociedad Española de Prótesis Sociedad Española de Prótesis Estomatológica y Estética (SEPES): Efecto de una molécula antagonista de GSK-3β en las propiedades viscoelásticas y morfológicas de la interfase resina-dentina. Sevilla. 10/12/24.

9.2. Publicaciones científicas

9.2.1. Toledano, M., Aguilera, F. S., **Fernández-Romero, E**., Lagos, A. J., Bonilla, M., Lynch, C. D., & Osorio, R. (2024). Dentin remineralization using a stimuli-responsive engineered small molecule GSK3 antagonists-functionalized adhesive. Dental materials: official publication of the Academy of Dental Materials, 40(3), 393–406. https://doi.org/10.1016/j.dental.2023.12.010

Índice de impacto: 4,6 Posición: 9/157 (Q1) Citaciones recibidas: 4

9.2.2. Toledano, M., **Fernández-Romero, E**., Aguilera, F. S., Osorio, E., Rodríguez-Santana, J. A., Garrido, M., Solís, P. A., García-Godoy, F., & Osorio, R. (2024). Tunable polymer-peptide hybrids for dentin tissue repair. Journal of dentistry, 148, 105027. https://doi.org/10.1016/j.jdent.2024.105027.

Índice de impacto: 4,8 Posición: 7/157 (Q1) Citaciones recibidas: 2

9.2.3. Toledano, M., **Fernández-Romero, E.**, Osorio, E., Aguilera, F. S., Lynch, C. D., Osorio, M. T., Toledano, R., & Osorio, R. (2024). Effect of the anti-Alzheimer drug GSK-3β antagonist on numerical modeling of the energy dissipation through the resin-dentin interface. Dental materials: official publication of the Academy of Dental Materials, S0109-5641(24)00271-9. Advance online publication. https://doi.org/10.1016/j.dental.2024.09.005

Índice de impacto: 4,6 Posición: 9/157 (Q1) Citaciones recibidas: 0

9.2.4. Toledano, M., **Fernández-Romero, E.**, Osorio, M. T., Osorio, E., Aguilera, F. S., Toledano, R., & Osorio, R. (2024). Investigation of the effect of Tideglusib on the hydroxyapatite formation, crystallinity and elasticity of conditioned resin-dentin interfaces. Journal of dentistry, 150, 105334. Advance online publication. https://doi.org/10.1016/j.jdent.2024.105334

Índice de impacto: 4,8 Posición: 7/157 (Q1) Citaciones recibidas: 1

Índice de calidad y posición de la revista según *Journal Citation Report*. Citacicones recibidas tomadas de *Scopus.*

10. Referencias Bibliográficas

[1] M. Bermudez, L. Hoz, G. Montoya, M. Nidome, A. Perez-Soria, E. Romo, U. Soto-Barreras, J. Garnica-Palazuelos, M. Aguilar-Medina, R. Ramos-Payan, C. Villegas-Mercado, Bioactive Synthetic Peptides for Oral Tissues Regeneration, Front. Mater. 8 (2021) 655495. https://doi.org/10.3389/fmats.2021.655495.

[2] N. Nakabayashi, M. Nakamura, N. Yasuda, Hybrid layer as a dentin-bonding mechanism, J. Esthet. Dent. 3 (1991) 133–138. https://doi.org/10.1111/j.1708-8240.1991.tb00985.x.

[3] L.-N. Niu, W. Zhang, D.H. Pashley, L. Breschi, J. Mao, J.-H. Chen, F.R. Tay, Biomimetic remineralization of dentin, Dent. Mater. Off. Publ. Acad. Dent. Mater. 30 (2014) 77–96. https://doi.org/10.1016/j.dental.2013.07.013.

[4] J. De Munck, P.E. Van den Steen, A. Mine, K.L. Van Landuyt, A. Poitevin, G. Opdenakker, B. Van Meerbeek, Inhibition of Enzymatic Degradation of Adhesive-Dentin Interfaces, J. Dent. Res. 88 (2009) 1101–1106. https://doi.org/10.1177/0022034509346952.

[5] P. Spencer, Q. Ye, J. Park, E.M. Topp, A. Misra, O. Marangos, Y. Wang, B.S. Bohaty, V. Singh, F. Sene, J. Eslick, K. Camarda, J.L. Katz, Adhesive/Dentin interface: the weak link in the composite restoration, Ann. Biomed. Eng. 38 (2010) 1989–2003. https://doi.org/10.1007/s10439-010-9969-6.

[6] D.G. Moussa, J.A. Kirihara, Z. Ye, N.G. Fischer, J. Khot, B.A. Witthuhn, C. Aparicio, Dentin Priming with Amphipathic Antimicrobial Peptides, J. Dent. Res. 98 (2019) 1112–1121. https://doi.org/10.1177/0022034519863772.

[7] A.C. Profeta, F. Mannocci, R. Foxton, T.F. Watson, V.P. Feitosa, B. De Carlo, R. Mongiorgi, G. Valdré, S. Sauro, Experimental etch-and-rinse adhesives doped with bioactive calcium silicate-based micro-fillers to generate therapeutic resin–dentin interfaces, Dent. Mater. 29 (2013) 729–741. https://doi.org/10.1016/j.dental.2013.04.001.

[8] J. Thadathil Varghese, F. Islam, P. Farrar, L. Prentice, B.G. Prusty, Multi-response optimisation analysis of material properties in dental restorative composites under

the influence of thermal and thermomechanical stimuli - A 3D finite element study, J. Mech. Behav. Biomed. Mater. 150 (2024) 106363. https://doi.org/10.1016/j.jmbbm.2023.106363.

[9] K.M. Moreira, L.E. Bertassoni, R.P. Davies, F. Joia, J.F. Höfling, F.D. Nascimento, R.M. Puppin-Rontani, Impact of biomineralization on resin/biomineralized dentin bond longevity in a minimally invasive approach: An "in vitro" 18-month follow-up, Dent. Mater. Off. Publ. Acad. Dent. Mater. 37 (2021) e276–e289. https://doi.org/10.1016/j.dental.2021.01.021.

[10] J. Cai, J.E.A. Palamara, M.F. Burrow, Effects of Collagen Crosslinkers on Dentine: A Literature Review, Calcif. Tissue Int. 102 (2018) 265–279. https://doi.org/10.1007/s00223-017-0343-7.

[11] M. Gungormus, F. Tulumbaci, Peptide-assisted pre-bonding remineralization of dentin to improve bonding, J. Mech. Behav. Biomed. Mater. 113 (2021) 104119. https://doi.org/10.1016/j.jmbbm.2020.104119.

[12] C. Wu, Y. Zhang, W. Fan, X. Ke, X. Hu, Y. Zhou, Y. Xiao, $CaSiO_3$ microstructure modulating the in vitro and in vivo bioactivity of poly(lactide-co-glycolide) microspheres, J. Biomed. Mater. Res. A 98 (2011) 122–131. https://doi.org/10.1002/jbm.a.33092.

[13] Y.-J. Yoo, I. Kwon, S.-R. Oh, H. Perinpanayagam, S.-M. Lim, K.-B. Ahn, Y. Lee, S.-H. Han, S.-W. Chang, S.-H. Baek, Q. Zhu, K.-Y. Kum, Antifungal Effects of Synthetic Human Beta-defensin-3-C15 Peptide on Candida albicans–infected Root Dentin, J. Endod. 43 (2017) 1857–1861. https://doi.org/10.1016/j.joen.2017.06.035.

[14] A.C. Rao, K.V. Venkatesh, V. Nandini, D. Sihivahanan, A. Alamoudi, H.A. Bahammam, S.A. Bahammam, B. Zidane, M.A. Bahammam, H. Chohan, N.H. Albar, P.K. Yadalam, S. Patil, Evaluating the Effect of Tideglusib-Loaded Bioactive Glass Nanoparticles as a Potential Dentine Regenerative Material, Mater. Basel Switz. 15 (2022) 4567. https://doi.org/10.3390/ma15134567.

[15] M. Chieruzzi, S. Pagano, S. Moretti, R. Pinna, E. Milia, L. Torre, S. Eramo, Nanomaterials for Tissue Engineering In Dentistry, Nanomaterials 6 (2016) 134. https://doi.org/10.3390/nano6070134.

[16] H. Negi, S.K. Saikia, R. Kanaujia, S. Jaiswal, R. Pandey, 3β-Hydroxy-urs-12-en-28-oic acid confers protection against ZnONPs induced adversity in Caenorhabditis elegans, Environ. Toxicol. Pharmacol. 53 (2017) 105–110. https://doi.org/10.1016/j.etap.2017.05.004.

[17] M.T. Arias-Moliz, P. Baca, C. Solana, M. Toledano, A.L. Medina-Castillo, M. Toledano-Osorio, R. Osorio, Doxycycline-functionalized polymeric nanoparticles inhibit Enterococcus faecalis biofilm formation on dentine., Int. Endod. J. 54 (2021) 413–426. https://doi.org/10.1111/iej.13436.

[18] R. Osorio, E. Osorio, A.L. Medina-Castillo, M. Toledano, Polymer nanocarriers for dentin adhesion, J. Dent. Res. 93 (2014) 1258–1263. https://doi.org/10.1177/0022034514551608.

[19] A.L. Medina-Castillo, J.F. Fernandez-Sanchez, A. Segura-Carretero, A. Fernandez-Gutierrez, Micrometer and Submicrometer Particles Prepared by Precipitation Polymerization: Thermodynamic Model and Experimental Evidence of the Relation between Flory's Parameter and Particle Size, Macromolecules 43 (2010) 5804–5813. https://doi.org/10.1021/ma100841c.

[20] R. Osorio, I. Cabello, A.L. Medina-Castillo, E. Osorio, M. Toledano, Zinc-modified nanopolymers improve the quality of resin-dentin bonded interfaces, Clin. Oral Investig. 20 (2016) 2411–2420. https://doi.org/10.1007/s00784-016-1738-y.

[21] R. Osorio, C.A. Alfonso-Rodríguez, A.L. Medina-Castillo, M. Alaminos, M. Toledano, Bioactive Polymeric Nanoparticles for Periodontal Therapy, PLOS ONE 11 (2016) e0166217. https://doi.org/10.1371/journal.pone.0166217.

[22] M. Toledano-Osorio, R. Osorio, F.S. Aguilera, A.L. Medina-Castillo, M. Toledano, E. Osorio, S. Acosta, R. Chen, C. Aparicio, Polymeric nanoparticles protect the resin-dentin bonded interface from cariogenic biofilm degradation, Acta Biomater. 111 (2020) 316–326. https://doi.org/10.1016/j.actbio.2020.05.002.

[23] M. Toledano, E. Osorio, M.T. Osorio, F.S. Aguilera, R. Toledano, E.F.- Romero, R. Osorio, Dexamethasone-doped nanoparticles improve mineralization, crystallinity and collagen structure of human dentin, J. Dent. 130 (2023) 104447. https://doi.org/10.1016/j.jdent.2023.104447.

[24] M. Toledano, F.S. Aguilera, E. Osorio, M. Toledano-Osorio, G. Escames, A.L. Medina-Castillo, R. Toledano, C.D. Lynch, R. Osorio, Melatonin-doped polymeric nanoparticles reinforce and remineralize radicular dentin: Morpho-histological, chemical and biomechanical studies, Dent. Mater. 37 (2021) 1107–1120. https://doi.org/10.1016/j.dental.2021.03.007.

[25] D. Cummins, Zinc citrate/Triclosan: a new anti-plaque system for the control of plaque and the prevention of gingivitis: short-term clinical and mode of action studies, J. Clin. Periodontol. 18 (1991) 455–461. https://doi.org/10.1111/j.1600-051x.1991.tb02316.x.

[26] L.H. Cobb, E.M. McCabe, L.B. Priddy, Therapeutics and delivery vehicles for local treatment of osteomyelitis, J. Orthop. Res. Off. Publ. Orthop. Res. Soc. 38 (2020) 2091–2103. https://doi.org/10.1002/jor.24689.

[27] X. Li, X. Huang, L. Li, J. Wu, W. Yi, Y. Lai, L. Qin, LL-37-Coupled Porous Composite Scaffold for the Treatment of Infected Segmental Bone Defect, Pharmaceutics 15 (2022) 88. https://doi.org/10.3390/pharmaceutics15010088.

[28] V.C.M. Neves, R. Babb, D. Chandrasekaran, P.T. Sharpe, Promotion of natural tooth repair by small molecule GSK3 antagonists, Sci. Rep. 7 (2017) 39654. https://doi.org/10.1038/srep39654.

[29] R.G. Carvalho, L.F. Patekoski, R.M. Puppin-Rontani, C.R. Nakaie, F.D. Nascimento, I.L.S. Tersariol, Self-assembled peptide P11-4 interacts with the type I collagen C-terminal telopeptide domain and calcium ions, Dent. Mater. 39 (2023) 708–717. https://doi.org/10.1016/j.dental.2023.06.004.

[30] M. Comeau-Gauthier, M. Tarchala, J.L.R.-G. Luna, E. Harvey, G. Merle, Unleashing β-catenin with a new anti-Alzheimer drug for bone tissue regeneration, Injury 51 (2020) 2449–2459. https://doi.org/10.1016/j.injury.2020.07.035.

[31] L.K. Zaugg, A. Banu, A.R. Walther, D. Chandrasekaran, R.C. Babb, C. Salzlechner, M. a. B. Hedegaard, E. Gentleman, P.T. Sharpe, Translation Approach for Dentine Regeneration Using GSK-3 Antagonists, J. Dent. Res. 99 (2020) 544–551. https://doi.org/10.1177/0022034520908593.

[32] C. Kornsuthisopon, K.A. Tompkins, T. Osathanon, Tideglusib enhances odontogenic differentiation in human dental pulp stem cells in vitro, Int. Endod. J. 56 (2023) 369–384. https://doi.org/10.1111/iej.13877.

[33] A. Lektemur Alpan, M. Calisir, A. Kizildag, M. Ozdede, O. Ozmen, Effects of a Glycogen Synthase Kinase 3 Inhibitor Tideglusib on Bone Regeneration With Calvarial Defects, J. Craniofac. Surg. 31 (2020) 1477–1482. https://doi.org/10.1097/SCS.0000000000006326.

[34] M. Toledano, F.S. Aguilera, E. Fernández-Romero, A.J. Lagos, M. Bonilla, C.D. Lynch, R. Osorio, Dentin remineralization using a stimuli-responsive engineered small molecule GSK3 antagonists-functionalized adhesive, Dent. Mater. Off. Publ. Acad. Dent. Mater. 40 (2024) 393–406. https://doi.org/10.1016/j.dental.2023.12.010.

[35] M. Toledano, R. Osorio, A. Albaladejo, F.S. Aguilera, F.R. Tay, M. Ferrari, Effect of Cyclic Loading on the Microtensile Bond Strengths of Total-etch and Self-etch Adhesives, Oper. Dent. 31 (2006) 25–32. https://doi.org/10.2341/04-161.

[36] M. Toledano-Osorio, I. Cabello, C.D. Lynch, F.S. Aguilera, Mild acids facilitate functional dentin remineralization under thermo-mechanical stimuli, Am. J. Dent. 31 (2018) 155–165.

[37] A. Besinis, R. van Noort, N. Martin, Remineralization potential of fully demineralized dentin infiltrated with silica and hydroxyapatite nanoparticles, Dent. Mater. 30 (2014) 249–262. https://doi.org/10.1016/j.dental.2013.11.014.

[38] T.F. Watson, A.R. Atmeh, S. Sajini, R.J. Cook, F. Festy, Present and future of glass-ionomers and calcium-silicate cements as bioactive materials in dentistry: biophotonics-based interfacial analyses in health and disease, Dent. Mater. Off. Publ. Acad. Dent. Mater. 30 (2014) 50–61. https://doi.org/10.1016/j.dental.2013.08.202.

[39] Y. Li, T.T. Thula, S. Jee, S.L. Perkins, C. Aparicio, E.P. Douglas, L.B. Gower, Biomimetic Mineralization of Woven Bone-Like Nanocomposites: Role of Collagen Cross-Links, Biomacromolecules 13 (2012) 49–59. https://doi.org/10.1021/bm201070g.

[40] J. Song, V. Malathong, C.R. Bertozzi, Mineralization of synthetic polymer scaffolds: a bottom-up approach for the development of artificial bone, J. Am. Chem. Soc. 127 (2005) 3366–3372. https://doi.org/10.1021/ja043776z.

[41] L.E. Bertassoni, S. Habelitz, J.H. Kinney, S.J. Marshall, G.W. Marshall Jr., Biomechanical Perspective on the Remineralization of Dentin, Caries Res. 43 (2009) 70–77. https://doi.org/10.1159/000201593.

[42] M. Toledano, I. Cabello, F.S. Aguilera, E. Osorio, M. Toledano-Osorio, R. Osorio, Improved Sealing and Remineralization at the Resin-Dentin Interface After Phosphoric Acid Etching and Load Cycling, Microsc. Microanal. Off. J. Microsc. Soc. Am. Microbeam Anal. Soc. Microsc. Soc. Can. 21 (2015) 1530–1548. https://doi.org/10.1017/S1431927615015317.

[43] M. Toledano, E. Osorio, F.S. Aguilera, S. Sauro, I. Cabello, R. Osorio, In vitro mechanical stimulation promoted remineralization at the resin/dentin interface, J. Mech. Behav. Biomed. Mater. 30 (2014) 61–74. https://doi.org/10.1016/j.jmbbm.2013.10.018.

[44] E. Lozupone, C. Palumbo, A. Favia, M. Ferretti, S. Palazzini, F.P. Cantatore, Intermittent compressive load stimulates osteogenesis and improves osteocyte viability in bones cultured “in vitro,” Clin. Rheumatol. 15 (1996) 563–572. https://doi.org/10.1007/BF02238545.

[45] M. Balooch, S. Habelitz, J.H. Kinney, S.J. Marshall, G.W. Marshall, Mechanical properties of mineralized collagen fibrils as influenced by demineralization, J. Struct. Biol. 162 (2008) 404–410. https://doi.org/10.1016/j.jsb.2008.02.010.

[46] H. Milly, F. Festy, T.F. Watson, I. Thompson, A. Banerjee, Enamel white spot lesions can remineralise using bio-active glass and polyacrylic acid-modified bio-active glass powders, J. Dent. 42 (2014) 158–166. https://doi.org/10.1016/j.jdent.2013.11.012.

[47] C. Krafft, G. Steiner, C. Beleites, R. Salzer, Disease recognition by infrared and Raman spectroscopy, J. Biophotonics 2 (2009) 13–28. https://doi.org/10.1002/jbio.200810024.

[48] J.A. Timlin, A. Carden, M.D. Morris, R.M. Rajachar, D.H. Kohn, Raman Spectroscopic Imaging Markers for Fatigue-Related Microdamage in Bovine Bone, Anal. Chem. 72 (2000) 2229–2236. https://doi.org/10.1021/ac9913560.

[49] R. Vanna, P. Ronchi, A.T.M. Lenferink, C. Tresoldi, C. Morasso, D. Mehn, M. Bedoni, S. Picciolini, L.W.M.M. Terstappen, F. Ciceri, C. Otto, F. Gramatica, Label-free imaging and identification of typical cells of acute myeloid leukaemia and myelodysplastic syndrome by Raman microspectroscopy, Analyst 140 (2015) 1054–1064. https://doi.org/10.1039/C4AN02127D.

[50] A. Bonifacio, C. Beleites, F. Vittur, E. Marsich, S. Semeraro, S. Paoletti, V. Sergo, Chemical imaging of articular cartilage sections with Raman mapping, employing uni- and multi-variate methods for data analysis, Analyst 135 (2010) 3193–3204. https://doi.org/10.1039/C0AN00459F.

[51] C. Wang, Y. Wang, N.T. Huffman, C. Cui, X. Yao, S. Midura, R.J. Midura, J.P. Gorski, Confocal Laser Raman Microspectroscopy of Biomineralization Foci in UMR 106 Osteoblastic Cultures Reveals Temporally Synchronized Protein Changes Preceding and Accompanying Mineral Crystal Deposition*, J. Biol. Chem. 284 (2009) 7100–7113. https://doi.org/10.1074/jbc.M805898200.

[52] K. Karan, X. Yao, C. Xu, Y. Wang, Chemical Profile of the Dentin Substrate in Non-Carious Cervical Lesions, Dent. Mater. Off. Publ. Acad. Dent. Mater. 25 (2009) 1205–1212. https://doi.org/10.1016/j.dental.2009.04.006.

[53] A.G. Schwartz, J.D. Pasteris, G.M. Genin, T.L. Daulton, S. Thomopoulos, Mineral Distributions at the Developing Tendon Enthesis, PLOS ONE 7 (2012) e48630. https://doi.org/10.1371/journal.pone.0048630.

[54] M. Toledano-Osorio, F.S. Aguilera, E. Muñoz-Soto, E. Osorio, M. Toledano, G. Escames, A.L. Medina-Castillo, M.T. Osorio, M.T. López-López, M. Vallecillo-Rivas, R. Osorio, Melatonin-doped polymeric nanoparticles induce high crystalline apatite formation in root dentin., Dent. Mater. Off. Publ. Acad. Dent. Mater. 37 (2021) 1698–1713. https://doi.org/10.1016/j.dental.2021.09.001.

[55] M. Toledano, M. Toledano-Osorio, A.L. Medina-Castillo, M.T. López-López, F.S. Aguilera, R. Osorio, Ion-modified nanoparticles induce different apatite formation

in cervical dentine, Int. Endod. J. 51 (2018) 1019–1029. https://doi.org/10.1111/iej.12918.

[56] Y. Liu, L. Tjäderhane, L. Breschi, A. Mazzoni, N. Li, J. Mao, D.H. Pashley, F.R. Tay, Limitations in bonding to dentin and experimental strategies to prevent bond degradation, J. Dent. Res. 90 (2011) 953–968. https://doi.org/10.1177/0022034510391799.

[57] K. Rezwan, Q.Z. Chen, J.J. Blaker, A.R. Boccaccini, Biodegradable and bioactive porous polymer/inorganic composite scaffolds for bone tissue engineering, Biomaterials 27 (2006) 3413–3431. https://doi.org/10.1016/j.biomaterials.2006.01.039.

[58] X. Niu, Y. Du, J. He, X. Li, G. Wen, Hydrothermal Synthesis of Co-Exposed-Faceted WO3 Nanocrystals with Enhanced Photocatalytic Performance, Nanomater. Basel Switz. 12 (2022) 2879. https://doi.org/10.3390/nano12162879.

[59] X. Deng, A. Hasan, S. Elsharkawy, E. Tejeda-Montes, N.V. Tarakina, G. Greco, E. Nikulina, J.M. Stormonth-Darling, N. Convery, J.C. Rodriguez-Cabello, A. Boyde, N. Gadegaard, N.M. Pugno, M. Al-Jawad, A. Mata, Topographically guided hierarchical mineralization, Mater. Today Bio 11 (2021) 100119. https://doi.org/10.1016/j.mtbio.2021.100119.

[60] J.H. Kinney, J. Oliveira, D.L. Haupt, G.W. Marshall, S.J. Marshall, The spatial arrangement of tubules in human dentin, J. Mater. Sci. Mater. Med. 12 (2001) 743–751. https://doi.org/10.1023/A:1011232912734.

[61] T. Karakida, K. Onuma, M.M. Saito, R. Yamamoto, T. Chiba, R. Chiba, Y. Hidaka, K. Fujii-Abe, H. Kawahara, Y. Yamakoshi, Potential for Drug Repositioning of Midazolam for Dentin Regeneration, Int. J. Mol. Sci. 20 (2019) 670. https://doi.org/10.3390/ijms20030670.

[62] K. Yoshihara, N. Nagaoka, A. Nakamura, T. Hara, S. Hayakawa, Y. Yoshida, B. Van Meerbeek, Three-dimensional observation and analysis of remineralization in dentinal caries lesions, Sci. Rep. 10 (2020) 4387. https://doi.org/10.1038/s41598-020-61111-1.

[63] A. Kiesow, M. Morawietz, J. Gruner, S. Gierth, L. Berthold, E. Schneiderman, S. St John, High-Resolution Characterization of Enamel Remineralization using Time-of-Flight Secondary Ion Mass Spectrometry and Electron Microscopy, Caries Res. (2024). https://doi.org/10.1159/000535979.

[64] A. Bigi, E. Boanini, M. Gazzano, M.A. Kojdecki, K. Rubini, Microstructural investigation of hydroxyapatite–polyelectrolyte composites, J. Mater. Chem. 14 (2004) 274–279. https://doi.org/10.1039/B308687A.

[65] Th. Leventouri, A. Antonakos, A. Kyriacou, R. Venturelli, E. Liarokapis, V. Perdikatsis, Crystal Structure Studies of Human Dental Apatite as a Function of Age, Int. J. Biomater. 2009 (2009) 698547. https://doi.org/10.1155/2009/698547.

[66] I.-M. Low, Depth-Profiling of Crystal Structure, Texture, and Microhardness in a Functionally Graded Tooth Enamel, J. Am. Ceram. Soc. 87 (2004) 2125–2131. https://doi.org/10.1111/j.1151-2916.2004.tb06369.x.

[67] J. Xue, A.V. Zavgorodniy, B.J. Kennedy, M.V. Swain, W. Li, X-ray microdiffraction, TEM characterization and texture analysis of human dentin and enamel, J. Microsc. 251 (2013) 144–153. https://doi.org/10.1111/jmi.12053.

[68] K.-D. Liss, A. Bartels, A. Schreyer, H. Clemens, High-Energy X-Rays: A tool for Advanced Bulk Investigations in Materials Science and Physics, Textures Microstruct. 35 (2003) 219–252. https://doi.org/10.1080/07303300310001634952.

[69] A. Moshaverinia, S. Ansari, M. Moshaverinia, N. Roohpour, J.A. Darr, I. Rehman, Effects of incorporation of hydroxyapatite and fluoroapatite nanobioceramics into conventional glass ionomer cements (GIC), Acta Biomater. 4 (2008) 432–440. https://doi.org/10.1016/j.actbio.2007.07.011.

[70] S. Ucar, S.H. Bjørnøy, D.C. Bassett, B.L. Strand, P. Sikorski, J.-P. Andreassen, Formation of Hydroxyapatite via Transformation of Amorphous Calcium Phosphate in the Presence of Alginate Additives, Cryst. Growth Des. 19 (2019) 7077–7087. https://doi.org/10.1021/acs.cgd.9b00887.

[71] L. Angker, M.V. Swain, Nanoindentation: Application to dental hard tissue investigations, J. Mater. Res. 21 (2006) 1893–1905. https://doi.org/10.1557/jmr.2006.0257.

[72] S. Habelitz, M. Balooch, S.J. Marshall, G. Balooch, G.W. Marshall, In situ atomic force microscopy of partially demineralized human dentin collagen fibrils, J. Struct. Biol. 138 (2002) 227–236. https://doi.org/10.1016/s1047-8477(02)00029-1.

[73] R. Osorio, E. Osorio, F.S. Aguilera, A.L. Medina-Castillo, M. Toledano, M. Toledano-Osorio, Silver improves collagen structure and stability at demineralized dentin: A dynamic-mechanical and Raman analysis, J. Dent. 79 (2018) 61–67. https://doi.org/10.1016/j.jdent.2018.10.003.

[74] M. Toledano, F.S. Aguilera, E. Osorio, I. Cabello, M. Toledano-Osorio, R. Osorio, Functional and molecular structural analysis of dentine interfaces promoted by a Zn-doped self-etching adhesive and an in vitro load cycling model, J. Mech. Behav. Biomed. Mater. 50 (2015) 131–149. https://doi.org/10.1016/j.jmbbm.2015.05.026.

[75] M. Toledano, F.-S. Aguilera, I. Cabello, M. Toledano-Osorio, E. Osorio, M.-T. López-López, F. García-Godoy, C.-D. Lynch, R. Osorio, Silver-loaded nanoparticles affect ex-vivo mechanical behavior and mineralization of dentin., Med. Oral Patol. Oral Cirugia Bucal 24 (2019) e156–e164. https://doi.org/10.4317/medoral.22885.

[76] H. Salehi, E. Terrer, I. Panayotov, B. Levallois, B. Jacquot, H. Tassery, F. Cuisinier, Functional mapping of human sound and carious enamel and dentin with Raman spectroscopy, J. Biophotonics 6 (2013) 765–774. https://doi.org/10.1002/jbio.201200095.

[77] H. Cölfen, Biomineralization: A crystal-clear view, Nat. Mater. 9 (2010) 960–961. https://doi.org/10.1038/nmat2911.

[78] F. Nudelman, K. Pieterse, A. George, P.H.H. Bomans, H. Friedrich, L.J. Brylka, P.A.J. Hilbers, G. de With, N.A.J.M. Sommerdijk, The role of collagen in bone apatite formation in the presence of hydroxyapatite nucleation inhibitors, Nat. Mater. 9 (2010) 1004–1009. https://doi.org/10.1038/nmat2875.

[79] C.M. Hayot, E. Forouzesh, A. Goel, Z. Avramova, J.A. Turner, Viscoelastic properties of cell walls of single living plant cells determined by dynamic nanoindentation, J. Exp. Bot. 63 (2012) 2525–2540. https://doi.org/10.1093/jxb/err428.

[80] D.M. Espino, D.E. Shepherd, D.W. Hukins, Viscoelastic properties of bovine knee joint articular cartilage: dependency on thickness and loading frequency, BMC Musculoskelet. Disord. 15 (2014) 205. https://doi.org/10.1186/1471-2474-15-205.

[81] J.H. Kinney, S. Habelitz, S.J. Marshall, G.W. Marshall, The Importance of Intrafibrillar Mineralization of Collagen on the Mechanical Properties of Dentin, J. Dent. Res. 82 (2003) 957–961. https://doi.org/10.1177/154405910308201204.

[82] P. Patil, K.S. Banga, A.M. Pawar, S. Pimple, R. Ganeshan, Influence of root canal obturation using gutta-percha with three different sealers on root reinforcement of endodontically treated teeth. An in vitro comparative study of mandibular incisors, J. Conserv. Dent. 20 (2017) 241. https://doi.org/10.4103/JCD.JCD_233_16.

[83] T. Brosh, Z. Metzger, R. Pilo, Circumferential root strains generated during lateral compaction with stainless steel vs. nickel-titanium finger spreaders, Eur. J. Oral Sci. 126 (2018) 518–525. https://doi.org/10.1111/eos.12569.

[84] M. Toledano, R. Osorio, E. Osorio, A.L. Medina-Castillo, M. Toledano-Osorio, F.S. Aguilera, Ions-modified nanoparticles affect functional remineralization and energy dissipation through the resin-dentin interface, J. Mech. Behav. Biomed. Mater. 68 (2017) 62–79. https://doi.org/10.1016/j.jmbbm.2017.01.026.

[85] A. Misra, P. Spencer, O. Marangos, Y. Wang, J.L. Katz, Micromechanical analysis of dentin/adhesive interface by the finite element method, J. Biomed. Mater. Res. B Appl. Biomater. 70B (2004) 56–65. https://doi.org/10.1002/jbm.b.30012.

[86] G.W. Marshall, S. Habelitz, R. Gallagher, M. Balooch, G. Balooch, S.J. Marshall, Nanomechanical Properties of Hydrated Carious Human Dentin, J. Dent. Res. 80 (2001) 1768–1771. https://doi.org/10.1177/00220345010800081701.

[87] A. Misra, P. Spencer, O. Marangos, Y. Wang, J.L. Katz, Parametric study of the effect of phase anisotropy on the micromechanical behaviour of dentin–adhesive

interfaces, J. R. Soc. Interface 2 (2005) 145–157. https://doi.org/10.1098/rsif.2005.0029.

[88] M. Toledano, E. Osorio, I. Cabello, F.S. Aguilera, M.T. López-López, M. Toledano-Osorio, R. Osorio, Nanoscopic dynamic mechanical analysis of resin–infiltrated dentine, under in vitro chewing and bruxism events, J. Mech. Behav. Biomed. Mater. 54 (2016) 33–47. https://doi.org/10.1016/j.jmbbm.2015.09.003.

[89] R. Agrawal, A. Nieto, H. Chen, M. Mora, A. Agarwal, Nanoscale Damping Characteristics of Boron Nitride Nanotubes and Carbon Nanotubes Reinforced Polymer Composites, ACS Appl. Mater. Interfaces 5 (2013) 12052–12057. https://doi.org/10.1021/am4038678.

[90] V. Gopalakrishnan, C.F. Zukoski, Delayed flow in thermo-reversible colloidal gels, J. Rheol. 51 (2007) 623–644. https://doi.org/10.1122/1.2736413.

[91] K.J. Koester, J.W. Ager, R.O. Ritchie, The effect of aging on crack-growth resistance and toughening mechanisms in human dentin, Biomaterials 29 (2008) 1318–1328. https://doi.org/10.1016/j.biomaterials.2007.12.008.

[92] Y. Shinno, T. Ishimoto, M. Saito, R. Uemura, M. Arino, K. Marumo, T. Nakano, M. Hayashi, Comprehensive analyses of how tubule occlusion and advanced glycation end-products diminish strength of aged dentin, Sci. Rep. 6 (2016) 19849. https://doi.org/10.1038/srep19849.

[93] L.E. Bertassoni, S. Habelitz, M. Pugach, P.C. Soares, S.J. Marshall, G.W. Marshall, Evaluation of surface structural and mechanical changes following remineralization of dentin, Scanning 32 (2010) 312–319. https://doi.org/10.1002/sca.20199.

[94] D.H. Pashley, F.R. Tay, C. Yiu, M. Hashimoto, L. Breschi, R.M. Carvalho, S. Ito, Collagen degradation by host-derived enzymes during aging, J. Dent. Res. 83 (2004) 216–221. https://doi.org/10.1177/154405910408300306.

[95] F.R. Tay, D.H. Pashley, Have dentin adhesives become too hydrophilic?, J. Can. Dent. Assoc. 69 (2003) 726–731.

11. Glosario de términos

- GSK-3β: Glucógeno sintasa quinasa 3 beta.
- TDg: Tideglusib.
- NPs: Nanopartículas.
- NPs-TDg: Nanopartículas funcionalizadas con tideglusib.
- HAp: Hidroxiapatita.
- FESEM: Microscopía electrónica de barrido de emisión de campo.
- SBFS: Solución de fluido corporal simulado.
- XRD: Difracción de rayos X.
- TEM: Microscopía electrónica de transmisión.
- AFM: Microscopía de fuerzas atómicas.
- nano-DMA: Análisis dinámico nanomecánico.
- ALP: Actividad Fosfatasa alcalina.
- EDS: Espectroscopía por dispersión de energía.
- SAED: Difracción de electrones en área seleccionada.
- FFT: Transformada rápida de Fourier.
- AGEs: Productos finales de glicación avanzada.
- ACP: Fosfato de calcio amorfo.
- OCP: Fosfato de calcio octacalcio.
- R_{hkl}: Índice de textura.

12. Anexos

Artículos publicados

Se adjunta en el anexo en el siguiente orden:

1. Publicación Toledano y cols (2024) que forma parte de la presente línea de investigación y que precede a los artículos que defienden esta tesis doctoral. Se adjunta también su material suplementario.
2. Artículo 1 que defiende esta tesis doctoral y material suplementario.
3. Artículo 2 que defiende esta tesis doctoral y material suplementario.
4. Artículo 3 que defiende esta tesis doctoral y material suplementario.

Dental Materials 40 (2024) 393–406

Contents lists available at ScienceDirect

Dental Materials

journal homepage: www.elsevier.com/locate/dental

Full length article

Dentin remineralization using a stimuli-responsive engineered small molecule GSK3 antagonists-functionalized adhesive

Manuel Toledano [a], Fátima S. Aguilera [a,*], Enrique Fernández-Romero [a], Alejandro JS. Lagos [a], Marco Bonilla [a], Christopher D. Lynch [b], Raquel Osorio [a]

[a] University of Granada, Faculty of Dentistry, Colegio Máximo de Cartuja s/n, 18071 Granada, Spain
[b] University Dental School & Hospital/Cork University Dental School & Hospital, Cork, Ireland

ARTICLE INFO

Keywords:
Dentin
Tideglusib
Mechanical
Collagenase
Nanoparticles
Remineralization
Confocal microscopy
Microtensile bond strength
Scanning electron microscopy

ABSTRACT

Objectives: Tideglusib has shown great performance in terms of dentin regenerative properties. This study aims to evaluate bonding ability, of demineralized dentin infiltrated with polymeric nanoparticles (NPs) doped with tideglusib (TG) (TG-NPs).

Methods: Dentin conditioned surfaces were infiltrated with NPs and TG-NPs. Bonded interfaces were created and stored for 24 h and then submitted to mechanical, chemical and thermal challenging. The resin-dentin interface was evaluated through a doubled dye fluorescent technique and a calcium chelator fluorophore under a confocal laser scanning microscopy, and by field emission scanning electron microscopy.

Results: Dentin surfaces treated with TG-NPs and load cycled produced higher bond strength than the rest of the groups. Immersion of dentin specimens treated with undoped-NPs in collagenase solution attained the lowest microtensile bond strength (MTBS) values. Both porosity and nanoleakage decreased when dentin was infiltrated with TG-NPs, that revealed strong signals of xylenol orange stain at both hybrid layer and dentinal tubules. The presence of NPs, in general, inducted the presence of mineralized interfaces after mechanical loading and thermocycling.

Conclusions: Nanoparticles doped with tideglusib promoted the highest dentin bonding efficacy among groups, as they facilitated the maximum bond strength values with creation of mineral deposits at the hybrid layer and dentinal walls. Tideglusib enabled scarce porosity, nanoleakage and advanced sealing among dentin groups.

Significance: Doping hydrophilic polymeric NPs with tideglusib, infiltrated in etched dentin represents a reproducible technique to create reparative dentin at the resin-dentin interface, by inducing therapeutic bioactivity.

1. Introduction

In dental caries, a discrepancy in the demineralization-remineralization balance is caused, leading to a clear loss of tooth minerals progressing to a cavity that need restoration [1]. The resin-dentin adhesive interface is considered the Achilles's heel of the restorations [2,3]. The adhesive bond layer integrity is the most significant factor that defines the longstanding accomplishment of restoratives to dentin [4–7]. Dentin adhesion requires a first step of conditioning, where the collagen matrix is exposed after demineralization. The hybrid layer (HL) is created after infiltration and polymerization of the adhesive resin into the demineralized collagen. At the bottom of the hybrid layer (BHL), a fringe of demineralized, non-resin infiltrated and unprotected collagen prone to hydrolytic degradation [8] is created; then, degradation is endorsed to the action of host-derived matrix metalloproteinases (MMPs) [9–11] or bacterial collagenases [11]. At the composite restorations, the BHL is the weakest bond [7] (Fig. S1). As a consequence, the bonding efficacy of adhesive restorations over time is compromised [12,13], with average life spans as short of 5 y [14]. Besides, bacterial microleakage complicates this failure, and recurrent caries is facilitated [4,5,15]. Biofilm formation at the restoration-tooth interface [16] is probably assisted by the interface degradation that enables the colonization of bacteria [17].

Polymeric NPs, in adding to anionic carboxylate (i.e., COO^-) groups placed throughout the backbone of the polymer, may be doped with zinc (Zn-NPs) or doxycycline (D-NPs) to remineralize dentin [18]. Zn-NPs dentin infiltration has been demonstrated to show combined antibacterial and remineralizing effects [19]. However, the antimicrobial effect

* Correspondence to: University of Granada, Faculty of Dentistry, Dental Materials Section, Colegio Máximo de Cartuja s/n, 18071 Granada, Spain.
E-mail address: fatimas@ugr.es (F.S. Aguilera).

https://doi.org/10.1016/j.dental.2023.12.010
Received 5 August 2023; Received in revised form 6 November 2023; Accepted 11 December 2023
Available online 19 December 2023

of Zn^{2+} lies on its bacteriostatic property since the inhibition of PTS, glycolysis, and F-ATPase were reversible procedures [20]. D-NPs did not remineralize the bonded interface, though they have exerted an antibacterial role [19]. Besides, the repeated antibiotic use is likely to induce local drug-resistant strains, limiting the ability to eradicate challenging biofilm-forming pathogens, that ultimately lead to treatment failure [21, 22]. The integration of alternative antimicrobial strategies is widely desirable to combat oral infections.

Recently, a more biological methodology towards dentin generation and remineralization has been advocated by Neves et al. (2017) [23], who described the role of the glycogen-synthase-kinase 3 (GSK-3) peptide. Some peptides have shown great performance in terms of regenerative properties and antibacterial activity [22]. Peptides, have also shown antibacterial activity without compromising the bonding properties [2]. In extracted human teeth, Spencer et al. (2021) [24], have also employed peptides to promote the remineralization of defective dentin matrices. Specific peptides have been reported as being feasible with regard to acting as a polymer matrix to firmly bind HAp crystals, improving bonding to dentin [25]. Others have been employed as template to induce HAp nucleation to promote biomimetic mineralization of initial demineralization lesions, serving as polyelectrolyte-calcium complexes [26]. Tideglusib (TG) (4-Benzyl-2-(-naphthalen-1-yl)-[1,2,4]thiadiazolidine-3,5-dione) [23] also known as PN-12 or NP031112 [27], is a selective and irreversible small molecule non-ATP-competitive glycogen synthase kinase-3β (GSK-3β) inhibitor [28] agonist of the canonical Wnt pathway [29]. TG is a potent anti-inflammatory, antioxidant and a definitive bioactive and regenerative drug [30]. TG is a bio-degradable organic material, at present in trial for Alzheimer's disease, that promotes dental caries repair and tooth re-growth [28]. Delivery of GSK-3 inhibitor drugs directly into experimentally created deep cavities in experimental animals resulted in upregulation of Wnt-activity in pulp stem cells [23], which enhanced reparative dentin formation within the whole cavity [31]. This overstimulation of stem cells activity might result in increased odontoblast differentiation resulting in more robust regenerative dentin formation [30–32]. In this respect, TG has been demonstrated to inhibit the cysteine-dependent enzymes-human cathepsin K (CatK) and GSK-3β [33,34]. At the moment, one of the most pressing challenges is how to carry TG. TG has been incorporated into biodegradable marine collagen sponges to trigger rapid peptide release. We believe that a better sustained method to maintain an adequate kinetic release, should be preferred instead [23]. NPs have become widespread as carriers for controlled drug administration because excellent loading, long-term release properties and increased surface area. Several drawbacks associated to poor stability and delivery of Wnt proteins have been identified [29]. Hydrophilic polymeric NPs used as carriers have been proposed in the present research. TG-loaded NPs (TG-NPs) have not been established for their application in regenerative dentin, yet, as well as in bone and soft tissue. An investigation into remineralizing agents that have the potential to limit the function of degradative enzymes and regenerate lost minerals is relevant [8].

The aim of the present study was to infiltrate TG-doped polymeric NPs within phosphoric acid-conditioned dentin, previous to the adhesive application, to facilitate mineral precipitation in order to protect the hybrid layer and to preserve bond strengths. To determine bond strength, mineral precipitation and mechanical recovery at the resin dentin interface, it has been employed different techniques: microtensile bond strength and a confocal laser microscopy (CLSM) analysis with a double-dying technique (rhodamine-B/fluoresceine). They report information about hybrid layer degradation, permeability and adhesive penetration at the bonded interface after thermo/mechanical and collagenase storage challenging [35,36], to determine the bacterial or endogenous proteolytic activity [37]. By using field emission scanning electron microscopy (FESEM), a qualitative assessment of the collagen encapsulation was completed to determining zones of remineralization after NPs application [38]. The tested null hypothesis was that TG-doped NPs application did not affect, at the short term or after mechanical, chemical and thermal challenging dentin remineralization, expressed in terms of bonding efficacy and morphological variations.

2. Materials and methods

2.1. Nanoparticles fabrication and characterization

The polymerization precipitation method was used to obtain the nanoparticles. A thermo-dynamic approach allowed controlling the precipitation process, that is, the Flory-Huggins model based on Hansen's solubility parameters. This model was based on the solvent molecules interactions and the growth of the polymer chains by hydrogen, polar bonding and dispersion forces [39]. The backbone monomer used for the NPs fabrication was 2-hydroxyethyl methacrylate (HEMA) (Sigma-Aldrich, Chemie Gmbh, Riedstr, Germany) (0.137 mL), the functional monomer was methacrylic acid (MAA) (Sigma-Aldrich) (0.045 mL), and ethylene glycol dimethacrylate (EDMA) (Sigma-Aldrich) (0.170 mL) was used as cross-linker; 14 mL of solvent were added. Then, and after the addition of 8.75 mg of azobis-isobutyronitrile (AIBN), the system was sonicated during 1 min, the mixture was cooled at − 8 ∘C and the O_2 was removed by purging the system whit a soft flow of N_2 during 3 min [40]. The complete synthesis of the nanoparticles is described by Medina-Castillo (2020) [39]. Half of the fabricated NPs were loaded with the peptide TG (Sigma-Aldrich). The NPs loading process was conducted by immersion of 100 mg of NPs in 1 mL of 0.0017 mg/mL TG solution for 2 h at room temperature under constant shaking (12 rpm) (rotator Orbit 300445, JP Selecta, Barcelona, Spain). Then, the NPs were left until the solvent was completely evaporated, ensuring that all the TG remains onto the NPs. Three experimental groups were formed: 1) control, 2) undoped-NPs and 3) TG-NPs. For size and Z-potential measurements, a 5 mg/mL suspension of TG-NPs in water was fixed. These analyses were also prepared in triplicate using a Zetasizer Nano ZS90 (Malvern Instrument Ltd, Malvern, UK) via dynamic light scattering (DLS).

NPs TEM characterization was also performed by placing 10 μl of diluted samples (1 mg/mL) on a copper grid; then, it was coated with activated carbon and next dried. The samples were negatively stained with uranyl acetate at 2%, for visualization [41]. A Fei Titan 80–300 TEM-STEM microscope (ThermoFisher Scientific, Waltham, USA) was employed to acquire images (at 300 kV) [42].

For Fourier-transform infrared spectroscopy (FTIR) characterization, NPs, and TG-NPs samples were exposed to a JASCO 6200 FTIR equipped with a diamond-tipped attenuated total reflectance (ATR) device (ATR Pro ONE, JASCO Inc., Maryland, USA). The frequency range was 400–4000 cm^{-1}, and the spectral resolution, 2 cm^{-1} during 75 scans. Samples did not require preparation to obtain the spectra, minimizing artifacts [42].

2.2. Specimen preparation for the bonding procedure, mechanical, chemical and thermal degradation assessment

Forty-eight extracted unerupted human third molars, which had previously been stored at 4 °C in a 0.5% chloramine T solution for a period no longer than 1 month, were used. Before subjects' participation and inclusion in the study, informed consent was obtained. The study conformed to the Declaration of Helsinki and was performed to the guidelines of good clinical practice. Ethical approval for the study involving human subjects was granted by the local Ethics Committee (1906/CEIH/2020).

Teeth were sectioned horizontally just below the dentin-enamel junction to obtain sound dentin surfaces. These surfaces were polished flat to acquire a clinically relevant smear layer, using 180-grit silicon carbide –SiC- abrasive paper. Dentin surfaces were then etched (with 37% phosphoric acid, for 15 s), rinsed and dried. The experimental teeth were randomly allocated to one of the three groups (n = 4) by means of a

Table 1
Mean and standard deviation (SD) of microtensile bond strength (MPa) to dentin of the different experimental groups.

Dentin Treatment	Mean (SD)			
	24 h SBFS	24 h Load	Collagenase (1 m)	Thermocycled
Control	18.92 (3.17) a1	19.30 (3.27) a1	16.71 (4.69) ab1	15.03 (4.97) a1
Undoped-NPs	14.81 (2.44) a1	19.27 (2.82) a1	13.18 (3.33) a1	13.20 (3.40) a1
TG-NPs	19.70 (4.63) a12	26.99 (4.01) b2	20.89 (3.51) b12	17.89 (4.91) a1

Abbreviations: SBFS, simulated body fluid solution; NPs, nanoparticles; TG, tideglusib.

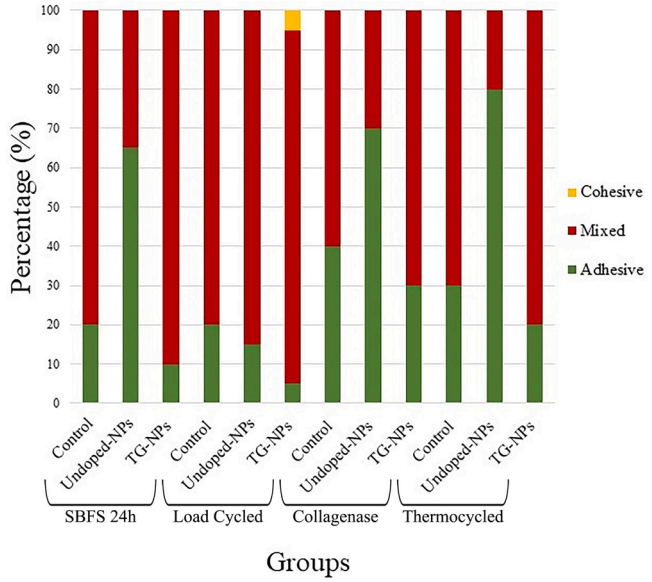

Graphic 1. Percentage distribution of failure mode of fractured specimens for the different tested groups. TG, tideglusib; NPs, Nanoparticles; SBFS, simulated body fluid solution immersion.

computer generated randomization list, according to the type of NP and storage time employed. The research random assignment tool used was http://www.randomizer.org/form.htm, and the teeth allocation to the treatment was concealed by means of sealed envelopes until the time of the bonding procedure. Just an ethanol solution was applied (30 s) (i), or an ethanol suspension of undoped-NPs (ii), and TG-NPs (iii) (10 mg/mL) in each of the three experimental groups (n = 4), acting as primers. Ethanol was then evaporated for 30 s and, finally, Single Bond (SB) resin (3 M ESPE, St. Paul, MN, USA) was applied according to the manufacturer's instructions, to fulfil the conventional adhesive protocol. The sample preparation was done by the same researcher and a common adhesion protocol, undertaken by other distinct researcher, was followed in all samples. For each tooth, a composite build-up (6 mm high) (Tetric EvoCeram, Ivoclar-Vivadent, Schaan, Liechtenstein) was constructed using the incremental technique, in five 1 mm resin layers, and light-cured with a Bluephase® polywave light-emitting diode light-polymerizing unit (Bluephase G2, Ivoclar Vivadent AG, Schaan, Liechtenstein) at 1000 mW/cm^2 for 20 s. The output intensity was monitored with a curing radiometer (Model Bluephase® meter, Ivoclar Vivadent AG, Schaan, Liechtenstein). A minimal output intensity of 1000 mW/cm^2 was employed for the experiments. The restored teeth were stored in a dark environment in simulated body fluid solution (SBFS) for 24 h.

The specimens were divided into four sub-groups, based on the type of challenging method that was followed: (1) Restored teeth stored in PBS for 24 h, (2) load cycling with sine wave form (259,200 cycles, 3 Hz) (S-MMT-250NB; Shimadzu, Tokyo, Japan). To proceed with the mechanical loaded samples, specimens were mounted in plastic rings using dental stone. A compressive load of 225 N was applied to the flat resin composite build-ups using a 5-mm diameter spherical stainless-steel plunger, while immersed in distilled water and proceeded as in Sauro et al., 2009 [43]. (3) A collagenase solution for ageing for 1 month, was used. The solution of collagenase was obtained by dissolving collagenase of *Clostridium histolyticum* (Sigma-Aldrich, St.Louis, MO, USA) into artificial saliva (20 mM HEPES buffer, 30 mM KCl, 4.0 mM KH_2PO_4, 0.2 mM $MgCl_2$, 6 H_2O, 0.7 mM $CaCl_2$, 0.3 mM NaN_3, pH 7.4) to achieve a concentration at 0.1 mg/mL. The specimens were stored in this collagenase solution at 37ºC, protected from light. After each 48 h, collagenase solutions were carefully removed through suction and renewed in order to avoid bacterial contamination. (4) Thermal cycling (100,000 cycles/ 5ºC and 55ºC) (SD Mechatronik GmbH, Germany) for 3 months, in distilled water (Fig. S2).

2.3. Specimens' preparation for microtensile bond strength (MTBS) and field emission scanning microscopy (FESEM)

These bonded teeth were sliced into beams with a cross-section of 1 mm^2 to provide approximately 10 per tooth. An Active Bencor Multi-T (Danville Engineering Co., Danville, CA, USA) notched device was used as gripping jig. Specimens were carefully aligned and a gel-like command-set glue (Zapit, Dental Ventures of America, Corona, CA, USA) was used, as it permits a controlled application sufficiently remote from the adhesive interface. The specimens were aligned in the soft glue gel prior to the application of the hardener (spray) to cure. Each beam was fixed to a modified Bencor Multi-T testing device. This device was assayed for failure in tension at a crosshead speed of 0.5 mm/min by a universal testing machine (Instron 4411; Instron Corporation, Canton, MA, USA). The specimens with enamel presence (those located peripherally) were avoided. A set of 2 digital calipers (Sylvac Ultra-Call III, Fowler Co., Inc., Newton, MA, USA) with an accuracy of 0.01 mm^2 were used to measure the cross-sectional area at the failure site. Some specimen failures occurred at any moment during samples preparation or testing (namely pre-testing failures). They were explicitly noted, but excluded from the statistical analysis. Values were calculated in MPa and, afterwards, analyzed by ANOVA and Student-Newman-Keuls multiple comparisons ($p < 0.05$), by the software SPSS/PC+ . A stereomicroscope (Olympus SZ-CTV; Olympus, Tokyo, Japan) was employed to define failure mode of fractured specimens at 40 × magnification. Failure modes were categorized as cohesive (C), mixed (M) or failure adhesive (A). To analyze the dentin sticks by field emission scanning electron microscopy (FESEM) (Gemini, Carl Zeiss, Oberkochen, Germany) at an accelerating voltage of 3 kV, detached dentin beams were selected and submitted to a critical drying point and, finally, coated with carbon.

2.4. Confocal microscopy evaluation (CLSM)

Four additional teeth per group were used for this assessment. Previous to the bonding application, bond resin was doped with 0.05 wt% Rhodamine-B (RhB:Sigma-Aldrich Chemie Gmbh, Riedstr, Germany). After that, the samples were divided in half into two groups: 1) the pulpal chamber was filled with 1 wt% aqueous/ethanol fluorescein (Sigma-Aldrich Chemie Gmbh, Riedstr, Germany) for 3 h, and 2) teeth were immersed in 0.5 wt% xylenol orange solution (XO: Sigma-Aldrich Chemie Gmbh, Riedstr, Germany), excited at 514 nm for 24 h, at 37 ºC (pH 7.2). Specimens were copiously rinsed with water and treated in an ultrasonic water bath for 2 min. Afterwards, they were sectioned in resin–dentin slabs and polished using ascending grit SiC abrasive papers (#1200 to #4000) on a water-cooled polishing device (Buehler-MetaDi, Buehler Ltd. Lake Bluff, IL, USA). The specimen preparation was

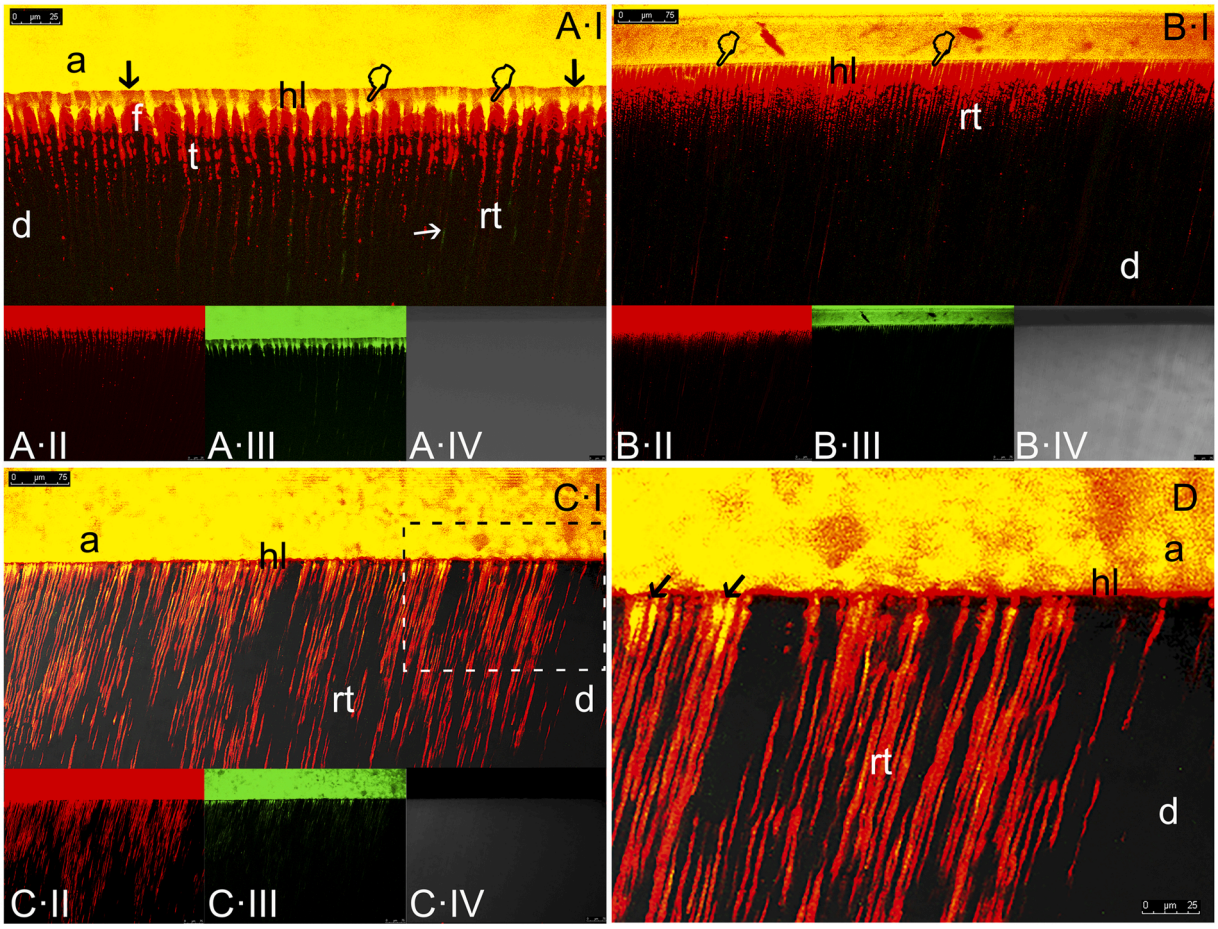

Fig. 1. CLSM images (reflexion/fluorescence) of the resin-dentin interfaces created, **A·I**: using phosphoric acid and Single Bond adhesive, after 24 h of storage, showing an extensive micropermeability (arrows) between dentin (d) and the adhesive layer (a). An intense nanoleakage signal from the hybrid layer (pointers) (hl) located underneath a thick adhesive layer, may be pointed out. A strong spectral overlap (yellow) in the emission of profile of both dyes (red and green), corresponds with clear signs of nanoleakage, even affecting to the adhesive. Funneling (f) of the tubular orifices is observable, with good penetration of the adhesive (a) into the entrance of tubules (t). The adhesive layer is characterized by an advanced dye sorption throughout its thickness and by the presence of a substantial number of narrow and short resin tags (rt) with discontinuities in the distribution of the intratubular resin when imaged in rhodamine excitation/emission mode A·II image of the red channel for rhodamine; A·III green channel image for fluorescein; and A·IV is the image of the reflected light channel. (Scale bar: 25 μm). **B·I,** using undoped nanoparticles, after 24 h of storage. Proper adhesive penetration and resin tags formation are observed in all cases. Fluoresceine emission was present at the hybrid layer (hl) (pointers), indicating inadequate resin infiltration of the etched dentin. Multiple resin tags (rt) are present. They are funnel shaped and thick at the base, indicating absence of degradation B·II image of the red channel for rhodamine; B·III green channel image for fluorescein; and B·IV is the image of the reflected light channel. (Scale bar: 75 μm). **C·I**, using TG-NPs application, after 24 h storage. Proper adhesive penetration and resin tags formation were observed in these specimens. Fluoresceine was scarcely present below the hybrid layer (hl), indicating adequate resin infiltration of the etched dentin, but fluoresceine did not pass through the hybrid layer. The dotted square, magnified, indicates Fig. 1D. C·II image of the red channel for rhodamine; C·III green channel image for fluorescein; and C·IV is the image of the reflected light channel. (Scale bar: 75 μm). **D**, using TG-NPs application. Just slight traces of fluoresceine are evident (arrows). It is important to note that fluoresceine did not reach the top of the hybrid layer (hl) and remains at the demineralized collagen in the intertubular dentin. Resin tags (rt) are numerous, funnel shaped and thick at the base (Scale bar: 75 μm). a, adhesive layer; d, dentin; f, funneling; hl, hybrid layer; rt, resin tags; t, dentinal tubules; TG, tideglusib.

concluded with a final ultrasonic cleaning (5 min). Analysis of bonded interfaces was performed by a dye-assisted confocal microscopy assessment, using a confocal laser scanning microscope equipped with × 60 lenses (SP5 Leica, Heidelberg, Germany). Rhodamine reveals resin diffusion and hybrid layer morphology; it is excited using green light (540 nm) and emits red in color (590 nm). Fluorescein discloses the interior of the dentinal tubules, it is activated by blue light (488–495 nm) and emits green/yellow (520 nm). Xylenol will show, coloured in yellow, new calcium deposits. CLSM images were obtained as described in Toledano et al., 2016 [44]. Micrographs representing the most common features of micropermeability observed along the bonded interfaces were selected and recorded.

3. Results

3.1. Nanoparticles fabrication and characterization

TEM images of NPs are displayed in Fig. S3. NPs presented a spherical shape and did not agglomerate. No differences in morphology were found after TG loading. FTIR-bands of the TG and NPs, basically, overlapped, so no practical information could be drawn. FTIR spectra of both groups had the same number of bands because the binding of TG did not provide new functional groups that can give rise to different vibrational modes. However, for TG-NPs, FTIR spectra showed the asymmetric stretching mode at the position 1144 (peak 9) and the different positions and intensities of the peak 14, as major differentiation features (Fig. S4). Some other slight discrepancies may be found after the analysis regarding both panels. In panel A (undoped-NPs) the stretch labeled as peak 13 corresponds to peak 14 in panel B (TG-NPs). In

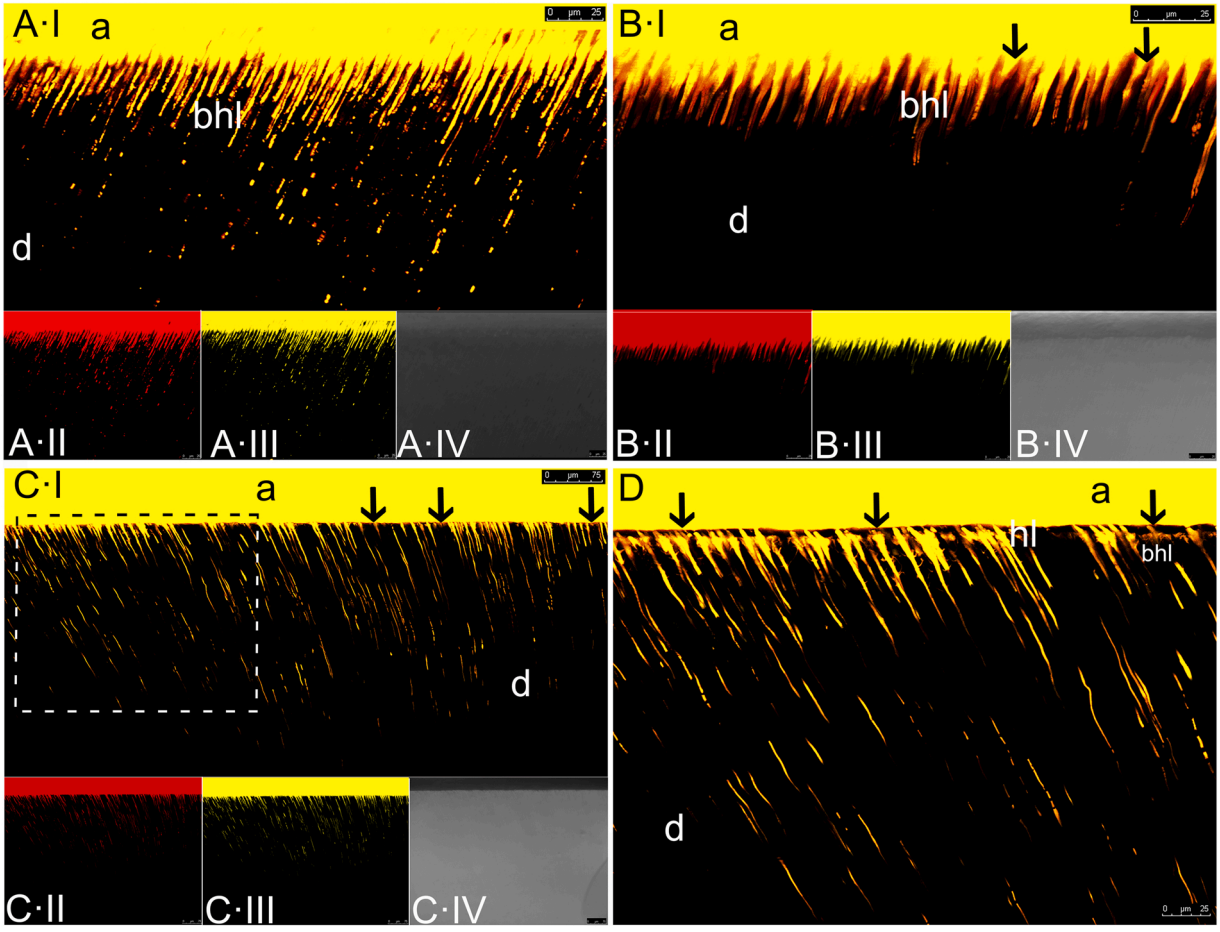

Fig. 2. CLSM single-projection images disclosing the fluorescence after the calcium chelator dye xylenol orange application, corresponding to the images obtained after 24 h evaluation, at the different experimental groups. **A**, phosphoric acid and Single Bond adhesive; **B**, undoped nanoparticles; **C**, TG-NPs. The dotted square in 2 C, magnified, indicates Fig. 2D (Scale bar: 75 μm). **D,** TG-NPs. In all groups, signals of orange stain were observed at the bottom of the hybrid layer (bhl) where resin is not present, and walls of the dentinal tubules appeared also clearly stained with the calcium chelator dye. A remarkable and differential fluorescence signal was shown throughout the entire hybrid layer (arrows) when TG-NPs and undoped NPs were applied and interfaces were evaluated, exhibiting mineral deposition, visualized within the hybrid layer (hl) and along the dentinal tubules, more specifically in C and D (Scale bar: 75 μm in A, C; 25 μm in B, D). A·I, B·I and C·I are the merged images of the different channels; A·II, B·II and C·II corresponds to red channel images for rhodamine; A·III, B·III and C·III are images of the orange xylenol channels; A·III, B·III and C·IV are images of the reflected light channel. a, adhesive layer; bhl, bottom of hybrid layer; d, dentin; hl, hybrid layer; TG, tideglusib.

fact, the stretch corresponding to peak 12 in panel A was divided into two peaks (12 and 13) in panel B.

3.2. Microtensile bond strength results, mechanical, chemical and thermal degradation assessments

Specimens submitted to 24 h SBFS immersion and thermal degradation did not show different MTBS values when the three groups of study were compared ($P < 0.05$) (Table 1). Dentin surfaces submitted to mechanical loading and treated with peptide-NPs produced higher bond strength than the rest of the groups. Immersion of dentin specimens treated with undoped-NPs in collagenase solution attained the lowest MTBS values ($P < 0.05$) (Table 1). Recorded failures were mainly mixed in all experimental groups. Specimens treated with TG-NPs have shown the lowest percentage of adhesive failures, which gathers a relevant significance (Graphic 1).

For each vertical column, same letter indicates no significant differences between treatment groups within the same storage method. For each row, same number indicates no significant differences between the storage method or challenge (24 h SBFS, 24 h load cycling, chemical aging for 1 month -collagenase- and 100,000 cycles thermocycled) in the same treatment group. Statistical significance was set at $p < 0.05$).

3.3. Confocal microscopy evaluation (CLSM)

Figs. 1 and 2 show the CLSM images of the resin-dentin interfaces attained at 24 h after bonding. At 24 h, when the dentin surfaces were treated with TG-NPs, both porosity and nanoleakage decreased (Fig. 1C, D), and mineralization augmented (Fig. 2C, D) at the resin dentin interface, in comparison with the rest of the groups (Figs. 1A, B, 2A, B). In general, the CLSM analysis revealed that resin-dentin interfaces of the control (PA+SB) (Fig. 1A) and undoped-NPs (Fig. 1B) groups were deficiently resin-hybridized. At these bonded interfaces, after multi-fluorescence examination, a rhodamine B-labeled hybrid layer and an adhesive layer completely affected by fluorescein penetration (nano-leakage) through the porous resin-dentin interface, was observed at 24 h evaluation. Porosity and nanoleakage diminished after using TG-NPs (Fig. 1D). Dentin infiltrated with TG-NPs disclosed the fluorescent calcium-chelators dye xylenol orange at the resin-dentin interface, revealing strong signals of xylenol orange stain at the top of resin-dentin interface, and within the dentinal tubules.

Thermocycled dentin samples treated with phosphoric acid and Single Bond showed resin dentin interfaces with strong micro-permeability, intense nanoleakage and funneling (Fig. 3A). When imaged in rhodamine, the adhesive layer is characterized by the presence of regular and long resin tags (Fig. 3B). Fluorescein water sorption

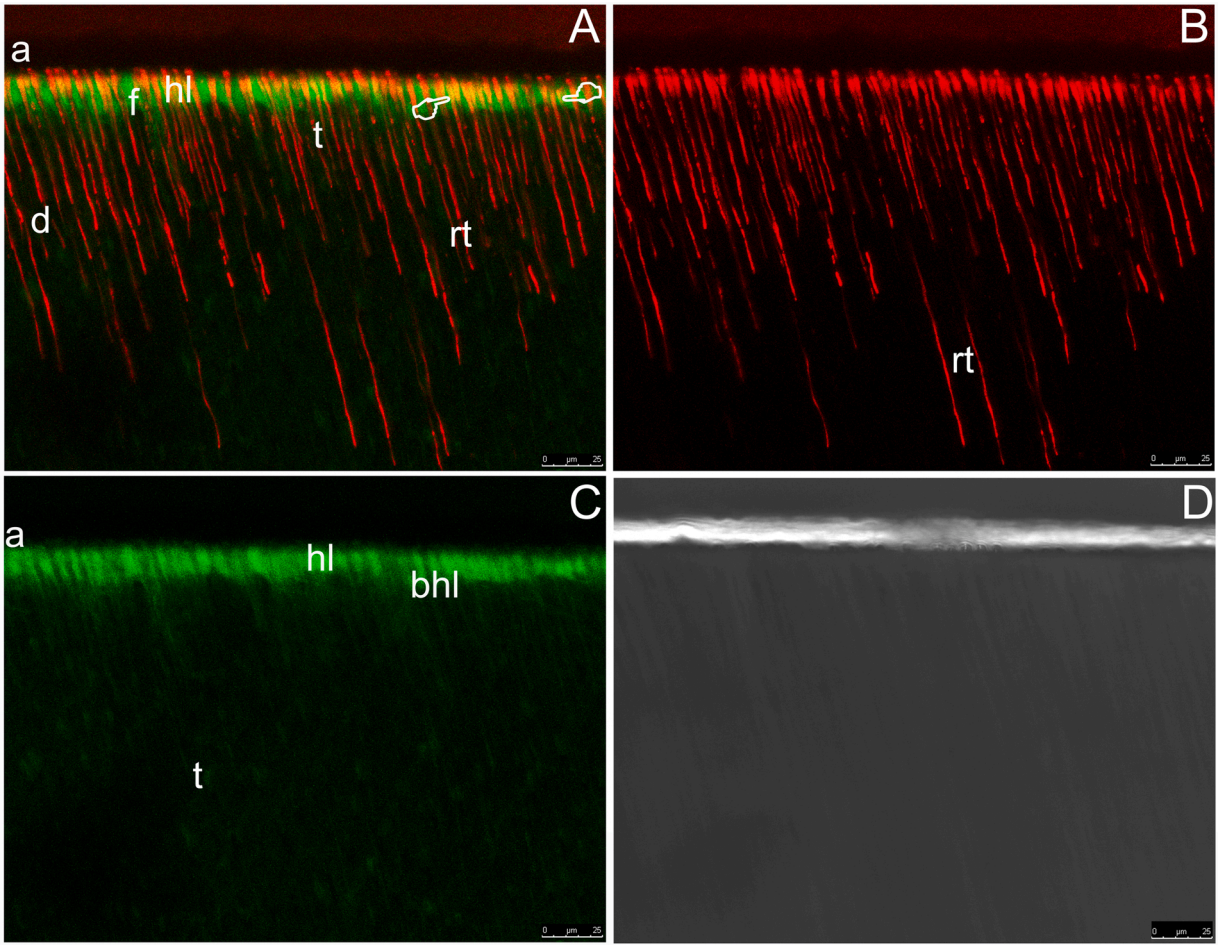

Fig. 3. A, CLSM image (reflexion/fluorescence) of the resin-dentin interface created using phosphoric acid and Single Bond adhesive (control group), after thermocycling, showing micropermeability (arrows) between dentin (d) and the adhesive layer (a). An intense nanoleakage signal from the hybrid layer (hl) (pointers) located underneath a thick adhesive layer may be determined. A strong spectral overlap (yellow) in the emission of profile of both dies (red and green), matches with clear signs of nanoleakage. Funnelling (f) of the tubular orifices is perceptible with good penetration of the adhesive (a) into the entrance of tubules (t). The adhesive layer is characterized by the existence of long resin tags (rt). (Scale bar: 25 μm). **B**, Represents the Fig. 3A, but imaged in rhodamine only, where the adhesive layer is characterized by the presence of regular and long resin tags (rt). Fluorescein water sorption was adverted within the thickness of the adhesive (a), hybrid layer (hl), bottom of the hybrid layer (bhl) and dentinal tubules (t) in **C**, and no reflective signals were observed along the entire interface that was analyzed in **D**. a, adhesive layer; bhl, bottom of hybrid layer; hl, hybrid layer; t, dentin tubules.

was adverted within the whole dentin interface (Fig. 3C), without any reflective signals (Fig. 3D). Dentin treated with undoped NPs and thermocycled displayed a resin-dentin interface devoid of nanolekage (Fig. 4A), that was totally absent in case of TG-NPs dentin infiltration (Fig. 5A).

The fluorescent calcium-chelator dye-XO technique permitted to observe moderate signals in the control group when specimens were mechanically loaded (Fig. 6A). Mineralized interfaces were detected when nanoparticles were included in the experimental adhesives after load cycling (Fig. 6B, C) and thermocycling (Fig. 7B, C).

3.4. Field Emission Scanning Electron Microscopy (FESEM)

Dentin samples infiltrated with TG-NPs and submitted to load cycling exhibited mineralized collars around the entrance of dentinal tubules and onto the intertubular dentin (Fig. 8A, B). Mineralized collagen fibers covering both the intertubular and peritubular dentin were also described on samples treated with TG (Fig. 8D).

Remineralization of the resin-dentin interface also occurred when undoped NPs were used for dentin infiltration and further load cycled. Strong resin tags and thick platforms of minerals covering intertubular and peritubular dentin appeared on the interface (Fig. 9A, B).

Collagen fibres appeared degraded or were absent after immersion of specimens in collagenase solution (Fig. 9C). Porous dentin surfaces were shown when samples were submitted to themocycling (Fig. 9D).

Strong processes of dentin mineralization were observable in load cycled specimens of the control group (Fig. 10B).

Degraded collagen characterized the dentin surface of specimens immersed in collagenase solution (Fig. 10C). Absent or non-hermetic resin tags were unveiled at the resin-dentin interface (Fig. 10D).

4. Discussion

Nanoparticles doped with tideglusib (TG-NPs) attained the highest microtensile bond strength (MTBS) in any group of study, though significant differences were only achieved in the groups submitted to load cycling and collagenase immersion (Table 1). The presence of TG-NPs at the resin-dentin interface decreased both porosity and nanoleakage,and promoted the formation of mineralized interfaces after mechanical loading and thermocycling. This fact may have contributed to the lowest percentage of adhesive failures recorded by this group of study (Graphic 1).

Currently, dental application of peptides include treatment of dental erosion, tooth whitening and dentinal caries [45]. In the treatment of

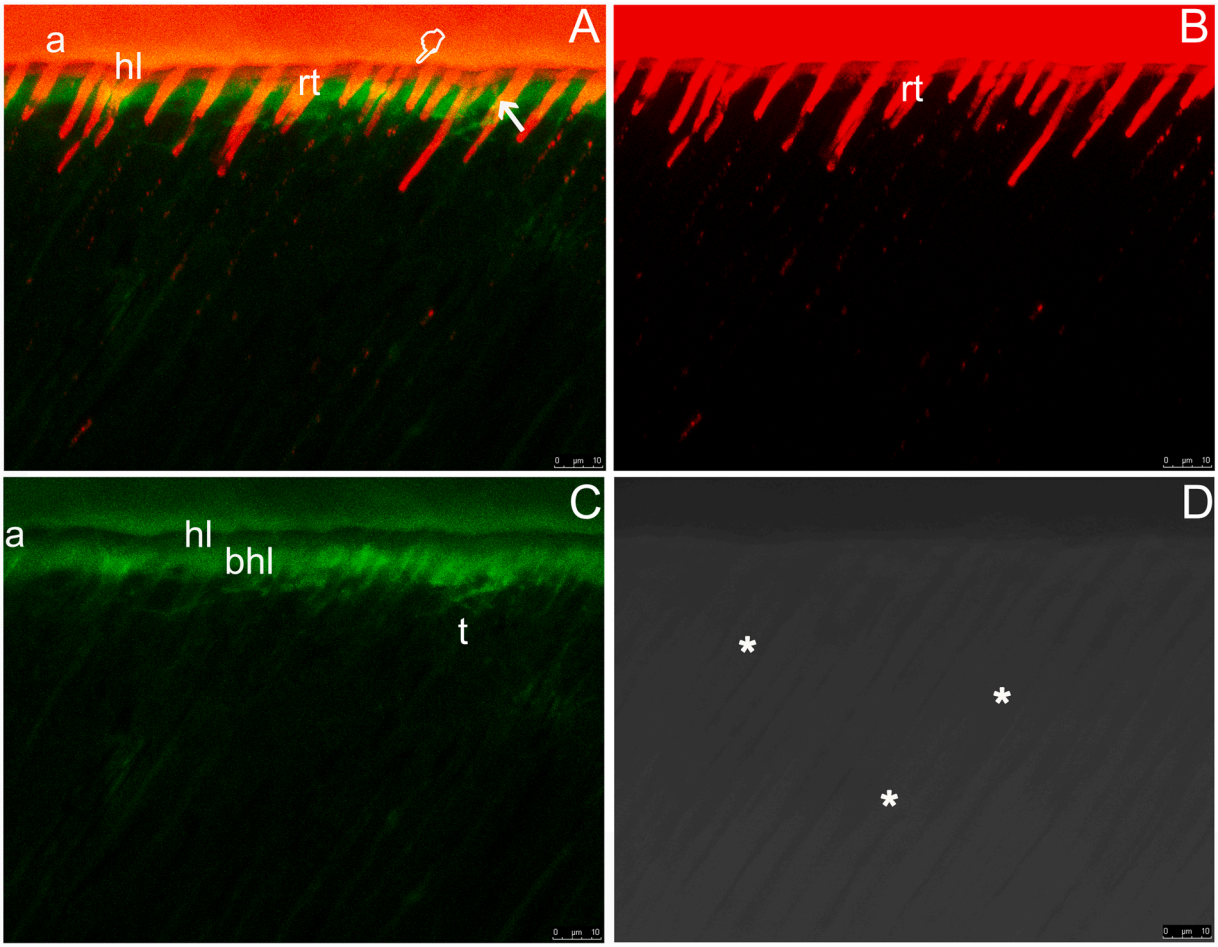

Fig. 4. A, A weak pattern of micropermeability within the dentinal tubules (arrow), and between the Rhodamine B-labeled adhesive layer (a) and the hybrid layer (hl) may be observed in dentin surfaces treated with undoped NPs after thermocycling. A light spectral overlap (yellow) (pointer) in the emission of profile of both dyes (red and green) was exhibited. Wider funnel-shaped resin tags (rt) underneath the adhesive layer characterize the resin-dentin interface (Scale bar: 10 μm). **B**, Represents the Fig. 4A, but imaged in rhodamine only, where the adhesive layer is characterized by the presence of wide and robust resin tags (rt)**.** Soft fluorescein water sorption was revealed within the thickness of the adhesive (a), hybrid layer (hl), bottom of the hybrid layer (bhl) and dentinal tubules (t) in **C**, and some perceptible reflective signals were detected throughout the length of the entire interface that was analyzed in **D** (asterisks). a, adhesive layer; bhl, bottom of hybrid layer; hl, hybrid layer; t, dentin tubules.

dental caries with resin restoration, bonding efficacy through bond strength measurements at the resin dentin interface is determinant [46]. Kim et al. (2020) [25] also obtained higher MTBS values after using elastin-like polypeptides, in comparison with the control group, at any checking time of their study. Other authors [2], on the contrary, have attained lower bond strength after doping Single Bond adhesive with 3–5% peptide (nisin). Probably, the high concentration that was used may have altered the degree of conversion of the doped adhesive. The presence of peptides at the interface may have created electrostatic attraction for the soluble ions, producing local increased of supersaturation zones that may have promoted nucleation [47]. These mineral deposits, that were observed in our study, may have contributed to the bond strength increase and low percentage of adhesive failures (Graphic 1), at 24 h storage, that was obtained in dentin infiltrated with TG-NPs (Table 1). The new mineral corresponded with the signals of orange stain that were observed at the bottom of the hybrid layer where resin is not present, and walls of the dentinal tubules that clearly stained with the calcium chelator dye (Fig. 2D). Significant differences in bond strength assessment were obtained by de Sousa et al. (2019) [48] when dentin was infiltrated with the self-assembling peptide P_{11}-4, which has a collagen specific binding-site region in its structure. P_{11}-4 interacts with calcium ions promoting dentin mineralization. It has been suggested that different ligands that are present in peptides such as carboxyl, carboxamide or hydroxyl groups may bind to calcium [49]. However, research is required to determine the exact type of interaction that is exerted by TG with the dentin structure. Our discrepant results may be explained as different peptides and substrates were used, artificial caries-affected dentin also produced an increase dentin porosity from the loss of minerals [50].

Ideally, a filling should chemically bond to the tooth structure, and perform mechanically like tooth itself in the oral environment, mainly when exposed to oral functions [51]. Mechanical loading significantly increased bonding efficacy after using TG-NPs (Table 1). Mineral precipitation at the hybrid layer, bottom of the hybrid layer and dentinal walls, with lower porosity and nanoleakage have contributed to this improved bonding efficacy and better sealing (Figs. 1D, 2D) [36,52] of the TG-NPs doped resin-dentin interface. This finding may be correlated with a higher percentage of mixed failures at the interface (Graphic 1). In vitro *stimulus* of dentin tissue repair behind TG treatment has demonstrated higher active β-catenin expression as compared to control [27]. The activation of Wnt/βCat signaling to tissue injury offers a potential route for improving natural repair by over-stimulating this pathway [23]. It has been demonstrated that the alkaline phosphatase activity is stimulated by intermittent compressive load. TG has produced a peak in alkaline phosphatase activity at 14 d of culture [28]. Alkaline phosphatase is present at all mineralization sites; it hydrolyzes

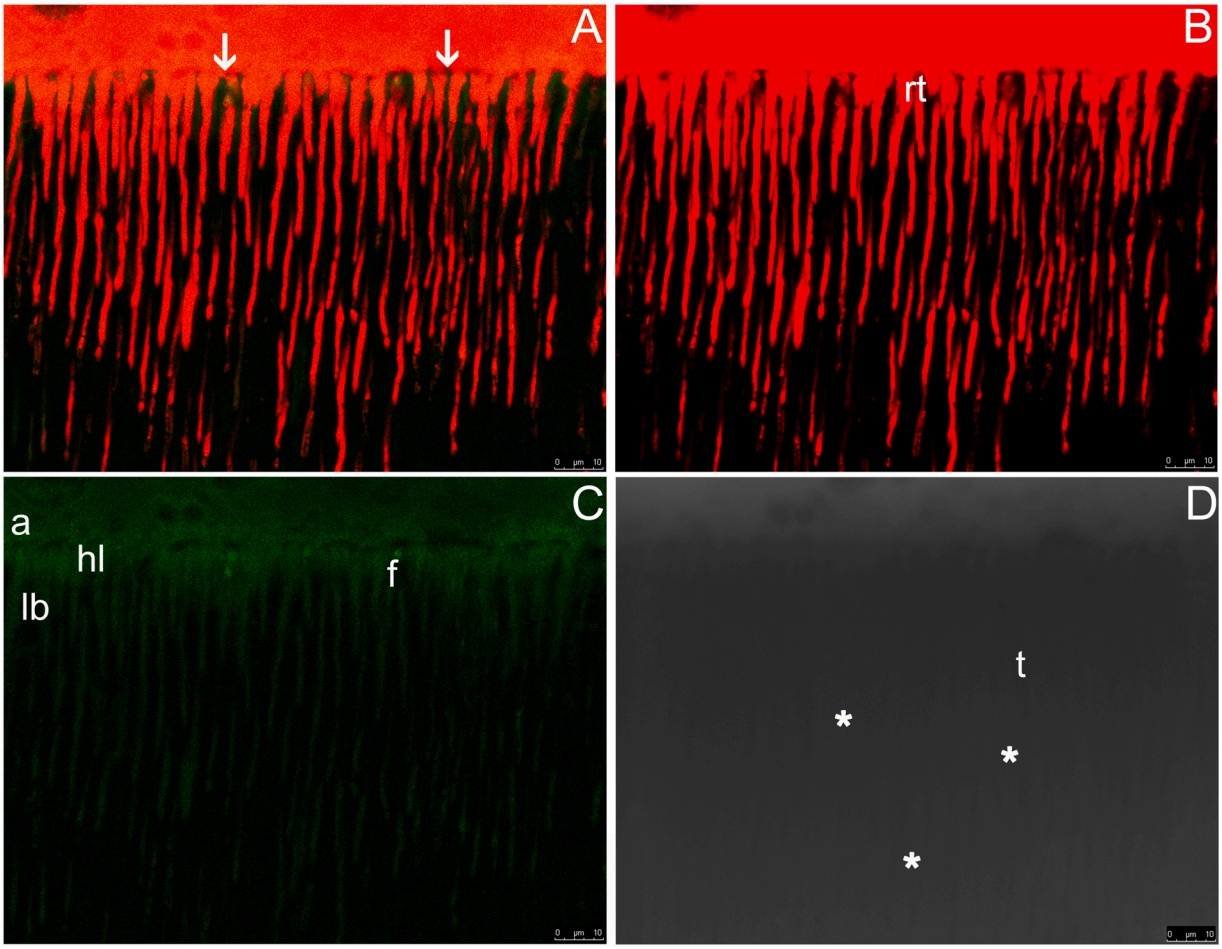

Fig. 5. A, CLSM image (reflexion/fluorescence), in dentin surfaces treated with TG-NPs after thermocycling, showing the interfacial characterization and micropermeability of the resin dentin interface. A definitive lack of signs of nanoleakage (arrows) is observed (Scale bar: 10 μm). (Scale bar: 10 μm). In the CLSM image captured in fluorescence mode, it is possible to observe an adhesive layer characterized by the presence of many middle-size, short and long resin tags (rt) when imaged with Rhodamine (**B**) underneath the adhesive layer (a) and a profuse dye sorption throughout its thickness when imaged with fluorescein (**C**). It is possible to observe a clear hybrid (hl) ~4 μm thick. Funneling (f) of the tubular orifices is evident with good penetration of the adhesive (a) into the tubules and their lateral branches (lb). Some reflective signals, in **D**, appeared at the entire interface (asterisks), specifically at the dentinal tubules (t). a, adhesive layer; d, dentin; f, funneling; hc, hybrid complex; lb, lateral branches; rt, resin tags; t, dentinal tubules; TG, tideglusib.

phosphate esters producing free phosphate, and thus apatite supersaturation [53], promoting penetration of amorphous calcium phosphate into collagen, finally inducing hierarchical mineralization [54]. TG has also been proved to promote dentin bridge formation [29]. Furthermore, mechanical loading also stimulates the resistance of collagen to enzymatic degradation in demineralized dentin. Load cycling, similarly, enhances dentin remineralization. These conditions reduced interfacial porosity and, therefore, better interface sealing [55] (Fig. 6C). FESEM analysis discovered new minerals forming collars around the tubuli entrances. The bond between the adhesive tags and peritubular dentin was sometimes deficient even though remineralized, resulting associated with layered minerals which mainly precipitated in strata, preferentially, at intertubular dentin, forming a consistent clump of crystals. Some tubules, nevertheless, remained empty (Fig. 8B).

In the present research, collagenase immersion of samples treated with TG-NPs attained the highest MTBS values among groups, significantly different when compared with dentin samples treated with undoped-NPs (Table 1). In vitro collagenase digestion has been proposed as an accelerated model for resin-dentin interface degradation [56]. Our results comply with those obtained by de Sousa et al. (2019) [48] after assessing immediate resistance of collagen type 1 fibers against collagenase activity, that increased after the application of self-assembling peptide P_{11}-4 in the dentin tissue. It is speculated that the presence of the NPs-carried peptide in the resin-dentin interface may have increased the collagen fiber stiffness at the dentin extracellular matrix, thus resulting in higher resistance to proteolysis of collagen type I fibers. Mineral precipitation was also observed through the FESEM images, where dentinal tubules appeared mostly occluded after TG-NPs infiltration, in comparison with the rest of the groups. Nevertheless, some other tubules were totally or partially empty, where few resin tags remained occluding the enlarged tubules. Mineralized collagen fibers were adverted at the intertubular dentin surface or even covering the tubular walls. In general, advanced mineralization of the dentin substrate and remineralized nanoparticles were observed (Fig. 8D). Integrity of the collagen fibers at the bottom of the hybrid layer was observed when the debonded interfaces were analyzed (Figs. 8B, 8D). Porosity and nanoleakage diminishes after applying TG-NPs (Fig. 1D), and both decreased even more after applying thermal and mechanical loading, where reduced fluorescent-dye uptake (nanoleakage) and XO-dye at the top of the hybrid layer was observed along the entire resin-dentin interface (Figs. 1D, 5, 6C). Xylenol orange was selected for the analysis of mineralization as it is fixed in newly formed calcified tissues where it remains until mineral removal [57]. Numerous resin tags and thick hybrid layers characterize this resin-dentin interface, and micropermeability was hardly encountered (Fig. 1D). It indicated that these TG-NPs did not alter adhesive penetration or hybrid layer formation

Fig. 6. A, Confocal microscopy evaluation (CLSM) single-projection image disclosing the fluorescent calcium-chelator dyeXO, showing the interfacial characterization of the resin-dentin interface created using phosphoric acid and Single Bond adhesive (control group), after load cycling, imaged with rhodamine and calcium-chelator dye XO. The adhesive layer is characterized by the presence of prominent and discontinuous resin tags (arrows). Moderate fluorescence signal of XO-dye within a wide hybrid layer (hl), but more remarkable within some dentinal tubules (t), revealed the presence of calcium complexes within both adhesive structures (Scale bar: 10 μm). B, Confocal microscopy evaluation (CLSM) single-projection image disclosing the fluorescent calcium-chelator dyeXO, showing the interfacial characterization of the resin-dentin interface created after undoped NPs infiltration and further load cycling, imaged with rhodamine and calcium-chelator dye XO. The interface disclosed a clear fluorescence signal within the adhesive layer (a), hybrid layer (hl) and dentinal tubules (t). XO-dye deposited at the top of the hybrid layer (arrows) and penetrated the first 10–20 μm of resin tags. The rest of resin-tags length appeared with the typical Rhodhamine B-labeled colorant (Scale bar: 10 μm). C, Confocal microscopy evaluation (CLSM) single-projection image disclosing the fluorescent calcium-chelator dyeXO, showing the interfacial characterization of the resin-dentin interface created after TG-NPs infiltration and further load cycling, imaged with rhodamine and calcium-chelator dye XO. The interface revealed a net fluorescence signal within the adhesive layer (a), hybrid layer (hl) and dentinal tubules (t). XO-dye strongly deposited at the top of the hybrid layer (arrows) (Scale bar: 10 μm). a, adhesive layer; hl, hybrid layer; t, dentinal tubules, TG, tideglusib.

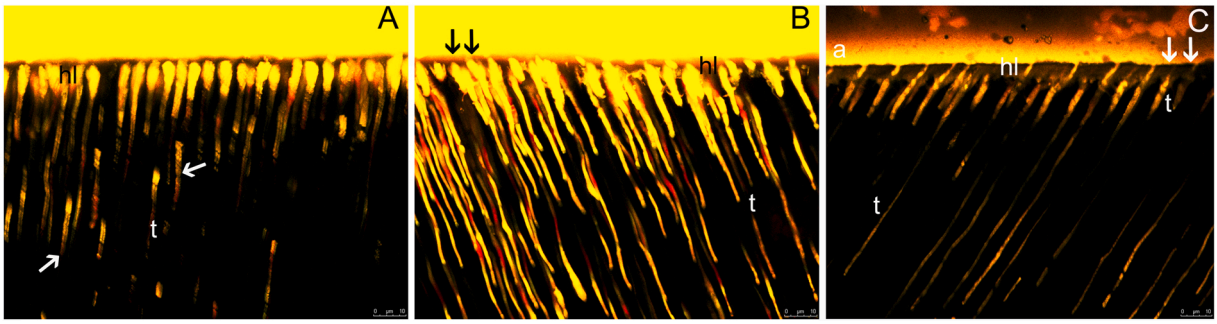

Fig. 7. A, Confocal microscopy evaluation (CLSM) single-projection image disclosing the fluorescent calcium-chelator dyeXO, showing the interfacial characterization of the resin-dentin interface created using phosphoric acid and Single Bond adhesive (control group), after thermocycling, imaged with rhodamine and calcium-chelator dye XO. The adhesive layer is characterized by the presence of noticeable and continuous resin tags (arrows). Clear fluorescence signal of XO-dye within a wide hybrid layer (hl), and within all dentinal tubules (t), revealed the presence of calcium complexes in both adhesive structures (Scale bar: 10 μm). **B,** Confocal microscopy evaluation (CLSM) single-projection image disclosing the fluorescent calcium-chelator dyeXO, showing the interfacial characterization of the resin-dentin interface created after undoped NPs infiltration and further thermocycling, imaged with rhodamine and calcium-chelator dye XO. The interface showed a net fluorescence signal within the hybrid layer (hl) and dentinal tubules (t). XO-dye deposited at the top of the hybrid layer (arrows) and penetrated the whole depth of resin tags. The resin-tags length appeared with the typical Rhodhamine B-labeled colorant (Scale bar: 10 μm). **C,** Confocal microscopy evaluation (CLSM) single-projection image disclosing the fluorescent calcium-chelator dyeXO, showing the interfacial characterization of the resin-dentin interface created after TG-NPs infiltration and further thermocycling, imaged with rhodamine and calcium-chelator dye XO. XO-dye deposited at the top of the hybrid layer (arrows) and infiltrated the whole depth of resin tags with a profound orange dye. (Scale bar: 10 μm). a, adhesive layer; hl, hybrid layer; t, dentinal tubules.

[58].

The peptide P_{11}-4 contributes to the development of a homogeneous hybrid layer with a reduced porosity after its dentin application [48], indicating collagen protection and remineralization. When interfaces were obtained with TG-NPs, CLSM single-projection image revealed the fluorescent calcium-chelators dye with strong signals of xylenol orange stain within the dentinal tubules, at the walls, and at the top of resin-dentin interface (Figs. 2C, 2D). Some peptides are absorbed, preferentially, on peritubular dentin, just where they have mostly developed their remineralizing role [14]. These findings established new mineral deposits [59] at the hybrid layer and at the first 5–20 μm of the tubule lengths with scarce adhesive failures (Graphic 1), and may be interpreted as remineralization of dentin [60]. After remineralization, TG-NPs might also have contributed to MMPs fossilization present in the dentin matrix, thereby protecting collagen fibers from proteolytic hydrolysis [48]. Dentin treatment with TG has provided a more mature dentin with a similar radiopacity as the surrounding primary/secondary dentin [28]. As a result, evidences of the therapeutic bioactivity of the experimental TG-NPs were attained. Additionally, the FTIR analysis has permitted to highlight the significant change occurred at the stretch corresponding to the peak 10 (Fig. S4), which is probably, the proof of TG binding. Further research is recommended, at this point.

When Single Bond adhesive was placed on phosphoric acid-etched dentin (control group), the resin diffused within the porous dentin forming a thick hybrid layer. Bonding efficacy, expressed through the MTBS evaluation was similar among the distinct experimental groups at 24 h of storage and among the different challenging tests (Table 1). Fluoresceine permeated through the hybrid layer making a yellow group at the adhesive layer (Fig. 1A). It clearly specifies that permeability exists, being a sigh of hybrid layer degradation. The dentin interface also presented funneled dentinal tubules (Fig. 1A). Funneling is interpreted as an essential sign of degradation of the scarcely resin-infiltrated demineralized and peritubular dentin [59], that was not present in the control specimens. Rhodamine B, similarly, passed along the tubules

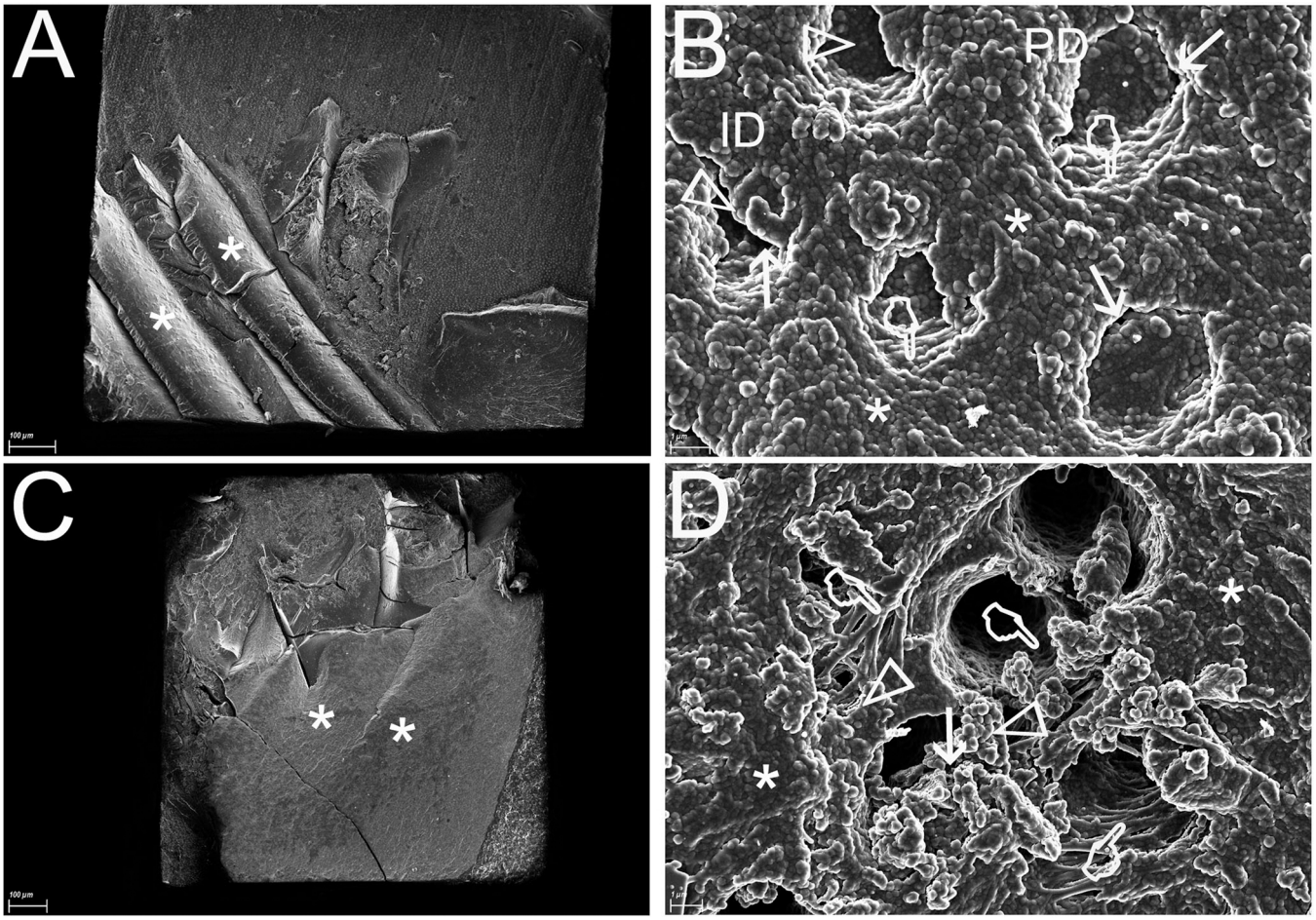

Fig. 8. **A**, FESEM observations of the fractured dentin surface of a specimen treated with TG-NPs after load cycling. A mixed failure, adhesive resin may be observed at lower left side (asterisks). (Scale bar: 100 μm). **B**, At higher magnification, new minerals formed a collar around the tubule lumen (pointers), and some were detected below a platform of crystals (asterisk). Integral collagen fibers were observed surrounding the walls of dentinal tubules. The bond between the adhesive tags and peritubular dentin (PD) was sometimes imperfect even though remineralized, resulted associated with layered minerals which mainly precipitated in strata, preferentially, at intertubular dentin (ID) forming a consistent clump of crystals. Some tubules remained empty (arrowheads). **C**, SEM observations of the fractured dentin surface of a specimen treated with TG-NPs after collagenase immersion for 1 month. A mixed failure, adhesive resin may be observed at the central part (asterisks). (Scale bar: 100 μm). (Scale bar: 1 μm). **D**, At a higher magnification of the periphery, main fracture is at the bottom of the hybrid layer, exposing the underlying dentin. Few rein tags remain partially occluding the enlarged tubules (arrow). Mineralized collagen, preserving its integrity, was adverted at the dentin surface or covering the tubular walls (pointers). In the top layers of the image, advanced mineralization of the substrate (asterisks) and remineralized nanoparticles were adverted (arrowheads). (Scale bar: 1 μm). TG, tideglusib.

through the hybrid zone by the interface. In this single labeled sample, discontinuities were also seen in the tubular filling of the resin tags (Fig. 1A). This specifies the intermittent passage of fluorescein from the lateral tubuli toward the main dentinal tubules [61]. FESEM analysis corroborated these findings, as though the adhesive resin was able to infiltrate the intertubular dentin, it could not form resin tags in some locations (Fig. 10A) or they were not sufficiently hermetic.

Dentin specimens infiltrated with undoped NPs and submitted to load cycling and collagenase immersion produced lower MTBS than those infiltrated with TG-NPs (Table 1). Water sorption and strong fluorescein dye penetration (i.e., micropermeability) were adverted within the resin infiltrated hybrid layer, increasing the percentage of adhesive failures (Graphic 1), when both control and undoped-NPs groups were assessed. These samples (Figs. 1B, 2B) exhibited a clear spectral overlap (yellow), in the emission of profile of both dyes (green and red). The resin-dentin interface was characterized by profuse large-size and funnel-shaped resin tags, in both groups (Figs. 1B, 2B). Moderate reflective signal inside the dentinal tubules and a discrete dye sorption throughout the thickness of the resin adhesive was unveiled, after treating with xylenol (Xo-dye), meaning the relative presence of some mineral components, when undoped-NPs were employed (Fig. 2B). FESEM analysis permitted to see compact resin tags within the dentinal tubules, and a generalized pattern of dentin remineralization including the collagen fibers when samples were load cycled (Fig. 9B). Collagen, partially, degraded after collagenase immersion (Fig. 9C), compromising the bonding efficacy (Table 1). Polymeric NPs do not reabsorb or dissolve and are capable to form amorphous calcium phosphate layer at their surface, they remain attached to the collagen fibrils and are integrated into the remineralized tissue [58].

Specimens tested at 24 h of storage and thermocycled performed similar, showing the same bonding efficacy (Table 1), but with dissimilar morphological performance. Only dentin infiltrated with TG-NPs and submitted to mechanical loading showed higher MTBS than the thermocycled specimens (Table 1). Dissimilar behavior was obtained by de Sousa et al. (2019) [48] after six months of water storage, but without applying thermocycling, that significantly decreased bond strength in the group of dentin-infiltrated peptides. Different methodology may have influenced our mutual outcomes. The confocal laser microscopy analysis brought supplementary support to the bond strength evaluation. The control group showed clear signs of nanoleakage and funneling (Fig. 3), with scarce resin tags formation evidenced through FESEM observation (Fig. 10A, D). Mineralized resin tags were observed, on the

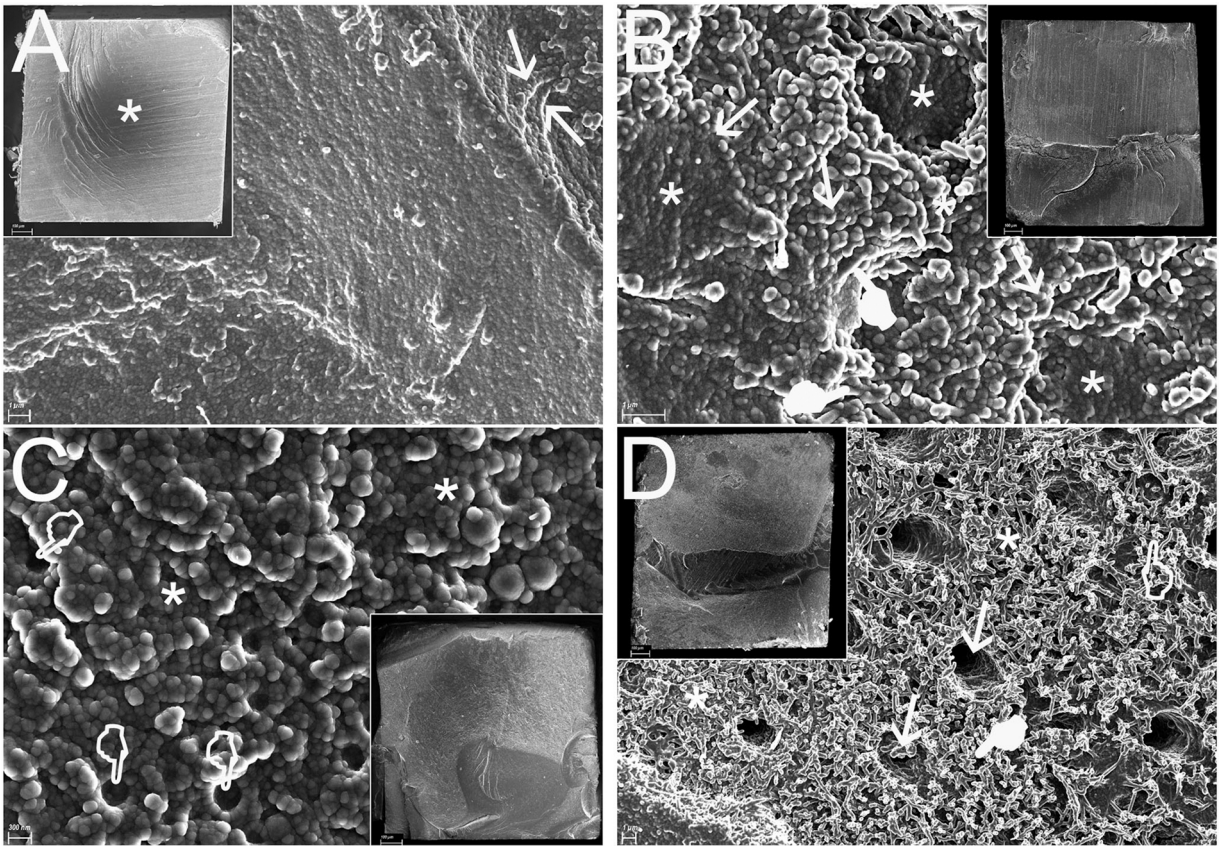

Fig. 9. **A**, FESEM observations of the fractured dentin surface of a specimen treated with undoped NPs at 24 h of storage (Scale bar: 1 μm). A generalized adhesive failure is observed, where residual adhesive resin (asterisk) may be shown at the inset (Scale bar: 100 μm). NPs, forming part of the adhesive layer are observable, following the trajectory of the collagen fibers in some locations (arrows). **B**, FESEM observations of the fractured dentin surface of a specimen treated with undoped NPs after load cycling, characterized by a mixed failure (inset -Scale bar: 100 μm-). Compact resin tags occupied the lumen of dentinal tubules (asterisks). A generalized dentin mineralization was observed at both peritubular and intertubular dentin (arrows). Remineralized collagen fibrils were apparent (pointers). (Scale bar: 1 μm). **C**, FESEM observations of the fractured dentin surface of a specimen treated with undoped NPs after collagenase solution immersion, characterized by a mixed failure (Scale bar: 300 nm). The main fracture occurred at the bottom of the hybrid layer because of the collagen degradation (inset) (Scale bar: 100 μm). Degradation of collagen fibrils permitted to see the agglomerated NPs surrounding the collagen fiber disappearance forming collars around the space that occupied the original fiber (pointes). Blocks of mineral, including NPs, were also observable (asterisks). **D**, FESEM observations of the fractured dentin surface of a specimen treated with undoped NPs after thermocycling, characterized by a mixed failure. The main fracture occurred at the bottom of the hybrid layer, permitting a fringe of adhesive resin at the middle of the surface (inset -Scale bar: 100 μm-). At a higher magnification, enlarged entrances of the dentinal tubules with scarce and poor resin tags are unveiled (arrows). Intertubular dentin seems porous and altered (asterisks). Fractured collagen fibers that are not mineralized or resin protected are apparent (pointers). Collagen fibers show loose ends, a reduced diameter and seem to be disrupted (Scale bar: 1 μm).

contrary, when those specimens were thermocycled (Fig. 7A), though not all dentinal tubules were resin-occupied (Fig. 10D). In fact, after thermal changes, stimulations of proteins synthesis and alkaline phosphatase activity have been probed in vivo and in vitro [62]. XO-dye deposited at the top of the hybrid layer and penetrated the whole depth of resin tags in both samples treated with undoped-NPs and TG-NPs, but in case of TG-NPs a profound orange dye was marked, indicating extensive remineralization throughout the entire resin dentin interface (Fig. 7B, C).

Through doping hydrophilic polymeric NPs with tideglusib we have outlined a reproducible technique to produce reparative dentin at the resin-dentin interface. To our knowledge, this is the first study demonstrating the effect of TG loaded bioactive NPs in operative dentistry targeted for coronal dentin remineralization. If the formed mineral deposits facilitate a certain degree of intrafibrillar mineralization (functional or biomimetic remineralization) deserves future research. Therefore, nanoindentation studies at the resin-dentin interface should be implemented in future strategies of research. Likewise, AFM and RAMAN studies should be performed and, if possible, TEM and XRD might complement the test cast to understand the adhesive reaction between tideglusib and dentin structure at the molecular level. Thereby, further research is required to determine the mechanisms by which tideglusib takes part in chemical reaction at the TG-NPs loaded-resin-dentin interface.

5. Conclusions

Nanoparticles doped with tideglusib promoted the highest dentin bonding efficacy among groups, as they attained the utmost bond strength values with creation of mineral deposits at the bottom of the hybrid layer and dentinal walls. Mechanical loading performed as a stimulus to enhance dentin remineralization and to reduce permeability through the dentin-bonded interface. Dentin infiltrated with polymeric nanoparticles doped with tideglusib contributed to mineral precipitation around the tubuli entrances, forming strata at intertubular dentin and favoring hermetic tags formation within the dentinal tubules. The mineral precipitation linked to the use of tideglusib endorsed lower porosity and nanoleakage, and better sealing in comparison with the rest of the groups.

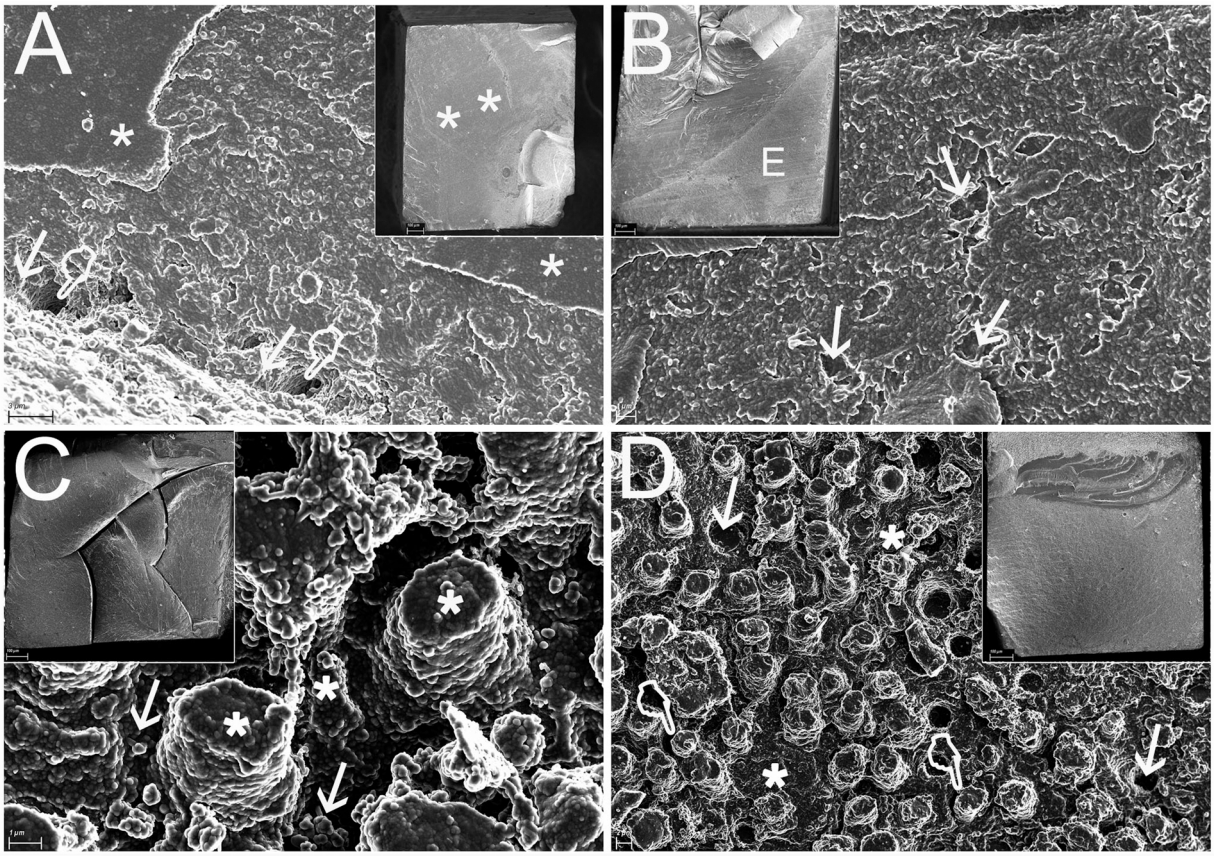

Fig. 10. A, FESEM observations of the fractured dentin surface of a specimen treated with phosphoric acid and Single Bond adhesive (control group) at 24 h of storage. A generalized adhesive failure is observed, where some part of the residual adhesive resin (asterisks) may be shown at the inset (Scale bar: 100 μm), and at two big extensions of the magnified image. The adhesive resin infiltrated the intertubular dentin (arrows), but in some locations could not form resin tags within the lumens of tubules, that appear empty (pointers). (Scale bar: 3 μm). **B**, FESEM observations of the fractured dentin surface of a specimen treated with phosphoric acid and Single Bond adhesive (control group) at 24 h after load cycling, characterized by a mixed failure and residual enamel E (inset -Scale bar: 100 μm-). Intertubular dentin appeared extensively covered by different strata hat permitted to see mineralized dentin in deep planes (arrows). **C,** FESEM observations of the fractured dentin surface of a specimen treated with phosphoric acid and Single Bond adhesive (control group) after collagenase solution immersion, characterized by a mixed failure. The main fracture occurred at the bottom of the hybrid layer because of the collagen degradation. Resin tags protruded at the interface (asterisks), that showed a damaged dentin substrate (arrows) (Scale bar: 1 μm). **D**, FESEM observations of the fractured dentin surface of a specimen treated with phosphoric acid and Single Bond adhesive (control group) after thermocycling, characterized by a mixed failure. The main fracture occurred at the bottom of the hybrid layer, permitting a fringe of adhesive resin at the middle of the surface (inset). (Scale bar: 100 μm). At a higher magnification, multiple empty dentinal tubules were observed (arrows). Intertubular dentin appeared correctly resin-infiltrated (asterisks) and numerous resin tags could not hermetically close all dentinal tubules (pointers). (Scale bar: 2 μm).

Declaration of Competing Interest

The authors declare that they have no known competing financial interests or personal relationships that could have appeared to influence the work reported in this paper.

Acknowledgements

This work was supported by Grant PID2020–114694RB-I00 funded by MCIN/AEI 10.13039/501100011033. The authors also thanks to the UGR@UGR (Undergraduate Research at University of Granada) program.

Appendix A. Supporting information

Supplementary data associated with this article can be found in the online version at doi:10.1016/j.dental.2023.12.010.

References

[1] Bermudez M, Hoz L, Montoya G, Nidome M, Perez-Soria A, Romo E, et al. Bioactive synthetic peptides for oral tissues regeneration. Front Mater 2021;8:655495. https://doi.org/10.3389/fmats.2021.655495.
[2] Lopes SR, Matuda AGN, Campos RP, Mafetano APVP, Barnabe AHM, Chagas GS, et al. Development of an antibacterial dentin adhesive. Polymers 2022;14:2502. https://doi.org/10.3390/polym14122502.
[3] Perdigão J. Current perspectives on dental adhesion: (1) Dentin adhesion - not there yet. Jpn Dent Sci Rev 2020;56:190–207. https://doi.org/10.1016/j.jdsr.2020.08.004.
[4] Ferracane JL. Models of Caries Formation around Dental Composite Restorations. J Dent Res 2017;96:364–71. https://doi.org/10.1177/0022034516683395.
[5] Kermanshahi S, Santerre JP, Cvitkovitch DG, Finer Y. Biodegradation of resin-dentin interfaces increases bacterial microleakage. J Dent Res 2010;89:996–1001. https://doi.org/10.1177/0022034510372885.
[6] Spencer P, Ye Q, Song L, Parthasarathy R, Boone K, Misra A, et al. Threats to adhesive/dentin interfacial integrity and next generation bio-enabled multifunctional adhesives. J Biomed Mater Res B Appl Biomater 2019;107:2673–83. https://doi.org/10.1002/jbm.b.34358.
[7] Spencer P, Ye Q, Park J, Topp EM, Misra A, Marangos O, et al. Adhesive/Dentin interface: the weak link in the composite restoration. Ann Biomed Eng 2010;38:1989–2003. https://doi.org/10.1007/s10439-010-9969-6.
[8] Moreira KM, Bertassoni LE, Davies RP, Joia F, Höfling JF, Nascimento FD, et al. Impact of biomineralization on resin/biomineralized dentin bond longevity in a minimally invasive approach: An "in vitro" 18-month follow-up. Dent Mater 2021;37:e276–89. https://doi.org/10.1016/j.dental.2021.01.021.

[9] Hashimoto M, Ohno H, Sano H, Kaga M, Oguchi H. In vitro degradation of resin-dentin bonds analyzed by microtensile bond test, scanning and transmission electron microscopy. Biomaterials 2003;24:3795–803. https://doi.org/10.1016/s0142-9612(03)00262-x.

[10] Hebling J, Pashley DH, Tjäderhane L, Tay FR. Chlorhexidine arrests subclinical degradation of dentin hybrid layers in vivo. J Dent Res 2005;84:741–6. https://doi.org/10.1177/154405910508400811.

[11] Pashley DH, Tay FR, Yiu C, Hashimoto M, Breschi L, Carvalho RM, et al. Collagen degradation by host-derived enzymes during aging. J Dent Res 2004;83:216–21. https://doi.org/10.1177/154405910408300306.

[12] Breschi L, Mazzoni A, Nato F, Carrilho M, Visintini E, Tjäderhane L, et al. Chlorhexidine stabilizes the adhesive interface: a 2-year in vitro study. Dent Mater 2010;26:320–5. https://doi.org/10.1016/j.dental.2009.11.153.

[13] Carrilho MR, Tay FR, Donnelly AM, Agee KA, Tjäderhane L, Mazzoni A, et al. Host-derived loss of dentin matrix stiffness associated with solubilization of collagen. J Biomed Mater Res B Appl Biomater 2009;90:373–80. https://doi.org/10.1002/jbm.b.31295.

[14] Moussa DG, Kirihara JA, Ye Z, Fischer NG, Khot J, Witthuhn BA, et al. Dentin Priming with Amphipathic Antimicrobial Peptides. J Dent Res 2019;98:1112–21. https://doi.org/10.1177/0022034519863772.

[15] Fugolin AP, Dobson A, Huynh V, Mbiya W, Navarro O, Franca CM, et al. Antibacterial, ester-free monomers: Polymerization kinetics, mechanical properties, biocompatibility and anti-biofilm activity. Acta Biomater 2019;100:132–41. https://doi.org/10.1016/j.actbio.2019.09.039.

[16] Kidd EAM, Beighton D. Prediction of Secondary Caries around Tooth-colored Restorations: A Clinical and Microbiological Study. J Dent Res 1996;75:1942–6. https://doi.org/10.1177/00220345960750120501.

[17] Choi KK, Condon JR, Ferracane JL. The Effects of Adhesive Thickness on Polymerization Contraction Stress of Composite. J Dent Res 2000;79:812–7. https://doi.org/10.1177/00220345000790030501.

[18] Toledano M, Aguilera FS, Osorio E, Toledano-Osorio M, Escames G, Medina-Castillo AL, et al. Melatonin-doped polymeric nanoparticles reinforce and remineralize radicular dentin: Morpho-histological, chemical and biomechanical studies. Dent Mater 2021;37:1107–20. https://doi.org/10.1016/j.dental.2021.03.007.

[19] Toledano-Osorio M, Osorio R, Aguilera FS, Medina-Castillo AL, Toledano M, Osorio E, et al. Polymeric nanoparticles protect the resin-dentin bonded interface from cariogenic biofilm degradation. Acta Biomater 2020;111:316–26. https://doi.org/10.1016/j.actbio.2020.05.002.

[20] Cummins D. Zinc citrate/Triclosan: a new anti-plaque system for the control of plaque and the prevention of gingivitis: short-term clinical and mode of action studies. J Clin Periodo 1991;18:455–61. https://doi.org/10.1111/j.1600-051x.1991.tb02316.x.

[21] Cobb LH, McCabe EM, Priddy LB. Therapeutics and delivery vehicles for local treatment of osteomyelitis. J Orthop Res 2020;38:2091–103. https://doi.org/10.1002/jor.24689.

[22] Li X, Huang X, Li L, Wu J, Yi W, Lai Y, et al. LL-37-coupled porous composite scaffold for the treatment of infected segmental bone defect. Pharmaceutics 2022;15:88. https://doi.org/10.3390/pharmaceutics15010088.

[23] Neves VCM, Babb R, Chandrasekaran D, Sharpe PT. Promotion of natural tooth repair by small molecule GSK3 antagonists. Sci Rep 2017;7:39654. https://doi.org/10.1038/srep39654.

[24] Spencer P, Ye Q, Kamathewatta NJB, Woolfolk SK, Bohaty BS, Misra A, et al. Chemometrics-Assisted Raman Spectroscopy Characterization of Tunable Polymer-Peptide Hybrids for Dental Tissue Repair. Front Mater 2021;8:681415. https://doi.org/10.3389/fmats.2021.681415.

[25] Kim H-J, Lee WS, Jeong J, Kim DS, Lee S-W, Kim S-Y. Effect of elastin-like polypeptide incorporation on the adhesion maturation of mineral trioxide aggregates. J Biomed Mater Res B Appl Biomater 2020;108:2847–56. https://doi.org/10.1002/jbm.b.34616.

[26] Li Z, Ren Q, Han S, Ding L, Qin X, Hu D, et al. Promoting effect of a calcium-responsive self-assembly β-sheet peptide on collagen intrafibrillar mineralization. Regen Biomater 2022;9:rbac059. https://doi.org/10.1093/rb/rbac059.

[27] Masuda Y, Sakagami H, Yokose S, Udagawa N. Effect of Small-molecule GSK3 Antagonist on Differentiation of Rat Dental Pulp Cells into Odontoblasts. Vivo Athens Greece 2020;34:1071–5. https://doi.org/10.21873/invivo.11877.

[28] Comeau-Gauthier M, Tarchala M, Luna JLR-G, Harvey E, Merle G. Unleashing β-catenin with a new anti-Alzheimer drug for bone tissue regeneration. Injury 2020;51:2449–59. https://doi.org/10.1016/j.injury.2020.07.035.

[29] Kornsuthisopon C, Tompkins KA, Osathanon T. Tideglusib enhances odontogenic differentiation in human dental pulp stem cells in vitro. Int Endod J 2023;56:369–84. https://doi.org/10.1111/iej.13877.

[30] Rao AC, Venkatesh KV, Nandini V, Sihivahanan D, Alamoudi A, Bahammam HA, et al. Evaluating the Effect of Tideglusib-Loaded Bioactive Glass Nanoparticles as a Potential Dentine Regenerative Material. Mater Basel Switz 2022;15:4567. https://doi.org/10.3390/ma15134567.

[31] Zaugg LK, Banu A, Walther AR, Chandrasekaran D, Babb RC, Salzlechner C, et al. Translation Approach for Dentine Regeneration Using GSK-3 Antagonists. J Dent Res 2020;99:544–51. https://doi.org/10.1177/0022034520908593.

[32] Atila D, Keskin D, Lee Y-L, Lin F-H, Hasirci V, Tezcaner A. Injectable methacrylated gelatin/thiolated pectin hydrogels carrying melatonin/tideglusib-loaded core/shell PMMA/silk fibroin electrospun fibers for vital pulp regeneration. Colloids Surf B Biointerfaces 2023;222:113078. https://doi.org/10.1016/j.colsurfb.2022.113078.

[33] Pomeislová A, Otmar M, Rubešová P, Benýšek J, Matoušová M, Mertlíková-Kaiserová H, et al. 1,2,4-Thiadiazole acyclic nucleoside phosphonates as inhibitors of cysteine dependent enzymes cathepsin K and GSK-3β. Bioorg Med Chem 2021;32:115998. https://doi.org/10.1016/j.bmc.2021.115998.

[34] Ghazanfari D, Noori MS, Bergmeier SC, Hines JV, McCall KD, Goetz DJ. A novel GSK-3 inhibitor binds to GSK-3β via a reversible, time and Cys-199-dependent mechanism. Bioorg Med Chem 2021;40:116179. https://doi.org/10.1016/j.bmc.2021.116179.

[35] Sauro S, Osorio R, Watson TF, Toledano M. Influence of phosphoproteins' biomimetic analogs on remineralization of mineral-depleted resin-dentin interfaces created with ion-releasing resin-based systems. Dent Mater 2015;31:759–77. https://doi.org/10.1016/j.dental.2015.03.013.

[36] Sauro S, Osorio R, Osorio E, Watson TF, Toledano M. Novel light-curable materials containing experimental bioactive micro-fillers remineralise mineral-depleted bonded-dentine interfaces. J Biomater Sci Polym Ed 2013;24:940–56. https://doi.org/10.1080/09205063.2012.727377.

[37] Toledano M, Osorio R, Osorio E, Aguilera FS, Yamauti M, Pashley DH, et al. Effect of bacterial collagenase on resin-dentin bonds degradation. J Mater Sci Mater Med 2007;18:2355–61. https://doi.org/10.1007/s10856-007-3161-z.

[38] Toledano-Osorio M, Osorio E, Aguilera FS, Luis Medina-Castillo A, Toledano M, Osorio R. Improved reactive nanoparticles to treat dentin hypersensitivity. Acta Biomater 2018;72:371–80. https://doi.org/10.1016/j.actbio.2018.03.033.

[39] Medina-Castillo AL. Thermodynamic Principles of Precipitation Polymerization and Role of Fractal Nanostructures in the Particle Size Control. Macromolecules 2020;53:5687–700. https://doi.org/10.1021/acs.macromol.0c00973.

[40] Medina-Castillo AL, Fernandez-Sanchez JF, Segura-Carretero A, Fernandez-Gutierrez A. Micrometer and Submicrometer Particles Prepared by Precipitation Polymerization: Thermodynamic Model and Experimental Evidence of the Relation between Flory's Parameter and Particle Size. Macromolecules 2010;43(13):5804. https://doi.org/10.1021/ma100841c.

[41] Schaffazick SR, Pohlmann AR, Mezzalira G, Guterres SS. Development of nanocapsule suspensions and nanocapsule spray-dried powders containing melatonin. J Braz Chem Soc 2006;17:562–9. https://doi.org/10.1590/S0103-50532006000300020.

[42] Toledano M, Osorio E, Osorio MT, Aguilera FS, Toledano R, Romero EF-, et al. Dexamethasone-doped nanoparticles improve mineralization, crystallinity and collagen structure of human dentin. J Dent 2023;130:104447. https://doi.org/10.1016/j.jdent.2023.104447.

[43] Sauro S, Mannocci F, Toledano M, Osorio R, Pashley DH, Watson TF. EDTA or H3PO4/NaOCl dentine treatments may increase hybrid layers' resistance to degradation: a microtensile bond strength and confocal-micropermeability study. J Dent 2009;37:279–88. https://doi.org/10.1016/j.jdent.2008.12.002.

[44] Toledano M, Osorio E, Cabello I, Aguilera FS, López-López MT, Toledano-Osorio M, et al. Nanoscopic dynamic mechanical analysis of resin–infiltrated dentine, under in vitro chewing and bruxism events. J Mech Behav Biomed Mater 2016;54:33–47. https://doi.org/10.1016/j.jmbbm.2015.09.003.

[45] Dawasaz AA, Togoo RA, Mahmood Z, Azlina A, Thirumulu Ponnuraj K. Effectiveness of Self-Assembling Peptide (P11-4) in Dental Hard Tissue Conditions: A Comprehensive Review. Polymers 2022;14:792. https://doi.org/10.3390/polym14040792.

[46] Kawamura M, Toida Y, Hoshika S, Islam MRR, Li Y, Yao Y, et al. Influence of Novel Experimental Light-Cured Resin Cement on Microtensile Bond Strength. Polymers 2022;14:4075. https://doi.org/10.3390/polym14194075.

[47] Gungormus M, Tulumbaci F. Peptide-assisted pre-bonding remineralization of dentin to improve bonding. J Mech Behav Biomed Mater 2021;113:104119. https://doi.org/10.1016/j.jmbbm.2020.104119.

[48] de Sousa JP, Carvalho RG, Barbosa-Martins LF, Torquato RJS, Mugnol KCU, Nascimento FD, et al. The Self-Assembling Peptide P11-4 Prevents Collagen Proteolysis in Dentin. J Dent Res 2019;98:347–54. https://doi.org/10.1177/0022034518817351.

[49] Carvalho RG, Patekoski LF, Puppin-Rontani RM, Nakaie CR, Nascimento FD, Tersariol ILS. Self-assembled peptide P11-4 interacts with the type I collagen C-terminal telopeptide domain and calcium ions. Dent Mater 2023;39:708–17. https://doi.org/10.1016/j.dental.2023.06.004.

[50] Shibata S, Vieira LCC, Baratieri LN, Fu J, Hoshika S, Matsuda Y, et al. Evaluation of microtensile bond strength of self-etching adhesives on normal and caries-affected dentin. Dent Mater J 2016;35:166–73. https://doi.org/10.4012/dmj.2014-330.

[51] Frankenberger R, Pashley DH, Reich SM, Lohbauer U, Petschelt A, Tay FR. Characterisation of resin-dentine interfaces by compressive cyclic loading. Biomaterials 2005;26:2043–52. https://doi.org/10.1016/j.biomaterials.2004.07.003.

[52] Sauro S, Osorio R, Watson TF, Toledano M. Therapeutic effects of novel resin bonding systems containing bioactive glasses on mineral-depleted areas within the bonded-dentine interface. J Mater Sci Mater Med 2012;23:1521–32. https://doi.org/10.1007/s10856-012-4606-6.

[53] Posner AS, Blumenthal NC, Boskey AL. Model of aluminum-induced osteomalacia: inhibition of apatite formation and growth. Kidney Int Suppl 1986;18:S17–9.

[54] Li X, Yu Z, Jiang S, Dai X, Wang G, Wang Y, et al. An amelogenin-based peptide hydrogel promoted the odontogenic differentiation of human dental pulp cells. Regen Biomater 2022;9:rbac039. https://doi.org/10.1093/rb/rbac039.

[55] Toledano M, Osorio E, Aguilera FS, Sauro S, Cabello I, Osorio R. In vitro mechanical stimulation promoted remineralization at the resin/dentin interface. J Mech Behav Biomed Mater 2014;30:61–74. https://doi.org/10.1016/j.jmbbm.2013.10.018.

[56] Terzi A, Storelli E, Bettini S, Sibillano T, Altamura D, Salvatore L, et al. Effects of processing on structural, mechanical and biological properties of collagen-based substrates for regenerative medicine. Sci Rep 2018;8:1429. https://doi.org/10.1038/s41598-018-19786-0.

[57] Rahn BA, Perren SM. Xylenol orange, a fluorochrome useful in polychrome sequential labeling of calcifying tissues. Stain Technol 1971;46:125–9. https://doi.org/10.3109/10520297109067836.
[58] Osorio R, Osorio E, Medina-Castillo AL, Toledano M. Polymer nanocarriers for dentin adhesion. J Dent Res 2014;93:1258–63. https://doi.org/10.1177/0022034514551608.
[59] Profeta AC, Mannocci F, Foxton R, Watson TF, Feitosa VP, De Carlo B, et al. Experimental etch-and-rinse adhesives doped with bioactive calcium silicate-based micro-fillers to generate therapeutic resin-dentin interfaces. Dent Mater 2013;29:729–41. https://doi.org/10.1016/j.dental.2013.04.001.
[60] Toledano M, Cabello I, Aguilera FS, Osorio E, Toledano-Osorio M, Osorio R. Improved sealing and remineralization at the resin-dentin interface after phosphoric acid etching and load cycling. Microsc Micro 2015;21:1530–48. https://doi.org/10.1017/S1431927615015317.
[61] Toledano M, Osorio R, Osorio E, Medina-Castillo AL, Toledano-Osorio M, Aguilera FS. Ions-modified nanoparticles affect functional remineralization and energy dissipation through the resin-dentin interface. J Mech Behav Biomed Mater 2017;68:62–79. https://doi.org/10.1016/j.jmbbm.2017.01.026.
[62] Lozupone E, Palumbo C, Favia A, Ferretti M, Palazzini S, Cantatore FP. Intermittent compressive load stimulates osteogenesis and improves osteocyte viability in bones cultured “in vitro. Clin Rheuma 1996;15:563–72. https://doi.org/10.1007/BF02238545.

Supporting Information

Glossary

AIBN: azobis-isobutyronitrile
ALP: alkaline phosphatase
ATR: attenuated total reflectance
BHL: bottom of the hybrid layer
BMP: bone morphogenetic protein
CLSM: confocal laser microscopy
Col-1: collagen type 1
DLS: dynamic light scattering
DMP: dentin matrix acidic phosphoprotein
DMSO: dimethyl sulfoxide
D-NPs: nanoparticles doped with doxycycline
DSPP: dentin sialophosphoprotein
EDMA: ethylene glycol dimethacrylate
F-ATPase: F-Type ATPase
FESEM: field emission scanning electron microscopy
FTIR: Fourier-transform infrared spectroscopy
GSK-3: glycogen-synthase-kinase 3
GSK-3β: glycogen synthase kinase-3β
HAp**:** hydroxyapatite
HL: hybrid layer
MAA: methacrylic acid
MMPs**:** matrix metalloproteinases
MTBS**:** microtensile bond strength
NPs: nanoparticles
OCN: osteocalcin
OSX: osterix
PA: phosphoric acid
PBS: phosphate-buffered saline
PTS: phosphotransferase
SB: single bond
SBFS: simulated body fluid solution
SiC: silicon carbide
TEM: transmission electron microscopy
TG: tideglusib
TG-loaded NPs: TG-NPs
Xo: xylenol
Zn-NPs: nanoparticles doped with zinc

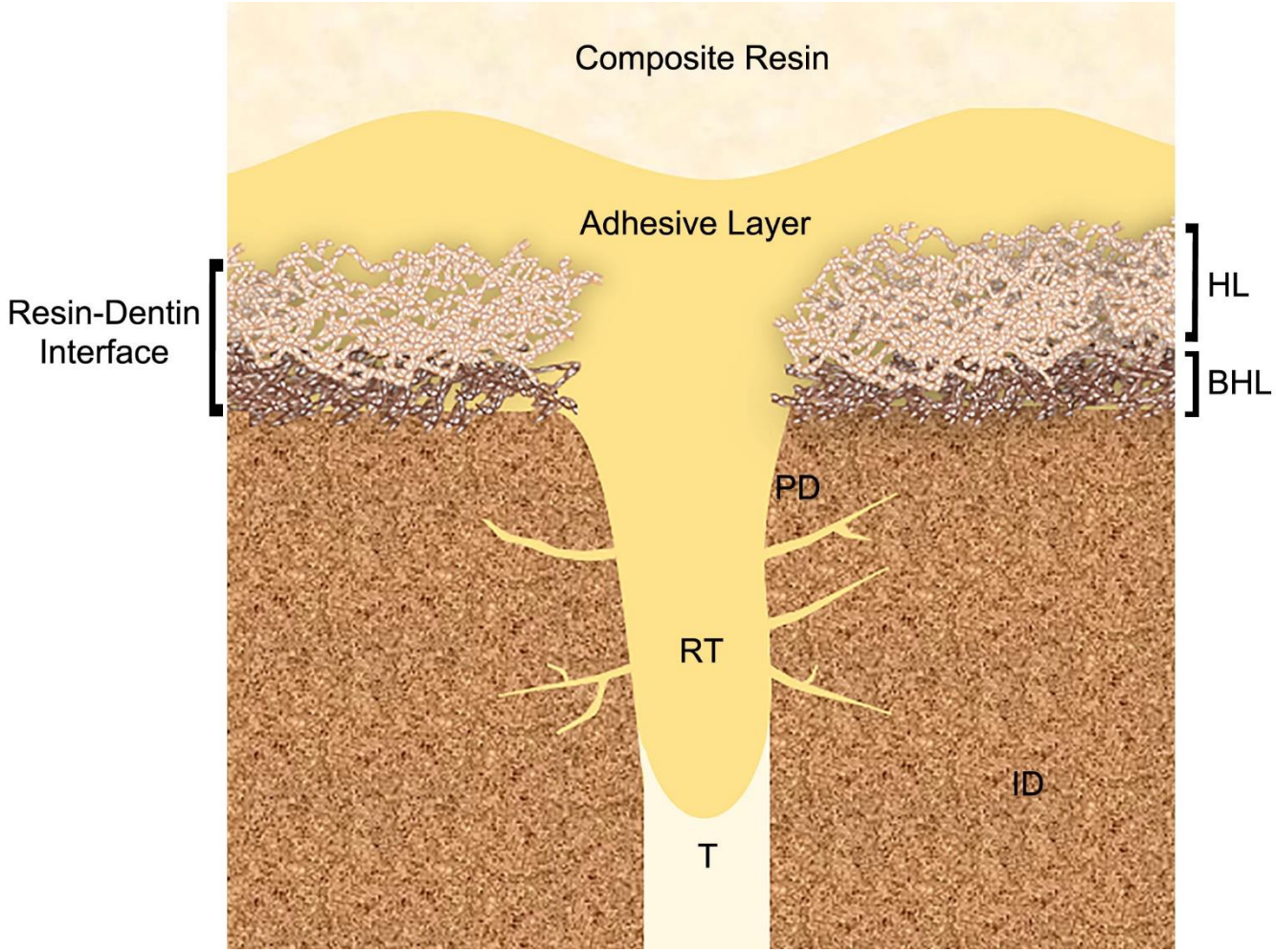

Figure S1. Schematic illustration of the resin-dentin interface. HL, hybrid layer; BHL, bottom of hybrid layer; PT, Peritubular Dentin; ID, Intertubular Dentin; RT, Resin Tags; T, Tubules.

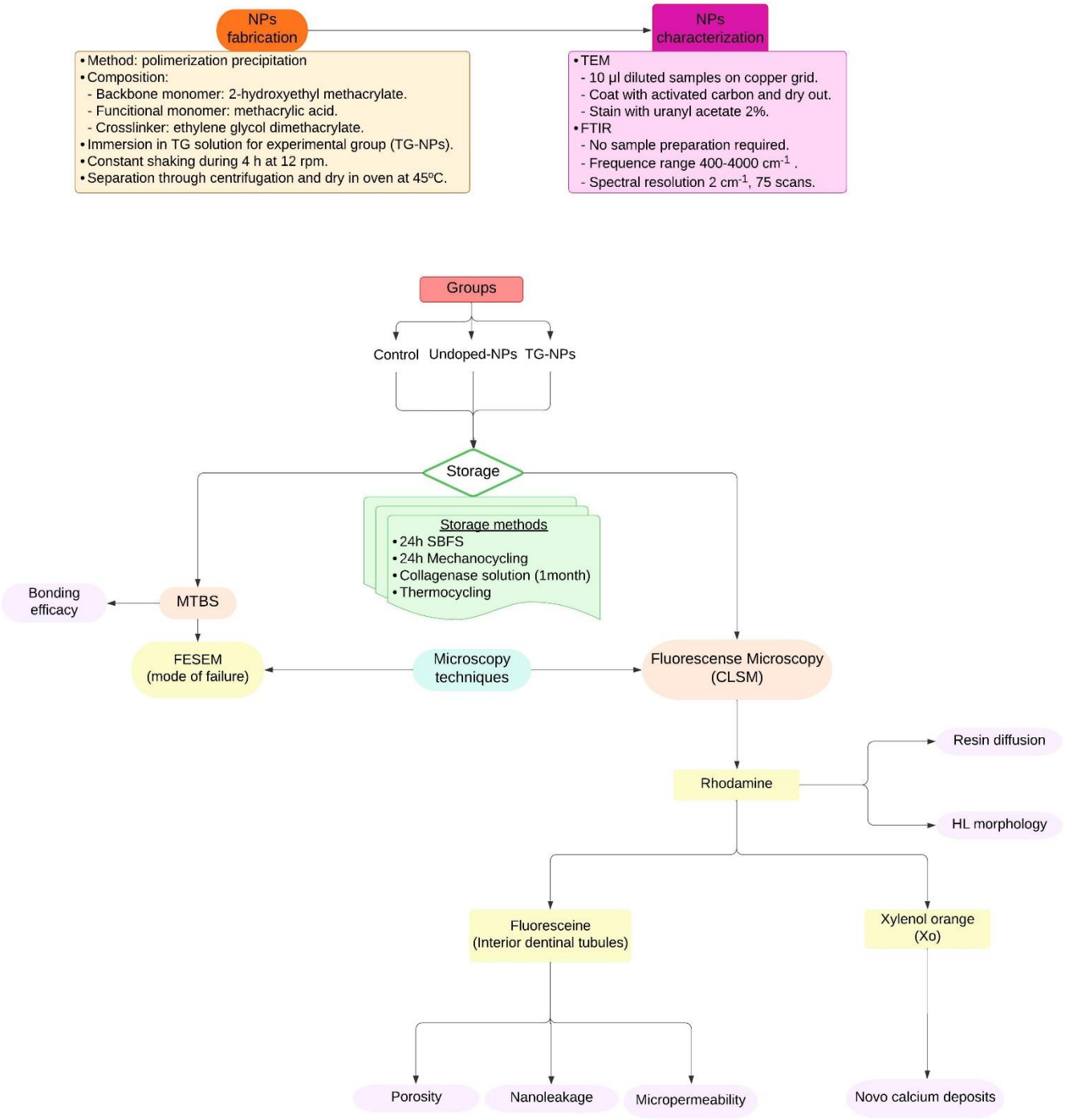

Figure S2. Flow chart diagram of study methodology. NPs, Nanopartículas; TG, Tideglusib; TEM, Transmission Electron Microscopy; FTIR, Fourier Transform Infrared Spectroscopy; MTBS, Microtensile Bond Strength; SBFS, Simulated Body Fluid Solution; LC, Load Cycled; FESEM, Field Emission Scanning Electron Microscopy; CLSM, Confocal Laser Scanning Microscopy.

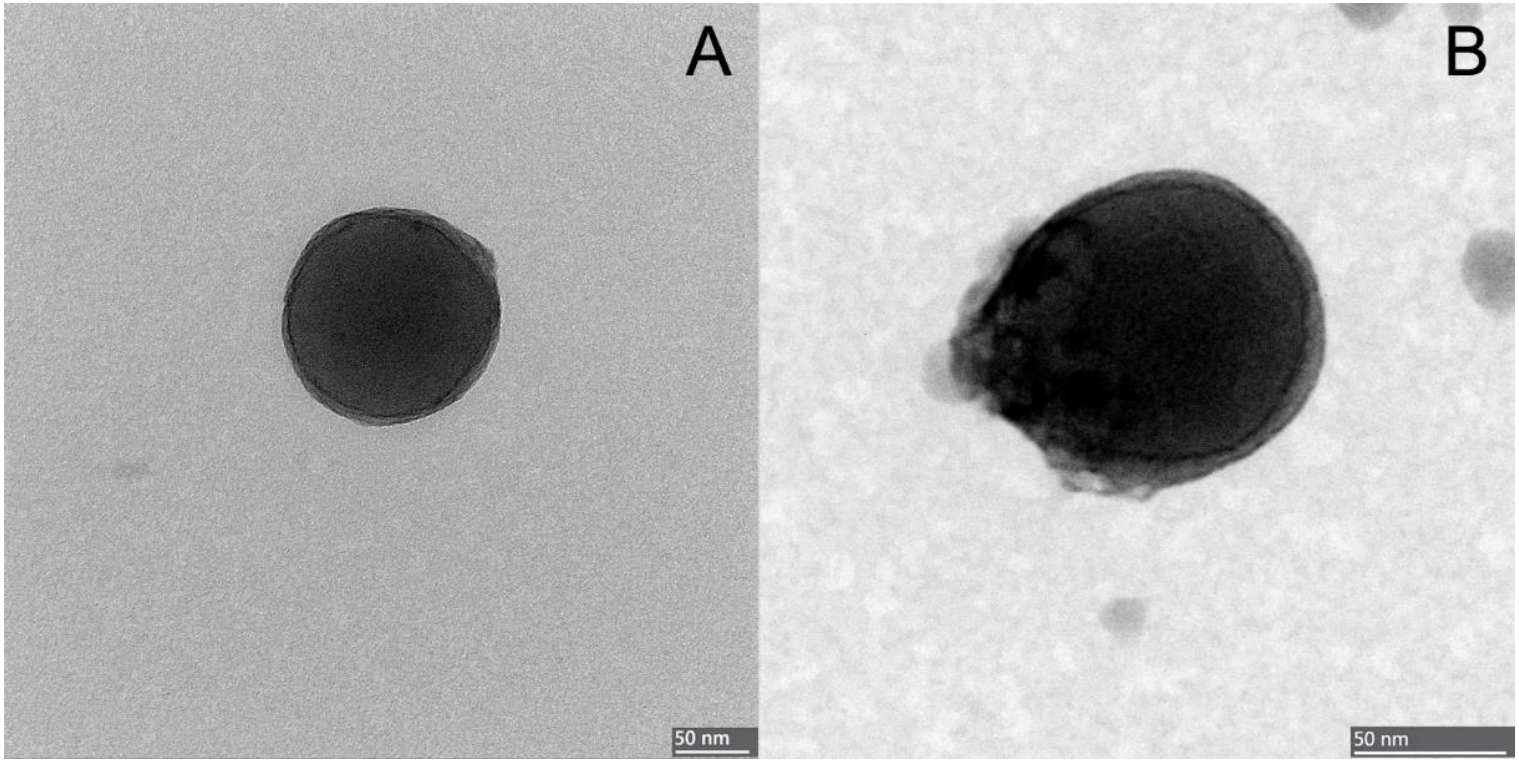

Figure S3. Transmission electron microscopic (TEM) images of undoped-nanoparticles (undoped-NPs) (**A**) and tideglusib-doped NPs (TG-NPs) (**B**). Dark and light objects inside the NPs were artifacts that developed during electron beam transmission. Scale bars are 50 nm in total length.

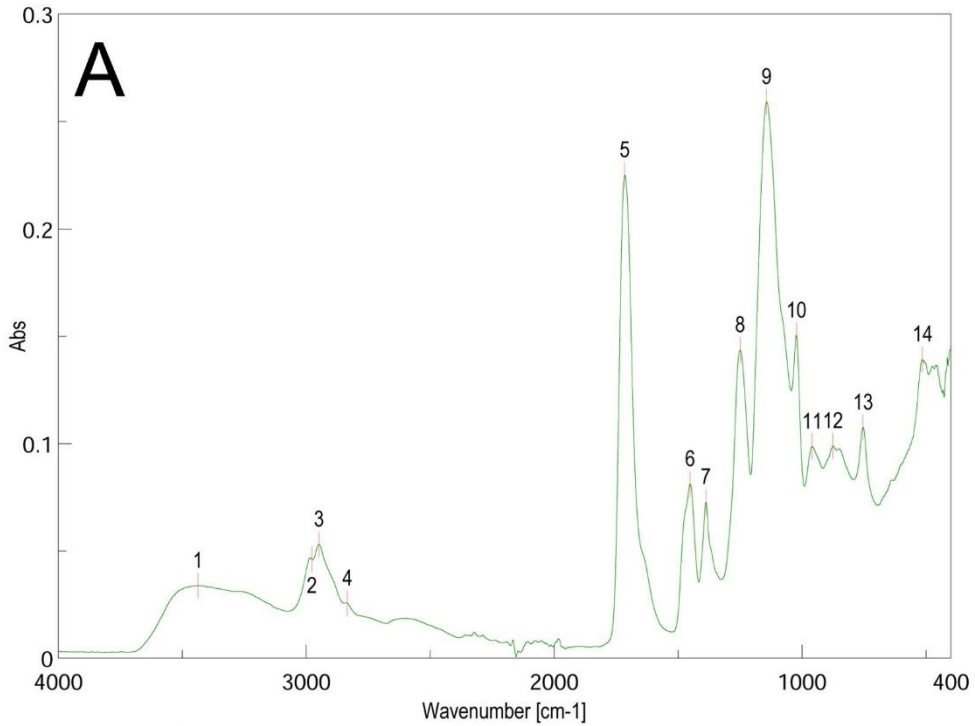

[Result of Peak Picking]

No.	Position	Intensity	No.	Position	Intensity
1	3437	0.0337594	2	2977	0.0461154
3	2949	0.0529977	4	2833	0.0255032
5	1715	0.224968	6	1451	0.0810956
7	1388	0.072705	8	1250	0.143476
9	1143	0.25908	10	1024	0.150297
11	959	0.098604	12	876	0.098776
13	754	0.107413	14	515	0.13911

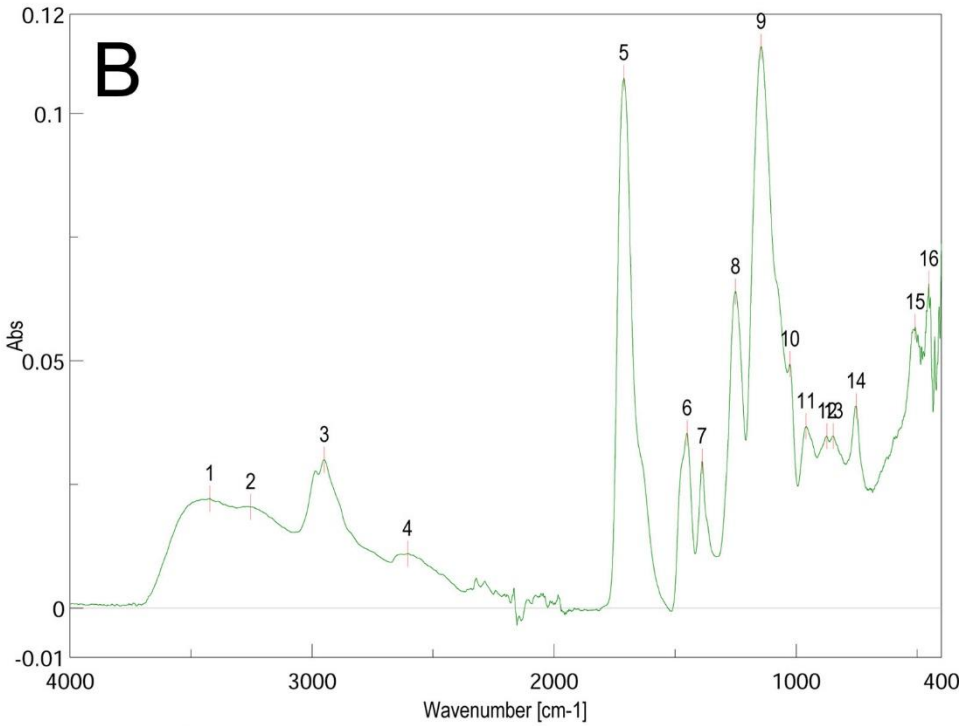

[Result of Peak Picking]

No.	Position	Intensity	No.	Position	Intensity
1	3423	0.0221135	2	3253	0.0204267
3	2949	0.0299356	4	2605	0.0109671
5	1712	0.107126	6	1451	0.0353192
7	1389	0.0296188	8	1251	0.0639357
9	1144	0.113427	10	1026	0.049243
11	958	0.0366806	12	873	0.0346962
13	847	0.0346994	14	753	0.0407866
15	508	0.0568067	16	452	0.0655155

Figure S4: FTIR spectra of the experimental groups, undoped-NPs (S4A), TG-NPs (S4B). The figures also report the Peak Picking with both positions and intensities.

Journal of Dentistry 148 (2024) 105027

Contents lists available at ScienceDirect

Journal of Dentistry

journal homepage: www.elsevier.com/locate/jdent

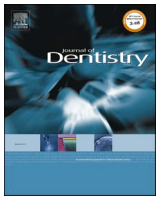

Tunable polymer-peptide hybrids for dentin tissue repair

Manuel Toledano [a], Enrique Fernández-Romero [a,b], Fátima S. Aguilera [a], Estrella Osorio [a,*], José A. Rodríguez-Santana [a], Macarena Garrido [a], Pedro A. Solís [a], Franklin García-Godoy [c], Raquel Osorio [a]

[a] University of Granada, Faculty of Dentistry. Colegio Máximo de Cartuja s/n, Granada 18071, Spain
[b] Medicina Clínica y Salud Pública PhD Programme, University of Granada, 18071 Granada, Spain
[c] Health Science Center, College of Dentistry, University of Tennessee, 875 Union Avenue, Memphis, TN 38103, United States

ARTICLE INFO

Keywords:
Dentin
Nanoparticles
Remineralization
Raman
Masson's trichrome staining
Tideglusib

ABSTRACT

Objectives: This study targets to assess the remineralization capability of conditioned dentin infiltrated with polymeric nanoparticles (NPs) doped with tideglusib (TDg) (TDg-NPs).
Methods: Dentin conditioned surfaces were infiltrated with NPs and TDg-NPs. Bonded interfaces were created, stored for 24 h and submitted to mechanical and thermal challenging. Resin-dentin interfaces were evaluated through nanohardness, Masson's trichrome staining microscopy, and Raman analysis.
Results: Dentin surfaces treated with TDg-NPs and load cycled produced higher nanohardness than the rest of the groups at the hybrid layer. At the bottom of the hybrid layer, all samples treated with TDg-NPs showed higher nanohardness than the rest of the groups. Active remineralization underneath the hybrid layer was detected in all groups after TDg application and load cycling, inducting new dentinal tubuli formation. After thermocycling, remineralization at the hybrid layer was not evidenced in the absence of NPs. Raman analysis showed increase mineralization, enriched carbonate apatite formation, and improved crosslinking and scaffolding of the collagen.
Conclusions: Mechanical loading on the specimens obtained after TDg-NPs dentin infiltration inducts an increase of mineralization at the resin/dentin interface, indicating remineralization of peritubular and intertubular dentin with augmented crystallographic maturity in crystals. Enriched collagen quality was produced, generating an adequate matrix organization to promote apatite nucleation, after tideglusib infiltration.
Clinical significance: At the present research, it has been proved the creation of reparative dentin, at the resin-dentin interface, after tideglusib dentin infiltration. Chemical stability, to favor integrity of the resin-dentin interface, is warranted in the presence of the TDg-NPs in the demineralized dentin collagen.

1. Introduction

Resin-composite restorations have usually exhibited a declined clinical effectiveness due to the challenges associated with the adhesive-resin–dentin bonds [1]. Adhesive dentistry aims to facilitate the complete infiltration of the resin across the entire thickness of the conditioned dentin, resulting in the formation of the hybrid layer (HL) [2,3]. Proteoglycans and Type I collagen fibrils are surrounded by a polymer chain, in this structure [3]. As a result of adhesive diffusion into demineralized dentin, a decreasing concentration gradient is formed, leaving collagen fibrils at the bottom of the HL (BHL) unprotected and vulnerable [4] (Fig. 1). However, dentin has demonstrated a considerable capacity for regeneration following damage [5].

Different mineral aggregate filling materials have been added into dental adhesives, in order to promote mineral deposition within the hybrid layer after an ion exchange [6]. Various resin fillers such as ceramic bioactive nanospheres made of hydroxyapatite (HAp), have also been suggested [7]. However, none of these materials offer an ptimal degradation kinetics and a sustained and controlled release [8]. The utilization of nanopolymeric particles (NPs) as calcium- and phosphate-sequestering materials have been presented as an alternative approach. These NPs are biocompatible and non-resorbable biomaterials, made of methacrylic acid, ethylene glycol dimethacrylate and 2-hydroxyethyl methacrylate, covalently connected [9,10]. Along the backbone of these polymeric NPs, there are chains of anionic carboxylate groups (i.e., COO-) that facilitate functionalization with metal cations or drugs containing amino groups [11].

* Corresponding author at: University of Granada, Faculty of Dentistry, Dental Materials Section, Colegio Máximo de Cartuja s/n, 18071 Granada, Spain.
E-mail address: meosorio@ugr.es (E. Osorio).

https://doi.org/10.1016/j.jdent.2024.105027
Received 13 February 2024; Received in revised form 23 April 2024; Accepted 25 April 2024
Available online 26 April 2024

Glossary

a.c.	arbitrary counts
AGE	advance glycation end products
β-cat	β-catenin
BHL	bottom of the hybrid layer
Bis-GMA	bisphenol A diglycidyl
DC	degree of conversion
EDX	energy dispersive X-ray
FWHM	full-width half-maximum
FTIR	Fourier-transform infrared spectroscopy
GMC	gradient in mineral content
GSK-3	glycogen-synthase-kinase 3
HAp	hydroxyapatite
HCA	hierarchical cluster analysis
HEMA	hydroxy ethyl methacrylate
Hi	nanohardness
HL	hybrid layer
KMC	K-means cluster
MMPs	matrix metalloproteinases
nano-DMA	nano-dynamic mechanical analysis
NPs	nanopolymeric particles
SB	single bond
SBFS	simulated body fluid solution
SiC	silicon carbide
TDg	tideglusib

Recently, Neves et al. (2017) [12] reported the performance of various small molecule GSK-3 antagonists which have been developed, in an effort to promote the natural processes of reparative dentin formation. Tideglusib (TDg), a small molecule GSK-3 inhibitor used in Alzheimer's disease treatment, has been proposed as a dentin repair agent [13]. Various methods for TDg delivery have been employed, such as a collagen sponge [12], or a hyaluronic acid-based hydrogel [5]. In the current research, hydrophilic polymeric nanostructured particles will serve as carriers to assess the in vitro clinical efficacy of TDg at the resin-dentin interface.

Exposure of demineralized unprotected collagen, either by resin or intrafibrillar mineral, may be subjected to degradation, mediated by endogenous matrix metalloproteinases (MMPs) in junction with their extracellular inhibitors. One in vitro method for testing consequences of aging involves challenging the resin-dentin interface with load cycling or testing the resistance of the resin-dentin interfaces when subjected to hydrolytic degradation under thermal stress. Load cycling and thermocycling of bonded specimens has been widely employed for in vitro assessment of resin-based dental materials [14].

The aim of this study was to evaluate the effect of the infiltration of polymeric nanoparticles doped with tideglusib into phosphoric acid-etched dentin before the adhesive application, in order to ascertain the ability to promote mineral deposition, to protect the hybrid layer, and to restore the original dentin mechanical properties at the decalcified hybrid layer. To evaluate mechanical recovery and remineralization at the hybrid layer, various techniques were used: Dentin mineral precipitation at the hybrid layer was indirectly assessed by evaluating nanohardness augmentation at the hybrid layer under various degradation methodologies and storage conditions [15]. By employing Masson's trichrome staining, we conducted a qualitative assessment of collagen encapsulation, observing color distinctions within the non-remineralized and remineralized interfacial areas. While the majority of research has concentrated on the mechanical features of the substrate, the microscopic or histological aspects of dentin, and the underlying molecular structure, essential for comprehending the impact of the disease on the mineral content and collagen matrix, has been scarcely investigated [16]. In this regard, Raman spectroscopy is a potent tool for directly obtaining data about the molecular composition of a specimen. Compared to traditional microscopic and histological techniques, Raman spectroscopy and cluster analysis are advantageous as they are fast, stain-free, non-intrusive and quantitative [17]. The null hypotheses to be tested are that TDg-NPs infiltration, into etched dentin, (1) does not affect nanomechanical properties at the resin-dentin interface and (2) does not enable mineral precipitation at the

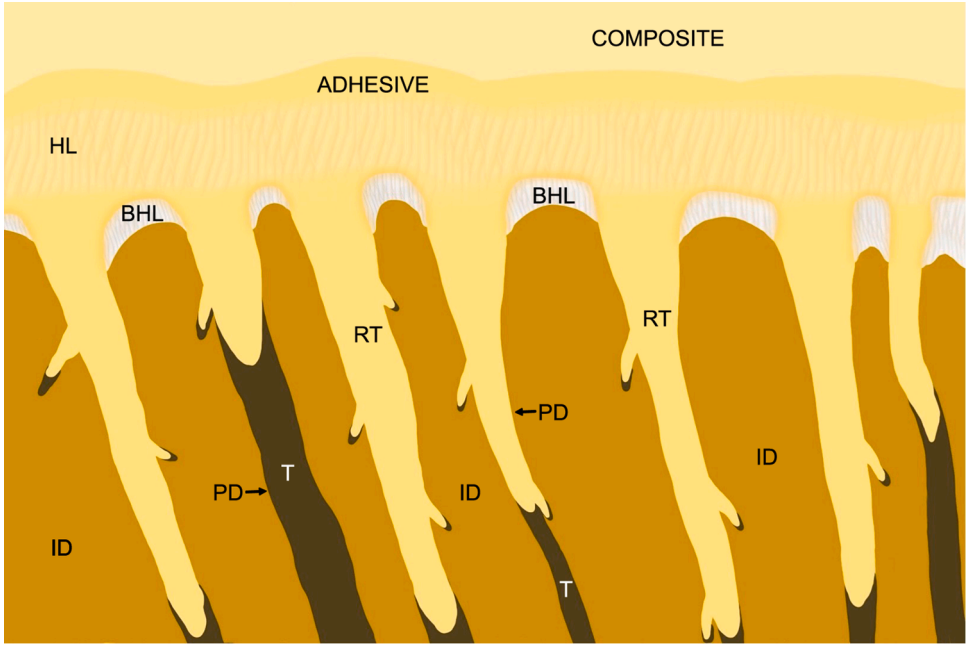

Fig. 1. Representative image, in scheme, of the resin-dentin interface. BHL, Bottom of the hybrid layer. Abbreviations: HL, Hybrid layer. ID, Intertubular dentin. PD, Peritubular dentin. T, Dentinal tubule. RT, Resin tag.

demineralized bonded interface.

2. Material and methods

2.1. Production of nanoparticles

The process of obtaining NPs applied the use of the polymerization precipitation method, which controlled the precipitation facilitated by a thermodynamic approach. Specifically, the Flory-Huggins model, based on Hansen's solubility parameters, was employed. This model centered on interactions among solvent molecules and the growth of polymer chains through hydrogen, polar bonding, and dispersion forces [18]. The backbone monomer for NPs design was 2-hydroxyethyl methacrylate, with methacrylic acid serving as the functional monomer, and ethylene glycol dimethacrylate employed as the cross-linker. Subsequently, half of the produced NPs were loaded with a peptide, tideglusib (Sigma-Aldrich, Chemie, Riedstr, Germany). The NPs loading process was conducted by immersion of 100 mg of NPs in 1 mL of 0.0017 mg/mL TDg solution for 2 h at room temperature under constant shaking (12 rpm) (rotator Orbit 300,445, JP Selecta, Barcelona, Spain). Then, the NPs were left until the solvent was completely evaporated, ensuring that all the TDg remains onto the NPs. Two types of NPs were obtained, undoped NPs and TDg-NPs.

2.2. Preparation of specimens for the bonding procedure, mechanical and thermal challenging

Thirty-six unerupted human third molars, preserved at 4 °C in a 0.5% chloramine T solution for no more than a month, were utilized for this study. Prior to their involvement, subjects provided informed consent, aligning with the Declaration of Helsinki and adhering to good clinical practice guidelines. The study received ethical approval from the Institutional Ethics Committee (1906/CEIH/2020).

The teeth were horizontally sectioned just below the dentin-enamel junction to expose sound dentin surfaces. These surfaces were then flatly polished to create a clinically relevant smear layer, utilizing 180-grit silicon carbide –SiC- abrasive paper. Subsequently, the dentin surfaces underwent etching (with 37% phosphoric acid, during 15 s), followed by rinsing and drying. Random allocation of experimental teeth ($n = 12$) to one of three groups was achieved through computer-generated randomization, facilitated by http://www.randomizer.org/form.htm. The allocation remained concealed in sealed envelopes until the time of bonding procedure. Just an ethanol solution was applied (30 s) (i), or an ethanol suspension of undoped-NPs (ii), and TDg-NPs (iii) (10 mg/mL) in each of the three experimental groups ($n = 12$), acting as primers. Ethanol was then evaporated for 30 s and, finally, Single Bond (SB) resin (3 M ESPE, St. Paul, MN, USA) was applied according to the manufacturer's instructions, to fulfill the conventional adhesive protocol. The sample preparation was conducted by one researcher, and a uniform adhesion protocol was implemented by a different researcher. For each tooth, a composite build-up (5 mm high) (Tetric EvoCeram, Ivoclar-Vivadent, Schaan, Liechtenstein) was performed using the incremental technique, in five 1 mm resin layers. The light-curing process was carried out with a Bluephase polywave light-emitting diode light-polymerizing unit (Bluephase G2, Ivoclar Vivadent AG, Schaan, Liechtenstein) at 1500 mW/cm^2 for 20 s. The output intensity was monitored with a curing radiometer (Model Bluephase meter, Ivoclar Vivadent AG, Schaan, Liechtenstein), ensuring a minimal output intensity of 1500 mW/cm^2 for all experiments. The restored teeth were stored in a dark environment and submerged in simulated body fluid solution (SBFS) for 24 h.

Three experimental groups were established, 1) control group, 2) undoped NPs and 3) TDg-NPs, with 12 specimens per group. The specimens were then divided into three sub-groups ($n = 4$) based on the challenging method: (1) Restored teeth stored in SBFS for 24 h, (2) load cycling with a sine wave form for 24 hs (259,200 cycles, 3 Hz) (S-MMT-250NB; Shimadzu, Tokyo, Japan) proceeding as in Sauro *et al.* 2009 [19], and (3) thermal cycling (100,000 cycles/ 5 °C and 55 °C) (SD Mechatronik, Germany) during approximately three months in distilled water [13]. Finally, the samples were sectioned into resin–dentin slabs and polished using ascending grit SiC abrasive papers (#1200 to #4000) on a water-cooled polishing device (Buehler-MetaDi, Buehler, Lake Bluff, IL, USA). The specimen preparation was concluded with a final ultrasonic cleaning (5 min) (Figure S1).

2.3. Nanoindentation testing

Dentin-resin slabs were submitted for nanoindentation testing. The nano-hardness was performed using a Hysitron Ti 950 nanoindenter (Hysitron, Minneapolis, MN). The nanoindenter was a Berkovich (three-sided pyramidal) diamond indenter tip (tip radius ~20 nm). It was calibrated against a fused quartz sample using a quasistatic force set-point of 5 μN. On each slab, three indentation lines 15(±5) μm from each other were made in different mesiodistal positions along the interface. Four indentation were performed in each straight line starting from the top of hybrid layer down to the underlying intertubular dentin in order to evaluate changes in the nanohardness (*Hi*) of the resin-dentin interface (Fig. 1). The apical-occlusal distance between each indentation was kept constant (5 ± 1 μm) by adjusting the distance intervals steps. Indentations were executed with a load of 4000 nN and a time function of 10 s. The procedure was performed in a hydrated condition by the application of a layer of ethylene glycol over the specimen surface, preventing water evaporation during a typical 25-to-30-min scanning period [20].

2.4. Masson's trichrome staining

Thirty-six resin–dentin bonded slices were used for the histomorphological evaluations. The medial aspects of each resin–dentin bonded slice were attached to a glass holder using a photocuring adhesive (Technovit 7210 VLC; Heraeus Kulzer, Werheim, Germany) and ground with SiC papers ranging from 800 to 4000 grits in a polisher (Apparatebau d-2000; Exakt Norderstedt, Germany) until reaching a thickness of approximately 10 μm. Masson's trichrome staining was applied to the slices in order to facilitate the differentiation of resin and non-resin encapsulation of the exposed collagen. This staining technique exhibits a high affinity for cationic elements of normally mineralized dentin type I collagen, resulting in green staining of collagen. In demineralized collagen, different colorations, generally red, appear. Collagen coated with adhesive stains orange, and pure adhesive appears beige. Subsequently, the stained sections on slides were dehydrated through ascending ethanol and xylene, cover-slipped, and examined under light microscopy (BH-2; Olympus, Tokyo, Japan) at $a \times 100$ magnification. One slice was prepared from each specimen, and the images were digitalized using a scanner (Agfa Twin 1200; Agfa-Gevaert NV, Mortsel, Belgium). Within each specimen, the presence or absence of a red band corresponding to demineralized dentin was observed. A qualitative assessment of collagen encapsulation was conducted by visualizing color differences within the interfacial zones of resin–dentin interfaces [17,21].

2.5. Raman spectroscopy and cluster analysis

A dispersive Raman spectrometer/microscope (Horiba Scientific Xplora, Villeneuve d'Ascq, France) was used to analyze dentin interfaces. A near-infrared diode laser spot size of ≈ 0.5μm^2, operating at 785 nm, was employed to measure the Raman signal (100 mW power at sample surface) from 400 to 1700 cm^{-1} Raman wavenumber. Chemical mappings of the interfaces were performed. For each specimen two areas 20 × 20 mm area of the interfaces at different sites were mapped using 1 mm spacing at X and Y axes, and each spectrum was measured by using 2 s acquisition time with 2 accumulations. For each mapping, using the

multivariate analysis tool (Isys, Horiba), a K-means cluster analysis (KMC) was performed, which includes a statistical pattern to generate independent clusters. The software to classify different natural groups of components used Hierarchical Cluster Analysis (HCA). The observed spectra were described at 400–1700 cm^{-1} with 10 complete overlapping Gaussian lines, suggesting homogeneous data for further calculations [22].

As the cluster centroids are essentially means of the cluster score for the elements of cluster, the mineral and organic components of the resin-dentin interface were examined for each cluster. A comparison of the spectra that were collected from the specimens which compose each subgroup might indicated complete overlap, suggesting similarity between both measurements. It was hence used for identifying significant spectral differences among distinct substrata. Clusters were created following Ward's technique and the dendrogram was calculated applying five factor spectra or principal components, corresponding with five different components at the resin-dentin interface (red, more mineralized dentin; green, dentin; blue, bottom of hybrid layer; purple, hybrid layer; yellow, adhesive). For each point of analysis, all spectra described for each cluster were averaged to obtain the mean cluster spectrum. At this point, the mineral (Table S1), organic components and degree of adhesive efficacy of dentin were calculated. a) The organic component of dentin was analyzed examining the following parameters:

Normalization: Phenyl group; the peak at 1003 cm^{-1}, which is assigned to C—C bond in the phenyl group, was used for normalization [23].

Crosslinking: AGEs (advance glycation end products)-pentosidine at 1550 cm^{-1}, interpreted as a marker of the aging process [24].

Nature and secondary structure of collagen: α-helices peak [1340 cm^{-1}]: This signal has been assigned to protein α-helices where intensity is sensitive to molecular orientation [22]. b) Degree of adhesive efficacy:

Degree of conversion of adhesive

Ratio 1637/1608. The peak appearing at 1637 cm^{-1} is associated with C = C of methacrylate, and the peak at 1608 cm^{-1} is related to C—C in phenyl of adhesive monomer [25].

Bis-GMA penetration

Ratio1113/1667. The peak appearing at 1113 cm^{-1} is associated with C—O-C of adhesive, and the peak at 1667 cm^{-1} is related to amide I [25,26].

Adhesive (Bis-GMA and HEMA) penetration

Ratio 1450/1667. The peak appearing at 1450 cm^{-1} is assigned to the CH_2 group of both Bis-GMA and HEMA, and the peak at 1667 cm^{-1} is related to amide I [25,26].

2.6. Statistical analysis

Mean nanohardness values were calculated in GPa and analyzed by analysis of variance including analysis of interactions ($p < 0.05$). NPs application and challenging method were independent factors. Student-Newman-Keuls ($p < 0.05$) was used for *post hoc* comparisons.

3. Results

3.1. Nanoindentation testing, nanohardness

Mean nanohardness (*Hi*) values (GPa) and Standard deviation (SD) attained at the different indentation zones in the experimental groups, are exposed in Fig. 2.

At the hybrid layer, samples treated with TDg-NPs after 24 h (0.55 GPa, SD 0.07) and mechanically loaded (0.49 GPa, SD 0.08) attained the highest nanohardness ($P < 0.05$). The control group after 24 h achieved the lowest *Hi* values (0.11 GPa, SD 0.03) ($P < 0.05$). The rest of the groups obtained intermediate values, without differences among them ($P > 0.05$), ranging from 0.35 GPa, SD 0.06 (dentin treated with TDg-NPs thermocycled) to 0.44 GPa, SD 0.10 (dentin treated with undoped NPs) (Fig. 2).

Any sample treated with TDg-NPs attained the highest *Hi* among all groups of study, at the bottom of the hybrid layer ($P < 0.05$), ranging from 0.62 GPa, SD 0.07 (dentin treated with TDg-NPs mechanically loaded) to 0.72 GPa, SD 0.12 (dentin treated with TDg-NPs after 24 h).

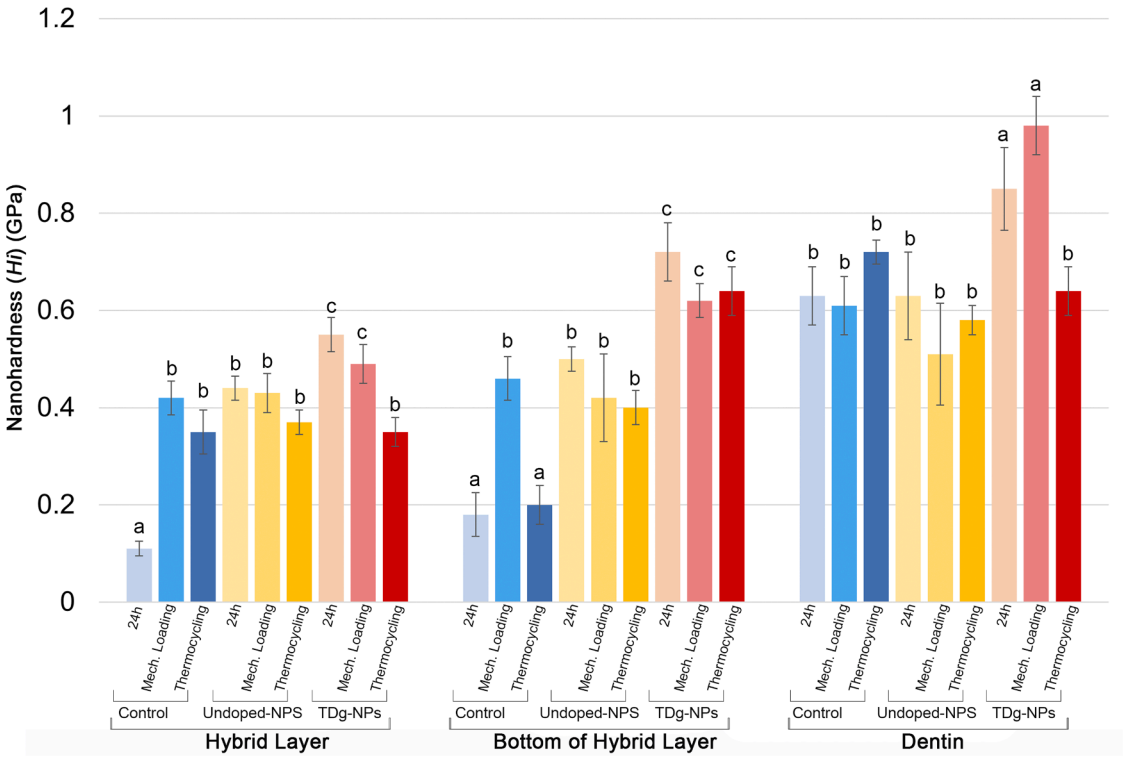

Fig. 2. Mean and standard deviation (SD) values of nanohardness (GPa) attained at the different experimental groups. Identical lowercase means no significant difference among distinct experimental groups at the same tested interface. Abbreviations: NPs, nanoparticles.

Specimens treated without NPs, except those mechanically loaded, achieved the lowest *Hi* values ($P < 0.05$) (0.18 GPa, SD 0.09 in the control group after 24 h; 0.20 GPa, SD 0.08 in the control group after thermocycling (Fig. 2).

At the intact dentin, those samples treated with TDg-NPs after 24 h (0.85 GPa, SD 0.17) and mechanically loaded (0.98 GPa, SD 0.12) showed the highest *Hi* among groups ($P < 0.05$) (Fig. 2).

3.2. Masson's trichrome staining

Representative images are shown in Fig. 3. An intense and wide red zone evidenced the existence of non-resin covered and demineralized dentin collagen in all groups, at 24 h of storage (Figs. 3A, 3B, 3C). Active remineralization at the base of the hybrid layer was detected in all groups after load cycling (Figs. 3D, 3E, 3F). Tubular dentin walls formation was detected, reproducing the sinusoidal primary curvatures (Fig. 3F). When specimens were thermocycled, remineralization at the hybrid layer was not evidenced in the absence of NPs (Fig. 3G) and in presence of undoped NPs (Fig. 3H). A faint and non-continuous red line was found at the hybrid layer that was formed after TDg-NPs dentin infiltration; green zones indicating intratubular and peritubular remineralization were observed within the resin-dentin interface (arrows), and some parts of the restoration showed total remineralization (Fig. 3I).

3.3. Raman spectroscopy and cluster analysis

3.3.1. Relative presence of minerals

Dentin treated with TDg-NPs showed higher phosphate peak intensities at both HL and BHL than dentin treated with undoped NPs, at 24 h of storage and after load cycling (Table 1). Thermocycling produced the maximum phosphate peak and area at the BHL of dentin samples treated with TDg-NPs, among groups (Table 1). The area of phosphate peak obtained the highest intensity at both the HL and BHL when TDg-NPs infiltrated the dentin at 24 h of storage and after load cycling, in comparison with the rest of the groups (control and undoped NPs). The carbonate peak intensity was highest at both the HL and BHL when TDg was used to infiltrate dentin after 24 h of storage and after load cycling. Thermocycling produced the highest carbonate intensity at the BHL when TDg was used for NPs doping. At 24 h of storage, the highest area of carbonate appeared when dentin was treated with TDg-NPs at both HL and BHL. When specimens were submitted to load cycling, those treated with TDg achieved the lowest carbonate area in comparison with the group of dentin treated with unloaded NPs. Thermocycling produced the lowest carbonate area among groups, at the HL of dentin treated with TDg, and produced the highest carbonate area at the BHL of dentin treated with TDg-NPs (Table 1).

3.3.2. Crystallinity

Crystallinity, at both HL and BHL, attained the lowest values when samples were treated with TDg-NPs and analyzed at 24 h of storage (Table 2). Between dentin groups infiltrated with NPs, those specimens load cycled and thermocycled and treated with TDg, attained the lowest crystallinity, referred to phosphate. In the case of carbonate, crystallinity at both HL and BHL attained the highest values when dentin was treated with TDg-NPs at specimens after 24 h of storage and load cycled. Those specimens achieved the lowest crystallinity when thermocycled (Table 2).

3.3.3. Gradient in mineral content (GMC)

GMC achieved the lowest value at both HL and BHL when samples were 24 h stored. When specimens were load cycled, at the HL, GMC obtained the lowest values when TDg-NPs was used to treat dentin. When specimens were thermocycled, dentin treated with TDg-NPs attained the highest GMC values at both HL and BHL (Table 2).

3.3.4. Crosslinking

When crosslinking was assessed, the HL of dentin treated with undoped NPs achieved the highest values among groups, and the BHL attained the highest intensity peak when dentin was infiltrated with TDg-NPs. Both HL and BHL in samples treated with TDg-NPs and submitted to load cycling and thermocycled showed the highest values among groups (Table 3).

3.3.5. Nature and secondary structure of collagen

Both HL and BHL of specimens load cycled showed the highest peak intensities after assessing Phenyl group. When nature and secondary structure of collagen were assessed, α-helices attained the highest peak intensities at both HL and BHL in interfaces created after TDg-NPs dentin infiltration in the groups of 24 h storage and thermocycled (Table 3).

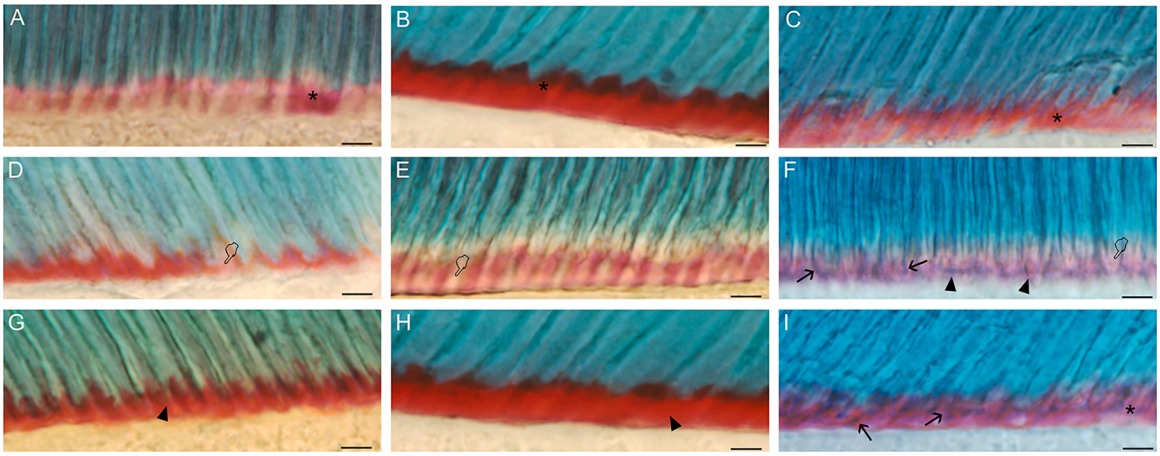

Fig. 3. Representative light micrographs of the interface specimens stained with Masson's trichrome. Mineralized dentin stained green/blue, adhesive stained beige, and exposed protein stained red. A-C Bonded resin–dentin interfaces, stained after 24 h of storage, without NPs, after undoped NPs, and TDg-NPs infiltration, respectively. A fringe of exposed collagen is observed at the hybrid layer in all groups (asterisks). d-F Bonded resin–dentin interfaces, stained after mechanical loading, in dentin treated without NPs, after undoped NPs, and TDg-NPs infiltration, respectively. The zone of exposed demineralized collagen was reduced. The intensity of the red color was diminished (pointers) and the intensity of the green/blue color raised at peritubular (arrows) and intertubular (arrow heads) dentin. G-I Bonded resin–dentin interfaces, stained after thermocycling, in dentin treated without NPs, after undoped NPs, and TDg-NPs infiltration, respectively. The demineralized collagen was not remineralized in absence of TDg, as the intensity of the red color was preserved (arrow heads). Clear signs of remineralization at the base of the hybrid layer was evidenced after TDg-NPs resin infiltration (arrows). *Scale bar* is 10 μm.

Table 1
Raman intensities and ratios of Relative Presence of Mineral components attained from experimental interfaces.

		Relative Presence of Mineral											
		Phosphate [961]						Carbonate [1070]					
		Peak			Area			Peak			Area		
		24 h	**LC**	**TC**	**24 h**	**LC**	**TC**	**24 h**	**LC**	**TC**	**24 h**	**LC**	**TC**
Control	HL	220.6	124.37	270.12	6291.19	4201.65	6988.84	44.14	33.24	48.78	6331.45	5289.68	6807.49
	BHL	306.54	337.24	282.8	8741.91	9452.03	7319.58	48.49	58.29	38.78	5824.48	3549.02	1874.94
	DEN 2	405.27	551.85	383.01	9857.57	14,020.80	9913.45	62.4	88.93	51.95	2763.46	3971.00	2300.53
	DEN 1	558.53	667.99	410.95	13,585.6	16,971.60	10,636.1	84.92	109.83	59.1	3760.75	4904.26	6404.52
Undoped-NPs	HL	164.16	94.56	207.24	4670.65	2745.32	6120.92	37.22	19.98	39.89	5135.48	3180.29	6028.51
	BHL	337.06	322.97	296.46	8175.92	9376.98	7513.23	56.46	49.79	42.31	3775.69	5609.18	5412.95
	DEN 2	459.52	501.76	417.65	11,146.30	12,999.70	10,584.4	77.86	75.10	56.41	4262.70	3659.21	2497.83
	DEN 1	577.39	708.54	569.82	14,005.20	17,600.10	14,441	88.93	103.45	76.49	4146.28	4619.31	3075.38
TDg-NPs	HL	198.87	393.14	115.33	6605.95	11,566.60	5286.88	44.74	63.05	33.19	6432.54	3064.6	5256.81
	BHL	377.40	526.37	327.61	10,957.30	15,486.40	9547.70	64.45	83.62	54.40	8268.00	4404.31	7567.83
	DEN 2	404.15	722.55	320.39	10,470.70	21,258.50	8285.10	61.00	115.94	46.50	2972.36	5163.43	2410.69
	DEN 1	578.43	776.55	521.26	14,444.10	19,591.10	13,002.80	87.10	121.83	75.32	3889.36	5425.84	3291.76

Abbreviations: NPs: nanoparticles; TDg: Tideglusib; HL: Hybrid layer; BHL: Bottom of hybrid layer; DEN: Dentin; 24 h: after 24 h of SBFS storage; LC: load cycling; TC: 100,000 thermal cycles. The peaks values had been normalized to the intensity of the Amide II band near 1510 cm^{-1}. Peaks positions are expressed in cm^{-1} and the intensity units are expressed in arbitrary counts (a.c.).

Table 2
Crystallinity and GMC ratio of mineral components attained from experimental interfaces.

		Crystallinity (FWHM)						GMC Ratio C/P		
		Phosphate $FWHM_P$			Carbonate $FWHM_C$					
		24 h	**LC**	**TC**	**24 h**	**LC**	**TC**	**24 h**	**LC**	**TC**
Control	HL	21.79	25.84	19.76	112.55	125.36	109.42	0.20	0.27	0.18
	BHL	21.79	21.41	19.76	93.73	46.84	37.10	0.16	0.17	0.14
	DEN 2	18.56	19.39	19.76	33.95	34.23	33.95	0.15	0.16	0.14
	DEN 1	18.56	19.39	19.76	33.95	34.23	84.32	0.15	0.16	0.14
Undoped-NPs	HL	21.73	22.18	19.76	108.11	125.36	109.42	0.23	0.21	0.18
	BHL	18.51	22.18	19.76	51.52	87.74	37.10	0.17	0.15	0.14
	DEN 2	18.51	19.78	19.76	42.07	37.39	33.95	0.17	0.15	0.14
	DEN 1	18.51	18.96	19.76	35.76	34.23	84.32	0.15	0.15	0.14
TDg-NPs	HL	25.40	22.48	35.16	112.84	37.30	124.73	0.22	0.16	0.29
	BHL	22.18	22.48	22.27	100.30	40.45	109.05	0.17	0.16	0.17
	DEN 2	19.78	22.48	19.74	37.39	34.14	39.81	0.15	0.16	0.15
	DEN 1	19.06	19.25	19.04	34.23	34.14	33.50	0.15	0.16	0.14

Abbreviations: NPs: nanoparticles; TDg: Tideglusib; HL: Hybrid layer; BHL: Bottom of hybrid layer; DEN: Dentin; FWHM: Full-width half-maximum; GMC: Gradient in mineral content (ratio 1070/961); 24 h: after 24 h of SBFS storage; LC: load cycling; TC: 100,000 thermal cycles. The peaks values had been normalized to the intensity of the Amide II band near 1510 cm^{-1}. Peaks positions are expressed in cm-1 and the intensity units are expressed in arbitrary counts (a.c.).

Table 3
Raman intensities and ratios of organics components attained from experimental interfaces (crosslinking and nature of collagen).

		Crosslinking			Nature and secondary structure of collagen					
		AGEs-Pentosidine [1550]			Phenyl (norm.) [1003]			α-helices [1340]		
		24 h	**LC**	**TC**	**24 h**	**LC**	**TC**	**24 h**	**LC**	**TC**
Control	HL	2.13	4.83	0.82	47.2	40.26	45.05	15.52	23.59	19.50
	BHL	1.26	4.58	1.10	32.27	43.97	24.18	10.61	16.78	10.37
	DEN 2	1.32	5.53	0.5	38.65	56.70	30.23	9.68	19.46	12.48
	DEN 1	1.85	5.20	0.88	49.00	69.21	42.44	11.35	16.89	16.42
Undoped-NPs	HL	4.45	7.55	2.03	35.15	24.59	40.64	22.48	18.71	13.77
	BHL	3.25	1.18	2.23	39.77	40.61	35.51	16.00	14.74	9.70
	DEN 2	2.02	1.99	1.48	62.37	53.92	36.83	14.43	13.76	7.49
	DEN 1	2.44	1.57	1.98	52.48	62.95	48.15	11.05	17.26	8.85
TDg-NPs	HL	3.25	8.91	2.67	42.20	40.89	41.71	31.03	17.24	25.43
	BHL	4.45	8.24	2.45	54.31	53.57	41.43	24.43	19.04	21.38
	DEN 2	2.02	8.63	1.22	37.96	69.83	25.92	16.59	19.58	15.35
	DEN 1	2.44	9.15	0.96	56.18	66.97	40.15	15.67	23.56	18.21

Abbreviations: NPs: nanoparticles; TDg: Tideglusib; HL: Hybrid layer; BHL: Bottom of hybrid layer; A: amide; AGEs: advanced glycation end products; norm: Normalization. 24 h: after 24 h of SBFS storage; LC: load cycling; TC: 100,000 thermal cycles. For the organics components the peaks values had been normalized to the intensity of the Amide II band near 1510 cm^{-1}. Peaks positions are expressed in cm^{-1}, and the intensity units are expressed in arbitrary counts (a.c.).

3.3.6. Adhesive

The highest degree of conversion of the adhesive (DC) at both HL and BHL, at 24 h of storage, was attained when specimens were infiltrated with undoped NPs. When samples were load cycled, HL and BHL of dentin infiltrated with TDg-NPs achieved the highest DC of the infiltrated resin adhesive, among groups. Among thermocycled specimens, the BHL of the interfaces promoted with TDg-NPs achieved the highest DC of the infiltrated resin. The highest Bis-GMA and adhesive penetrations at both HL and BHL were obtained in the samples after 24 h storage and in the thermocycled specimens (Table 4).

The corresponding HCA Raman images (clusters) and results (centroids) are reflected at the Figs. 4 and 5, respectively. The chemical compounds and the spatial distribution of the main spectra were revealed by HCA results and exhibited five different clustered groups in contiguous traces of the scatter plots (Fig. 5). Two clusters were analyzed in the present research (Fig. 4), the hybrid layer and the bottom of the hybrid layer. Hybrid layer of samples treated with TDg-NPs and mechanically loaded showed the highest phosphate peak among groups when HCA were analyzed (Fig. 4F). Figs. 4C, 4F and 4I exposed higher existence of phosphate at the bottom of the hybrid layer than in the rest of the groups when NPs were doped with TDg, regardless the type of challenging. The analysis of variances only made to correspond a 21 % of the total mapping to the bottom of the hybrid layer (Figs. 4F, 5F, blue area), in comparison to control group (Figs. 4D, 5D) when specimens were load cycled. This trend was similarly followed after thermocycling (Figs. 4G, 5G blue area, 4I, 5I blue area). The hybrid layer of specimens treated with TDg-NPs and thermocycled reflected the highest variance (27 %) (Fig. 4I, purple area) and the lowest phosphate peak (115.33 a.c. -arbitrary counts-) (Table 1) intensity (Fig. 6I, red area), among groups. Dentin samples treated with TDg-NPs, after load cycling, attained the highest phosphate peak intensity among groups (Fig. 6F).

4. Discussion

At a whole, resin dentin interfaces treated with TDg-NPs showed the highest nanomechanical performance, in terms of nanohardness (*Hi*), at both HL and BHL among groups (Fig. 2). Therefore, the first null hypothesis to be tested must be rejected. Mineral precipitation at the HL, BHL and even at intact dentin, may have contributed to this improved nanomechanical performance [27,28] of the TDg-NPs doped resin-dentin bonded interfaces [13]. At the clinical scenarios, nanocrystalline hydroxyapatite is segregated into extrafibrillar and intrafibrillar mineral components. Hence, the rise in *Hi* of the partially demineralized and infiltrated collagen is properly associated with minerals deposits at the resin-dentin interface [29], particularly within the intrafibrillar section [30,31]. Thus, tideglusib appeared to promote mineral deposits onto the demineralized dentin facilitating functional mineralization, allowing mineral precipitation within the demineralized collagen. This was observed as a reduction in the red color intensity at the resin-dentin interface (Fig. 3C), indicating a relative advancement of the remineralization front. As a result, certain non-uniform and discontinuous zones beneath the adhesive layer display fewer pink and red areas (Fig. 3C). At the Masson's trichrome staining, this was indicative of a greater mineral precipitation into the demineralized collagen [15]. The existence of peptides at the interface could have generated electrostatic attraction for soluble ions, leading to a localized increase in supersaturation zones. This phenomenon may have facilitated mineral nucleation [32].

Mechanical loading significantly increased *Hi* at both HL and BHL, after using TDg-NPs (Fig. 2). According to the Masson's trichrome staining results, there are evidences of remineralization at the resin-dentin interface in all experimental groups submitted to mechanical loading, regardless the presence or not of NPs (Figs. 2, 3D, 3E, 3F). Mineralized dentin, appearing as new green/blue stained peritubular and intertubular dentin, is remarkable, especially when TDg-NPs were infiltrated, which showed an almost absence of unprotected collagen layer. Additionally, a development of new dentinal tubuli crossing the demineralized collagen was noted, signifying the remineralization of both peritubular and intertubular dentin. (Fig. 3F). Specific peptides are preferentially absorbed onto peritubular dentin, precisely in the locations where they predominantly exert their remineralizing functions [33]. The new precipitated occurred not only at the HL but at the first 5–20 μm of the tubule lengths [34,35]. On the other hand, undoped NPs dentin infiltration revealed a clear presence of unprotected decalcified dentin at the interface, allowing to observe the poor mineral gain at the partially-demineralized dentin layer (Figs. 3B, 3E, 3H). Moreover, mechanical loading has been observed to enhance the resistance of collagen against enzymatic degradation of unprotected [36].

A remineralized collagen fringe, in samples treated with TDg-NPs, was adverted covering the tubular walls and even at intertubular dentin (Fig. 3I) in comparison with both control group (Fig. 3G) and samples treated with undoped-NPs (Fig. 3H) when specimens were thermocycled. Masson's trichrome staining observations established a limited red zone, indicating decalcified and resin uncovered dentin in all specimens submitted to thermocycling (Figs. 3G, 3H), except when TDg-NPs (Fig. 3I) were used for resin-dentin infiltration. The observed outcome can be attributed to the limited remineralization capacity within the intrafibrillar section [30], *i.e.*, it is simply a precipitation of mineral [37] in interfaces without TDg (Fig. 2). Furthermore, the more pronounced reddish coloration was a consequence of the lower degree of Bis-GMA [1113/A-1], adhesive penetration [1453/1667] and degree of conversion of the adhesive that attained these two groups, *i.e.*, control and undoped NPs (Table 4). Even more, after using TDg-NPs, any signs of demineralized and/or exposed protein (red stain) were detectable in

Table 4
Raman intensities ratios of adhesive components attained from experimental interfaces after proposal challenges.

		Adhesive											
		1113			DC [1637/1608]			Bis-GMA Penetration [1113/A-I]			Adhesive Penetration [1453/1667]		
		24 h	**LC**	**TC**	**24 h**	**LC**	**TC**	**24 h**	**LC**	**TC**	**24 h**	**LC**	**TC**
Control	ADH	55.69	50.02	65.67	0.70	0.40	0.48	3.31	5.95	4.42	5.39	6.60	6.45
	HL	47.56	52.95	47.98	0.74	0.53	0.74	2.78	2.87	2.70	4.43	4.21	4.11
	BHL	27.95	29.97	15.41	0.78	0.69	0.90	2.56	1.99	1.77	3.66	2.81	2.44
Undoped-NPs	ADH	45.77	103.71	60.59	1.03	0.62	0.59	1.88	164.62	4.05	3.42	117.71	6.05
	HL	29.27	38.55	48.05	0.94	0.69	0.63	1.70	3.42	3.30	2.78	5.19	4.93
	BHL	22.09	27.37	33.05	1.17	1.10	0.72	1.46	1.69	2.66	2.10	2.73	3.92
TDg-NPs	ADH	14.64	49.83	102.38	0.26	0.66	0.43	9.76	2.91	26.05	10.65	4.30	27.97
	HL	45.00	23.96	62.26	0.80	0.89	0.83	2.95	1.55	2.82	5.38	1.77	5.12
	BHL	43.87	31.57	45.36	1.00	1.09	0.89	2.26	1.62	2.26	3.65	1.96	4.22

Abbreviations: NPs: nanoparticles; TDg: Tideglusib; ADH: Adhesive; HL: Hybrid layer; BHL: Bottom of hybrid layer; DEN: Dentin; DC: Degree of conversion of adhesive; Bis-GMA: bisphenol A diglycidyl methacrylate; A-I: Amide I; 24 h: after 24 h of SBFS storage; LC: load cycling; TC: 100,000 thermal cycles. The peaks values had been normalized to the intensity of the Amide II band near 1510 cm^{-1}. Peaks positions are expressed in cm^{-1} and the intensity units are expressed in arbitrary counts (a.c.).

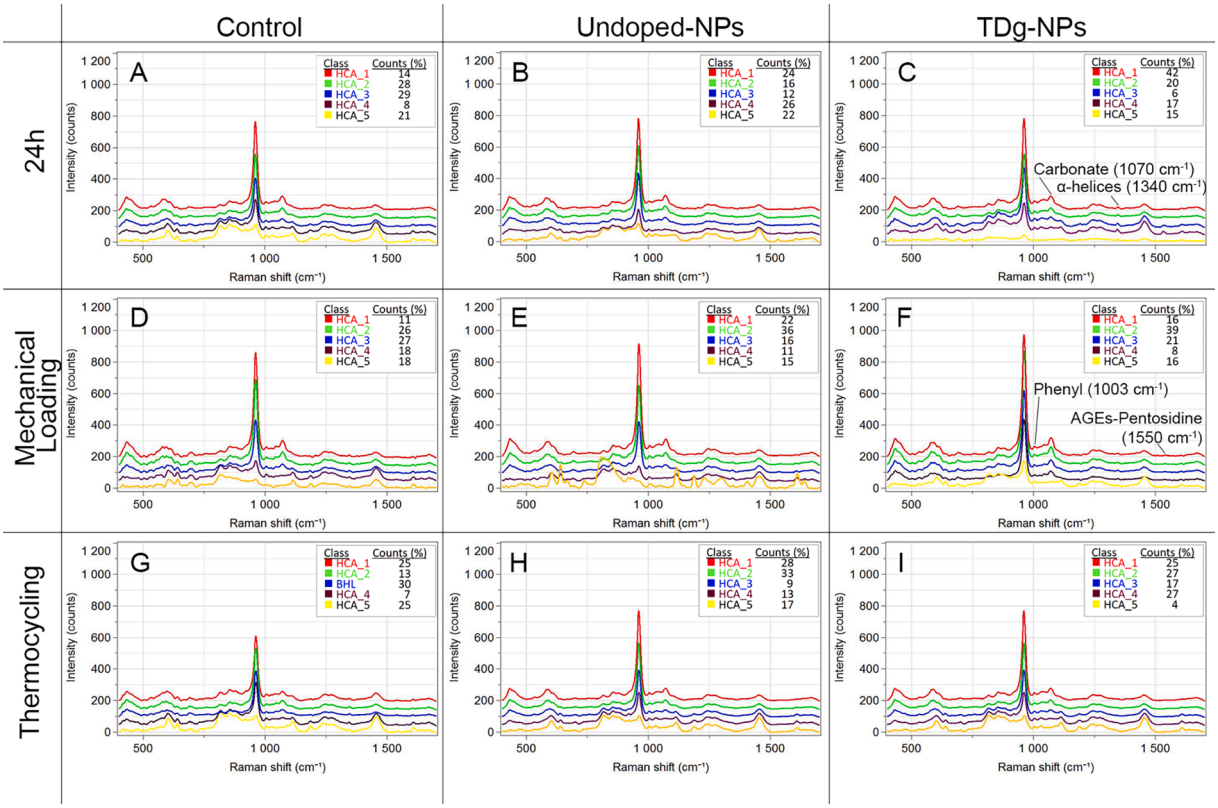

Fig. 4. Spectra from hierarchical cluster analysis (HCA) results (centroids) of the dentin interfaces analyzed at 24 h of storage: control group (A), treated with undoped-NPs (B) and tideglusib-doped NPs (C). Images from same groups when submitted to mechanical loading (D, E, F, respectively) and to thermocycling (G, H, I, respectively). HL, hybrid layer; BHL, bottom of hybrid layer.

some parts of the restoration (Fig. 3I). Thus, porosity may have diminished after applying TDg-NPs, as both red color intensity and width were clearly reduced. After thermocycling, synthesis and alkaline phosphatase activity and stimulations of proteins have been demonstrated in vivo and in vitro [13,38], and after using in vitro prebiotic peptides [39]. As a consequence, a more protected HL and BHL was shown along the whole resin-dentin interface when using TDg-NPs at the interface (Fig. 3I).

The Raman analysis further confirmed these findings. Dentin interfaces treated with TDg-NPs exhibited the highest mineralization observed, as evidenced by the peak (Fig. 4C) and area values of both phosphate (PO_4) (961 cm^{-1}) and carbonate (CO_3^{2-}) (1070 cm^{-1}) bands, particularly when NPs were doped with tideglusib (Table 1). Therefore, the second null hypothesis must also be rejected. Tetrahedral PO_4 group (P-O bond) within hydroxyapatite is characterized by the Raman phosphate peak at 961 cm^{-1}. Monitoring the intensity of this peak has been used to assess the potential increase in phosphate content [40], reflecting the augmentation in phosphate peak intensities when the 2D micro-Raman analysis was performed (Figs. 6C, 6F). In the present study, similar trend was followed by the CO_3^{2-} group, indicating the formation of new mineral in the previous partially demineralized dentin regions. These indexes complied with the highest relative degree of mineralization [41,42] (Table 1). The higher relative presence of minerals affected, at the whole resin-dentin interface but, specifically at the BHL that unveiled the maximum intensity peaks not only at 24 h of storage, but at all challenging groups (load cycling and thermocycling) (Table 1). This meant major presence of calcium phosphate precipitates at the resin-dentin interface, that was appreciated even when samples became treated with TDg-NPs and stored for 24 h (Fig. 3C) and after measuring the intensity of the phosphate peak (Fig. 6A). The referred interface showed exposed collagen but with a patent mineralization front at the base of the HL, reducing its wideness. A strong remineralization fringe was noticed at the BHL when samples treated with TDg were load cycled (Fig. 3F) or thermocycled (Fig. 3I). The remineralization front was more discontinuous in thermocycled samples than in load cycled specimens treated with TDg-NPs, but mechanical loading facilitated more advanced intratubular and peritubular mineralization (Fig. 3F).

A single-point spectroscopy approach proves insufficient for accurately characterizing the biochemical composition of the dentin substrate. Instead, the incorporation of bi-dimensional (2D) data analysis techniques with spatial information is crucial [43,44]. Our 2D-micro-Raman analysis, as confirmed by HCA results and cluster analysis, revealed the spatial distribution of main spectra and chemical compounds. HCA demonstrated five distinguishable clustered groups in adjacent traces of the scatter plots, in function of similar conditions of featuring [45], with each cluster represented by a different color [46]. At the interface of specimens treated with TDg-NPs, the corresponding HCA Raman results (centroids) obtained when specimens were subjected to load cycling demonstrated a general increase in the phosphate peak (Fig. 4F), in comparison with the samples treated with unloaded NPs (Fig. 4E), indicating mineral gain. This phosphate peak augmentation was clearly represented at the 2D micro-Raman map of 961 cm^{-1} intensities, where the redder area was visibly greater in mechanically loaded samples treated with TDg-NPs (Fig. 6F). The centroid corresponding to the hybrid layer (HCA_4) (Figure 5F/purple area), purple plot in Fig. 4F, slightly decreased the area of the hybrid layer (from 11 to 8 intensity counts) after load cycling of samples treated with TDg-NPs in comparison with unloaded NPs. The mineral gain that occurred at the demineralized collagen made to decrease the percentage of variance at dentin treated with TDg-NPs. This trend was reverted at the bottom of the hybrid layer (HCA_3), where variances changed from 11% in samples infiltrated with unloaded NPs until 21% when specimens infiltrated with TDg-NPs were mechanically loaded. These outcomes need further

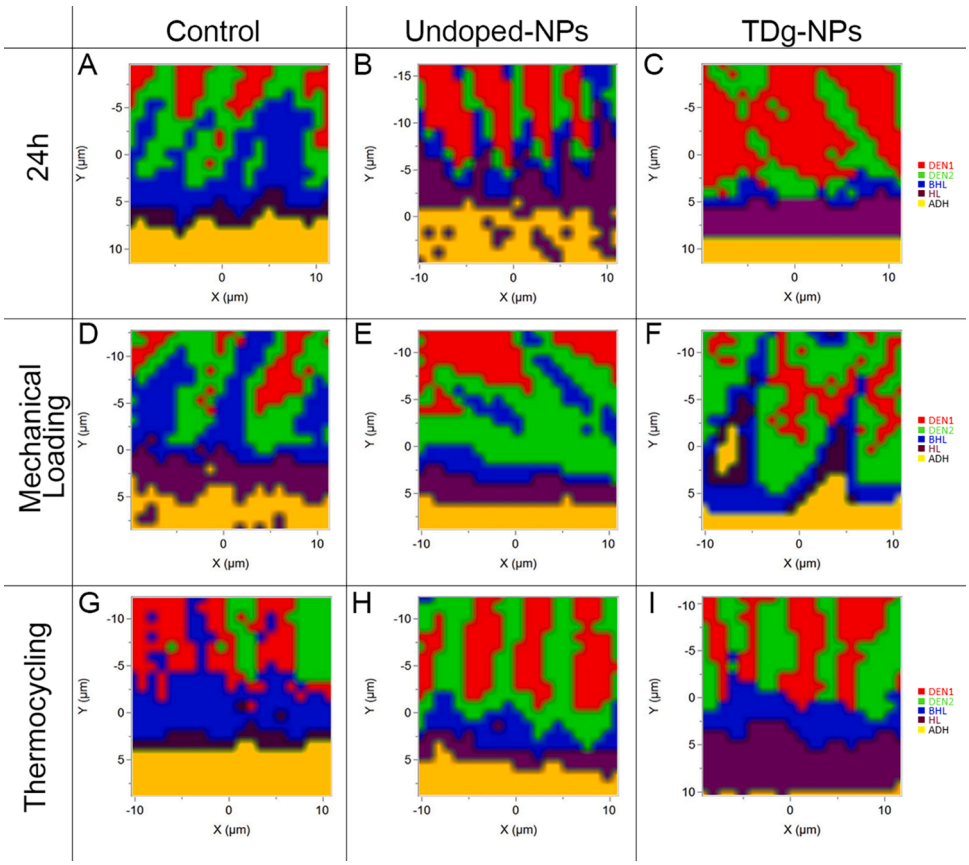

Fig. 5. Raman analysis [K-means clustering (KMC) map of the Raman profile] of the dentin interfaces analyzed at 24 h of storage: control interfaces (A), treated with undoped NPs (B) and tideglusib-doped NPs (C). Images from the same groups when submitted to mechanical loading (D, E, F, respectively) and thermocycling (G, H, I, respectively). Three levels of HCA clustering are shown. Areas of distinct colors have differences in Raman spectral distribution and chemical composition. Each cluster is assigned to a different color (red and green, dentin; purple, hybrid layer; blue, bottom of hybrid layer; yellow, adhesive), thus obtaining a false color-image of the substrate on the basis of similar spectral features. At the 2D micro-Raman, blue represents the lowest peak intensity, while the red represents the highest. DEN1 and DEN2, dentin 1 and dentin 2; HL, hybrid layer; BHL, bottom of hybrid layer; ADH, adhesive.

research in future investigations.

The formed hybrid layers when specimens were treated with TDg-NPs and submitted to thermocycling increased their percentages of variances (27%) (Fig. 4I) and the purple area (cluster in Fig. 5I), in comparison with the control group (7 %) (Fig. 4G), and with the group where unloaded NPs were used (Figs. 4H) (13%) (clusters in Figs. 5G, 5H, respectively). It is speculated that the augmented area of the hybrid layer that may be perceived at the Fig. 5I may be associated to an increase of extrafibrillar mineral, considering that this group did not increase its values of nanohardness after thermal cycling (40) (Fig. 2). The opposite occurred when HCA regarding the bottom of the hybrid layer was analyzed, that ranged from 30% of variance in the control group (Fig. 4G), until 9% in specimens treated with unloaded NPs (Fig. 4H). This reduction makes sense, as a gain of minerals at the demineralized collagen web is linked to a reduction in unprotected collagen [30]. Peaks at 1340 cm^{-1} associated with α-helices were also heightened in samples treated with tideglusib (Fig. 4), indicating increased sensitivity to molecular orientation aimed at facilitating further crystallization [22] (Table 3). The gradient in mineral content (GMC) at the hybrid layer of interfaces promoted by TDg-NPs thermocycled achieved the highest values among groups (0.29), but the lowest values of nanohardness (Fig. 2). This relative increase in mineral at HL was of amorphous nature, but crystalline at the BHL, where lower values of GMC were obtained, with high *Hi* values. The highest GMC that was obtained at the BHL at interfaces created after TDg-NPs infiltration at 24 h (0.17) (Table 2) correlates with the maximum *Hi* value (0.64 GPa) obtained when compared with both control and undoped NPs groups (Fig. 2). Hence, a much thinner unprotected demineralized collagen layer than those seen for both control and undoped NPs groups were observed (Fig. 3C). GMC, as result, meaning lower carbonate substitution for phosphate, pointing out higher maturity and crystallinity in comparison with the control group, related to a decline of amorphous calcium phosphate compounds [41,42].

Crystallinity, in general showed an amorphization process in all groups of study after infiltrating dentin with TDg-NPs (Table 2), as the full-width half-maximum (FWHM) increased at both HL and BHL, except when carbonate was assessed in the load cycled specimens (Table 2). Carbonated apatite is a precursor of hydroxyapatite [22], as it is unstable. Biological apatite is calcium deficient and contains substantial amounts of carbonate. The observed increase in the carbonate peak (1070 cm^{-1}) in samples treated with TDg-NPs (Table 1), indicates a higher presence of carbonate apatite in these samples when compared with the rest of the groups. This amorphization is likely associated with the incorporation of carbonate as a substituent for PO_4^3 in the apatite lattice [22]. Alterations in the phosphate band and peak in response to the existence of carbonate in the lattice or changes in the spectral region related to carbonate content can be manifested as the growth of a carbonate peak [47]. FWHM shows a broad increase in crystallographic maturity, or crystallinity, in minerals at the interface [42] (Table 2). This was numerically evidenced at Table 2 and graphically at Figs. 4C and 4F. Thereupon, the hybrid layer at mechanically loaded interfaces obtained after TDg-NPs infiltrated dentin have shown the lowest peak values (22.48) (crystallinity) and, by contrast, the bottom of the hybrid layer obtained the highest values (22.48) (amorphization). Amorphous

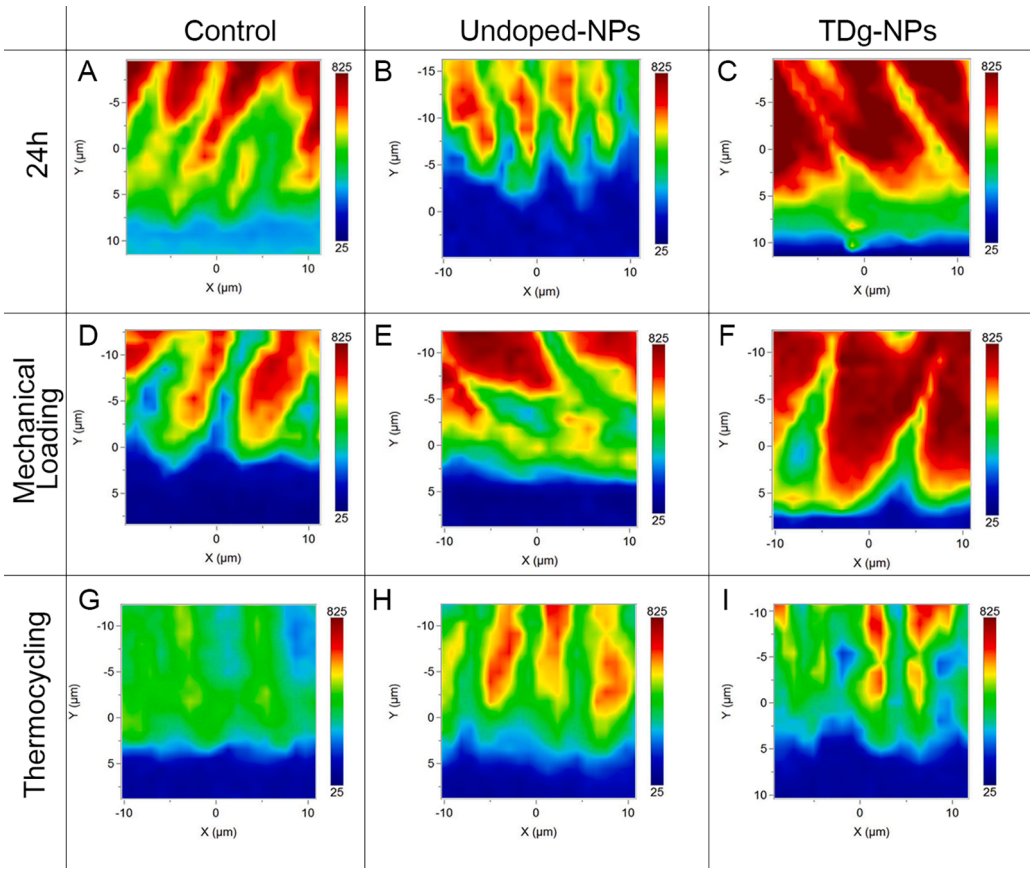

Fig. 6. Raman analysis [2D micro-Raman map of 961 cm^{-1} intensities] of the dentin interfaces analyzed at 24 h of storage: control (A), treated with undoped NPs (B) and tideglusib-doped NPs (C). Interfaces from the same groups when submitted to mechanical loading (D, E, F, respectively) and thermocycling (G, H, I, respectively). At the 2D micro-Raman, blue represents the lowest peak intensity, while the red represents the highest.

calcium phosphate establishes a localized environment rich in ions, providing favorable conditions for the in situ formation of prenucleation clusters. Consequently, this process facilitates further remineralization of dentin [48]. On the contrary, if crystalline calcium phosphates are formed, they will have long degradation times, requiring months or even years to release ions for remineralization [49].

The increase in mineral content was concurrently linked to the maximum crosslinking of collagen in samples treated with TDg-NPs (Table 3). Typically, an elevation in collagen crosslinking takes place following mineral precipitation [50,51], that may be considered to be the base for the enhancement of mechanical performance of dentin (Fig. 2) [52]. In general, resin-dentin interfaces infiltrated with TDg-NPs submitted to load cycling attained the highest peak of AGEs-pentosidine, at 1550 cm^{-1} (Table 3). After the application of tideglusib, mechanical loading could have triggered the conversion of keto-amines (immature cross-links), resulting in a more pronounced and sharper peak with a noticeable shift at 1550 cm^{-1}, at both HL and BHL. Pentosidine, identified as the primary component of advanced glycation end products (AGE) [53], strongly indicates ribose or ribonucleotide metabolites as potential precursors [24]. The high relative intensity peak corresponding to the AGES-pentosidine, at 1550 cm^{-1}, is generally associated with the formation of non-reducible crosslinks, suggesting that the initial remineralization process is intrafibrillar. Consequently, collagen can be viewed as an active scaffold promoting the formation of oriented crystalline hydroxyapatite within the fibrils [54,55].

Improvements in the nature and secondary structure of collagen were exhibited across the resin-dentin interface, following the infiltration of dentin with TDg-NPs, as the peak intensity of the phenyl group (1003 cm^{-1}) reached the highest values when the peptide was nanocarried into the demineralized collagen (Table 3). In contrast, specimens not treated with tideglusib displayed poor collagen matrix quality, characterized by a lack of conformation and organization [56, 57]. Mechanical stimuli applied to dentin infiltrated with TDg-NPs improved the nature and secondary structure of collagen throughout the entire resin-dentin interface compared to dentin infiltrated with other biomaterials (Table 3). Prior to the appearance of hydroxyapatite crystals, an increase in the protein-dependent spectral signal at phenylalanine was observed [22].

The present research provides evidence of the therapeutic activity of the experimental TDg-NPs, representing, to the best of our knowledge, the only available results from combined methodologies, including nano-indentation, Raman spectroscopy, and Masson's trichrome staining, to analyze TDg-NPs resin-dentin interfaces subjected to mechanical loading and thermocycling.

These outcomes have sufficiently provided information on biophysic-chemical structure of dentin treated with peptides-NPs carried-drugs for essential clinical applications. Reparative dentin formation at the resin-dentin interface has been demonstrated after tideglusib dentin infiltration. Among other factors, remineralization can occur through modifications in mechanical properties, (nanoindentation) [58–60], changes in mineral composition (X-ray diffraction, EDX, or FTIR spectroscopy analysis) [34,58], and changes in histomorphological and microstructural appearance evaluated through microradiography, μCT, AFM, scanning probe microscopy, scanning electron microscopy or dye-assisted optical or confocal microscopy [58,59]. While there is usually some correlation between these analyses, they are complementary, and the study acknowledges certain limitations, emphasizing the need for further research. The interpretation of low-resolution stained images may introduce uncertainty regarding the significance of observed differences in mineral apposition at the resin-dentin interface

among the tested groups. It highlights the necessity for transmission electron microscopy associated with diffraction analysis for accurate assessment of intrafibrillar collagen remineralization at the hybrid layer.

5. Conclusion

The application of mechanical loading to specimens subjected to TDg-NPs dentin infiltration induces an increase in mineralization at the resin/dentin interface. Dentin surfaces conditioned and infiltrated with TDg-NPs doped adhesive promote remineralization of peritubular and intertubular dentin. Following load cycling, this group forms minerals characterized by Raman bands indicative of an enriched carbonated apatite with enhanced crystallographic maturity at the interface. Despite an overall increase in mineral presence and phosphate and carbonate peak intensities after load cycling, the interface experiences diminished crystallinity and a gradient of mineral content. Collagen crosslinking ratios shift towards higher frequencies after load cycling, particularly in the presence of tideglusib at the interface, highlighting collagen's favorable nature for scaffolding and subsequent mineralization.

Dentin surfaces treated with TDg-NPs, resin-infiltrated, and subjected to load cycling exhibit elevated nanomechanical properties. Consequently, thinner unprotected collagen layers are observed compared to control and undoped NPs groups. Moreover, many samples show no signs of demineralization at the bottom of the resin-dentin inter-diffusion zone. The associated mineral precipitation is linked to an increase in the relative presence of minerals. Furthermore, the organic components enable the observation of an enriched collagen matrix quality, generating an organized matrix to facilitate apatite nucleation.

CRediT authorship contribution statement

Manuel Toledano: Writing – review & editing, Writing – original draft, Visualization, Validation, Supervision, Project administration, Methodology, Investigation, Funding acquisition, Formal analysis, Conceptualization. **Enrique Fernández-Romero:** Writing – review & editing, Visualization, Methodology, Data curation. **Fátima S. Aguilera:** Writing – review & editing, Writing – original draft, Visualization, Methodology, Investigation, Data curation. **Estrella Osorio:** Writing – review & editing, Writing – original draft, Visualization, Software, Resources, Methodology, Investigation, Data curation. **José A. Rodríguez-Santana:** Writing – review & editing, Investigation. **Macarena Garrido:** Writing – review & editing, Investigation. **Pedro A. Solís:** Writing – review & editing, Investigation. **Franklin García-Godoy:** Writing – review & editing, Writing – original draft, Visualization, Resources, Investigation, Data curation. **Raquel Osorio:** Writing – review & editing, Writing – original draft, Visualization, Supervision, Project administration, Methodology, Investigation, Funding acquisition, Formal analysis, Conceptualization.

Declaration of competing interest

The authors declare that they have no known competing financial interests or personal relationships that could have appeared to influence the work reported in this paper.

Acknowledgements

The present study was supported by Grant PID2020–114694RB-I00 funded by MCIN/AEI 10.13039/501100011033. This research is part of E. F-R.'s Ph.D. research study.

Supplementary materials

Supplementary material associated with this article can be found, in the online version, at doi:10.1016/j.jdent.2024.105027.

References

[1] J. Kim, R.M. Vaughn, L. Gu, R.A. Rockman, D.D. Arola, T.E. Schafer, K.K. Choi, D. H. Pashley, F.R. Tay, Imperfect hybrid layers created by an aggressive one-step self-etch adhesive in primary dentin are amendable to biomimetic remineralization in vitro, J. Biomed. Mater. Res. A 93A (2010) 1225–1234, https://doi.org/10.1002/jbm.a.32612.

[2] J. De Munck, P.E. Van den Steen, A. Mine, K.L. Van Landuyt, A. Poitevin, G. Opdenakker, B. Van Meerbeek, Inhibition of Enzymatic Degradation of Adhesive-Dentin Interfaces, J. Dent. Res. 88 (2009) 1101–1106, https://doi.org/10.1177/0022034509346952.

[3] L. Breschi, A. Mazzoni, F. Nato, M. Carrilho, E. Visintini, L. Tjäderhane, A. Ruggeri, F.R. Tay, E.D.S. Dorigo, D.H. Pashley, Chlorhexidine stabilizes the adhesive interface: a 2-year in vitro study, Dent. Mater. 26 (2010) 320–325, https://doi.org/10.1016/j.dental.2009.11.153.

[4] D.H. Pashley, F.R. Tay, L. Breschi, L. Tjäderhane, R.M. Carvalho, M. Carrilho, A. Tezvergil-Mutluay, State of the art etch-and-rinse adhesives, Dent. Mater. 27 (2011) 1–16, https://doi.org/10.1016/j.dental.2010.10.016.

[5] A. Alaohali, C. Salzlechner, L.K. Zaugg, F. Suzano, A. Martinez, E. Gentleman, P. T. Sharpe, GSK3 Inhibitor-Induced Dentinogenesis Using a Hydrogel, J. Dent. Res. 101 (2022) 46–53, https://doi.org/10.1177/00220345211020652.

[6] R. Osorio, M. Yamauti, S. Sauro, T.F. Watson, M. Toledano, Experimental resin cements containing bioactive fillers reduce matrix metalloproteinase-mediated dentin collagen degradation, J. Endod. 38 (2012) 1227–1232, https://doi.org/10.1016/j.joen.2012.05.011.

[7] A. Besinis, R. van Noort, N. Martin, Remineralization potential of fully demineralized dentin infiltrated with silica and hydroxyapatite nanoparticles, Dent. Mater. 30 (2014) 249–262, https://doi.org/10.1016/j.dental.2013.11.014.

[8] C. Wu, Y. Zhang, W. Fan, X. Ke, X. Hu, Y. Zhou, Y. Xiao, $CaSiO_3$ microstructure modulating the in vitro and in vivo bioactivity of poly(lactide-co-glycolide) microspheres, J. Biomed. Mater. Res. A 98 (2011) 122–131, https://doi.org/10.1002/jbm.a.33092.

[9] A.L. Medina-Castillo, J.F. Fernandez-Sanchez, A. Segura-Carretero, A. Fernandez-Gutierrez, Micrometer and Submicrometer Particles Prepared by Precipitation Polymerization: Thermodynamic Model and Experimental Evidence of the Relation between Flory's Parameter and Particle Size, Macromolecules 43 (2010) 5804–5813, https://doi.org/10.1021/ma100841c.

[10] R. Osorio, C.A. Alfonso-Rodríguez, A.L. Medina-Castillo, M. Alaminos, M. Toledano, Bioactive Polymeric Nanoparticles for Periodontal Therapy, PLOS ONE 11 (2016) e0166217, https://doi.org/10.1371/journal.pone.0166217.

[11] M.T. Osorio, R. Toledano, H. Huang, M. Toledano-Osorio, R. Osorio, C.Y.C. Huang, F. García-Godoy, Effect of doxycycline doped nanoparticles on osteogenic/cementogenic and anti-inflammatory responses of human cells derived from the periodontal ligament, J. Dent. 137 (2023), https://doi.org/10.1016/j.jdent.2023.104668.

[12] V.C.M. Neves, R. Babb, D. Chandrasekaran, P.T. Sharpe, Promotion of natural tooth repair by small molecule GSK3 antagonists, Sci. Rep. 7 (2017) 39654, https://doi.org/10.1038/srep39654.

[13] M. Toledano, F.S. Aguilera, E. Fernández-Romero, A.J.S. Lagos, M. Bonilla, C. D. Lynch, R. Osorio, Dentin remineralization using a stimuli-responsive engineered small molecule GSK3 antagonists-functionalized adhesive, Dent. Mater. (2023), https://doi.org/10.1016/j.dental.2023.12.010.

[14] F. Monticelli, R. Osorio, M. Toledano, F.R. Tay, M. Ferrari, In vitro hydrolytic degradation of composite quartz fiber-post bonds created by hydrophilic silane couplings, Oper. Dent. 31 (2006) 728–733, https://doi.org/10.2341/05-151.

[15] R. Osorio, I. Cabello, A.L. Medina-Castillo, E. Osorio, M. Toledano, Zinc-modified nanopolymers improve the quality of resin-dentin bonded interfaces, Clin. Oral Investig. 20 (2016) 2411–2420, https://doi.org/10.1007/s00784-016-1738-y.

[16] Y. Liu, X. Yao, Y.W. Liu, Y. Wang, A Fourier transform infrared spectroscopy analysis of carious dentin from transparent zone to normal zone, Caries Res 48 (2014) 320–329, https://doi.org/10.1159/000356868.

[17] M. Toledano, F.S. Aguilera, E. Osorio, I. Cabello, M. Toledano-Osorio, R. Osorio, Self-etching zinc-doped adhesives improve the potential of caries-affected dentin to be functionally remineralized, Biointerphases 10 (2015) 031002, https://doi.org/10.1116/1.4926442.

[18] A.L. Medina-Castillo, Thermodynamic principles of precipitation polymerization and role of fractal nanostructures in the particle size control, Macromolecules 53 (2020) 5687–5700, https://doi.org/10.1021/acs.macromol.0c00973.

[19] S. Sauro, F. Mannocci, M. Toledano, R. Osorio, D.H. Pashley, T.F. Watson, EDTA or H3PO4/NaOCl dentine treatments may increase hybrid layers' resistance to degradation: a microtensile bond strength and confocal-micropermeability study, J. Dent. 37 (2009) 279–288, https://doi.org/10.1016/j.jdent.2008.12.002.

[20] A.G. Schwartz, J.D. Pasteris, G.M. Genin, T.L. Daulton, Stavros Thomopoulos, Mineral distributions at the developing tendon enthesis, PloS One 7 (2012) e48630, https://doi.org/10.1371/journal.pone.0048630.

[21] M. Toledano, F.S. Aguilera, E. Osorio, I. Cabello, R. Osorio, Microanalysis of thermal-induced changes at the resin-dentin interface, Microsc. Microanal. 20 (2014) 1218–1233, https://doi.org/10.1017/S1431927614000944.

[22] C. Wang, Y. Wang, N.T. Huffman, C. Cui, X. Yao, S. Midura, R.J. Midura, J. P. Gorski, Confocal Laser Raman Microspectroscopy of Biomineralization Foci in UMR 106 Osteoblastic Cultures Reveals Temporally Synchronized Protein Changes Preceding and Accompanying Mineral Crystal Deposition, J. Biol. Chem. 284 (2009) 7100–7113, https://doi.org/10.1074/jbc.M805898200.

[23] C. Xu, Y. Wang, Cross-linked demineralized dentin maintains its mechanical stability when challenged by bacterial collagenase, J. Biomed. Mater. Res. B Appl. Biomater. 96 (2011) 242–248, https://doi.org/10.1002/jbm.b.31759.

[24] D.R. Sell, V.M. Monnier, Structure elucidation of a senescence cross-link from human extracellular matrix: implication of pentoses in the aging process, J. Biol. Chem. 264 (1989) 21597–21602, https://doi.org/10.1016/S0021-9258(20)88225-8.
[25] C. Xu, Y. Wang, Collagen cross-linking increases its biodegradation resistance in wet dentin bonding, J. Adhes. Dent. 14 (2012) 11–18, https://doi.org/10.3290/j.jad.a21494.
[26] Y. Wang, P. Spencer, Hybridization efficiency of the adhesive/dentin interface with wet bonding, J. Dent. Res. 82 (2003) 141–145, https://doi.org/10.1177/154405910308200213.
[27] A.A. Dawasaz, R.A. Togoo, Z. Mahmood, A. Azlina, K.Thirumulu Ponnuraj, Effectiveness of self-assembling peptide (P11-4) in dental hard tissue conditions: a comprehensive review, Polymers 14 (2022) 792, https://doi.org/10.3390/polym14040792.
[28] A.C. Profeta, F. Mannocci, R. Foxton, T.F. Watson, V.P. Feitosa, B. De Carlo, R. Mongiorgi, G. Valdré, S. Sauro, Experimental etch-and-rinse adhesives doped with bioactive calcium silicate-based micro-fillers to generate therapeutic resin–dentin interfaces, Dent. Mater. 29 (2013) 729–741, https://doi.org/10.1016/j.dental.2013.04.001.
[29] Y. Li, T.T. Thula, S. Jee, S.L. Perkins, C. Aparicio, E.P. Douglas, L.B. Gower, Biomimetic mineralization of woven bone-like nanocomposites: role of collagen cross-links, Biomacromolecules 13 (2012) 49–59, https://doi.org/10.1021/bm201070g.
[30] M. Balooch, S. Habelitz, J.H. Kinney, S.J. Marshall, G.W. Marshall, Mechanical properties of mineralized collagen fibrils as influenced by demineralization, J. Struct. Biol. 162 (2008) 404–410, https://doi.org/10.1016/j.jsb.2008.02.010.
[31] L.E. Bertassoni, S. Habelitz, J.H. Kinney, S.J. Marshall, G.W. Marshall Jr., Biomechanical Perspective on the Remineralization of Dentin, Caries Res 43 (2009) 70–77, https://doi.org/10.1159/000201593.
[32] M. Gungormus, F. Tulumbaci, Peptide-assisted pre-bonding remineralization of dentin to improve bonding, J. Mech. Behav. Biomed. Mater. 113 (2021) 104119, https://doi.org/10.1016/j.jmbbm.2020.104119.
[33] D.G. Moussa, J.A. Kirihara, Z. Ye, N.G. Fischer, J. Khot, B.A. Witthuhn, C. Aparicio, Dentin priming with amphipathic antimicrobial peptides, J. Dent. Res. 98 (2019) 1112–1121, https://doi.org/10.1177/0022034519863772.
[34] A.C. Profeta, F. Mannocci, R. Foxton, T.F. Watson, V.P. Feitosa, B. De Carlo, R. Mongiorgi, G. Valdré, S. Sauro, Experimental etch-and-rinse adhesives doped with bioactive calcium silicate-based micro-fillers to generate therapeutic resin-dentin interfaces, Dent. Mater. 29 (2013) 729–741, https://doi.org/10.1016/j.dental.2013.04.001.
[35] M. Toledano, I. Cabello, F.S. Aguilera, E. Osorio, M. Toledano-Osorio, R. Osorio, Improved sealing and remineralization at the resin-dentin interface after phosphoric acid etching and load cycling, Microsc. Microanal. 21 (2015) 1530–1548, https://doi.org/10.1017/S1431927615015317.
[36] M. Toledano, E. Osorio, F.S. Aguilera, S. Sauro, I. Cabello, R. Osorio, In vitro mechanical stimulation promoted remineralization at the resin/dentin interface, J. Mech. Behav. Biomed. Mater. 30 (2014) 61–74, https://doi.org/10.1016/j.jmbbm.2013.10.018.
[37] Y. Xu, J. Wu, H. Wang, H. Li, N. Di, L. Song, S. Li, D. Li, Y. Xiang, W. Liu, X. Mo, Q. Zhou, Fabrication of electrospun poly(L-lactide-co-ε-caprolactone)/collagen nanoyarn network as a novel, three-dimensional, macroporous, aligned scaffold for tendon tissue engineering, Tissue Eng. Part C Methods 19 (2013) 925–936, https://doi.org/10.1089/ten.TEC.2012.0328.
[38] E. Lozupone, C. Palumbo, A. Favia, M. Ferretti, S. Palazzini, F.P. Cantatore, Intermittent compressive load stimulates osteogenesis and improves osteocyte viability in bones cultured “in vitro, Clin. Rheumatol. 15 (1996) 563–572, https://doi.org/10.1007/BF02238545.
[39] J.A. Cowan, Influence of the weak nuclear force on metal-promoted autocatalytic strecker synthesis of amino acids: formation of a chiral pool of precursors for prebiotic peptide and protein synthesis, Life Basel Switz 14 (2023) 66, https://doi.org/10.3390/life14010066.
[40] H. Milly, F. Festy, T.F. Watson, I. Thompson, A. Banerjee, Enamel white spot lesions can remineralise using bio-active glass and polyacrylic acid-modified bio-active glass powders, J. Dent. 42 (2014) 158–166, https://doi.org/10.1016/j.jdent.2013.11.012.
[41] K. Karan, X. Yao, C. Xu, Y. Wang, Chemical profile of the dentin substrate in non-carious cervical lesions, Dent. Mater. 25 (2009) 1205–1212, https://doi.org/10.1016/j.dental.2009.04.006.
[42] A.G. Schwartz, J.D. Pasteris, G.M. Genin, T.L. Daulton, S. Thomopoulos, Mineral distributions at the developing tendon enthesis, PLOS ONE 7 (2012) e48630, https://doi.org/10.1371/journal.pone.0048630.
[43] C. Krafft, G. Steiner, C. Beleites, R. Salzer, Disease recognition by infrared and Raman spectroscopy, J. Biophotonics 2 (2009) 13–28, https://doi.org/10.1002/jbio.200810024.
[44] J.A. Timlin, A. Carden, M.D. Morris, R.M. Rajachar, D.H. Kohn, Raman spectroscopic imaging markers for fatigue-related microdamage in bovine bone, Anal. Chem. 72 (2000) 2229–2236, https://doi.org/10.1021/ac9913560.
[45] R. Vanna, P. Ronchi, A.T.M. Lenferink, C. Tresoldi, C. Morasso, D. Mehn, M. Bedoni, S. Picciolini, L.W.M.M. Terstappen, F. Ciceri, C. Otto, F. Gramatica, Label-free imaging and identification of typical cells of acute myeloid leukaemia and myelodysplastic syndrome by Raman microspectroscopy, Analyst 140 (2015) 1054–1064, https://doi.org/10.1039/C4AN02127D.
[46] A. Bonifacio, C. Beleites, F. Vittur, E. Marsich, S. Semeraro, S. Paoletti, V. Sergo, Chemical imaging of articular cartilage sections with Raman mapping, employing uni- and multi-variate methods for data analysis, Analyst 135 (2010) 3193–3204, https://doi.org/10.1039/C0AN00459F.
[47] A. Awonusi, M.D. Morris, M.M.J. Tecklenburg, Carbonate assignment and calibration in the raman spectrum of apatite, Calcif. Tissue Int. 81 (2007) 46–52, https://doi.org/10.1007/s00223-007-9034-0.
[48] Y. Liu, L. Tjäderhane, L. Breschi, A. Mazzoni, N. Li, J. Mao, D.H. Pashley, F.R. Tay, Limitations in bonding to dentin and experimental strategies to prevent bond degradation, J. Dent. Res. 90 (2011) 953–968, https://doi.org/10.1177/0022034510391799.
[49] K. Rezwan, Q.Z. Chen, J.J. Blaker, A.R. Boccaccini, Biodegradable and bioactive porous polymer/inorganic composite scaffolds for bone tissue engineering, Biomaterials 27 (2006) 3413–3431, https://doi.org/10.1016/j.biomaterials.2006.01.039.
[50] R. Osorio, E. Osorio, F.S. Aguilera, A.L. Medina-Castillo, M. Toledano, M. Toledano-Osorio, Silver improves collagen structure and stability at demineralized dentin: A dynamic-mechanical and Raman analysis, J. Dent. 79 (2018) 61–67, https://doi.org/10.1016/j.jdent.2018.10.003.
[51] M. Toledano, F.S. Aguilera, E. Osorio, M.T. López-López, I. Cabello, M. Toledano-Osorio, R. Osorio, On modeling and nanoanalysis of caries-affected dentin surfaces restored with Zn-containing amalgam and in vitro oral function, Biointerphases 10 (2015) 041004, https://doi.org/10.1116/1.4933243.
[52] M. Toledano, E. Muñoz-Soto, F.S. Aguilera, E. Osorio, M.P. González-Rodríguez, M. C. Pérez-Álvarez, M. Toledano-Osorio, R. Osorio, A zinc oxide-modified hydroxyapatite-based cement favored sealing ability in endodontically treated teeth, J. Dent. 88 (2019) 103162, https://doi.org/10.1016/j.jdent.2019.06.009.
[53] H. Salehi, E. Terrer, I. Panayotov, B. Levallois, B. Jacquot, H. Tassery, F. Cuisinier, Functional mapping of human sound and carious enamel and dentin with Raman spectroscopy, J. Biophotonics 6 (2013) 765–774, https://doi.org/10.1002/jbio.201200095.
[54] H. Cölfen, Biomineralization: A crystal-clear view, Nat. Mater. 9 (2010) 960–961, https://doi.org/10.1038/nmat2911.
[55] F. Nudelman, K. Pieterse, A. George, P.H.H. Bomans, H. Friedrich, L.J. Brylka, P.A. J. Hilbers, G. de With, N.A.J.M. Sommerdijk, The role of collagen in bone apatite formation in the presence of hydroxyapatite nucleation inhibitors, Nat. Mater. 9 (2010) 1004–1009, https://doi.org/10.1038/nmat2875.
[56] L. Angker, M.V. Swain, Nanoindentation: Application to dental hard tissue investigations, J. Mater. Res. 21 (2006) 1893–1905, https://doi.org/10.1557/jmr.2006.0257.
[57] S. Habelitz, M. Balooch, S.J. Marshall, G. Balooch, G.W. Marshall, In situ atomic force microscopy of partially demineralized human dentin collagen fibrils, J. Struct. Biol. 138 (2002) 227–236, https://doi.org/10.1016/s1047-8477(02)00029-1.
[58] S. Sauro, R. Osorio, T.F. Watson, M. Toledano, Influence of phosphoproteins’ biomimetic analogs on remineralization of mineral-depleted resin-dentin interfaces created with ion-releasing resin-based systems, Dent. Mater. 31 (2015) 759–777, https://doi.org/10.1016/j.dental.2015.03.013.
[59] S. Sauro, R. Osorio, E. Osorio, T.F. Watson, M. Toledano, Novel light-curable materials containing experimental bioactive micro-fillers remineralise mineral-depleted bonded-dentine interfaces, J. Biomater. Sci. Polym. Ed. 24 (2013) 940–956, https://doi.org/10.1080/09205063.2012.727377.
[60] S. Sauro, R. Osorio, T.F. Watson, M. Toledano, Therapeutic effects of novel resin bonding systems containing bioactive glasses on mineral-depleted areas within the bonded-dentine interface, J. Mater. Sci. Mater. Med. 23 (2012) 1521–1532, https://doi.org/10.1007/s10856-012-4606-6.

SUPPLEMENTARY MATERIAL

Figure S1. Flow chart diagram of study methodology. NPs, Nanoparticles; TDg: Tideglusib; SBFS, Simulated Body Fluid Solution; HL: Hybrid Layer; BHL: Bottom of Hybrid Layer; Bis-GMA: bisphenol A-glycidyl methacrylate.

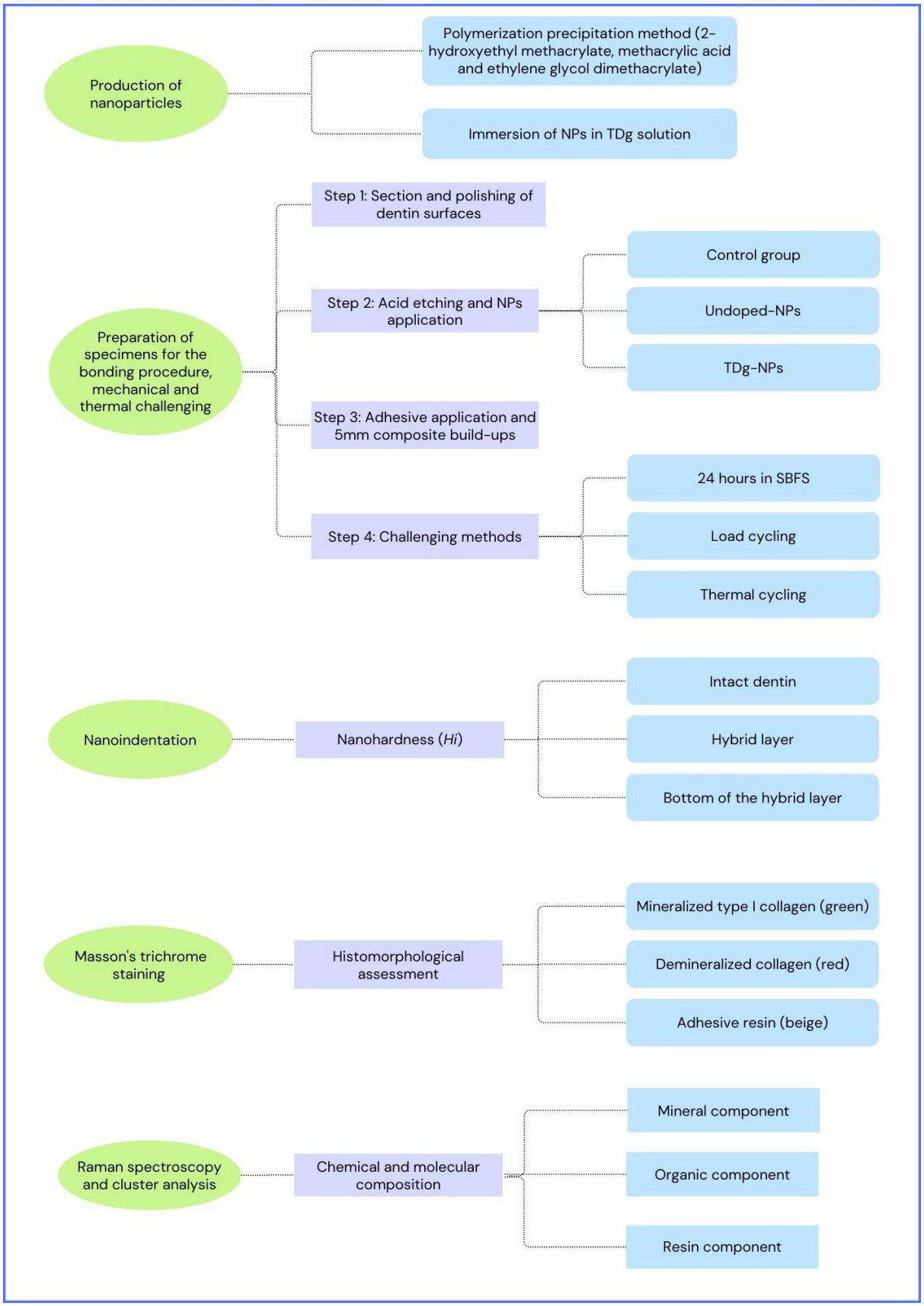

Table S1: Band assignments in Raman spectra of dentin mineral component [Karan et al., 2009; Schwartz et al., 2012].

Parameter	Raman band (cm^{-1})	Assignment	Biochemical relevance
Phosphate peak	960	v_1 of Phosphate (PO_4^{3-})	Mineral phosphate and carbonate content
Carbonate Peak	1,070	v_1 of Carbonate (CO_3^{2-})	
$FWHM_P$	960	Phosphate *Crystallinity*	Crystallographic or relative atomic order, narrower peaks suggest less structural variation in bond distances and angles
$FWHM_C$	1,070	Carbonate *Crystallinity*	
GMC	1,070 and 960	Ratio 1,070/960	indicating carbonate substitution for phosphate

Abbreviations: FWHM: Full Width at Half Maximum of the selected band, referred to phosphate ($_P$) or carbonate ($_C$); GMC: Gradient in mineral content or carbonate content of the mineral crystallites.

- *K. Karan, X. Yao, C. Xu, Y. Wang, Chemical Profile of the Dentin Substrate in Non-Carious Cervical Lesions, Dent. Mater. 25 (2009) 1205–1212. https://doi.org/10.1016/j.dental.2009.04.006.*
- *A.G. Schwartz, J.D. Pasteris, G.M. Genin, T.L. Daulton, S. Thomopoulos, Mineral Distributions at the Developing Tendon Enthesis, PLOS ONE 7 (2012) e48630. https://doi.org/10.1371/journal.pone.0048630.*

Dental Materials xxx (xxxx) xxx

Contents lists available at ScienceDirect

Dental Materials

journal homepage: www.elsevier.com/locate/dental

Effect of the anti-Alzheimer drug GSK-3β antagonist on numerical modeling of the energy dissipation through the resin-dentin interface

Manuel Toledano [a], Enrique Fernández-Romero [a,b], Estrella Osorio [a,*], Fátima S. Aguilera [a], Christopher D. Lynch [c], María T. Osorio [a], Raquel Toledano [a], Raquel Osorio [a]

[a] University of Granada, Faculty of Dentistry, Colegio Máximo de Cartuja s/n, 18071 Granada, Spain
[b] Medicina Clínica y Salud Pública PhD Programme, University of Granada, 18071 Granada, Spain
[c] University Dental School & Hospital/Cork University Dental School & Hospital, Cork, Ireland

ARTICLE INFO

Keywords:
Mineralized dentin
Tideglusib
Nano-DMA
Nanoparticles
Atomic Force Microscopy. Stress concentration
Complex modulus
Tan delta

ABSTRACT

Objectives: The aim of this study was to determine the viscoelastic performance and energy dissipation of conditioned dentin infiltrated with polymeric nanoparticles (NPs) doped with tideglusib (TDg) (TDg-NPs).
Methods: Dentin conditioned surfaces were infiltrated with NPs and TDg-NPs. Bonded interfaces were created, stored for 24 h and submitted to mechanical and thermal challenging. Resin-dentin interfaces were evaluated through nano-DMA/complex-loss-storage moduli-tan delta assessment and atomic force microscopy (AFM) analysis.
Results: Dentin infiltrated with NPs and load cycled attained the highest complex modulus at hybrid layer and bottom of hybrid layer. Intertubular dentin treated with undoped NPs showed higher complex modulus than peritubular dentin, after load cycling, provoking energy concentration and breakdown at the interface. After infiltrating with TDg-NPs, complex modulus was similar between peri-intertubular dentin and energy dissipated homogeneously. Tan delta at intertubular dentin was higher than at peritubular dentin, after using TDg-NPs and load cycling. This generated the widest bandwidth of the collagen fibrils and bridge-like mineral structures that, as sight of energy dissipation, fastened active dentin remodeling. TDg-NPs inducted scarce mineralization after thermo-cycling, but these bridging processes limited breakdown zones at the interface.
Significance: TDg-based NPs are then proposed for effective dentin remineralization and tubular seal, from a viscoelastic approach.

1. Introduction

The guarantee of a correct adhesion to dentin is the formation of an adequate hybrid layer (HL). The HL is formed when the mineral component from the dentin has been removed and the adhesive resin has been infiltrated undergoing complete in situ polymerization [1]. Hence, a three-dimensional collagen-resin biopolymer is created, facilitating a linkage between the dentin substrate and the adhesive [2]. Nevertheless, after demineralization and further resin infiltration, a volume of unprotected collagen is generated at the bottom of the hybrid layer (BHL) [3]. This collagen is vulnerable to the action of matrix metalloproteinases (MMPs) [4–6], causing degradation and jeopardizing the longevity of bonded restorations [7,8]. Thus, remineralization of the unprotected collagen has pivotal implications in the improvement of bonding features. Thereby, a refined adhesive formulation for minimally invasive dentistry has to offer a durable and stronger adhesion to dental tissues. This biomaterial should also promote remineralization and protection of the interface by deploying bioactivity, even more in challenging conditions [9], as mechanic and thermal cyclic fatigue under functional stress [10].

Classical bioactive materials for functionalization of adhesives raise concerns respect to the regrowth of minerals at the demineralized dentin [11]. Engineered polymeric and hydrophilic nanoparticles (NPs) have been proposed as carriers of some biological factors to manage dentin remineralization [12]. In addition, Neves et al. (2017) [13], have proposed a biologically oriented methodology for dentin generation and remineralization. They reported the performance of the glycogen-synthase-kinase 3 (GSK-3) peptide in remineralization. GSK-3 phosphorylates Axin and β-catenin (β-cat), being a capital intracellular constituent of the Wnt/β-cat signaling pathway. Tideglusib (TDg), used

* Correspondence to: University of Granada, Faculty of Dentistry, Dental Materials Section, Colegio Máximo de Cartuja s/n, 18071 Granada, Spain.
E-mail address: meosorio@ugr.es (E. Osorio).

https://doi.org/10.1016/j.dental.2024.09.005
Received 25 June 2024; Received in revised form 10 September 2024; Accepted 10 September 2024

in the treatment of Alzheimer's disease, as GSK-3 inhibitor, was postulated as a dentin repair therapy [14]. In the present research, the in vitro viscoelastic mechanical behavior of polymeric NPs serving as TDg carriers will be assessed, at the resin-dentin interface.

The mechanical performance of the dentin structure will be affected by the quality and the degree of the mineralization [15]. The precipitation of minerals at the intrafibrillar compartment of the demineralized collagen at the resin-dentin interface [16] is directly related to an increase of the mechanical properties [15,17]. One of the most commonly means of testing the mechanical behavior of substrates or materials [18], is the atomic force microscopy (AFM) nano-indentation. AFM represents, at nanoscale [19], a suitable method for the determination of the viscoelasticity of hard tissues [15,20]. The nano-dynamic mechanical analysis (nano-DMA) has demonstrated that the dampening (or viscous) behavior of dentin is highly sensitive to the structural changes that appear with the oral function [21].

The storage (elastic) and loss (damping) moduli are two modulus components of the complex modulus [22]. The ability to store energy by the sample during a cycle of loading [23] is characterized by the storage modulus (E') (also called dynamic stiffness), which is then available for elastic recoil. The ability of the material to dissipate energy is characterized by the loss modulus (E''). Stiffness and damping are measured by DMA. The tan delta (δ) is the ratio of the loss to the storage. The load cycling of the masticatory function significantly influences the interactions between restorative materials and dental tissues. The bonded interface should support and dissipate this energy, which is transmitted by the forces. Discrepancies in viscoelastic properties values within the distinct structures located within the resin-dentin interface pose a risk for cracking and breakdown. In relatively high elastic modulus regions, low modulus regions provoke stress concentration [2], accounting for catastrophic failures of the restored teeth. Peritubular (PD) and intertubular dentin (ID) represent two phases with a pivotal role in viscolestic properties of dentin. Both morpho and nanomechanical properties can be obtained by integrating nano-DMA and AFM [24].

The aim of the current research was to infiltrate tideglusib-loaded nanoparticles into phosphoric acid conditioned dentin, before the application of the adhesive resin, in order to evaluate a potential improvement of viscoelasticity after mineral precipitation at the resin-dentin interface submitted to thermal and mechanical loading. The null hypotheses to be tested are that tideglusib loaded nanoparticles infiltration into conditioned dentin, (1) does not affect the dynamic mechanical behavior at the resin-dentin interface, after thermal or mechanical challenging, (2) does not facilitate remineralization at the demineralized bonded interface, and (3) morphological characteristics at the resin dentin interface do not differ after infiltration of tideglusib-loaded nanoparticles.

2. Material and methods

2.1. Production of nanoparticles

The process of obtaining NPs applied the use of the polymerization precipitation method, which controlled the precipitation facilitated by a thermodynamic approach. Specifically, the Flory-Huggins model, based on Hansen's solubility parameters, was employed. This model centered on interactions among solvent molecules and the growth of polymer chains through hydrogen, polar bonding, and dispersion forces [25]. The backbone monomer for NP design was 2-hydroxyethyl methacrylate, with methacrylic acid serving as the functional monomer, and ethylene glycol dimethacrylate employed as the cross-linker. Subsequently, half of the produced NPs were loaded with a peptide, tideglusib (Sigma-Aldrich, Chemie GmbH, Riedstr, Germany). The NPs loading process was conducted by immersion of 100 mg of NPs in 1 mL of 0.0017 mg/mL TDg solution for 2 h at room temperature under constant shaking (12 rpm) (rotator Orbit 300445, JP Selecta, Barcelona, Spain). Then, the NPs were left until the solvent was completely evaporated, ensuring that all the TDg remains onto the NPs. Two types of NPs were obtained, undoped NPs and TDg-NPs.

2.2. Preparation of specimens for the bonding procedure, mechanical and thermal challenging

Thirty-six unerupted human third molars, preserved at 4ºC in a 0.5% chloramine T solution for no more than a month, were utilized for this study. Prior to their involvement, subjects provided informed consent, aligning with the Declaration of Helsinki and adhering to good clinical practice guidelines. The study received ethical approval from the local Ethics Committee (1906/CEIH/2020).

The teeth were horizontally sectioned just below the dentin-enamel junction to expose sound dentin surfaces. These surfaces were then flatly polished to create a clinically relevant smear layer, utilizing 180-grit silicon carbide –SiC- abrasive paper. Subsequently, the dentin surfaces underwent etching (with 37% phosphoric acid, during 15 s), followed by rinsing and drying. Random allocation of experimental teeth (n = 12) to one of three groups was achieved through computer-generated randomization, facilitated by http://www.randomizer.org/form.htm. The allocation remained concealed in sealed envelopes until the time of bonding procedure. Just an ethanol solution was applied (30 s) (i), or an ethanol suspension of undoped NPs (ii), and TDg-NPs (iii) (10 mg/mL) in each of the three experimental groups (n = 12), acting as primers. Ethanol was then evaporated for 30 s and, finally, Single Bond (SB) resin (3 M ESPE, St. Paul, MN, USA) was applied according to the manufacturer's instructions, to fulfill the conventional adhesive protocol. The sample preparation was conducted by one researcher, and a uniform adhesion protocol was implemented by a different researcher. For each tooth, a composite build-up (5 mm high) (Tetric EvoCeram, Ivoclar-Vivadent, Schaan, Liechtenstein) was performed using the incremental technique, in five 1 mm resin layers. The light-curing process was carried out with a Bluephase® polywave light-emitting diode light-polymerizing unit (Bluephase G2, Ivoclar Vivadent AG, Schaan, Liechtenstein) at 1500 mW/cm^2 for 20 s. The output intensity was monitored with a curing radiometer (Model Bluephase® meter, Ivoclar Vivadent AG, Schaan, Liechtenstein), ensuring a minimal output intensity of 1500 mW/cm^2 for all experiments. The restored teeth were stored in a dark environment and submerged in simulated body fluid solution (SBFS) for 24 h.

The specimens, within each experimental group, were then divided into three sub-groups (n = 4) based on the challenging method: (1) Restored teeth stored in SBFS for 24 h, (2) load cycling with a sine wave form for 24 h (259,200 cycles, 3 Hz) (S-MMT-250NB; Shimadzu, Tokyo, Japan) proceeding as in Sauro *et al.* 2009 [26], and (3) thermal cycling (100,000 cycles/ 5ºC and 55ºC) (SD Mechatronik GmbH, Germany) during approximately three months in distilled water [14]. Finally, the samples were sectioned into resin–dentin slabs and polished using ascending grit SiC abrasive papers (#1200 to #4000) on a water-cooled polishing device (Buehler-MetaDi, Buehler Ltd. Lake Bluff, IL, USA). The specimen preparation was concluded with a final ultrasonic cleaning (5 min). A schematic representation of the final resin-dentin interface is provided in the Fig. S1.

2.3. Nano-DMA analysis

Four resin-dentin slabs from each treated dentin were submitted for nano-DMA and AFM analysis in hydrated conditions. Property mappings were conducted using a Ti-750D (Hysitron, Inc., Minneapolis, MN) equipped with nano-DMA III, a commercial nano-DMA package. The indenter tip was calibrated against a fused quartz sample using a quasistatic force setpoint of 5μN to maintain contact between the tip and the sample surface. A dynamic (oscillatory) force of 5μN was superimposed on the quasistatic signal at a frequency of 200 Hz. Based on a calibration modulus of the tip value of 1.1400E+ 3 N/mm^2 for the fused quartz, the best-fit spherical radius approximation for tip was found to be 150 nm,

for the selected nano-DMA scanning parameters. Modulus mapping of our samples was conducted by imposing a quasistatic force setpoint, F_q= 5μN, to which we superimposed a sinusoidal force of amplitude F_A = 1.8μN and frequency f = 200 Hz.

Under steady conditions (application of a quasistatic force) the indentation modulus of the tested sample, E, was obtained by application of different models that relate the indentation force, F, and depth D [27]. Most of these theories assume proportionality between the force and the indentation modulus:

$$F = g(D)E \quad \rightarrow E = \frac{F}{g(D)} \tag{1}$$

Where g (D) is a function on the indentation depth, which depends on the geometry of the probe of the indenter. For example, for a spherical probe, the Hertzian contact theory predicts [27,28]:

$$g \quad (D) = \quad \frac{4R^{1/2} \quad D^{3/2}}{3(1 - \quad \nu^2)} \tag{2}$$

In this equation R is the radius of the spherical probe and v is the Poissonś ration of the tested sample. As mentioned above, in nano-DMA experiments an oscillatory force is superimposed to a quasistatic force:

$$F = \quad F_q + \quad F_A \quad \sin(2\pi ft) \tag{3}$$

With t being the time. Under this imposed force, the indentation depth takes the following form:

$$D = \quad D_q \quad + \quad D_A \quad \sin \quad (2\pi ft - \delta) \tag{4}$$

This means that the indentation depth also oscillates around a quasistatic value, with the same frequency that the oscillating force and delayed by a phase lag δ. In the limit of $F_A << F_q$ it can be expanded the Eq. (1) to a first order Taylor approximation, to obtain:

$$F_q + F_A \sin(2\pi ft) = g(D_q)E + g'(D_q)|E^*| \quad D_A \sin(2\pi ft - \delta). \tag{5}$$

In this equation, g´is the first derivate of g, and E * is the complex dynamic indentation modulus. Now, it can be equaled the time-dependent terms and change the time origin, to write:

$$F_A \sin(2\pi ft + \delta) = g(\acute{D_q})|E^*|D_A \sin(2\pi ft) \tag{6}$$

Now, the oscillating force can be decomposed into two terms, the in-phase term, F´, and the out-of-phase term, F˝ [29].

$$\begin{aligned} F_A \sin(2\pi ft + \delta) = \quad & F_A \quad \cos\delta \sin(2\pi ft) + F_A \sin\delta \cos(2\pi ft) \\ = \quad & F_A' \sin(2\pi ft) + \quad F_A'' \cos(2\pi ft) = F' + F'' \end{aligned} \tag{7}$$

Then, from this decomposition two dynamics moduli can be extracted:

$$E' = \quad |E^*|\cos\delta \quad = \quad \frac{F_A \cos\delta}{g(\acute{D_q})D_A} = \quad \frac{F_A'}{g(\acute{D_q})D_A} \tag{8}$$

Which is the in-phase or storage (elastic) modulus.

$$E'' = \quad |E^*|\sin\delta = \quad \frac{F_A \quad \sin\delta}{g(\acute{D_q}) \quad D_A} \quad = \quad \frac{F_A''}{g(\acute{D_q}) \quad D_A} \tag{9}$$

which is the out-phase or loss (viscous) modulus. Note the position of the phase lag, δ, in these equations. As mentioned above, these coefficients are directly related with measured parameters, without any particular assumption, except the consideration of the system consisting of the sample and the instrument tip as a driven simple oscillating under stationary conditions. From the application of different models relating indentation force (F) and depth (D), the indentation modulus of the tested sample (E) under application of a quasi-static force (stable conditions) was obtained [27].

The dentin discs were then removed from the SBFS immersion and scanned under hydrated conditions. To eliminate problems associated to the meniscus forces transferred from fluid droplets to the indenter [30], and to preserve hydration of the dentin surfaces, a drop (1.5 mL) of 99.4 % ethylene glycol [31] was applied on the polished surface of the specimen. For each dentin disc, three modulus mappings were recorded. Data from regions approximately 30 × 30 μm in size were collected using a scan rate of 0.2 Hz. Each scan resulted in a 256 × 256 pixel data array.

For each mapping and for each type of resin-dentin interface, 15 value points of complex modulus (E *), storage modulus (E'), loss modulus (E'') and tan delta (δ) were acquired for each zone of the interface, excluding the adhesive resin, i.e, hybrid layer (HL), bottom of hybrid layer BHL), intertubular dentin (ID) and peritubular dentin (PD) (Fig. S1).

2.4. Atomic Force Microscopy (AFM) analysis, collagen fibril diameter

For the topographical mapping, an atomic force microscope (AFM Nanoscope V, Digital Instruments, Veeco Metrology group, Santa Barbara, CA, USA) was employed, in this study, for surface analysis of the same samples. The imaging process was undertaken using a taping mode with an oscillating cantilever calibrated vertical-engaged piezo-scaner (Digital Instrument, Santa Barbara, CA, USA). A 10 nm radius silicon nitride tip (Veeco) was mounted at the end of an oscillating cantilever that came into intermittent contact with the surface at the lowest oscillation point. Vertical modifications of the AFM tip with a resonance frequency close to 330 kHz resulted in the height of the images shown as dark and bright zones. With a slow scan rate (0.1 Hz), digital images (2 ×2 μm) were captured for each dentin surface. To facilitated dentin surfaces observation, AFM images were tilted using a specific software (Nanoscope Analysis v. 1.40, Bruker Corporation, Billerica, MA, USA). To observe the fibril width of all groups, 5 random images (2 ×2 μm) were recordered from the samples. Collagen fibril diameter (in nanometers) were determined from the images by section analysis with data that were modified only by plane-fitting. The collagen fibril diameter was preferentially determined from fibrils that were exposed along their complete widths. Five fibrils and their interfibrillar spacings were analyzed from each image. Measurements were corrected for tip-broadening [32] by the equation $e = 2r$, where e is the error in the horizontal dimension and r is the tip's radius [33].

2.5. Statistical methods

Numerical data were further analyzed by ANOVA and Student-Newman-Keuls multiple comparison tests, with $p < 0.05$ as statistical significance. The validity of the assumptions of normality and homoscedasticity of the data had been previously verified.

3. Results

3.1. Nano-DMA analysis

Concerning the type of challenging within each group (capital letters in Table 1), at the hybrid layer, the highest E * was obtained at dentin infiltrated with undoped NPs load cycled, and dentin infiltrated with TDg-NPs load cycled. The control group thermo-cycled showed the lowest E * . In general, loss modulus, E'', performed similar regardless the type of NPs. The lowest E'' was obtained in the control specimens thermo-cycled. Dentin specimens treated with undoped NPs and mechanically loaded showed the highest E' among samples of this group. Specimens treated with TDg-NPs and thermo-cycled attained the highest storage modulus E' among samples of this group (Table 1). Tan (δ) practically performed similar in all groups (Table 1). At the bottom of the hybrid layer, the highest E * was obtained at dentin infiltrated with undoped NPs and load cycled, and dentin infiltrated with TDg-NPs load cycled. The property map of the interface promoted by demineralized dentin infiltrated with undoped NPs and TDg-NPs, both load cycled,

Table 1
Mean and SD of Complex, Loss, Storage Modulus (GPa) and Tan (δ) attained from experimental interfaces after 24 h, load cycling (LC) and thermo-cycling (TC).

	CONTROL			UNDOPED-NPs			TIDEGLUSIB-NPs		
	24 H	LC	TC	24 H	LC	TC	24 H	LC	TC
HYBRID LAYER									
E *	45.79 (6.34)Aa1	56.48 (11.89)Aa1	40.87 (3.73)Aa1	64.65 (16.77)Aa1	119.05 (27.27)Bb12	56.63 (13.20)Aa1	51.31 (8.92)Aa1	151.71 (30.94)Bb1	100.69 (13.17)Cb1
E ”	4.73 (6.22)Aa1	3.70 (2.93)Aa1	1.20 (1.28)Aa1	6.09 (1.82)Aa2	5.64 (4.79)Aa1	3.20 (2.26)Aa1	4.96 (4.84)Aa1	5.66 (2.49)Aa1	4.06 (2.98)Aa12
E´	44.10 (6.45)Aa1	55.67 (6.11)Ba1	40.32 (8.14)Aa2	50.71 (9.03)Aa2	194.21 (60.88)Bb1	48.52 (9.40)Aa1	50.20 (11.48)Aa1	45.60 (16.48)Aa1	151.62 (61.24)Bb2
Tan (δ)	–	0.18 (0.10)Aa1	0.09 (0.04)Aa1	0.22 (0.06)Aa2	0.12 (0.11)Aa1	0.20 (0.09)Aa1	0.17 (0.11)Aa1	0.18 (0.10)Aa1	0.26 (0.33)Aa12
BOTTOM OF HYBRID LAYER									
E *	61.07 (5.81)Aa2	53.93 (3.81)Aa1	43.26 (5.97)Ba1	44.15 (8.16)Ab11	156.79 (51.02)Bb12	62.08 (10.76)Ab1	117.08 (26.93)Ac2	185.22 (37.70)Bb1	83.37 (19.75)Ab1
E”	6.72 (5.17)Aa1	5.91 (6.34)Aa1	1.31 (1.97)Aa1	11.04 (4.57)Aa2	9.41 (4.56)Aa1	6.19 (0.98)Ab2	5.69 (4.59)Aba1	11.96 (2.73)Aa2	5.87 (3.19)Ab12
E´	63.89 (19.74)Aa12	53.89 (10.04)Aa1	45.69 (7.00)Aa2	30.21 (8.69)Ab1	139.27 (43.32)Bb1	55.07 (6.32)Ca1	115.67 (39.13)Ac2	210.27 (41.07)Bb2	45.67 (8.48)Ca1
Tan (δ)	–	0.30 (0.15)Aa1	0.07 (0.03)Ba1	0.24 (0.04)Aa2	0.16 (0.16)Aa1	0.24 (0.09)Ab1	0.18 (0.19)Aa1	0.26 (0.05)Aa1	0.49 (0.23)Ab2
INTERTUBULAR DENTIN									
E *	82.45 (9.21)Aa3	57.31 (11.24)Ba1	53.85 (13.42)Ba1	86.57 (12.85)Aa2	87.62 (21.09)Aab1	73.95 (13.60)Aa12	119.84 (34.33)Aa2	106.73 (36.64)Ab1	111.73 (30.85)Aa1
E”	5.45 (5.65)Aab1	3.17 (3.79)Aa1	3.36 (1.12)Aa2	16.44 (7.11)Aa2	11.58 (6.70)Aa1	7.82 (6.72)Aa12	3.97 (2.90)Ab1	10.14 (7.70)Aa2	7.52 (1.92)Aa2
E´	74.26 (22.02)Aa2	63.71 (20.02)Aa1	51.34 (11.15)Aa23	83.90 (22.76) Aa2	78.36 (18.69)Aa2	68.62 (9.31)Aab1	99.12 (43.89)Aa12	68.93 (13.16)Aa1	90.40 (21.55)Ab2
Tan (δ)	–	0.18 (0.15)Aa1	0.22 (0.10)Aa12	0.26 (0.11)Aa2	0.24 (0.11)Aa1	0.27 (0.10)Aa1	0.22 (0.11)Aa1	0.26 (0.09)Aa1	0.22 (0.20)Aa12
PERITUBULAR DENTIN									
E *	80.17 (15.15)Aa3	55.13 (9.65)Ba1	54.38 (11.41)Ba1	128.50 (13.83)Ab3	134.49 (21.65)Ab2	102.71 (17.00)Ab3	131.89 (19.74)Ab2	119.96 (35.40)Ab1	126.42 (34.10)Ab1
E”	48.49 (13.36)Aa2	27.87 (8.04)Aab2	23.34 (0.95)Aa1	30.99 (0.71)Aa3	27.57 (5.15)Aa2	27.93 (5.06)Aa3	10.72 (4.27)Ab	14.78 (5.13)Ab2	11.19 (1.57)Ab3
E´	133.50 (15.09)Aa3	118.50 (24.42)Aa2	98.83 (39.84)Aa3	120.27 (15.25)Aa2	107.94 (9.92)Aa2	98.57 (11.27)Aa2	171.30 (41.74)Aa2	130.52 (46.80)Aa2	149.25 (41.26)Aa2
Tan (δ)	0.42 (0.09)Aa	0.20 (0.05)Ba1	0.24 (0.06)Ba2	0.26 (0.07)Ab2	0.25 (0.03)Aa1	0.28 (0.06)Aa1	0.07 (0.01)Ac1	0.09 (0.02)Ab2	0.08 (0.02)Ab1

Abbreviations: TDg: Tideglusib; NPs: nanoparticles; LC: Load cycled; TC: Thermo-cycled E * (GPa): E * : Complex Modulus (GPa), *E''*: Loss Modulus (GPa), E´: Storage Modulus. Same capital letter indicates no significant difference between 24 h, load cycled and thermo-cycled groups, i.e, type of challenging, at the same interface zone and same experimental procedure. Identical lower case letter indicates no significant differences between different experimental procedure groups, i.e, similar type of challenging among the different groups. Same number indicates no significant differences between distinct zones within the same experimental procedure. Significance was set at $p < 0.05$.

achieved the highest resistance to dynamic deformation at the bottom of the hybrid layer, that corresponded with several discontinuous red collars in the mappings (Figs. 1A, 1B). In general terms, the control group achieved the lowest E * (Fig. 1D). Loss modulus *E''* performed similar in specimens treated with undoped NPs and TDg-NPs (Figs. S2B, S2D, respectively). Samples treated with any kind of NP and mechanically loaded attained the highest storage modulus *E'* (Figs. S3C, S3D). Tan (δ) practically performed similar in all groups (Table 1) (Fig. 2). At both intertubular and peritubular dentin, specimens infiltrated with any kind of NPs performed similar, showing the same E * , *E''*, *E'* and Tan (δ), regardless the type of challenging (Table 1).

Concerning the same type of challenging among different groups (lower case letters in Table 1), at the hybrid layer, specimens tested at 24 h showed the same E * , regardless the group of study (Fig. 1D). Samples treated with any kind of NPs and mechanically loaded had similar E * and performed superior than the control group. Specimens infiltrated with TDg-NPs thermo-cycled (Fig. 1C) achieved higher E * than the rest of the groups, that performed similar. Loss modulus *E''* and tan (δ) showed the same values at 24 h, and after both load and thermal cycling, when the three groups were compared (Fig. S4C). Storage modulus *E'* attained the same values at 24 h, and after both load and thermal cycling when the three groups were compared, except samples treated with undoped NPs that showed the highest values among groups (194.21 GPa) (Table 1) (Fig. S3C). At the bottom of the hybrid layer, the highest complex modulus E * was achieved by samples infiltrated with TDg-NPs, at 24 h storage. Samples treated with any kind of NPs and mechanically or thermal loaded had similar E * and performed superior than the control group. At 24 h storage and after load cycling, all samples showed similar loss modulus *E''* (Fig. S2). After thermo-cycling, samples treated with any kind of NPs had similar *E''* and performed superior than the control group. At 24 h storage, the highest storage modulus *E'* corresponded to specimens infiltrated with TDg-NPs (Fig. S3D). Samples treated with any kind of NPs and mechanically loaded had similar *E'* and performed superior than the control group (Fig. S3A). After thermo-cycling, all samples performed similar. All specimens showed the same tan (δ) at 24 h storage and after load cycling. Samples treated with any kind of NPs and thermically loaded had similar tan (δ) and performed superior than the control group (Fig. 2A).

At intertubular dentin, samples 24 h storage performed similar, showing the same E * values. After load cycling, specimens infiltrated with TDg-NPs showed the highest E * (Fig. 1B), and when samples were thermocycled they obtained similar E * . At 24 h of storage, samples treated with TDg-NPs attained the lowest loss modulus *E''* (Fig. S2C). The control group and samples treated with any kind of NPs, mechanically and thermically loaded achieved similar *E''*. At 24 h storage and mechanically loaded samples, all specimens attained the same storage modulus *E'*. Samples treated with any kind of NPs and thermically loaded achieved similar *E'* and performed superior than the control group (Fig. S3A). All specimens showed the same tan (δ), regardless the

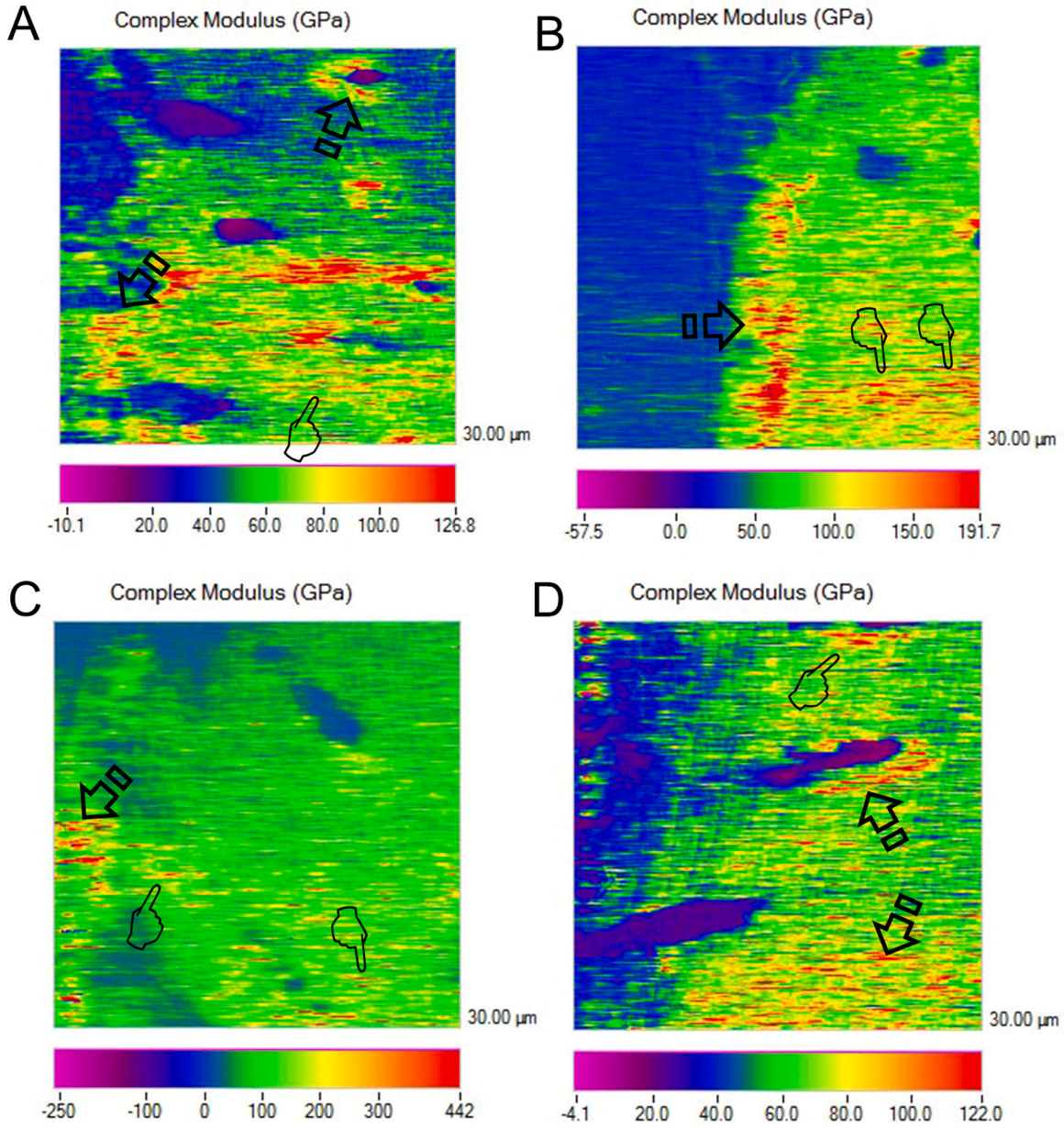

Fig. 1. Scanning mode nano-DMA analysis of the map of the complex modulus at the dentin infiltrated with undoped nanoparticles (NPs) in specimens load cycled (**A**), at dentin infiltrated with NPs doped with tideglusib (TDg-NPs) load cycled (**B**), at dentin infiltrated with NPs doped with tideglusib (TDg-NPs) thermo-cycled (**C**) and control group load cycled (**D**). In the color scheme shown, the dark color corresponds to lower values of the locally measured complex modulus E * . Discontinuous red collar point out areas of maximum E * (arrows). Closed loops in yellow to red traces signalize regions of maximum E * coinciding with peritubular viscoelasticity (pointers). Green zones within the red collar of high E * values suggest intratubular precipitation of crystals. Irregular blue circles spread out in the scan surface and most of them appeared framed by a collar of multiple red spots.

type of challenging (Table 1) (Fig. 2). At peritubular dentin, samples treated with any kind of NPs performed with similar E * , and superior than the control group at 24 h storage, after load cycling (Fig. 1D) and after thermo-cycling (Fig. 1C). At 24 h of storage and after load cycling, samples treated with TDg-NPs attained the lowest loss modulus *E″*. Samples treated with TDg-NPs and thermically loaded achieved the lowest *E″* (Fig. S2). All specimens showed the same storage modulus *E′* (Fig. S3), regardless the type of challenging. At 24 h storage, specimens infiltrated with TDg-NPs achieved the lowest tan (δ). After load cycling and thermo-cycling, specimens infiltrated with TDg-NPs achieved the lowest tan (δ) values (Table 1) (Figs. 2C, 2D).

Regarding the distinct zones within the same experimental procedure (numbers in Table 1), the control group specimens, regardless the subgroup (24 h storage, load cycling or thermo-cycling), exhibited the same E * throughout the resin-dentin interface without significant differences (Fig. 1D). Dentin infiltrated with undoped NPs, at 24 h storage, showed similar E * at both the HL and the BHL, and increased at intertubular dentin, attaining the highest complex modulus at peritubular dentin. Dentin infiltrated with undoped NPs, after load cycling, achieved the lowest E * at intertubular dentin, and significantly increased at peritubular dentin. Similar specimens, after thermo-cycling showed similar E * values at the interface, except at peritubular dentin, that increased their values. When demineralized dentin was infiltrated with TDg-NPs, samples stored for 24 h exhibited the same E * through the whole interface, but the HL had the lowest values (Fig. 1B). The groups infiltrated with both kind of NPs showed similar E * throughout the whole interface, regardless the type of challenging (Table 1).

Concerning the loss modulus *E″*, the highest values of the control

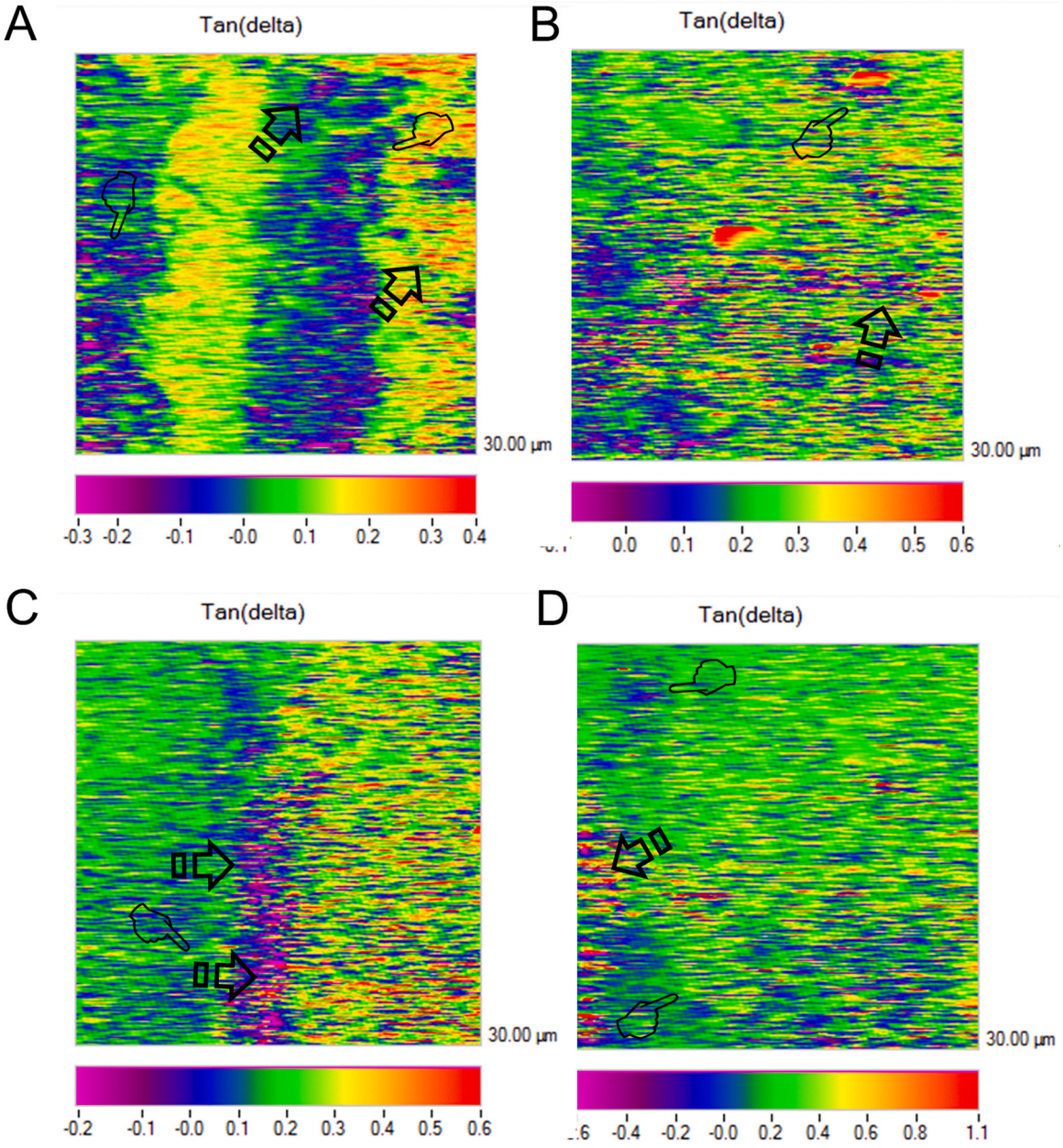

Fig. 2. Scanning mode nano-DMA analysis of the map of the tan (δ) at the control group thermo-cycled (**A**), at dentin infiltrated with undoped NPs load cycled (**B**), dentin infiltrated with NPs doped with tideglusib (TDg-NPs) load cycled (**C**) and dentin infiltrated with NPs doped with tideglusib (TDg-NPs) thermo-cycled (**D**). In the color scheme shown, the red color corresponds to the highest value of the locally tan (δ) value moduli, potentially associated to tan (δ) of intratubular and intertubular mineral precipitation (arrows). The capacity for getting rid of the energy at peritubular dentin is represented by the blue-green diffused marks (pointers), at the mapping.

group 24 h storage were obtained at peritubular dentin, and the rest of the interface performed similar. No changes were adverted after load cycling, and the highest values after thermo-cycling were achieved at intertubular dentin. Specimens with undoped NPs infiltration, regardless the type of challenging, showed similar E'' at the resin-dentin interface, but significantly increased at the peritubular dentin. Samples with TDg-NPs infiltration 24 h storage showed similar E'' throughout the resin-dentin interface (Fig. S2C). Those specimens, after load cycling, performed similar, but at the HL, E'' achieved the lowest values. After thermo-cycling the highest E'' values were obtained at the peritubular dentin (Table 1).

Respect to storage modulus E', samples of the control group 24 h storage and load cycled (Fig. S3A) exhibited higher E' at peritubular dentin than at intertubular dentin. After thermo-cycling, peritubular dentin achieved the highest E', but was not distinct to intertubular dentin. Demineralized dentin infiltrated with undoped NPs 24 h storage showed higher E' at peritubular dentin than at intertubular dentin. Both intertubular and peritubular dentin attained higher E' than both HL and BHL, after load cycling (Fig. S3C). After thermo-cycling, peritubular dentin attained the highest E' through the resin-dentin interface. After TDg-NPs, 24 h storage specimens showed the lowest E' at the hybrid layer. After load cycling, peritubular dentin exhibited higher E' than intertubular dentin. E' resulted similar after thermo-cycling (Table 1) (Fig. S3D).

Tan (δ) of control specimens load cycled did not change through the resin-dentin interface, but after thermo-cycling both hybrid layer and intertubular dentin attained the lowest values. Specimens treated with undoped NPs did not vary their tan (δ) regardless the typo of challenging

(Fig. 2B). Samples infiltrated with TDg-NPs, after load cycling, showed higher tan (δ) values at peritubular dentin than at intertubular dentin (Table 1) (Fig. S3C). The property map of the interface promoted by dentin infiltrated with undoped NPs and TDg-NPs both load cycled achieved the highest stored energy, mostly at HL and BHL in case of undoped NPs, and BHL and peritubular dentin in case of TDg-NPs and peritubular dentin (Figs. S3C, S3D).

3.2. Atomic Force Microscopy (AFM) analysis and collagen fibril diameter measurements

In the control group, resin dentin infiltration was observed at both peritubular and intertubular dentin at 24 h of storage. After load cycling, dentin tubules appeared occluded, but with mineralized peritubular dentin and some "bridging" processes. Located areas of mineralizarion were observed after thermo-cycling, and some other zones were not remineralized or scarcely mineralized (Fig. S4).

Some big processes of dentin remineralizarion were determined after 24 h of storage when demineralized dentin was infiltrated with undoped NPs. When these interfaces were load cycled, some samples showed breakdown zones at the interface, located at the limits between the peritubular and intertubular dentin, being parallel to the intratubular mineral deposits. Layered minerals which precipitated, preferentially, at intertubular dentin forming a consistent clump of crystals, were noticeable when dentin infiltrated with undoped NPs was thermo-cycled (Fig. 3).

Processes of intertubular and intratubular mineralization are taken place at interfaces of resin-dentin specimens infiltrated with TDg-NPs, and observed after 24 h of storage (Fig. 4A). Load cycling of these specimens permitted to perceive some stick-slip images, in radial direction, of nucleated minerals appearing as bridges and rod-like new mineral formations that surrounded the intratubular crystals. These precipitated crystals anchored the intratubular deposits of mineral to the peritubular dentin reducing the tubule entrances (Fig. 4B). These mineral beams remained attached, directly or indirectly through crack-bridging or bridging-like structures, likewise, when specimens were thermo-cycled (Fig. 4C).

Dentin specimens infiltrated with TDg-NPs showed the highest bandwidth among samples (Fig. 5). Most of the collagen fibrils exhibited their characteristics staggered pattern on the surface (Fig. S5).

4. Discussion

Resin-dentin interfaces promoted with both undoped NPs or TDg-NPs facilitated dentin crack formation after the dissipation of discrepant values of viscoelastic properties, but the presence of tideglusib favored the mineralization of the breakdown zones. Taking into account that both the loss modulus (E'') and the storage modulus (E') are implicated in the viscoelastic definition of the complex modulus (E *) and tan (δ), only E * and tan (δ) will be extensively discussed.

The highest values of complex modulus at both the hybrid layer (HL) and the bottom of the hybrid layer (BHL) were achieved when samples treated with undoped NPs or TDg-NPs were mechanically load cycled. Therefore, the first null hypothesis must be rejected. This greatest resistance to dynamic deformation, E * , that showed these two resin-dentin interfaces based on NPs dentin infiltration, is due to mineral precipitation at the intrafibrillar collagen of both HL and BHL [34]. Mineralization at the intrafibrillar collagen plays a crucial role in enhancing the mechanical properties performance [17]. The extrafibrillar minerals function as a granular material capable of withstand loads, especially in the lack of intrafibrillar mineralization. As a consequence, the second null hypothesis must, again, be rejected. Thereby, this absence is a crucial factor for predicting biomineralization [35]. Intermittent compressive loads have promoted mineralization in the present research and have enhanced alkaline phosphatase activity. Tissue alkaline phosphatase, existing at all mineralization locations, is a zinc-metalloenzyme that protects collagen [36], hydrolyzing a wide spectrum of phosphate monoesters [37]. This hydrolysis promotes apatite supersaturation [38], which facilitates the penetration of amorphous calcium phosphate into collagen. Calcium pyrophosphate plus non-crystalline amorphous and unstable complexes such as calcium phosphate finally are deposited under high phosphate concentrations around the collagen fibrils [39]. The present NPs perform as phosphate- and calcium- sequestering materials [11], functioning as biomimetic analogs that nucleate minerals [40] promoting dentin mineralization [12]. Polymeric NPs do not dissolve or reabsorb and are able to synthesize amorphous calcium phosphate layer at their surface, they endure bind to the collagen fibrils and are incorporated into the remineralized tissue [12]. The growth of calcium phosphate may be template by the carboxylate groups (COOH), as it has been beforehand proved in other diverse synthetic polymers [41,42]. The presence of NPs in the

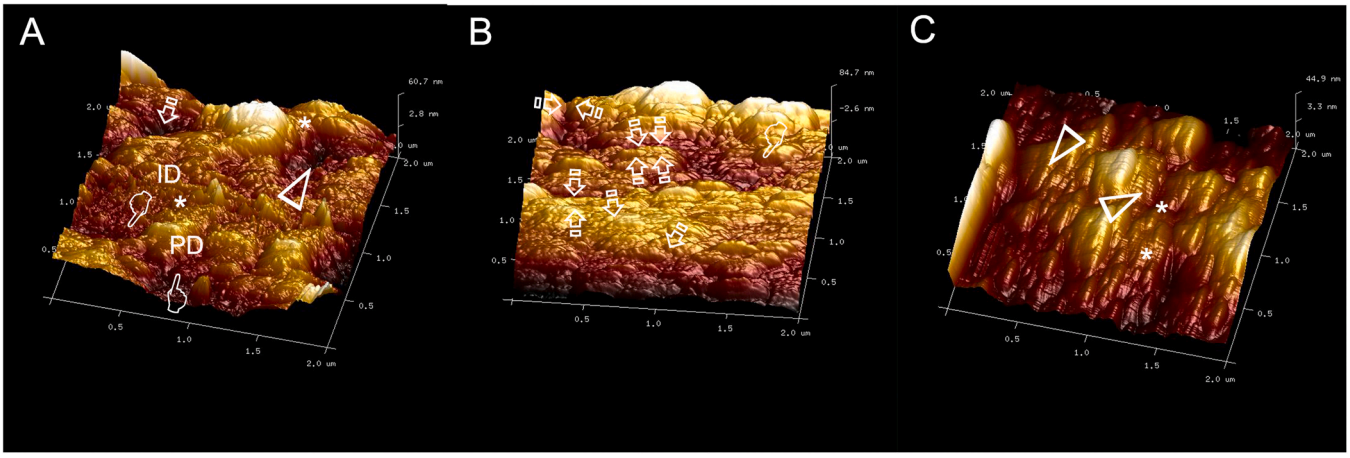

Fig. 3. Topography mapping of dentin obtained by AFM after applying undoped NPs, at 24 h time point (**A**). Some dentinal tubules appeared totally (pointers) or partially (arrowhead) mineral filled. Some other tubules were empty (arrow). Peritubular (PD) and intertubular dentin (ID) are clearly differentiated. Homogeneous transition between peritubular and intertubular dentin is evidenced (asterisks). (**B**), Nudes or mineral-integrated NPs, at both peritubular an intertubular locations, were observed (single arrows). The bond between the resin tag and the peritubular dentin was not perfect (pointer). The crack deflection and branching, around the peritubular cuff, may be observed at the dentinal wall of filled tubules (faced arrows) of dentin treated with undoped NPs, submitted to load cycling, showing clear neat stick-slip images as sight of energy dissipation. (**C**), Morphologically, homogeneous transition between peritubular and intertubular dentin characterizes the dentin surface (asterisks) in thermo-cycled specimens. Zones-free from breakdown were observed anywhere. Partially mineralized collagen fibbers may be observed (arrowheads).

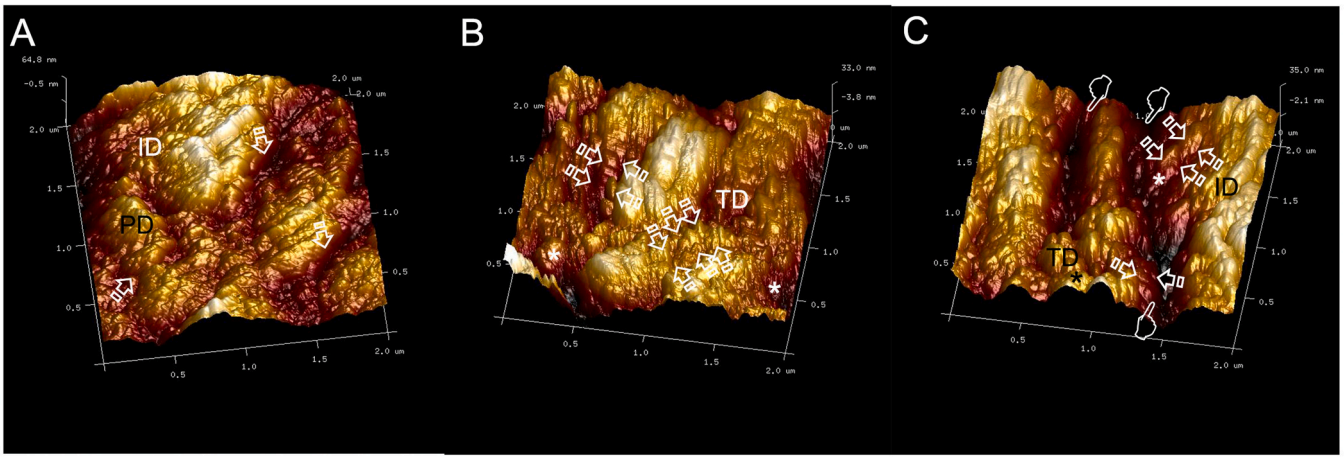

Fig. 4. Topography mapping of dentin obtained by AFM after applying TDg-NPs and 24 h time point (**A**). Peritubular (PD) and intertubular (ID) dentin mineralization is evident and open dentinal tubules are not observable (arrows). (**B**), After load cycling, intratubular dentin (TD) is totally occluding the dentinal tubules (asterisks). Stick-slip images and little rod-like minerals (faced arrows), as bridge-like structures indicating sight of energy dissipation at the limits between both PD and ID are present. (**C**), After thermocycling, NPs were scarcely observed, most of them covered by a layer of mineral (asterisks) that could not totally fill the tubule lumen (pointers). Little rod-like new minerals surrounding the intratubular crystals, directly or indirectly (faced arrows) anchored on the intratubular deposits of mineral to the peritubular dentin forming the "bridging" processes, limiting breakdown zones (asterisks).

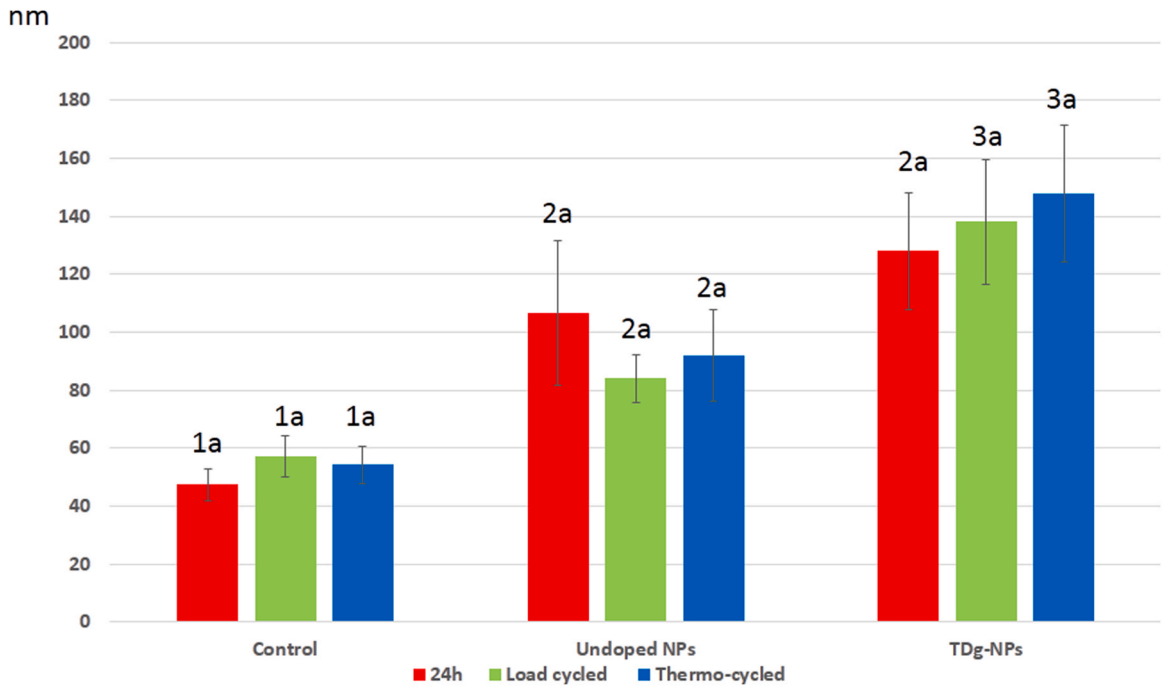

Fig. 5. Fibrils diameter at the different experimental resin-dentin interfaces. Identical lower case letters indicate no significant differences among samples treated with similar material. Identical numbers indicate no significant differences among distinct groups submitted to the same challenge. NPs, nanoparticles; TDg-NPs, Tideglusib doped NPs.

infiltrated collagen facilitated the dissipation of energy throughout the resin-dentin interface, as both hybrid layer and bottom of hybrid layer shared similar E * . TDg-NPs infiltration was dependent on the specific characteristics of the NPs [11,12]. Therefore, tested NPs have been previously characterized. They are spherical in shape and posse a hydrodynamic size of 250 nm (independently of their functionalization) [24,25]. Due to the negative zeta potential of NPs, they do not agglomerate [24].

Peritubular dentin has shown significantly higher E * than intertubular dentin (~1.5 fold) when undoped NPs were used and specimens were mechanically loaded (134.49 vs 87.62 GPa) (Table 1). Thereby, nano-DMA results have revealed, between peritubular and intertubular dentin, heterogeneity in the distribution of mechanical property after undoped NPs dentin infiltration in load cycled samples (Fig. 1A). Within the peritubular cuff, it means an increase of the energy concentration. Via deformation in radial and axial directions throughout a frictional pullout and bridging procedure, energy dissipation can occur at tubular structures. This process complies with mineral nucleation at micro and nano-scale planes [43]. The excess of energy, through cracking the dentin substrate, may be dissipated, interfering the energy transfer, affecting dentin remineralization and remodeling [44]. Red color reflected high E * values at peritubular locations (Fig. 1A). Clear circles of relevant values were exhibited by the complex modulus mapping, ranging from red to yellow intensities, being represented as diffuse

spheres septum-split in the majority of the figures. Therefore, discrepant properties of viscoelasticity at the distinct structures within the dentin, are a risk for the breakdown of this substrate, as in relatively high elastic modulus regions low modulus regions lead to energy concentration [2]. Both intertubular and peritubular dentin have been identified, scanning the interfaces, as the most pivotal junction in preventing crack generation and propagation throughout the boundary between the two different phases [45]. At the peritubular-intertubular dentin limit, the AFM topography image established the existence of a neat stick-slip image (Fig. 3B). These precipitates may be interpreted as frictional pullout, originated as a result of the discrepant viscoelastic outcomes between both structures [43].

On the contrary, when TDg-NPs were used to infiltrate dentin, after load cycling, E * at peritubular dentin was ~1.1 fold higher than intertubular dentin, but without significant differences (Table 1), revealing homogeneity in the mechanical feature distribution between intertubular and peritubular dentin, facilitating, thereby throughout their structures, the dissipation of the energy [43]. Nevertheless, tan (δ) at intertubular dentin of load cycled samples treated with TDg-NPs showed significant higher values (~2.9 fold) than at peritubular dentin. The ratio of the energy dissipated by the system to the energy stored in the system that enables its elastic recoil is equivalent to tan (δ). It assures how rightly a material can get rid of the energy [46]. The 3-D contour map of the tan (δ) distribution reflects this viscoelastic performance (Fig. 2C), showing close areas, i.e, intertubular and peritubular dentin, with opposite tan (δ) values. For recoil and/or failure, the lower tan (δ), the greater the proportion of energy available in the system [47]. Red intensity occupying most of the intertubular dentin area reflected this viscoelastic response (Fig. 2C). Intratubular mineral precipitation became potentially associated to the highest tan (δ) values, in the present study, promoting total occlusion of the dentinal tubules creating thick platforms of mineral (Fig. 4B). Dentin mechanical properties may be affected by occluded tubules. Microcracking of unfilled tubules (Fig. 3A, S2B) have been shown if compared with filled tubules, acting as uncracked-ligament bridging [44,48]. Minerals that precipitated are also observed at the intertubular-peritubular dentin limit (Fig. 4B). It has been established the existence of stick-slip figures at the intertubular-peritubular dentin edge, in specimens treated with TDg-NPs (Fig. 4). Besides, TDg-NPs infiltrated dentin, after mechanical (Fig. S5B) and thermal (Fig. S5C) cycling have promoted a significant increase of the fibrils width (Fig. 5), which commonly happens when cross-linking is maintained or intrafibrillar or functional mineralization exists [2,49]. TDg promotes dentin bridge formation [50]. At micro and nano-scale damage zones, nucleating minerals represented by these bridges of slipped mineralized dentin, might be influential in effectively resisting crack propagation and further fracture [44]. The stick-slips formation when TDg-NPs were applied on dentin, it is speculated that depends on the presence of tideglusib in the chemical formulation of the nanoparticle, which originated new crystals precipitation, making not possible to observe open dentinal tubules or demineralized collagen (Fig. 4). For this reason, it must be rejected the third null hypothesis. Surrounding the intratubular crystals and at peritubular dentin, these mineral precipitates were shown as multiple rod-like figures [38] (Figs. 4B, 4C), and they were absent in samples treated with undoped NPs analyzed after 24 h of storage (Fig. 3A), and also after thermo-cycling (Fig. 3C).

Different reasons have been advocated to explain the role of TDg in mineralization of hard tissues, as *i*) at the interface, the presence of the tested peptides may have inducted electrostatic attraction for the soluble ions, generating local increased of supersaturation zones that promote nucleation [51]; *ii*) distinct ligands that are existing in TDg such as hydroxyl groups, carboxyl, or carboxamide may bind to calcium [52]; *iii*) the collagen fiber stiffness may have increased due to the existence of the TDg loaded NPs in the resin-dentin interface, at the dentin extracellular matrix, thus causing a higher resistance to proteolysis of type I collagen fibers [14]; *iv*) besides, peritubular dentin preferentially absorbs some peptides, just the location where the remineralizing role has been advanced [53]. These findings are in agreement with the existence of new mineral deposits [9] at the resin-dentin interface and at the first 5–20 μm of the tubule dimensions [14].

At the HL, demineralized dentin infiltrated with TDg-NPs and thermo-cycled showed higher E * at the dentin interface than the specimens treated with undoped NPs. In general, load cycling promoted higher E * than thermo-cycling (Table 1) (Fig. 1B, 1C), with morphological implications (Fig. 4B, 4C). It confirms that mechanical loading facilitated intrafibrillar, biomimetic or functional remineralization [34], further than thermo-cycling. Noneless, after thermal cycling, the stimulation of alkaline phosphatase activity and proteins synthesis has been proved in vitro and in vivo [54], contributing to a reduction in exposed collagen [15], though associated to a non-functional mineralization [17].

The dentin specimens of the control group did show similar values of E * , regardless the different zones of the resin-dentin interface and the type of challenge (Table 1) (Fig. 1D). Nevertheless, the resistance to dynamic deformation, E * , attained generalized lower values than specimens treated with NPs-treated mechanically and thermo-mechanically loaded. Single Bond adhesive infiltrated at the phosphoric acid-conditioned dentin (control group) has been shown to exhibit high hydrophilicity at the resin-dentin interface, with excessive water adsorption and resin degradation. Even more, though adhesive resin infiltrated the intertubular dentin, many resin tags were absent, favoring nanoleakage and further degradation [55] (Fig. S2).

In relatively higher elastic modulus areas with low flexibility, lower storage modulus (E') regions with high flexibility conducts to stress concentration [47] and scarce dissipation of energy that favors breaking with failure at the resin-dentin interface [56]. Control specimens and those treated with TDg-NPs, after load cycling, attained an average increase of the storage modulus (E') at the peritubular dentin in comparison with the intertubular dentin of ~1.9 and 1.8 folds, respectively (Table 1), which was accompanied by mineral deposits at the peritubular-intertubular dentin limits, as confirmed both topographic mappings obtained by AFM. These precipitates appeared as bridge-like structures (Figs. S4A, 4B). A dispersed distribution of values with scarce resolution of the scans was revealed by the storage modulus map (Figs. S3A, S3D). Punctual red signals, simulating undefined circles of higher E', surrounded by lower E' results, were exhibited by the colored marks. Failure or fracture, from the stress distribution mapped by Misra et al. (2004) [2] could probably recruit at three different locations within the dentin and the hybrid layer (Fig. S1): *i*) at the interface between the adhesive tag and the peritubular dentin of the lumen wall due to stress concentration [57], *ii*), at the adhesive tag proximal to the hybrid layer due to stress concentration, *iii*), close to the bottom of the hybrid layer due to a high strain. Furthermore, if the bond between peritubular dentin and the adhesive tags is not perfect, as in Fig. 3B, then, within the hybrid layer the stress concentration zones are very likely to be focused, and the integrity of the resin-dentin interface will result damaged [58]. E' in samples treated with undoped NPs also showed higher average values at the peritubular dentin than at the intertubular dentin (~1.5 fold), but without significant differences (Table 1). Little rod-like minerals and stick-slip images were absent in specimens thermo-cycled (Fig. 3C).

This is to the best of our knowledge, the solely available results from AFM analysis and nano-DMA tests on tideglusib-doped NPs infiltrating the resin-dentin interface. Complementary techniques, such as SEM, TEM and XRD have yielded results that are in line with those obtained in the present research [14,59]. Thereby, this investigation poses the first try to measure the dentin ability to dissipate mechanical energy in function of the time-dependent behavior, in the presence of tideglusib. Nevertheless, the present study also has several shortcomings, as longer duration of thermal cycling, or selection of other bioactive ions and remineralizing agents into the chemical formula of the NPs. Other mechanical properties as fracture modulus and compressive modulus in

combination with studies of surface topography would have lengthened the message of this manuscript. The assessment of visible cracks would also contribute to the understanding of this mechanic-biology event. For an accurate mechanistic evaluation, the interpretation of the low-resolution of the mappings and the scanned images might introduce uncertainty concerning the contribution of the observed differences in the viscoelastic values at the resin-dentin interface among the tested groups. Future research should also be conducted to analyze by micro-computed tomography these rein-dentin bonded interfaces. The lack of this technique in this study may be considered as a limitation of the preset investigation.

5. Conclusions

The highest resistance to dynamic deformation at both the hybrid layer and the bottom of the hybrid layer was attained when specimens infiltrated with undoped nanoparticles or nanoparticles doped with tideglusib were mechanically load cycled, performing similar. Nano-DMA results revealed heterogeneity in the mechanical property distribution between peritubular and intertubular dentin after undoped nanoparticles dentin infiltration in samples submitted to load cycling, promoting frictional pullout between peritubular and intertubular dentin, due to stress concentration. Demineralized dentin infiltrated with nanoparticles doped with tideglusib and load cycled revealed homogeneity in the mechanical properties distribution between peritubular and intertubular dentin, facilitating, thereby, the dissipation of the energy throughout their structures when the complex modulus was assessed. Tan delta at both intertubular and peritubular dentin showed discrepant values, after load cycling of samples treated with TDg-doped nanoparticles, unveiling stick-slip images and multiple rod-like figures of mineral deposits mostly close to the peritubular dentin. This biomimetic mineralization occurred in collagen fibrils whose width resulted augmented after TDg infiltration.

Declaration of Competing Interest

The authors declare that they have no known competing financial interests or personal relationships that could have appeared to influence the work reported in this paper.

Acknowledgments

The present study was supported by Grant PID2020–114694RB-I00 funded by MCIN/AEI 10.13039/501100011033. This research is part of E. F-R.'s Ph.D. research study.Open Acess funding by Universidad de Granada / CBUA .

Appendix A. Supporting information

Supplementary data associated with this article can be found in the online version at doi:10.1016/j.dental.2024.09.005.

References

[1] Nakabayashi N, Pashley DH. Hybridization of Dental Hard Tissues. Quintessence Publishing Company; 1998.
[2] Misra A, Spencer P, Marangos O, Wang Y, Katz JL. Micromechanical analysis of dentin/adhesive interface by the finite element method. J Biomed Mater Res B Appl Biomater 2004;70B:56–65. https://doi.org/10.1002/jbm.b.30012.
[3] Toledano-Osorio M, Osorio R, Aguilera FS, Medina-Castillo AL, Toledano M, Osorio E, et al. Polymeric nanoparticles protect the resin-dentin bonded interface from cariogenic biofilm degradation. Acta Biomater 2020;111:316–26. https://doi.org/10.1016/j.actbio.2020.05.002.
[4] Hashimoto M, Ohno H, Sano H, Kaga M, Oguchi H. In vitro degradation of resin-dentin bonds analyzed by microtensile bond test, scanning and transmission electron microscopy. Biomaterials 2003;24:3795–803. https://doi.org/10.1016/s0142-9612(03)00262-x.
[5] Hebling J, Pashley DH, Tjäderhane L, Tay FR. Chlorhexidine arrests subclinical degradation of dentin hybrid layers in vivo. J Dent Res 2005;84:741–6. https://doi.org/10.1177/154405910508400811.
[6] Pashley DH, Tay FR, Yiu C, Hashimoto M, Breschi L, Carvalho RM, et al. Collagen degradation by host-derived enzymes during aging. J Dent Res 2004;83:216–21. https://doi.org/10.1177/154405910408300306.
[7] Breschi L, Mazzoni A, Nato F, Carrilho M, Visintini E, Tjäderhane L, et al. Chlorhexidine stabilizes the adhesive interface: a 2-year in vitro study. Dent Mater 2010;26:320–5. https://doi.org/10.1016/j.dental.2009.11.153.
[8] Carrilho MR, Tay FR, Donnelly AM, Agee KA, Tjäderhane L, Mazzoni A, et al. Host-derived loss of dentin matrix stiffness associated with solubilization of collagen. J Biomed Mater Res B Appl Biomater 2009;90:373–80. https://doi.org/10.1002/jbm.b.31295.
[9] Profeta AC, Mannocci F, Foxton R, Watson TF, Feitosa VP, De Carlo B, et al. Experimental etch-and-rinse adhesives doped with bioactive calcium silicate-based micro-fillers to generate therapeutic resin–dentin interfaces. Dent Mater 2013;29:729–41. https://doi.org/10.1016/j.dental.2013.04.001.
[10] Thadathil Varghese J, Islam F, Farrar P, Prentice L, Prusty BG. Multi-response optimisation analysis of material properties in dental restorative composites under the influence of thermal and thermomechanical stimuli - a 3D finite element study. J Mech Behav Biomed Mater 2024;150:106363. https://doi.org/10.1016/j.jmbbm.2023.106363.
[11] Besinis A, van Noort R, Martin N. Remineralization potential of fully demineralized dentin infiltrated with silica and hydroxyapatite nanoparticles. Dent Mater 2014;30:249–62. https://doi.org/10.1016/j.dental.2013.11.014.
[12] Osorio R, Osorio E, Medina-Castillo AL, Toledano M. Polymer nanocarriers for dentin adhesion. J Dent Res 2014;93:1258–63. https://doi.org/10.1177/0022034514551608.
[13] Neves VCM, Babb R, Chandrasekaran D, Sharpe PT. Promotion of natural tooth repair by small molecule GSK3 antagonists. Sci Rep 2017;7:39654. https://doi.org/10.1038/srep39654.
[14] Toledano M, Aguilera FS, Fernández-Romero E, Lagos AJ, Bonilla M, Lynch CD, et al. Dentin remineralization using a stimuli-responsive engineered small molecule GSK3 antagonists-functionalized adhesive. Dent Mater 2024;40:393–406. https://doi.org/10.1016/j.dental.2023.12.010.
[15] Balooch M, Habelitz S, Kinney JH, Marshall SJ, Marshall GW. Mechanical properties of mineralized collagen fibrils as influenced by demineralization. J Struct Biol 2008;162:404–10. https://doi.org/10.1016/j.jsb.2008.02.010.
[16] Li Y, Thula TT, Jee S, Perkins SL, Aparicio C, Douglas EP, et al. Biomimetic mineralization of woven bone-like nanocomposites: role of collagen cross-links. Biomacromolecules 2012;13:49–59. https://doi.org/10.1021/bm201070g.
[17] Bertassoni LE, Habelitz S, Kinney JH, Marshall SJ, Marshall Jr GW. Biomechanical perspective on the remineralization of dentin. Caries Res 2009;43:70–7. https://doi.org/10.1159/000201593.
[18] Poon B, Rittel D, Ravichandran G. An analysis of nanoindentation in linearly elastic solids. Int J Solids Struct 2008;45:6018–33. https://doi.org/10.1016/j.ijsolstr.2008.07.021.
[19] Hu S, Li J, Liu L, Dai R, Sheng Z, Wu X, et al. Micro/nanostructures and mechanical properties of trabecular bone in ovariectomized rats. Int J Endocrinol 2015;2015:e252503. https://doi.org/10.1155/2015/252503.
[20] Bar-On B, Daniel Wagner H. Elastic modulus of hard tissues. J Biomech 2012;45:672–8. https://doi.org/10.1016/j.jbiomech.2011.12.003.
[21] Ryou H, Romberg E, Pashley DH, Tay FR, Arola D. Importance of age on the dynamic mechanical behavior of intertubular and peritubular dentin. J Mech Behav Biomed Mater 2015;42:229–42. https://doi.org/10.1016/j.jmbbm.2014.11.021.
[22] Wilkinson TM, Zargari S, Prasad M, Packard CE. Optimizing nano-dynamic mechanical analysis for high-resolution, elastic modulus mapping in organic-rich shales. J Mater Sci 2015;50:1041–9. https://doi.org/10.1007/s10853-014-8682-5.
[23] Hayot CM, Forouzesh E, Goel A, Avramova Z, Turner JA. Viscoelastic properties of cell walls of single living plant cells determined by dynamic nanoindentation. J Exp Bot 2012;63:2525–40. https://doi.org/10.1093/jxb/err428.
[24] Toledano-Osorio M, Osorio E, Aguilera FS, Luis Medina-Castillo A, Toledano M, Osorio R. Improved reactive nanoparticles to treat dentin hypersensitivity. Acta Biomater 2018;72:371–80. https://doi.org/10.1016/j.actbio.2018.03.033.
[25] Medina-Castillo AL. Thermodynamic principles of precipitation polymerization and role of fractal nanostructures in the particle size control. Macromolecules 2020;53:5687–700. https://doi.org/10.1021/acs.macromol.0c00973.
[26] Sauro S, Mannocci F, Toledano M, Osorio R, Pashley DH, Watson TF. EDTA or H3PO4/NaOCl dentine treatments may increase hybrid layers' resistance to degradation: a microtensile bond strength and confocal-micropermeability study. J Dent 2009;37:279–88. https://doi.org/10.1016/j.jdent.2008.12.002.
[27] Han L, Grodzinsky AJ, Ortiz C. Nanomechanics of the cartilage extracellular matrix. Annu Rev Mater Res 2011;41:133–68. https://doi.org/10.1146/annurev-matsci-062910-100431.
[28] Hertz H. Über die Berührung fester elastischer Körper. J Reine Angew Math 1881;92:156.
[29] Macosko C.W. Rheology principles. Meas Appl 1994.
[30] Ryou H, Niu L-N, Dai L, Pucci CR, Arola DD, Pashley DH, et al. Effect of biomimetic remineralization on the dynamic nanomechanical properties of dentin hybrid layers. J Dent Res 2011;90:1122–8. https://doi.org/10.1177/0022034511414059.
[31] Pashley DH, Tay FR, Carvalho RM, Rueggeberg FA, Agee KA, Carrilho M, et al. From dry bonding to water-wet bonding to ethanol-wet bonding. A review of the interactions between dentin matrix and solvated resins using a macromodel of the hybrid layer. Am J Dent 2007:20.

[32] Habelitz S, Balooch M, Marshall SJ, Balooch G, Marshall GW. In situ atomic force microscopy of partially demineralized human dentin collagen fibrils. J Struct Biol 2002;138:227–36. https://doi.org/10.1016/s1047-8477(02)00029-1.
[33] Takeyasu K, Omote H, Nettikadan S, Tokumasu F, Iwamoto-Kihara A, Futai M. Molecular imaging of Escherichia coli F0F1-ATPase in reconstituted membranes using atomic force microscopy. FEBS Lett 1996;392:110–3. https://doi.org/10.1016/0014-5793(96)00796-x.
[34] Kinney JH, Habelitz S, Marshall SJ, Marshall GW. The importance of intrafibrillar mineralization of collagen on the mechanical properties of dentin. J Dent Res 2003;82:957–61. https://doi.org/10.1177/154405910308201204.
[35] Qin C, Brunn JC, Cadena E, Ridall A, Tsujigiwa H, Nagatsuka H, et al. The expression of dentin sialophosphoprotein gene in bone. J Dent Res 2002;81:392–4. https://doi.org/10.1177/154405910208100607.
[36] Patil P, Banga KS, Pawar AM, Pimple S, Ganeshan R. Influence of root canal obturation using gutta-percha with three different sealers on root reinforcement of endodontically treated teeth. An in vitro comparative study of mandibular incisors. J Conserv Dent 2017;20:241. https://doi.org/10.4103/JCD.JCD_233_16.
[37] Brosh T, Metzger Z, Pilo R. Circumferential root strains generated during lateral compaction with stainless steel vs. nickel-titanium finger spreaders. Eur J Oral Sci 2018;126:518–25. https://doi.org/10.1111/eos.12569.
[38] Toledano M, Osorio R, Osorio E, Medina-Castillo AL, Toledano-Osorio M, Aguilera FS. Ions-modified nanoparticles affect functional remineralization and energy dissipation through the resin-dentin interface. J Mech Behav Biomed Mater 2017;68:62–79. https://doi.org/10.1016/j.jmbbm.2017.01.026.
[39] Sui T, Sandholzer MA, Baimpas N, Dolbnya IP, Walmsley A, Lumley PJ, et al. Multiscale modelling and diffraction-based characterization of elastic behaviour of human dentine. Acta Biomater 2013;9:7937–47. https://doi.org/10.1016/j.actbio.2013.04.020.
[40] Watson TF, Atmeh AR, Sajini S, Cook RJ, Festy F. Present and future of glass-ionomers and calcium-silicate cements as bioactive materials in dentistry: biophotonics-based interfacial analyses in health and disease. Dent Mater 2014;30:50–61. https://doi.org/10.1016/j.dental.2013.08.202.
[41] Li Y, Aparicio C. Discerning the subfibrillar structure of mineralized collagen fibrils: a model for the ultrastructure of bone. PloS One 2013;8:e76782. https://doi.org/10.1371/journal.pone.0076782.
[42] Song J, Malathong V, Bertozzi CR. Mineralization of synthetic polymer scaffolds: a bottom-up approach for the development of artificial bone. J Am Chem Soc 2005;127:3366–72. https://doi.org/10.1021/ja043776z.
[43] Agrawal R, Nieto A, Chen H, Mora M, Agarwal A. Nanoscale damping characteristics of boron nitride nanotubes and carbon nanotubes reinforced polymer composites. ACS Appl Mater Interfaces 2013;5:12052–7. https://doi.org/10.1021/am4038678.
[44] Shinno Y, Ishimoto T, Saito M, Uemura R, Arino M, Marumo K, et al. Comprehensive analyses of how tubule occlusion and advanced glycation end-products diminish strength of aged dentin. Sci Rep 2016;6:19849. https://doi.org/10.1038/srep19849.
[45] Marshall GW, Habelitz S, Gallagher R, Balooch M, Balooch G, Marshall SJ. Nanomechanical Properties of Hydrated Carious Human Dentin. J Dent Res 2001;80:1768–71. https://doi.org/10.1177/00220345010800081701.
[46] Espino DM, Shepherd DE, Hukins DW. Viscoelastic properties of bovine knee joint articular cartilage: dependency on thickness and loading frequency. BMC Musculoskelet Disord 2014;15:205. https://doi.org/10.1186/1471-2474-15-205.
[47] Gopalakrishnan V, Zukoski CF. Delayed flow in thermo-reversible colloidal gels. J Rheol 2007;51:623–44. https://doi.org/10.1122/1.2736413.
[48] Koester KJ, Ager JW, Ritchie RO. The effect of aging on crack-growth resistance and toughening mechanisms in human dentin. Biomaterials 2008;29:1318–28. https://doi.org/10.1016/j.biomaterials.2007.12.008.
[49] Bertassoni LE, Habelitz S, Pugach M, Soares PC, Marshall SJ, Marshall GW. Evaluation of surface structural and mechanical changes following remineralization of dentin. Scanning 2010;32:312–9. https://doi.org/10.1002/sca.20199.
[50] Kornsuthisopon C, Tompkins KA, Osathanon T. Tideglusib enhances odontogenic differentiation in human dental pulp stem cells in vitro. Int Endod J 2023;56:369–84. https://doi.org/10.1111/iej.13877.
[51] Gungormus M, Tulumbaci F. Peptide-assisted pre-bonding remineralization of dentin to improve bonding. J Mech Behav Biomed Mater 2021;113:104119. https://doi.org/10.1016/j.jmbbm.2020.104119.
[52] Carvalho RG, Patekoski LF, Puppin-Rontani RM, Nakaie CR, Nascimento FD, Tersariol ILS. Self-assembled peptide P11-4 interacts with the type I collagen C-terminal telopeptide domain and calcium ions. Dent Mater 2023;39:708–17. https://doi.org/10.1016/j.dental.2023.06.004.
[53] Moussa DG, Kirihara JA, Ye Z, Fischer NG, Khot J, Witthuhn BA, et al. Dentin priming with amphipathic antimicrobial peptides. J Dent Res 2019;98:1112–21. https://doi.org/10.1177/0022034519863772.
[54] Lozupone E, Palumbo C, Favia A, Ferretti M, Palazzini S, Cantatore FP. Intermittent compressive load stimulates osteogenesis and improves osteocyte viability in bones cultured “in vitro. Clin Rheuma 1996;15:563–72. https://doi.org/10.1007/BF02238545.
[55] Tay FR, Pashley DH. Have dentin adhesives become too hydrophilic? J Can Dent Assoc 2003;69:726–31.
[56] Angker L, Swain MV. Nanoindentation: application to dental hard tissue investigations. J Mater Res 2006;21:1893–905. https://doi.org/10.1557/jmr.2006.0257.
[57] Misra A, Spencer P, Marangos O, Wang Y, Katz JL. Parametric study of the effect of phase anisotropy on the micromechanical behaviour of dentin–adhesive interfaces. J R Soc Interface 2005;2:145–57. https://doi.org/10.1098/rsif.2005.0029.
[58] Toledano M, Osorio E, Cabello I, Aguilera FS, López-López MT, Toledano-Osorio M, et al. Nanoscopic dynamic mechanical analysis of resin–infiltrated dentine, under in vitro chewing and bruxism events. J Mech Behav Biomed Mater 2016;54:33–47. https://doi.org/10.1016/j.jmbbm.2015.09.003.
[59] Toledano M, Fernández-Romero E, Osorio MT, Osorio E, Aguilera FS, Toledano R, et al. Investigation of the effect of Tideglusib on the hydroxyapatite formation, crystallinity and elasticity of conditioned resin-dentin interfaces. J Dent 2024;150:105334. https://doi.org/10.1016/j.jdent.2024.105334.

Supporting Information

Glossary
HL: hybrid layer.
BHL: bottom of the hybrid layer.
MMPs: matrix metalloproteinases.
NPs: nanoparticles.
GSK3: glycogen-synthase-kinase 3.
β-cat: β-catenin.
TDg: tideglusib.
AFM: atomic force microscopy.
Nano-DMA: nanodynamic mechanical analysis.
PD: peritubular dentin.
ID: intertubular dentin.
TDg-NPs: tideglusib doped nanoparticles.
SiC: silicon carbide.
SB: Single Bond.
SBFS: simulated body fluid solution.
E′: storage modulus.
E”: loss modulus.
*E**: complex modulus.

Figure S1.

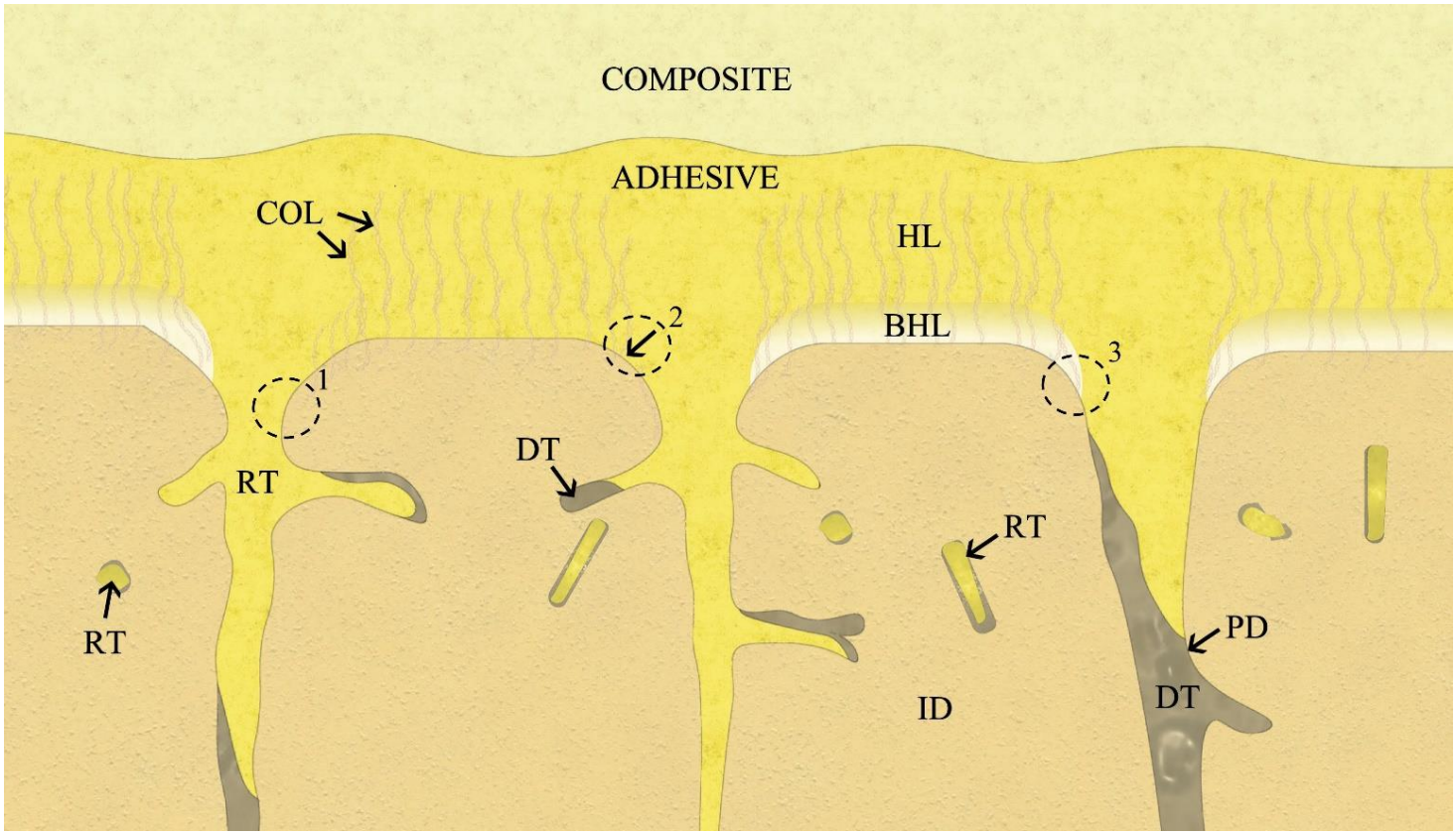

Figure S1. Representative image, in scheme, of the resin-dentin interface. Abbreviations: HL, Hybrid layer. BHL, Bottom of the hybrid layer. ID, Intertubular dentin. PD, Peritubular dentin. DT, Dentinal tubule. RT, Resin tag. Numbers 1, 2, 3: Locations where failure or fracture can be initiated, following the stress distribution mapped by Misra et al. (2004).

Figure S2.

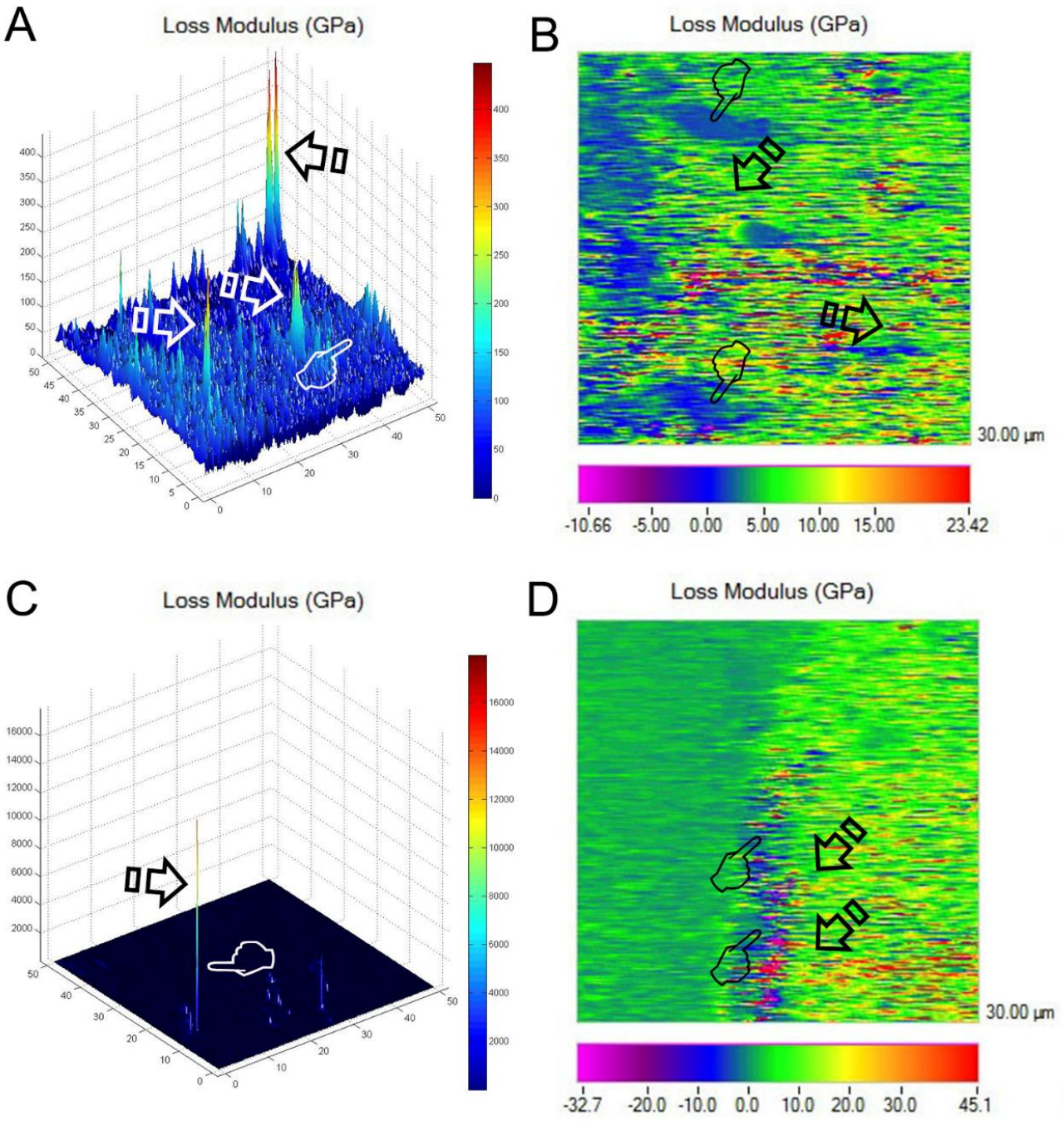

Figure S2. Scanning mode nano-DMA analysis of the map of the loss modulus at the control dentin load cycled (**A**), at dentin infiltrated with undoped nanoparticles (NPs) and load cycling (**B**), at dentin infiltrated with NPs doped with tideglusib (TDg-NPs) 24 h time point (**C**), and at dentin infiltrated with TDg-NPs load cycled (**D**). In the color scheme shown, the dark color corresponds to lower values of the locally measured loss modulus *E''*. The average ability to dissipate energy at the infiltrated dentin was achieved close to the green areas in load cycled specimens infiltrated with any kind of NPs (arrows), that corresponded with the bottom of the hybrid layer. Lower levels of dissipated energy were located around the blue areas, close to the hybrid layer (pointers).

Figure S3.

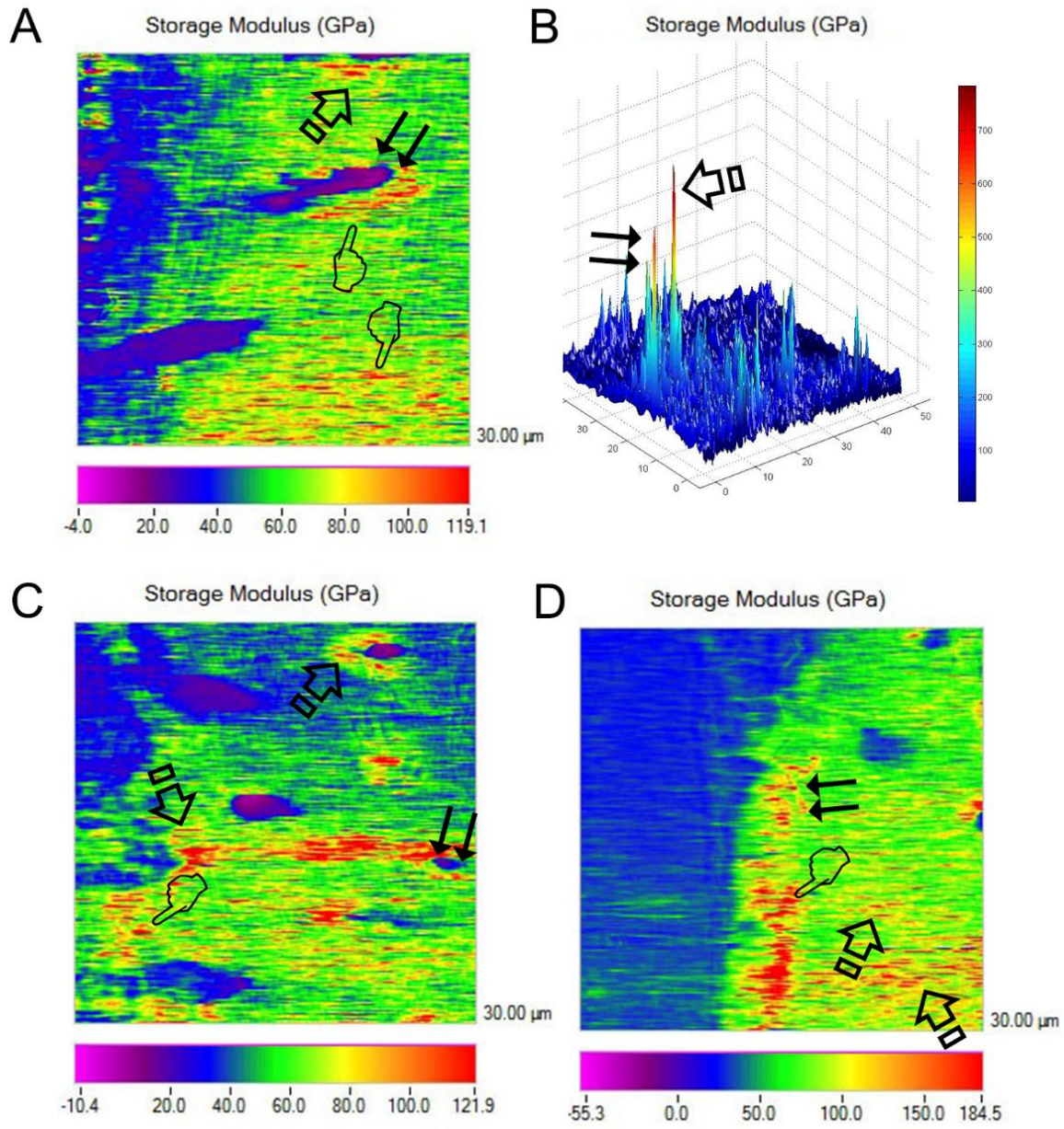

Figure S3. Scanning mode nano-DMA analysis of the map of the storage modulus at the Control dentin load cycled (NPs) (**A**), at dentin infiltrated with undoped NPs at 24 h (**B**), at dentin infiltrated with undoped NPs (NPs) load cycled (**C**) and dentin infiltrated with NPs doped with tideglusib (TDg-NPs) load cycled (**D**). In the color scheme shown, the dark color corresponds to lower values of the locally measured storage modulus E'. Punctual red signals surrounded by blue to green regions, and non-regular yellow to red collars were adverted in the scans, pointing out areas of maximum E' (arrows). Rings of a sharp yellow to red colors signalize maximum E' (pointers). Clear signals of high energy stored at peritubular dentin are shown (double arrows). Different zones with lower storage modulus surrounded by other areas with high storage modulus, may be observes, especially in control specimens load cycled (A) and those treated with TDg-NPs (D), where the excess energy may be dissipated through cracking the tissue.

Figure S4.

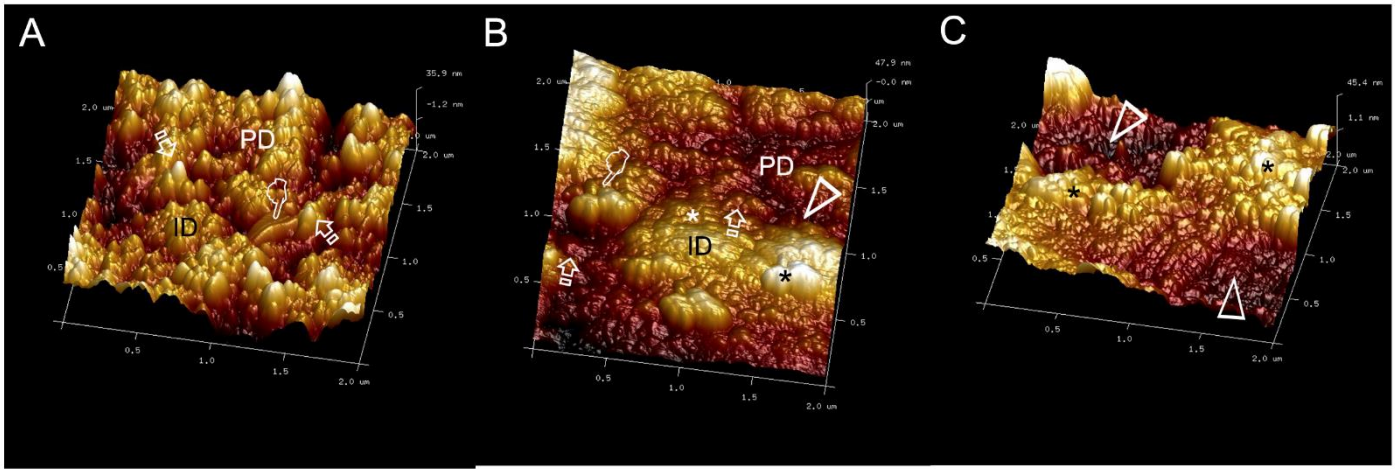

Figure S4. Topography mapping of dentin obtained by AFM after applying Single Bond adhesive (control group), at 24 h time point (**A**). Both peritubular (PD) and intertubular dentin (ID) were evidenced. Some partially demineralized collagen fibrils were observable (pointer), just where the resin failed to envelop the collagen network properly. These fibrils exhibited the characteristic periodical striation. Some minerals forming bridge-like structures appeared at the limits between the peritubular-intertubular dentin (arrows). (**B**), Some dentinal tubules appeared totally (pointer) or partially (arrowhead) mineral filled after load cycling of control specimens. Clear processes of intertubular (ID) and peritubular (PD) dentin mineralization and mineralized collagen fibers (arrows) are observed. Morphologically, homogeneous transition between peritubular and intertubular dentin characterizes the dentin surface at the present mapping (asterisks). Zones-free from breakdown were observed anywhere. (**C**), Dentin zones of mineralization (asterisks) and scarce remineralization (arrowheads) were determined at the mapping of control specimens thermo-cycled.

Figure S5.

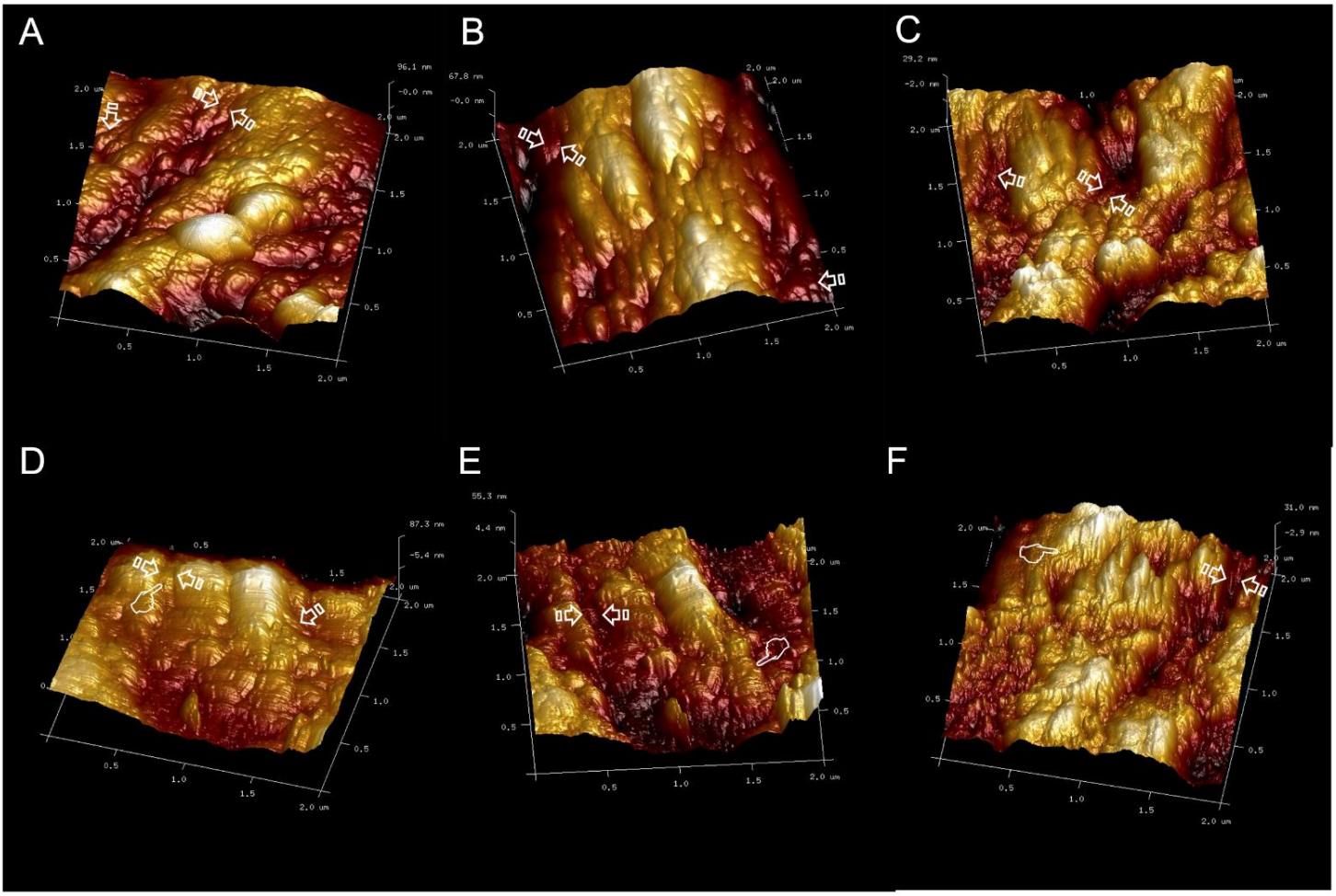

Figure S5: AFM plot image (2x2 µm) showing the bandwidth of the collagen fibrils in specimens treated with TDg-NPs at 24 h (**A**), after load cycling (**B**) and after thermo-cycling (**C**) are presented. Dentin samples infiltrated with undoped NPs submitted to thermo-cycling (**D**), load cycling (**E**) and a control specimen submitted to load cycling (**F**) are shown. Collagen fibrils (arrows), the diameter of these fibrils and the wider bandwidth (faced arrows) with the staggered pattern of collagen fibrils (pointers) are shown.

Journal of Dentistry 150 (2024) 105334

Contents lists available at ScienceDirect

Journal of Dentistry

journal homepage: www.elsevier.com/locate/jdent

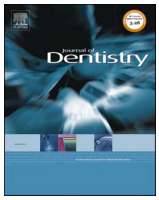

Investigation of the effect of Tideglusib on the hydroxyapatite formation, crystallinity and elasticity of conditioned resin-dentin interfaces

Manuel Toledano [a], Enrique Fernández-Romero [a,b], María T. Osorio [a], Estrella Osorio [a], Fátima S. Aguilera [a,*], Raquel Toledano [a], Raquel Osorio [a]

[a] University of Granada, Faculty of Dentistry, Colegio Máximo de Cartuja s/n, Granada 18071, Spain
[b] Medicina Clínica y Salud Pública PhD Programme, University of Granada, Granada 18071, Spain

ARTICLE INFO

Keywords:
Dentin
Microscopy
Remineralization
TEM
Tideglusib
XRD

ABSTRACT

Objectives: To investigate the effect of dentin infiltration with polymeric nanoparticles (NPs) doped with tideglusib (TDg) (TDg-NPs) on hydroxyapatite formation, crystallinity and elasticity of conditioned resin-dentin interfaces.

Methods: Dentin conditioned surfaces were infiltrated with NPs or TDg-NPs. Bonded interfaces were created, stored for 24 h and submitted to mechanical and thermal challenging. Resin-dentin interfaces were evaluated through nanoindentation to determine the modulus of elasticity, X-ray diffraction and transmission electron microscopy through selected area diffraction and bright-filed imaging.

Results: TDg-NPs provoked peaks narrowing after the diffraction-intensity analysis that corresponded with high crystallinity, with an increased modulus of Young after load cycling in comparison with the samples treated with undoped NPs. New minerals, in the group of TDg-NPs, showed the greatest both deviation of line profile from perfect crystal diffraction and dimension of the lattice strain, *i.e.*, crystallite, grain size and microstrain and 002 plane-texture. The new minerals generated after TDg-NPs application and mechanical loading followed a well defined lineation. Undoped NPs mostly produced small hydroxyapatite crystallites, non crystalline or amorphous in nature with poor maturity.

Conclusions: Tideglusib promoted the precipitation of hydroxyapatite, as a major crystalline phase, at the intrafibrillar compartment of the collagen fibrils, enabling functional mineralization. TDg-NPs facilitated nucleation of crystals randomly oriented, showing less structural variation in angles and distances that improved crystallographic relative order of atoms and maturity. Nanocrystals inducted by TDg-NPs were hexagonal prisms of submicron size. Thermal challenging of dentin treated with TDg-NPs have provoked a decrease of functional mineralization and crystallinity, associated to immature hydroxyapatite.

Clinical significance: New polycrystalline lattice formation generated after TDg-NPs infiltration may become correlated with high mechanical performance. This association can be inferred from the superior crystallinity that was obtained in presence of tideglusib. Immature crystallites formed in dentin treated with undoped NPs will account for a high remineralizing activity.

1. Introduction

In adhesive dentistry, adhesive resin infiltration is incomplete at the bottom of the hybrid layer [1] after dentin conditioning, generating a volume of demineralized and unprotected collagen. This collagen is vulnerable to the action of host-derived matrix metalloproteinases [2–4], causing degradation and jeopardizing the longevity of bonded restorations [5,6]. Thereby, a refined dentin adhesive formulation should protect and remineralize the dentin interfaces, triggering the natural bioactivity of the dentin substrate regardless the harsh conditions of the oral environment [7], as mechanic and thermal cyclic fatigue under functional stress [8]. The gain of minerals and the production of biogenic minerals are aimed to increase the clinical performance of adhesive restorations [9].

Engineered polymeric and hydrophilic nano-particles matrices (NPs) have been proposed as carriers of some biological drugs to manage

* Corresponding author.
E-mail address: fatimas@ugr.es (F.S. Aguilera).

https://doi.org/10.1016/j.jdent.2024.105334
Received 22 July 2024; Received in revised form 28 August 2024; Accepted 29 August 2024
Available online 30 August 2024

dentin remineralization [10]. In dentin, growth and mineral nucleation are regulated by the supramolecular organization of organic matrices through the interaction with the inorganic elements [11]. To potentiate the role of the organic phase, *i.e.*, collagen, dentin phosphophoryn-inspired phosphopeptides with (SSD3) motifs have been developed [12]. Furthermore, self-assembling elastin-like recombinamer (ELR) fibers have promoted collagen-like intrafibrillar, functional or biomimetic mineralization throughout ELR β-spiral structures [13]. Elastin-like recombinamers are an example of an extraordinary convergence of different properties that is not found in any other polymer system. These materials are highly biocompatible, stimuli-responsive, show unusual self-assembly properties and can include bioactive domains along the polypeptide chain [14]. To potentiate the role of the inorganic phase, *i.e.*, hydroxyapatite (HAp), polymeric NPs have been doped with several bioactive formulas, obtaining functional remineralization, improving crystallographic maturity, crystallinity and even refining maturity and secondary structure of dentin collagen [15,16]. Spencer et al. [17] have recently employed peptides to facilitate the remineralization of imperfect dentin matrices.

Neves et al. [18], proposed a biologically oriented methodology for dentin remineralization. They reported the performance of the glycogen-synthase-kinase 3 (GSK-3) in remineralization. This objective was achieved through the activation of Wnt/β-cat signaling as a prompt reaction to tissue damage [18]. Tideglusib (TDg) (NP-12, NPO3112), a small molecule GSK-3 inhibitor used in Alzheimer's disease treatment, has been postulated as a dentin repair agent, after doping nanostructured polymeric particles [19], in an attempt of drug repurposing. Drug repurposing is when, for existing drugs, new therapeutic applications are pointed out. Drug repurposing relies in stablishing new medical uses for already known drugs. It permits to simplify the testing safety [19].

An adequate delivery method easy to use is required for the clinical application of this drug [20]. As a delivery vehicle, hydrophilic nanostructured NPs have been used to synthesize TDg-NPs. Previously, other authors used collagen sponges [18], or a hyaluronic acid-base hydrogel [20]. Beforehand, it has been demonstrated that TDg-NPs enhanced osteoblasts proliferation, increasing mineral nodules formation and alkaline phosphatase production. The detrimental effect of bacterial lipopolysaccharide has been counteracted by avoiding the decrease on mineralization and osteoblasts proliferation. An overexpression of bone-promoting and proliferative genes on human primary osteoblasts have also been achieved [21].

Dentin constitutes the bulk of the tooth being a mineralized connective tissue. It is constituted by 70 % inorganic HAp crystal by weight or 50 % HAp crystal by volume, forming sub-micrometer to nanometer-sized carbonate rich, calcium deficient apatite crystallites (~5 × 30 × 100 nm) [22]. X-ray diffraction reflections (XRD) analyzes the hierarchical structure of dentin, by interpreting the diffraction lines that depend on the crystallite size and form, and the lattice microstrain [9].

The arrangement at higher size scales, to guide mineralization, of individual nanocrystals is determined by their both physical stability and mechanical performance [11]. The mechanical properties are affected by the morphology and dimensions of the formed HAp crystallites [23], pre-determining its clinical service. The dimensions of crystallites have been associated to mineralization, crystallinity and maturity of the formed HAp [24]. The orientation and alignment, *i.e.*, lineation, of the apatite crystals (texture) and the strain distribution will influence the mechanical properties of macroscopic dentin [25]. XRD analysis can also be used to perform quantitative measurements of both the lattice strain and the crystal orientation on the tooth surface [26]. The preferred orientation of crystallites, and the deviation of line profile from perfect crystal diffraction will determine the grain size. Microstrain is related with the dimension of the lattice strain [27]. High-resolution structural information along with crystallographic information when combined with Selected Area Electron Diffraction (SAED), is provided by Transmission Electron Microscopy (TEM). Combined with TEM, Energy-Dispersive X-ray Spectroscopy (EDS) may also be used. Accompanied techniques, as scanning TEM (STEM), and Fast Fourier Transform (FFT) when using High Resolution TEM (HRTEM) are commonly also employed.

The purpose of this study was to investigate the effect of dentin infiltration with polymeric nanoparticles doped with tideglusib (TDg-NPs) on hydroxyapatite formation, crystallinity and elasticity of conditioned resin-dentin interfaces. The null hypotheses to be tested were that TDg-NPs infiltration, into conditioned dentin, (1) do not affect the modulus of elasticity at the resin-dentin interface and (2) do not provoke differences in crystal structure, morphology, crystallinity and texture of dentin.

2. Material and methods

2.1. Production of nanoparticles

The process of obtaining NPs applied the use of the polymerization precipitation method, which controlled the precipitation facilitated by a thermodynamic approach. Specifically, the Flory-Huggins model, based on Hansen's solubility parameters, was employed. This model focused on the interactions among solvent molecules and the growth of polymer chains through hydrogen, polar bonding, and dispersion forces [28]. The backbone monomer for NP design was 2-hydroxyethyl methacrylate, with methacrylic acid serving as the functional monomer, and ethylene glycol dimethacrylate employed as the cross-linker. Subsequently, half of the produced NPs were loaded with a peptide, tideglusib (Sigma-Aldrich; Chemie, Riedstr, Germany). The NPs loading process was conducted by the immersion of 100 mg of NPs in 1 mL of 0.0017 mg/mL TDg solution for 2 h at room temperature under constant shaking (12 rpm) in a rotator Orbit 300,445 (JP Selecta; Barcelona, Spain). Then, the NPs were left until the solvent was completely evaporated, ensuring that all the TDg remains onto the NPs. Two types of NPs were obtained, undoped NPs and TDg-NPs.

2.2. Preparation of specimens for the bonding procedure, mechanical and thermal challenging

Thirty-six unerupted human third molars, preserved at 4 °C in a 0.5 % chloramine T solution for no more than a month, were used for this study. Prior to their involvement, subjects provided informed consent, aligning with the Declaration of Helsinki and adhering to good clinical practice guidelines. The study received ethical approval from the local Ethics Committee (1906/CEIH/2020).

The teeth were horizontally sectioned just below the dentin-enamel junction to expose sound dentin surfaces. These surfaces were then flatly polished to create a clinically relevant smear layer, utilizing 180-grit silicon carbide –SiC- abrasive paper. Subsequently, the dentin surfaces underwent etching (with 37 % phosphoric acid, during 15 s), followed by rinsing and drying. Random allocation of experimental teeth ($n = 12$) to one of three groups was achieved through computer-generated randomization, facilitated by http://www.randomizer.org/form.htm. The allocation remained concealed in sealed envelopes until the time of bonding procedure. Just an ethanol solution was applied (30 s) (i), or an ethanol suspension of undoped-NPs (ii), and TDg-NPs (iii) (10 mg/mL) in each of the experimental groups ($n = 12$), acting as primers. Ethanol was then evaporated for 30 s and, finally, Single Bond (SB) resin (3 M ESPE; St. Paul, MN, USA) was applied according to the manufacturer's instructions, to fulfill the conventional adhesive protocol. Standard resin-dentin interfaces were, therefore, generated (Fig. 1). The sample preparation was conducted by one researcher, and a uniform adhesion protocol was implemented by a different researcher. For each tooth, a composite build-up (5 mm high) with Tetric EvoCeram (Ivoclar-Vivadent; Schaan, Liechtenstein) was performed using the incremental technique, in five 1 mm resin layers. The light-curing process was carried out with a Bluephase G2 polywave light-emitting diode light-

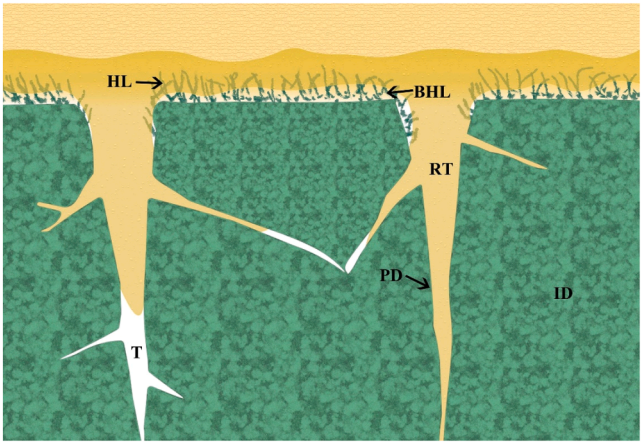

Fig. 1. Representative image, in scheme, of the resin-dentin interface. Abbreviations: HL, Hybrid layer; BHL, Bottom of the hybrid layer; ID, Intertubular dentin; PD, Peritubular dentin; T, Dentinal tubule; RT, Resin tag.

polymerizing unit (Ivoclar Vivadent; Schaan, Liechtenstein) at 1500 mW/cm^2 for 20 s. The output intensity was monitored with a Bluephase meter curing radiometer (Ivoclar Vivadent; Schaan, Liechtenstein), ensuring a minimal output intensity of 1500 mW/cm^2 for all experiments. The restored teeth were stored in a dark environment and submerged in simulated body fluid solution (SBFS) for 24 h.

Three experimental groups were established, 1) control group, 2) undoped NPs and 3) TDg-NPs, with 12 molars per group. The teeth were then randomly assigned to three sub-groups, in order to apply different challenging methods: Restored teeth were (1) stored in SBFS for 24 h, (2) load cycled with a sine wave form for 24 h (259,200 cycles, 3 Hz) (S-MMT-250NB, Shimadzu; Tokyo, Japan) proceeding as in Sauro et al. [29], and (3) thermal cycled (100,000 cycles/ 5 °C and 55 °C) in a Thermocycler 1100 (SD-Mechatronik; Westerham, Germany); the procedure took approximately three months and it was performed with the teeth immersed in distilled water [19]. Finally, each tooth was sectioned into at least three resin–dentin slabs and polished using ascending grit SiC abrasive papers (#1200 to #4000) on a water-cooled polishing device (Buehler-MetaDi, Buehler; Lake Bluff, IL, USA). The specimen preparation was concluded with a final ultrasonic cleaning (5 min).

2.3. Nanoindentation testing

A total of ten slabs from each subgroup (at least two from each tooth) were submitted to nanoindentation testing. The modulus of Young was performed using a Hysitron Ti 950 nanoindenter (Hysitron; Minneapolis, MN, USA). The nanoindenter was a Berkovich (three-sided pyramidal) diamond indenter tip (tip radius ~20 nm). It was calibrated against a fused quartz sample using a quasistatic force setpoint of 5 μN. On each slab, three indentation lines 15 ± 5 μm from each other were made in different mesio-distal positions along the interface. Four indentations were performed in each straight line starting from the top of hybrid layer down to the underlying intertubular dentin in order to evaluate changes in the modulus of Young (Ei) of the resin-dentin interface. The apical-occlusal distance between each indentation was kept constant (5 ± 1 μm) by adjusting the distance intervals steps. Indentations were executed with a load of 4000 nN and a time function of 10 s. The procedure was performed in a hydrated condition by the application of a layer of ethylene glycol over the specimen surface, preventing water evaporation during a typical 25-to-30-min scanning period [30]. Sample size calculation was performed using Macro!NSize V2010.06.30 (confidence level 95 %, power of analysis 80 %). Attained modulus of Young tooth dependency was discarded. Mean modulus of Young in each experimental group were calculated in GPa and tested by analysis of variance including analysis of interactions ($p < 0.05$). Type of NPs (control, undoped NPs, TDg-NPs) and challenging procedure (24 h storing, mechanical loading, thermocycling) were considered as the independent factors. ANOVA and Student-Newman-Keuls for post hoc comparisons were used. Significance was set at $p < 0.05$. HSD Tukey test was used to compute adjusted exact P values of multiple comparisons.

2.4. X-Ray diffraction (XRD) analysis

A convenience sample was randomly selected from the dentin slabs for each group and submitted to XRD analysis. The X-ray micro-diffractometer (μXRD^2) used in this study was a single crystal diffractometer with a 2-dimensional detector system Cmos Photon 100 (Bruker-D8 Venture; Wien, Austria), equipped with kappa geometry based goniometer 2D Detector and XRD 2D Scan software. The X-ray beam (Cu Kα line, λ = 1.5418 Å) was generated by a Cu Microforms source Iμs and generator settings of 50.00 kV/1.00 mA were employed. The 2D position sensitive detector had 1024 × 1024 pixels. Both the starting and ending positions were: distance, 40.00 mm; 2θ: 40.00°; Omega: 20.00°; Phi: 270.00°; Chi: 50.00° Wavelength of 1.54184 Å (Cu). The distance from the sample to the detector was 40.00 mm, 2θ scanning angle range was from 10° to 80° All measurements were performed at room temperature (25 °C ± 2 °C) and an exposure time of 60 s. A voltage of 50.00 kV, a current of 1.000 mA with the anode of Cu were used for the generator. Three images were obtained from each specimen. The final refined μXRD2 profile and Debye-Scherrer rings image (pole image) of each group were obtained by accumulating all X-ray energies (wavelengths) in a single image. The intensities concentrated in arcs within the Debye diffraction rings (corresponding to specific d-spacing/ diffraction lines) were integrated to obtain a unidimensional scan (i.e., 2Theta pattern). The results were commonly presented as maximum positions in 2θ (x) and X-ray counts (intensity) (y) in the form of an x-y chart. The XRD2DScan software [31] was employed, as it allows all images to be integrated into a representative single image. The whole batch of the measured frames was loaded and all frames were processed; then a single file was created. This file contained the variation of intensity along the Debye ring associated with the selected reflection as a function of angle, for every processed frame. All this information was used to construct the final refined μXRD2 profile and pole image. Finally, data were analyzed using GNU/Octave software (https://octave.org/).

From the X-ray micro-diffraction pattern, the size and the preferred orientation of the crystallites were calculated [24,32]:

$$d = \frac{K\lambda}{\beta \cos\theta} \quad (1)$$

In this equation d is the mean size of the crystallites, K is a dimensionless shape factor, with a value close to unite –note that in the case of dentin, $K \approx 0.94$ [24], and β is the peak full width at half maximum (FWHM) of the line broadening. In order to obtain the crystallite length and width, this formula was used for the line broadenings corresponding to 002 (H) and 310 (L) reflections, respectively (see data in Table 1). In order to determine the interaction of variables with the HAp structure the ratio H/L [9] was also measured. The preferred orientation of the crystallites (texture) from the following intensity ratios [24]:

$$R_{hkl} = k_{hkl}\frac{I_{211}}{I_{hkl}} \quad (2)$$

In this expression I_{211} and I_{hkl} are the intensities corresponding respectively to line reflections 211 and *hkl*, and

$$k_{hkl} = \frac{I^{st}_{hkl}}{I^{st}_{211}}, \quad (3)$$

where the superscript *st* refers to intensities calculated according to the JCPDS card [24,33]. Diffraction was acquired on an imaging plate, and from those digital plate data the intensity relationship was obtained using Origin Pro 2015 (Origin Lab; Northampton, MA, USA). The

Table 1
Micro-X-ray diffraction pattern analysis approach of the different test groups sorted by dentin treatment (Control, Undoped-NPs and TDg-NPs) and by challenges (24 h in SBFS, after Load Cycling and after Thermocycling) corresponding to 002 (H) and 310 (L) reflections.

Dentin Treatment	Challenge or Storage method	002 plane					310 plane					*H/L*
		FWHM	*H*: Scherrer equation (nm) (τ)	Scherrer-Wilson equation (nm)	Microstrain %	R_{hkl}	FWHM	*L*: Scherrer equation (nm) (τ)	Scherrer-Wilson equation (nm)	Microstrain %	R_{hkl}	
	24 h SBFS	0.0074	19.99	19.48	1.35×10^{-6}	0.607	0.0229	6.74	6.35	1.2×10^{-5}	1.265	2.96
Control	Load Cycling	0.0083	17.84	17.40	1.69×10^{-6}	0.612	0.0229	6.72	6.33	1.2×10^{-5}	1.219	2.65
	Thermocycled	0.0082	18.15	17.70	1.63×10^{-6}	0.654	0.0229	6.72	6.33	1.2×10^{-5}	1.147	2.70
	24 h SBFS	0.0080	18.69	18.22	1.54×10^{-6}	0.561	0.0233	6.61	6.23	1.3×10^{-5}	1.140	2.83
Undoped	Load Cycling	0.0076	19.46	18.97	1.42×10^{-6}	0.560	0.0219	7.02	6.62	1.1×10^{-5}	1.286	2.77
	Thermocycled	0.0077	19.28	18.80	1.45×10^{-6}	0.704	0.0212	7.26	6.84	1.1×10^{-5}	1.367	2.66
	24 h SBFS	0.0086	17.25	16.82	1.81×10^{-6}	0.580	0.0244	6.30	5.94	1.4×10^{-5}	1.165	2.74
TDg-NPs	Load Cycling	0.0067	22.20	21.65	1.09×10^{-6}	0.778	0.0133	11.56	10.89	0.4×10^{-5}	1.134	1.92
	Thermocycled	0.0074	20.20	16.69	1.32×10^{-6}	0.612	0.0214	7.21	6.80	1.1×10^{-5}	1.200	2.80

Abbreviations: FWHM, Full-width half-maximum; NPs: undoped/unloaded nanoparticles; SBFS, simulated body fluid solution; R_{hkl}: Ratio of preferred orientation of crystallites (or texture); TDg: Tideglusib.

diffraction peak positions were described to HAp in the JCPDS Card 9–432. The relative intensity (%) of the hydroxyapatite diffraction planes were also obtained.

2.5. Transmission electron microscopy (TEM) analysis, selected area diffraction and bright-field imaging

A Fei Titan 80–300 TEM-STEM microscope was used to analyze the specimens, operating at 200 kV, and equipped with a Cs CEOS image corrector and a high brightness electron gun (X-FEG) (ThermoFisher Scientific; Waltham, USA). The microscope is integrated with 4 energy dispersive X-ray spectroscopy (EDS) detectors (FEI microanalysis Super X) as well as a high angle annular dark field detector (HAADF). Selected area electron diffraction (SAED) and Bright-field (BF) patterns were also recorded. Scanning TEM (STEM) bright-field images were performed using the Super-X EDS system in the TEM [16]. To characterize each experimental group, selected mineral areas of interest were displayed by the high-resolution transmission electron (HRTEM) imaging. A FEI Ceta camera was used for HRTEM images. The Fei Titan microscope was employed also to acquire two-dimensional compositional elemental mappings of the specimen using image drift correction and 200 kV of accelerating voltage. The map acquisition and two-dimensional compositional elemental analysis were completed within 5 min. STEM images from HAADF were acquired. All these images and the obtained maps were processed using the VELOX software package (ThermoFisher Scientific; Waltham, USA) [34]. In HRTEM imaging, Fast Fourier transforms (FFT) were computed from selected image areas.

3. Results

3.1. Nanoindentation testing, modulus of young

Mean Young's modulus (*Ei*) values (GPa) and SD attained at the different indentation zones in the experimental groups, are exposed in Fig. 2.

At the hybrid layer, the highest values of elasticity, among groups, were achieved when undoped NPs-infiltrated dentin after 24 h, TDg-NPs-infiltrated dentin after 24 h, and mechanically loaded-dentin infiltrated with TDg-NPs were analyzed, ranging from 12.49, SD 2.4 (undoped-NPs, 24 h) to 14.18, SD 1.4 GPa (TDg-NPs load cycled). The lowest Young's modulus was obtained by the control group at 24 h (1.73, SD 0.5 GPa). Among the thermo-cycled groups, samples treated with TDg-NPs showed the highest modulus of elasticity (11.54, SD 0.9 GPa)(Fig. 2).

At the bottom of the hybrid layer, samples treated with both TDg-NPs after 24 h (17.71, SD 1.0 GPa) and those submitted to mechanical loading (17.12, SD 1.6 GPa) attained the highest *Ei* values. The lowest *Ei* values were shown by the control (SB) group at 24 h (1.41, SD 0.2 GPa) and thermocycled (2.17, SD 0.7 GPa). The rest of the groups achieved intermediate values ranging from 9.28, SD 2.2 GPa (undoped NPs thermocycled) to 15.14, SD 2.0 GPa (control mechanically loaded) (Fig. 2).

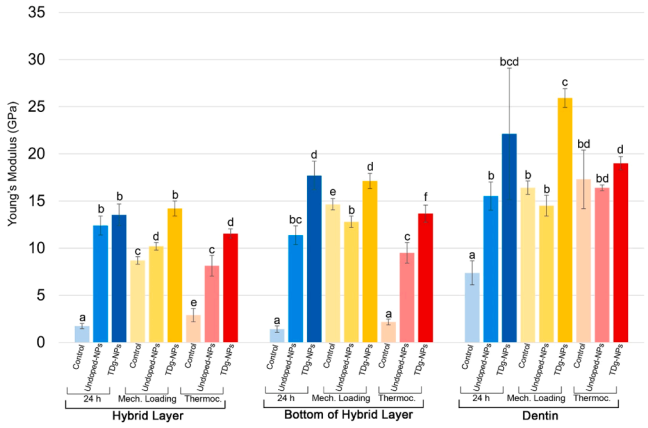

Fig. 2. Mean and standard deviation (SD) values of Young Modulus (GPa) in the different test groups sorted by challenges, 24 h in SBFS -Control-, after Load Cycling and after Thermocycling, in different zones of interfaces (Hybrid layer, bottom of Hybrid layer and Dentin). Identical lowercase means no significant difference among distinct NPs at the experimental interfaces. Student-Newman-Keuls ($p < 0.05$) was used for *post hoc* comparisons. Abbreviations: NPs, nanoparticles; LC, Load cycled; SBFS, simulated body fluid solution; TC, Thermocycled.

At intact dentin, groups where TDg was present and the control group thermocycled showed the highest *Ei*, ranging from 17.35, SD 6.1 GPa (control group thermocycled) to 25.92, SD 1.9 GPa (dentin infiltrated with TDg-NPs mechanically loaded). The intact dentin, in the control group after 24 h showed the lowest modulus of elasticity (7.22, SD 2.5 GPa)(Fig. 2).

Adjusted exact P values after multiple comparisons are displayed in the Table 2.

3.2. X-Ray diffraction (XRD) analysis

μXRD[2] analysis profiles of dentin showed that the physical broadening full width half maximum (FWHM) of peaks at 002 reflection, parallel to the *c*-axes, (2θ, 25.900°; centroid peak position θhkl, 0/0/−2; I, 10,977,386) reflection, after noting data plotted by the reduced full width and extended height at half maximum of the phosphate band, was

Table 2
Adjusted exact P values after multiple comparisons of mean Modulus of Young, computed by HSD Tukey test. Significance was considered if $p < 0.05$.

	Control			Undoped-NPs			Tideglusib-NPs		
HL	24h	Mech	Thermo	24h	Mech	Thermo	24h	Mech	Thermo
24h	1	0.000	0.04	1	0.03	0.000	1	0.47	0.04
Mech.		1	0.000		1	0.04		1	0.000
BHL	24h	Mech	Thermo	24h	Mech	Thermo	24h	Mech	Thermo
24h	1	0.000	0.11	1	0.17	0.07	1	0.71	0.000
Mech.		1	0.0001		1	0.001		1	0.000
DENTIN	24h	Mech	Thermo	24h	Mech	Thermo	24h	Mech	Thermo
24h	1	0.000	0.000	1	0.5	0.7	1	0.15	0.26
Mech.			0.87		1	0.1		1	0.04

	24h			Mechanical Loading			Thermocycling		
HL	Ctrl	Undop	TDg	Ctrl	Undop	TDg	Ctrl	Undop	TDg
Control	1	0.0001	0.000	1	0.02	0.000	1	0.000	0.000
Undoped		1	0.20		1	0.000		1	0.000
BHL	Ctrl	Undop	TDg	Ctrl	Undop	TDg	Ctrl	Undop	TDg
Control	1	0.000	0.000	1	0.03	0.001	1	0.000	0.000
Undoped		1	0.000		1	0.000		1	0.000
DENTIN	Ctrl	Undop	TDg	Ctrl	Undop	TDg	Ctrl	Undop	TDg
Control	1	0.001	0.000	1	0.06	0.000	1	0.86	0.57
Undoped		1	0.009		1	0.000		1	0.28

Abbreviations: NPs, nanoparticles; Mech, mechanical loading; Thermo, thermocycling; Ctrl, control; Undop, undoped nanoparticles; TDg, Tideglusib nanoparticles; HL, hybrid layer; BHL, bottom of the hybrid layer.

lower in dentin samples treated with TDg-NPs and load cycled (0.0067) when compared with the rest of the studied groups (Table 1). Peaks at 310, perpendicular to the *c*-axis, (2θ, 40.127° centroid peak position θhkl, −3/1/0; I, 1,380,390), after load cycling, dentin treated with TDg-NPs presented the lowest FWHM (0.0133), denoting a crystalline status (Table 1) and high crystallographic purity (Fig. 3). At 24 h of storage, dentin surfaces treated with Single Bond (control group) achieved the lowest FWHM among the different groups, *i.e.*, the highest crystallinity, at both 002 (0.0074) and 310 (0.0229) peaks (Table 1) (Figure S1). Similar trend was followed by the undoped NPs infiltrated dentin groups, where those 24 h storage attained the lowest crystallinity at both 002 and 310 planes (0.0080 and 0.0236, respectively Table 1) (Figure S2). Dentin specimens treated with TDg-NPs 24 h storage showed the highest FWHM among groups, at both 002 plane (0.0086) and at 310 plane (0.0244), denoting the lowest crystallinity, *i.e.*, the highest amorphous status (Fig. 3, insets A and B). When TDg-NPs and load cycling were applied, after detecting the reflection at 211 peak (Fig. 3A) and the diffraction ring equivalent to 211 and 112 planes (Fig. 3C), it may be distinguished higher crystallinity values than those obtained in the other groups (Table 1).

Table 1 presents a qualitative approximation of the size of the coherently scattering domain (*i.e.*, the crystallite size). The longest

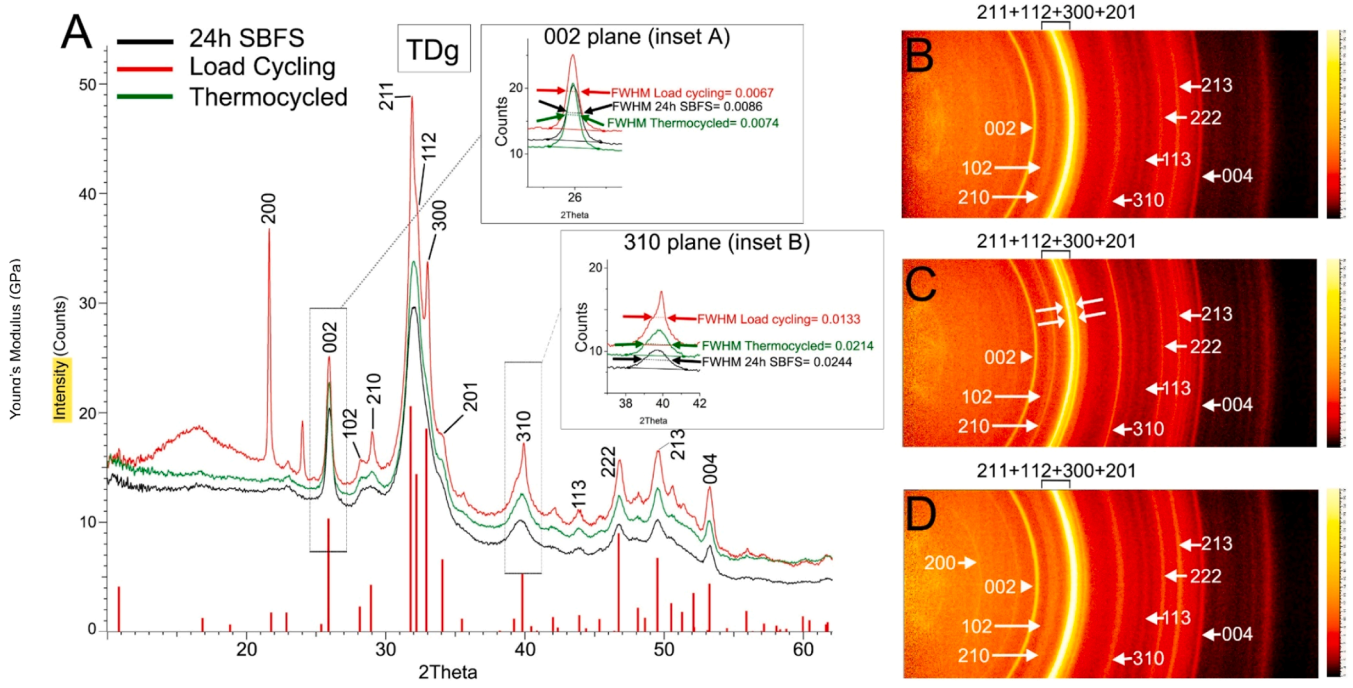

Fig. 3. Refined μXRD^2 profiles of the samples treated with TDg-NPs, after load cycling and after thermo-cycling (**A**). Vertical bars represent hydroxyapatite (HAp) peaks derived 2-theta versus diffraction-intensity relationships in the correspondence JCPDS cards. Inset A, 002 plane. Inset B, 310 plane. FWHM: Full Width at Half Maximum. Debye-Scherrer rings of the TDg-NPs group at 24 h storage (**B**), after load cycling (**C**) and after thermo-cycling (**D**) are shown. Double arrows, i n D, mean strong diffraction rings.

[τ002 (*H*)] crystallite size, corresponded to dentin treated with TDg-NPs load cycled (22.20 nm) (Table 1). The widest [τ310 (*L*)] crystallite size, corresponded to dentin treated with TDg-NPs load cycled (11.56 nm) (Table 1). The smallest crystallite sizes, in length and width, were those from demineralized dentin treated with TDg-NPs at 24 h storage (17.25 nm and 6.30 nm, respectively (Table 1).

Dentin treated with TDg-NPs load cycled obtained the highest grain size at both 002 (21.65 nm) and 310 (10.89 nm) planes (Table 1). At 002 plane, the smallest grain size was obtained after treating dentin with TDg-NPs and thermo-cycled. At 310 plane, the smallest grain size corresponded to dentin treated with TDg-NPs assessed at 24 h storage (Table 1).

The highest microstrain occurred in dentin samples treated with TDg-NPs load cycles at both 002 (1.09×10^{-6}) and 310 (0.4×10^{-5}) planes (Table 1). The lowest microstrain succeeded in dentin specimens infiltrated with TDg-NPs and assessed, at 002 (1.81×10^{-6}) and 310 (1.4×10^{-5}) planes, at 24 h storage (Table 1).

Texture indices (R*hkl*) in dentin poly-crystalline structures were calculated. At 002 plane, the texture assessed with TDg-NPs solution infiltrated in dentin samples attained the highest texture, 0.778. In 310 plane, dentin infiltrated with undoped NPs achieved the highest texture (1.286) (Table 1).

3.3. Transmission electron microscopy (TEM) analysis (selected area diffraction and bright-field imaging), fast Fourier transform (FFT) spectroscopy and EDS analysis

Representative examples of HRTEM are included (Figs. 4–8, S3-S7). Minerals obtained from dentin samples treated with undoped NPs and load cycled showed typical polymorph/polyhedral apatite crystals shaped by plate-like overlapped polygons. The observed crystal size of the crystals agglomerate reported in the Fig. 4A was approximately 30–70 nm.

The TEM images reveal that the precipitates show a heterogenous microstructure. There are parts with a compact structure and regions of less dense hydroxyapatite (HAp) crystallites. A higher magnification image (4B) of the precipitate revealed that it consisted of nanorods (red arrows) and bulky materials (black arrows). Aggregations of nanorods and lattice image of nanorods may be observed (insets I and II, respectively). Figure 4B·II is showing that the crystal comprised well-defined single crystal grains sharing a common direction. The lector diffraction analysis showed the typical pseudo-crystalline structure of crystals. Interplanar distances, *d*, (Fig. 4C) of 0.172 nm in a trajectory in inner circle revealing the diffraction plane {004}, were obtained. Interplanar distances, *d*, of 0.348 nm corresponded to {002} for HAp, with a margin of error <1.5 %. Both trajectories showed low and high relative intensities.

The relative intensity of the diffraction plane in each calcium phosphate crystal provided important information for identifying the calcium phosphate phase, *i.e.*, crystalline or amorphous status of the crystal, when the orientation of the crystals was random. The relative intensity of the {002} diffraction plane, in the group of dentin treated with undoped NPs was 53 % (Table S1), denoting relative crystallinity. Ca and P were detected as part of the elemental analysis by Energy dispersive X-ray (EDX) (Fig. 4D). STEM bright-field (Fig. 4E) and EDS-STEM two-dimensional elemental mappings at high magnification for calcium, phosphate and calcium phosphate (Fig. 4F, 4G, 4H) are shown. Ca density exceeded P density.

Geometric parameters of the crystallites from the compact regions seem to be a similar order of magnitude as for those observed in intact dentin; *i.e.*, the nanostructure is comparable to sound HAp. HR-TEM analysis of specimens treated with TDg-NPs and load cycled exhibited mineral structures organized in three-dimensional agglomerated crystals (Fig. 5A, S3A) or in starry poligonal needle–like apatite crystals of polycrystalline nature (Fig. 5C). The observed crystal sizes commonly ranged from 65 to 85 nm. Interplanar distances (Fig. 5B) were obtained, *d*, of 0.355 nm in a trajectory in inner circle revealing the diffraction plane {002}. Interplanar distances, *d*, of 0.171 nm corresponded to {004} for HAp. Both trajectories showed relative high intensities, denoting moderate crystallinity. EDX area scanning indicated that the distribution of various elements is uniform. EDX also confirmed the successful assembly of elements onto the HAp support (Figs. 6D-6I).

Dentin treated with TDg-NPs and thermo cycled generated irregular nano-rods and plate-like overlapped crystals (Figures S4A, S4C). EDX also confirmed the successful assembly of elements onto the HAp support (Figures S4D-I).

A large amount of irregular morphology nanocrystals, mainly polyhedral and starry polygonal block-like apatite crystals, with a size of ~ 28–160 nm, were detected after load cycling when the control group was analyzed (Figure S5A). The electron diffraction analysis exposed the typical amorphous structure of crystals (Inset Fig. 6A). Interplanar distances (Figure S5A) were obtained, *d*, of 0.238 nm in a trajectory in inner circle revealing the diffraction plane {310}. Interplanar distances, *d*, of 0.156 nm corresponded to {330} for HAp. Both trajectories showed high intensities, denoting amorphization.

Other crystals appeared as polyhedral apatite juxtaposed crystals (Figure S5B). Ca and P densities were scarce (Fig. 6 S5F).

Specimens infiltrated with TDg-NPs 24 h storage unveiled apatite crystals with plate-like overlapped mineral surfaces with multiple needle-like mineral formations (Figures S6A, S6B) with dimensions that ranged from approximately 40 nm to 73 nm (Fig. 6B). SAED analysis showed a relative amorphization (Figure S6C) of the analyzed mineral with specific crystallite lattice (Figure S6D). The nanometer-sized apatite composition of calcium and phosphate (Figure S7B) as part of the dimensional elemental analysis (Figure S7F) was determined, in case of specimens treated with undoped NPs and load cycling. New crystals showed drop-like morphologies combined with flake-like platforms of minerals, amorphous in nature.

Samples treated with TDg-NPs and load cycled originated plate and block-like apatite crystals ordered in three-dimensional agglomerated multiform mineral clusters (Fig. 8A), where the nanorods showed randomized orientation (Fig. 8B). The nanometer-sized apatite composition of the elemental analysis showed high levels oh of calcium and phosphate atoms (Figures 8D·I, 8D·II).

4. Discussion

Resin dentin interfaces treated with nanoparticles doped with tideglusib (TDg-NPs) submitted to 24 h storage or load cycling, attained the highest nanomechanical performance, in terms of modulus of Young (E_i) (Fig. 2). Consequently, as *Ei* was affected after TDg-NPs dentin infiltration, the first null hypothesis to be tested must be rejected. This highest modulus of elasticity, after using TDg-NPs in load cycled resin-dentin interfaces, was accompanied by a growth of crystallinity in the new mineral deposits, mainly constituted of hydroxyapatite, as major crystalline phase. These minerals also showed the greatest crystallite and grain size, microstrain and 002 plane-texture. New minerals were mostly hexagonal prisms in shape of submicron size which followed a right-defined lineation. Thereby, the second null hypothesis must be rejected.

In the present research, resin-dentin interfaces created after TDg-NPs infiltration, and subjected to load cycling have promoted the highest *Ei* among the different groups of study (Fig. 2). Elevated nanomechanical properties have become associated to the utmost bond strength values and the highest dentin bonding efficacy [19]. Thereby, the main body of the current discussion will be in the field of mechanical cycling. To this improved nanomechanical performance, it may have contributed mineral precipitation at the hybrid layer, bottom of hybrid layer and even at intertubular intact dentin [7,35] of the TDg-NPs doped resin-dentin bonded interfaces [19] (Table 1). Zaugg et al. [36] have reported an average of 17 GPa at intertubular dentin, used as control. Clinically, nanocrystalline HAp is segregated into intrafibrillar and extrafibrillar

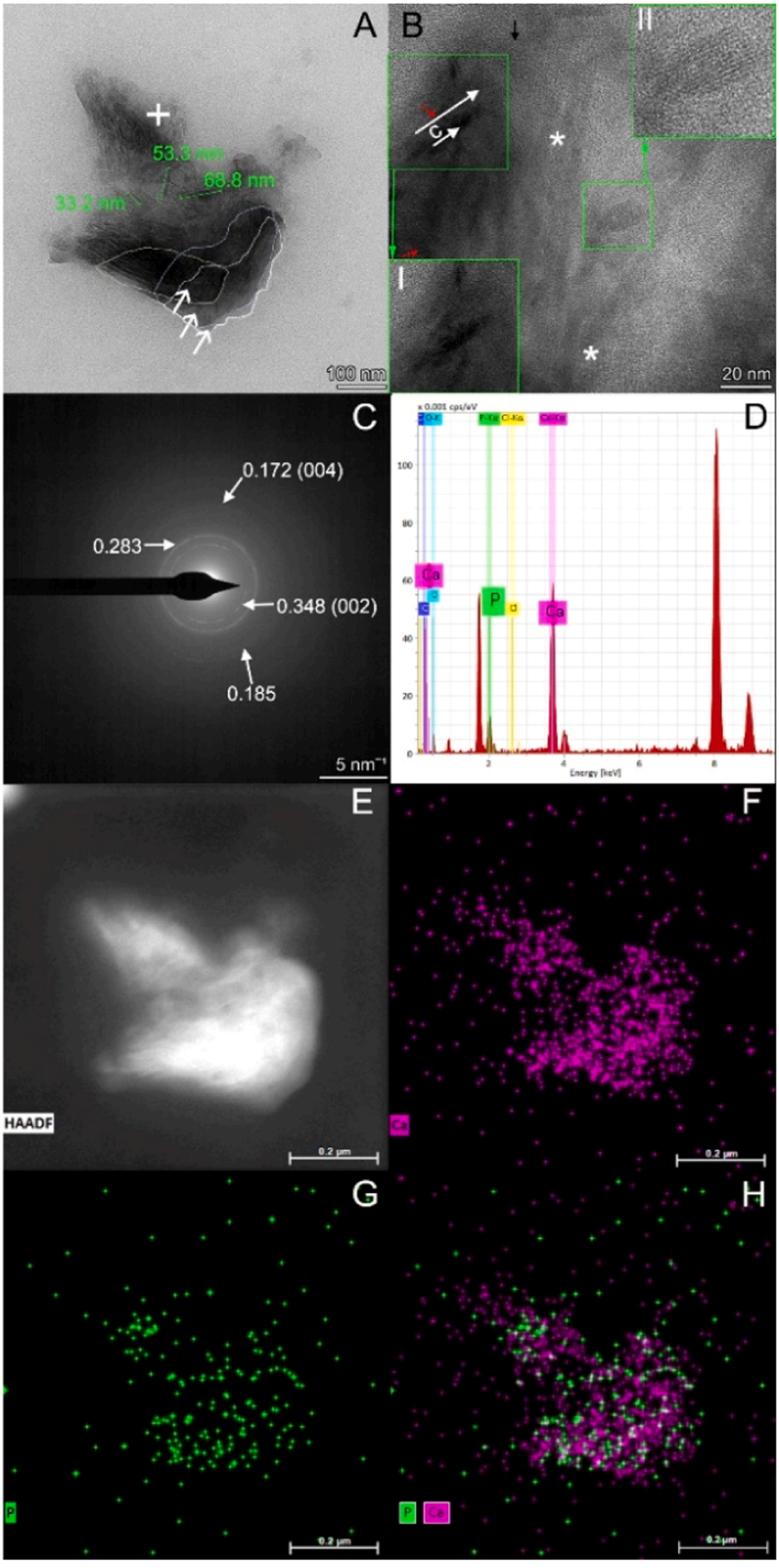

(caption on next page)

Fig. 4. A, Bright-field of an assembly of polymorphic apatite crystals of dentin treated with undoped NPs and load cycled. Agglomerated crystals of plate-like crystallites characterized these polygonal minerals (polygonal lines). **B**, High resolution TEM (HRTEM) image of a single hydroxyapatite nanocristal, extracted from (A) showing the growth orientation and crystallite size. Many nanorods (red arrows) and bulky materials (black arrow) were observed. Aligned crystal arrays may be shown (white arrows) (scale bars: 20 nm). The interspatial lattice spacing of the HAp heterostructure may be seen (asterisks). Insets reflect narrow area TEM images of nanorods. I, Aggregation of nanorods. The orientation of each rod was random, and lattice fringes were observed in the rods. II, HR-TEM image of a rod, and crystals sharing a common direction. The lattice image of the rod is visible and describes the atomic arrangement. **C**, A crystal (+) shown in (A), at nanoscale, displaying a selected area electron diffraction pattern (SAED) that shows a generalized faint intensity, containing differentiated halo rings and clear d spacing values. Measurements were done at 10 μm ϕ. Four Debye rings, with low (0.172 nm) and high (0.348 nm) intensities were observed. **D**, Representative Energy-dispersive X-ray spectroscopy (EDS) of the crystal (+) observed in (A) showing the nanometer-sized apatite composition of calcium and phosphate as part of the elemental analysis. **E**, Scanning TEM (STEM) bright-field image and EDS-STEM mapping of the crystals (+) observed in (A). **F**, Two dimensional elemental mappings of calcium [Ca] and phosphate [P] (**G**), and two-dimensional elemental mappings of calcium phosphate [PCa] (**H**).

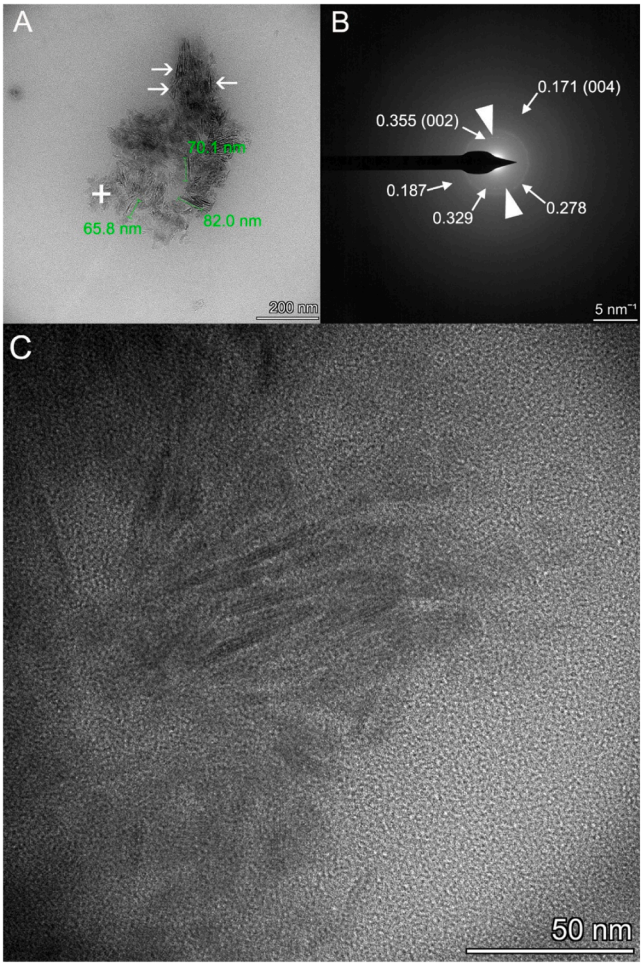

Fig. 5. **A**, Bright-field of an assembly of polyhedral apatite crystals formed by plate-like overlapped crystals of dentin treated with TDg-NPs and load cycled. It may be observed the in detailed polyhedral apatite appearance of crystallites. Aligned crystal arrays may be shown (arrows) (scale bars: 200 nm). **B**, A SAED of the crystal (+) shown in (A), at nanoscale. Two semicircles corresponding to 002 plane may be observed (arrowheads). Five Debye rings, with low (0.171 nm) and high (0.355 nm) intensities and clear d spacing values were also observed. Measurements were done at 10 μm ϕ. **C**, High Resolution TEM (HRTEM) image of compressed hexagonal prismatic single rod-shaped hydroxyapatite nanocrystals showing the growth orientation and crystallite lattice, from a dentin sample treated with TDg-NPs and load cycled. The image highlights the mineralized structures with different co-alignment between apatite nanocrystals growing in star-shaped topography.

mineral constituents. Hence, the increase in *Ei* of the infiltrated collagen is rightly linked with minerals deposits at the interface [37], particularly within the intrafibrillar section [38,39]. Thus, tideglusib seemed to promote and conduct mineralization onto the demineralized dentin enabling, biomimetic, functional or hierarchical mineralization [40], facilitating mineral precipitation which has been proved to be HAp (Fig. 3A). Hence, the power X-ray diffraction patterns indicate that these crystals are mainly constituted of HAp as major crystalline phase. The arrangement at higher size scales and the intricate organization of individual nanocrystals will determine the mechanical properties of substrata and the clinical role of the resulting materials [11]. As a consequence, the capacity to guide mineralization with spatial control is critical. Besides, the collagen fiber stiffness may have increased due to the existence of the TDg loaded NPs in the resin-dentin interface, at the dentin extracellular matrix, thus causing a higher resistance to proteolysis of type I collagen fibers favoring and leading minerals precipitation [19].

The highest crystallinity (lowest FWHM) among groups, in both 002 and 310 planes, after load cycling, was obtained by samples treated with TDg-NPs (Table 1). Narrower peaks (Fig. 3A) mean less structural variation in both angles and distances, as lower FWHM pointed out an improved crystallographic relative order of atoms [41], showing high crystallographic purity [42]. The morphology of these minerals corresponded with assembled plate-like overlapped crystals, after bright field analysis (Figs. 5A, 6A). Deng et al. [11] μXRD^2 profiles assessment also determined high intensities in samples treated with TDg-NPs mechanically loaded at 112 and 211 peaks where diffractography outlines unveil HAp existence (red bars) with sharp and narrow crystalline peaks (Fig. 3A). Similarly, the diffraction evaluation reflected brighter rings, after using TDg-NPs in dentin with load cycling, than in the other samples (Fig. 3C), meaning higher line narrowing of peaks. Improved tissue maturation and crystallinity have been associated [43]. On the other hand, thermo-cycling of restored dentin samples produced crystals with polyhedral apatite appearance (Figure S4A), and a broadening of the diffraction peaks (Fig. 3A, insets A and B). Thermal challenging also provoked a decrease of mechanical properties, with crystal amorphization (lower crystallinity) associated with higher degrees of impurities [16], on both 002 and 310 planes (Table 1), of crystallites at the whole resin-dentin interface. Low crystalline HAp becomes linked to immature HAp and high biodegradability. The hydroxyapatite dissolution originates ion-rich environments that raises supersaturation, nucleation velocities and growth of apatite nanocrystals [44] (Figure S4J). At the interface, the presence of the tested peptide may have inducted electrostatic attraction for these soluble ions, generating local increased of zones with supersaturation that trigger the referred nucleation [45].

Table 1 is reporting, considering the Scherrer equation, the crystallite size as a dimension estimation of the coherently scattering domain, where a rise of the mean crystallite size along with a direction parallel (*H*, height of crystallites) [002(*H*)] and perpendicular (*L*, longer base diagonal) to the *c*-axis [310(*L*)] was achieved when TDg-NPs were infiltrated in dentin and compared with the rest of the treated specimens. The Scherrer equation reveals equal width data (6.74 nm in the control group (Table 1), with those attained by Kinney et al. [46] who stated ~5.0 nm thickness. The planar CO_3 group substitution for the larger tetrahedral PO_4 group originates the expansion of the *c*-axis occurs. When the OH groups is substituted, the opposite effect occurs [47]. Crystallite size, that resulted from Eqs. (1) and (2), increases with the tissue maturation [48] when tissues are calcified, which is associated to crystallinity [49]. Crystallinity, in the present work, has also become

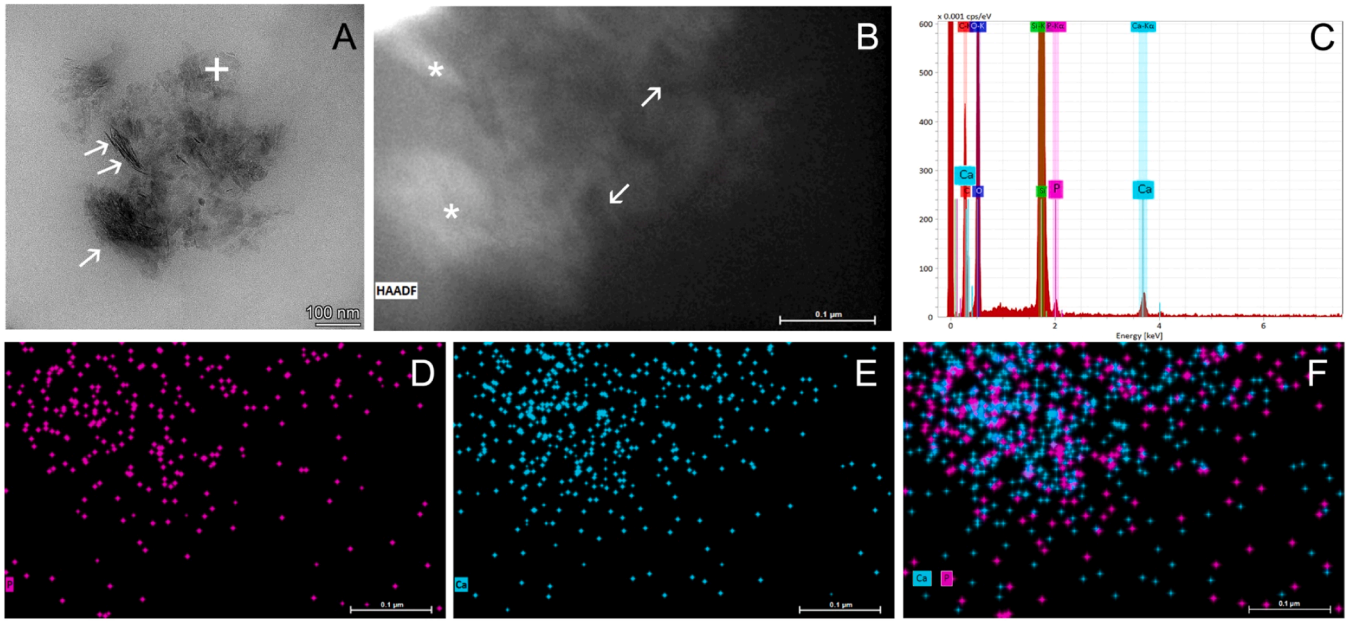

Fig. 6. **A**, Bright-field of an assemblage of block-like and needle-like overlapped apatite crystals of dentin treated with TDg-NPs and load cycled. It may be observed the in detailed polyhedral apatite appearance of crystallites. Aligned crystal arrays may be shown (arrows) (scale bars: 100 nm). **B**, High-angle annular dark-field scanning transmission electron microscopy (HAADF and S-TEM image or Z-contrast imaging) reflecting the collection of the electrons scattered through very large angles, within the nanocrystals. This resulted image shows mass- (or Z-) contrast with higher atomic number regions of the sample appearing brighter (asterisks) than light element regions (arrows). **C**, Representative Energy-dispersive X-ray spectroscopy (EDS) of the crystal (+) observed in (A) showing the nanometer-sized apatite composition of calcium and phosphate as part of the elemental analysis. Two dimensional elemental mapping of phosphate [P] (**D**), calcium [Ca] (**E**), and calcium phosphate [CaP] (**F**).

linked to the highest crystallite size, *i.e.*, high *H* and *L* values (22.20 nm and 11.56 nm, respectively) after TDg-NPs infiltration in demineralized dentin, and load cycling (Table 1). Besides, the diffractography patterns progressively range from broad diffusing peaks at dentin treated with TDg-NPs at 24 h, to more crystalline and sharper peaks after infiltrating those specimens with TDg-NPs load cycled (Fig. 3A, 3B, 3C), guaranteeing that the amorphization is a dynamic process [47]. Similarly, the adverted amorphization that has been discovered on minerals deposited at the resin-dentin interface, load cycled, promoted with undoped NPs (FWHM 0.0076, 002 plane; FWHM 0.0219, 310 plane), when compared with TDg-NPs (Table 1) (Fig. 4C), has been associated to lower crystallite size (*H* values: 17.46 nm, 002 plane; *L* values: 7.02 nm, 310 plane), and low Young's modulus (Fig. 1). Furthermore, the crystal size decrease has been linked not only with amorphous state [50,51] but also with polyelectrolyte or ions content increases [9]. This "shrinkage" resulted related with lower crystallite size, crystallinity, *H* and *L* values, and with lesser grain size (Table 1), influencing the mechanical and clinical performance of dentin [47]. Further research is required, to explain the results of all these associated variables. After analyzing these outcomes, it is possible to (*i*) relate both higher crystallinity in dentin treated with TDg-NPs load cycled and growing along the orthogonal direction to the *c*-axis and (*ii*) to moderately take up that the highest crystallites thickness, at dentin substrates treated with TDg-NPs load cycled (22.20 and 10.89 nm at 002 and 310 planes, respectively) (Table 1) fits with a higher mineralization and maturity of the dentin substrate.

Dentin treatment with TDg-NPs and load cycling was analyzed through SAED and EDS elemental mapping, to define the crystal structure of mineral deposits. Load cycled samples of resin-dentin interfaces promoted with TDg-NPs infiltration revealed a high P and Ca presence (Fig. 6G, 6H, 6I). Similarly, the SAED obtained (Fig. 5B) complied with the formed brighter rings at 002, 211 and 112 planes showed by the diffraction XRD that was achieved (Fig. 3C, double arrows), in comparison with the 24 h time-point group (Fig. 3B) or thermo-cycled group (Fig. 3D), indicating low peaks line broadening. The simulated SAED corresponding to the {002} direction of Figs. 4C and 5B was consistent with the FFT image in Fig. 8C, indicating that the nanorods were indeed HAp [52]. The P and Ca content, in our observations, indirectly reveals the formation of HAp [53] (Fig. 6F). The highest relative intensities, after TEM analysis, of the {002} in the 0.352 nm (high intensity) [31 % (Table S1)] and {004} in the 0.171 nm (low intensity) [74 % (Table S1)] diffraction planes assured the higher HAp content in the mineral formations when TDg-NPs were used to treat dentin and then load cycled, as showed by the brighter rings intensities (Fig. 5B), and so by the vertical red bars that appeared at the XRD analysis (Fig. 3A). The samples morphology is clearly affected by the presence of tideglusib. Normally, HAp is mostly constituted of plate-shaped morphology tiny crystals [9]. Biogenic HAp generated after TDg-NPs application in dentin submitted to load cycled exhibited clustering of thin and long crystals at a whole (Figs. 5C, S3C). The rod-shaped nanocrystals with a length of 22.20 nm and a width of 11.56 nm (Table 1) were observed (Fig. 5C). These HR-TEM images revealed that the nanorods possess the referred single-crystal structure. The presence of an apatite phase, therefore, can still be concluded [54]. The FFT analysis has revealed a crystalline nature of minerals, as {002} and {310} crystallographic planes described corresponded to HAp [52] (Fig. 8C).

After undoped NPs infiltration and mechanical loading, partial dentin remineralization was adverted in the present study, as a drop of the mechanical properties, especially at the bottom of the hybrid layer (Fig. 2) may be interpreted as a sign of dentin demineralization and interface degradation [51], indicating low remineralization potential at the intrafibrillar section [39]. Crystals obtained after resin-dentin infiltration promoted with undoped NPs attained lower crystallinity than those obtained with TDg-NPs, both after load cycling (Table 1). Scherrer equations (*H* and *L*) also showed lower crystallite sizes generated at the interface after using undoped NPs (Table 1). This contraction, when compared with biogenic apatite from TDg-NPs application, was higher alongside the orthogonal direction to the *c*-axis, which indicates a superior interaction of the ions with the HAp [9].

Thus, specimens treated with TDg-NPs has shown higher levels of

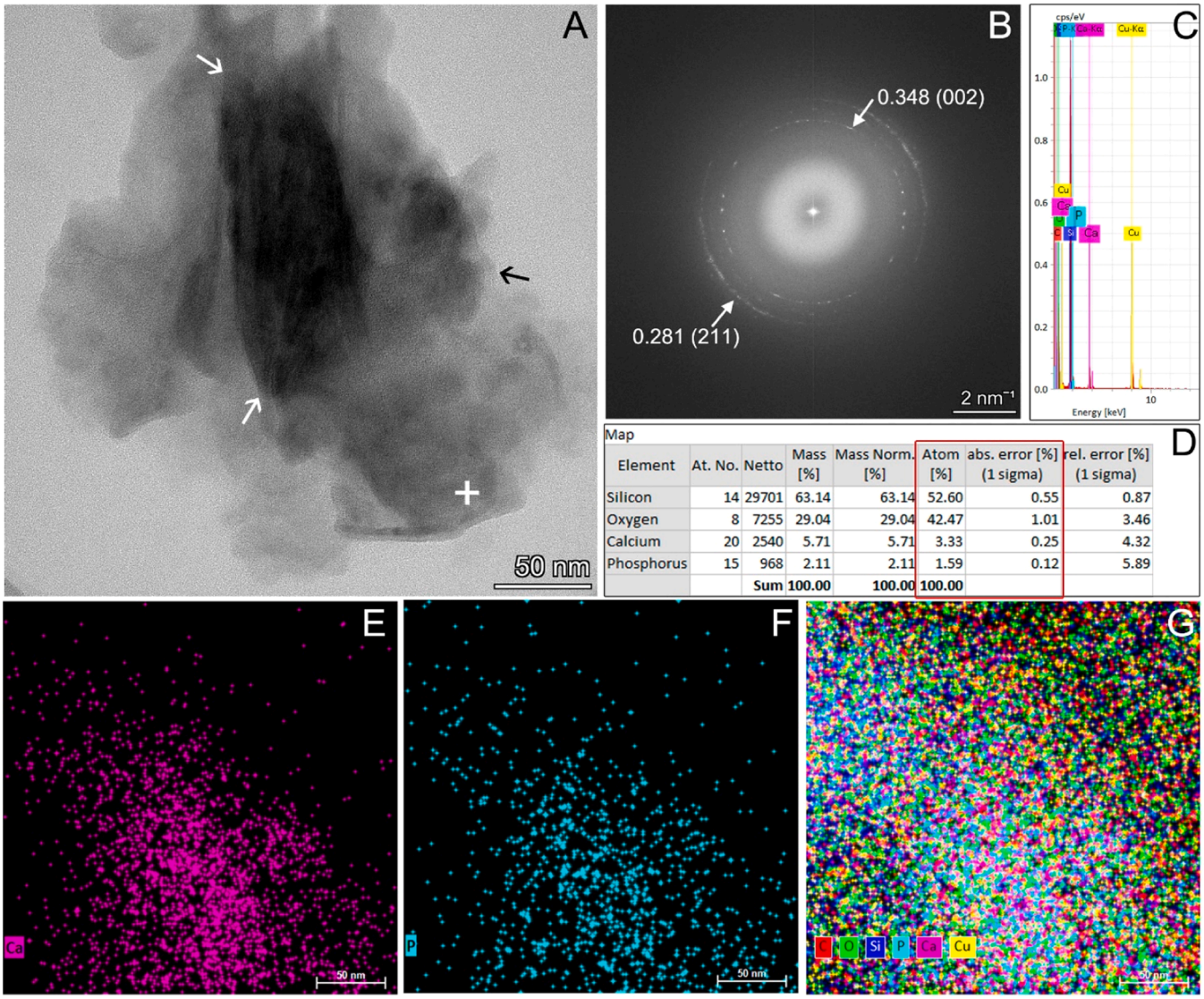

Element	At. No.	Netto	Mass [%]	Mass Norm. [%]	Atom [%]	abs. error [%] (1 sigma)	rel. error [%] (1 sigma)
Silicon	14	29701	63.14	63.14	52.60	0.55	0.87
Oxygen	8	7255	29.04	29.04	42.47	1.01	3.46
Calcium	20	2540	5.71	5.71	3.33	0.25	4.32
Phosphorus	15	968	2.11	2.11	1.59	0.12	5.89
		Sum	100.00	100.00	100.00		

Fig. 7. **A**, Bright-field of plate-like overlapped crystals of dentin treated with undoped NPs and load cycled, showing a slightly elongated drop-like forms in flake-like mineral platforms (arrows) (scale bars: 50 nm). **B**, the calculated fast Fourier transform (FFT) image of a rod from the crystal (+) shown in (A), at nanoscale of the single phase of low-crystalline HAp showed crystal lattice unveiling the interplanar distances of 0.281 nm and 0.348 nm, which correspond to the 211 and 002 crystallographic planes, respectively. **C**, Energy dispersive X-ray spectroscopy (EDS) of the resulted crystal (+) shown in (A), at nanoscale. **D**, Elements and content in a TDg-NPs-induced precipitate measured by STEM-EDS obtained from C. Two dimensional elemental mappings of calcium [Ca] (**E**), phosphate [P] (**F**), and calcium phosphate [PCa] in junction with additional elemental components (**G**). Cu is a sample holder contaminant.

calcium and phosphate atoms (Figures 8D·I, 8D·II), than samples treated with undoped NPs, which also showed the presence of some contaminants, as Cu (Fig. 7D). The Fei Titan 80–300 TEM-STEM microscope is integrated with 4 energy dispersive X-ray spectroscopy (EDS) detectors (FEI microanalysis Super X) as well as a high angle annular dark field detector (HAADF). To acquire two-dimensional compositional elemental mappings of samples, the selected mineral areas were analyzed. As this type of analysis is performed beyond the bulk sample, some elemental contents of the sample holder are irretrievably captured showing the presence of local enrichment of some contaminant after atomization, as Cu in this case. Cu is easily differentiated by its yellow color, but it does not affect the interpretation of the results, since it is previously identified [55]. Similarly, FFT analysis corroborates the presence of additional spots due to overlapping of the nano-sized grains [56] in case of using tideglusib (Figs. 7B vs 8C). The diffuse ring shown at SAED (Fig. 4C) when dentin was infiltrated with undoped NPs pointed out a decline in crystallinity [23], likely amorphous calcium phosphate or single phase of low-crystalline HAp [52,57] (Fig. 4F, 4G, 4H) in junction with other elements as chloride, carbon and oxygen (data nor shown). At a later stage, amorphous calcium phosphate may be transformed into HAp [53]. The FFT analysis has revealed a relative amorphous nano-crystalline HAp nature, as {002} and {211} crystallographic planes described corresponded to HAp and OCP [52] (Fig. 7B). Distinct ligands that are existing in TDg such as hydroxyl groups, carboxyl, or carboxamide may bind to calcium accelerating nucleation [45,58].

The grain size, measured by the applied Scherrer–Wilson equation, has shown that dentin crystals became smaller (~1.14 fold) in dentin treated with undoped NPs (18.97 nm) than in samples treated with TDg-NPs (21.65 nm) (Table 1), after load cycling, at (002) reflections. At 310 reflections, differences augmented (~1.65 fold) (Table 1). Different atoms displacement regarding their reference position within a perfect lattice, provokes the strain. Strain broadening is order-dependent, whereas size broadening is independent from the reflection order [9]. In both 002 and 310 planes, dentin infiltrated with TDg-NPs and load cycled achieved the lowest microstrain values (1.09×10^{-6} and 0.4×10^{-5}, respectively) (Table 1). Tooth stiffness, as strength bearing tissue

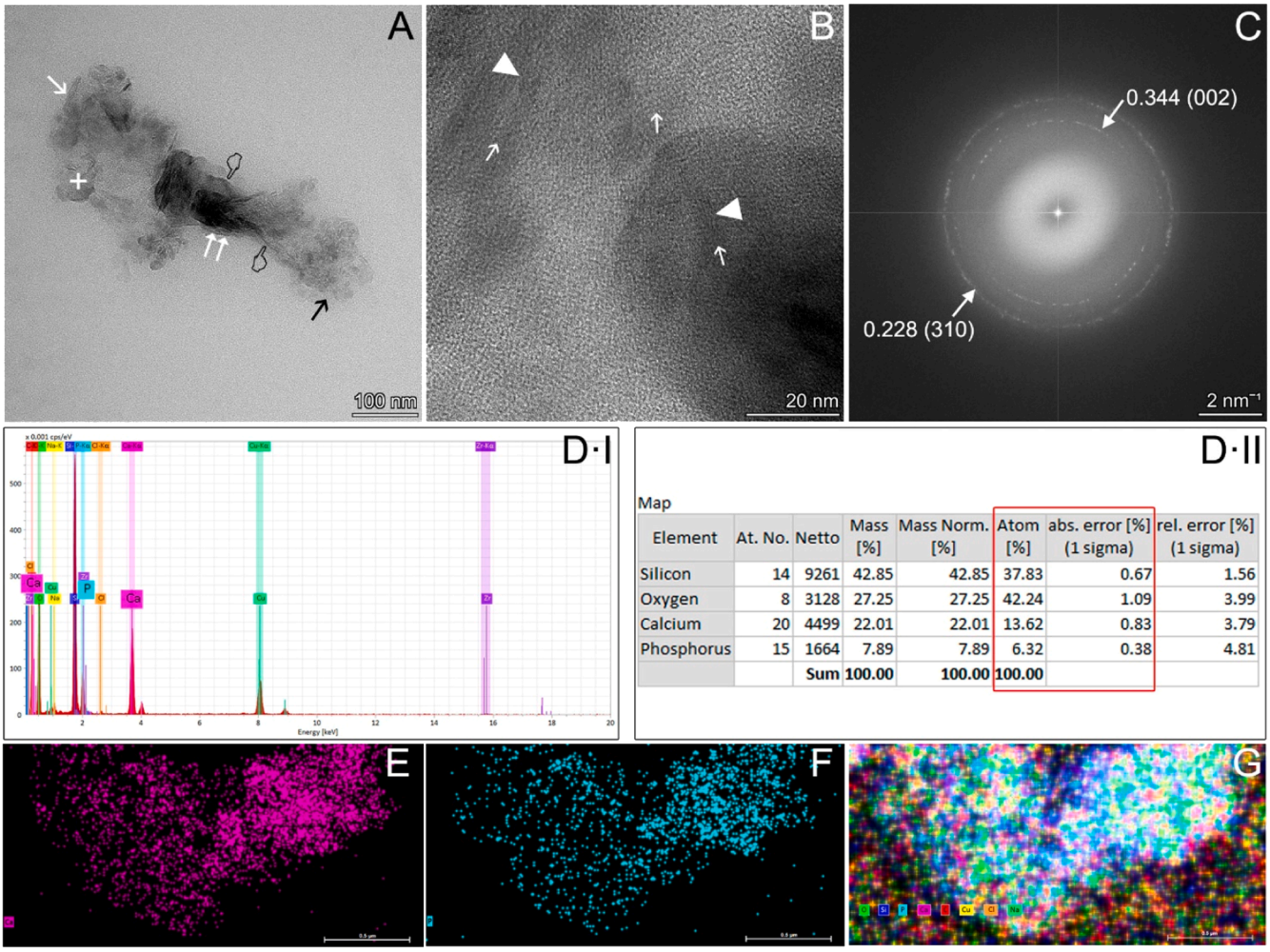

Element	At. No.	Netto	Mass [%]	Mass Norm. [%]	Atom [%]	abs. error [%] (1 sigma)	rel. error [%] (1 sigma)
Silicon	14	9261	42.85	42.85	37.83	0.67	1.56
Oxygen	8	3128	27.25	27.25	42.24	1.09	3.99
Calcium	20	4499	22.01	22.01	13.62	0.83	3.79
Phosphorus	15	1664	7.89	7.89	6.32	0.38	4.81
		Sum	**100.00**	**100.00**	**100.00**		

Fig. 8. **A**, Bright-field of plate-like (arrows), needle-like (pointers) and block-like apatite crystals (double arrows) of dentin treated with TDg-NPs and load cycled, ordered in three-dimensional agglomerated multiform crystals (scale bars: 100 nm). **B**, Aggregated narrow-area TEM images of nanorods, unveiling the random orientation of several rods (arrows) with their lattice fringes (arrowheads). **C**, The calculated fast Fourier transform (FFT) image of a rod from the crystal (+) shown in (A), at nanoscale of the nano-crystalline HAp showed the crystal lattice unveiling interplanar distances of 0.228 nm and 0.344 which correspond to the 310 and 002 crystallographic planes, respectively.**D**, I, Representative Energy-dispersive X-ray spectroscopy (EDS) of the crystal (+) observed in (A) showing the nanometer-sized apatite composition of calcium and phosphate as part of the elemental analysis. II, Elements and content in a TDg-NPs-induced precipitate measured by STEM-EDS obtained from I. Two dimensional elemental mappings of calcium [Ca] (**E**), phosphate [P] and (**F**), and calcium phosphate [PCa] in junction with additional elemental components, as oxygen and silicon (**G**).

at biting, is indicated by the strain distribution [26]. These lower strain data accounted, speculating, for the peaks narrowing (0.0067) in spite of the highest grain size (21.65 nm) [9] at 002 plane (Table 1). The different mean crystallite sizes is conditioned by the strain influence to the peaks narrowing [9], i.e., more crystallite size (Figs. 5C, S3C) with diminished microstrain data and lattice distortion [59,60] (Table 1). The carbonate for phosphate (β-type) substitution in HAp, causes the well-known lattice disorder which is correlated with the distortion of the phosphate tetrahedron. This event is named as 'carbonate substitution problem' [61], and occurred when specimens were treated with undoped NPs. Carbonate ions the crystal structure of HAp influences its nature. In acidic environment, there is an increase in solubility, decreasing the crystallinity and retarding crystal growth [62]. Thus, demineralized dentin specimens infiltrated with undoped NPs, have shown the highest values of both FWHM (Figures S3A, S3C) and microstrain when compared with TDg-NPs (Table 1). It has been established an association between the values of microstrain, higher in dentin treated with undoped NPs, amorphization and remarkable increase of polyelectrolytes or ions [9]. Nevertheless, the apatite composition of the elemental analysis showed higher levels of calcium and phosphate atoms in samples treated with TDg-NPs than in those treated with undoped NPs (Figs. 7D, 8D·I, 8D·II). This outcome might partially confirm that the presence of tideglusib at the interface has inducted electrostatic ions attraction and further nucleation [45].

In dentin polycrystalline structures, texture indices (R_{hkl}) were obtained according to Eq. (3). *R* values greater or lower than 1.0 determines the preferred grain orientation or texture [24,33]. Texture greatly influence the materials properties, as cracking resistance, and it regulates microstructure changes [63]. Samples treated with TDg-NPs achieved the closest values to this number, after load cycling, at 002 and 310 planes (0.778 and 1.134, respectively) (Table 1), hence showing the highest randomly orientation, related with strong chemical stability [64]. The calcium phosphate phase in case of random orientation (Figure S3C) may be explained by the relative intensity of the diffraction plane (Figure S3B) in each calcium phosphate crystal [52]. Therefore, confined angles and regions in function of the surface topographies [11] can describe different organization of nanocrystals subjected to the type of applied NPs (Figs. 5A, 5C, 6A, 6B). Hence, crystals produced by TDg-NPs infiltration showed less spaced nanocrystals, with much lower co-alignment angles (Figs. 5A, 5C, 6A), than in case of undoped NPs

application (Fig. 4A). The relative intensities at {002} (HAp) in the 0.348 nm (high intensity) [53 % (Table S1)] and at {211} in the 0.283 (low intensity) [100 % (Table S1)] was weakened (Fig. 5B), where three Debye rings, varying from high (0.355 nm) to low (0.171 nm) intensity from the center, were detected. It is speculated that both β-TCP and OCP may appear more than crystalline HAp, due to the relative high intensities of {121} and {1010}, respectively, of these two amorphous components analyzed by Karakida et al. [52]. Minerals generated after TDg-NPs application and load cycling consisted of multiple domains of crystal arrays of submicron size, locally oriented, showing a well-defined lineation (Fig. 3A, 3C, S6A, S6C). Furthermore, TEM observation of a single nanocrystal with its fast Fourier transform (FFT) pattern exposed 15–30 nm length flat-ended nanocrystals with proper composition of P and Ca and HAp morphology (Fig. 6G, 6H, 6I) developed along the c-axis. These outcomes were further complemented by searching crystallographic orientation using high-resolution TEM (HRTEM) (Figs. 5C, S3C) that mostly exhibited as hexagonal prisms and SAED (Figs. 5B, S3B). Additional findings corroborate that the TEM data trend is reliable with our referenced values of texture.

Differences in co-alignment and growth orientation may be associated with the nanocrystals preferential growth, significantly affecting the mineralized structures respect to both morphology and mechanical properties at macroscale [11]. Our modulus of Young results (Fig. 2) agree with those reported by Deng et al. [11], who obtained in their specimens 12.7 GPa in the perpendicular and preference growth, with high co-alignment, of mineral precipitates. Apatite crystallites generated under the influence of tideglusib precipitated with a controlled mineralization procedure [65], at least at 002 plane, after observing the faint preferred orientation (R_{hkl}) of dentin treated with TDg-NPs load cycled (0.778), in comparison with samples treated with undoped NPs (0.560) (Table 1). When TDg-NPs samples were load cycled, the principal ring pattern corresponding to 002 planes that performed in the way of two semicircles instead of a continuous ring (Fig. 5B) illustrates that the crystallites possess specific orientation in c-direction [66]. These samples show the trend towards random orientation, at 002 plane with negative nano-degradation [33] at 310 plane, as R_{hkl} decreased from 24 h time point (1.165) until load cycled specimens (1.134) (Table 1). At the Debye ring that corresponds to the diffraction planes detected in dentin infiltrated with TDg-NPs confirmed the presence of crystalline HAp in both thermocycled and load cycled type of specimens (Figs. 5B, S4B, respectively). TEM pictures of untreated dentin (control) exhibited polymorphic apatite crystals of ~30–160 nm (Figures S5A, S5B), leading to an amorphization process. Samples treated without NPs showed intermediate intensities at both Debye rings (Figure S5B, inset) of HAp high {310} (0.238 nm) and low {330} (0.156 nm) intensities, probably due to a new protagonist role of amorphous components (ACP), as OCP and β-TCP (Table S1). Nevertheless, the change from the ACP precursor to HAp remains unknown and it poses a topic of active debate and future research [67].

The objective of the current study was achieved in the present manuscript, as it has been shown that TDg-NPs provoked peak narrowing (low FWHM) and high crystallinity with an increased modulus of Young after load cycling in comparison with the undoped NPs. Undoped NPs mostly produced HAp in amorphous state, that likely resulted linked to the intake of carbonate into the apatite crystal. The amorphization process originated crystals imperfections, i.e., lattice distortion with increased microstrain data and lesser crystallite size. This is biologically remarkable, as the increase in carbonate presence means an augmentation in HAp solubility [61]. On the other hand, the presence of TDg at the interface produced HAp with narrow and sharp peaks through diffractography. The highest crystallites length and thickness that were obtained after TDg-NPs dentin infiltration fulfills a major mineralization and maturity, that associated with low solubility, high stability of the greatly crystalline structures [61] and specific crystal morphologies as needle and star-like, block-like and plate-like profiles, prevailing a slightly elongated form [62]. Wnt/βcatenin signaling has, thus, emerged as a major target in dentin tissue regeneration, remineralization and repair by using a small molecule agonist, as tideglusib. Nevertheless, key challenges remain, such as guiding the orientation of crystal growth, to produce rationally designed hierarchical macrostructures and ultimately the capacity to control kinetics of crystal precipitation. Through the use of the GSK-3 inhibitor tideglusib, we have approached the crucial objective of regenerative medicine, which is to restore the original functions, properties, and composition of lost tissue components [36]. Some of these goals have been achieved; others are pending.

These are, to the best of our knowledge, the only available results from nanoindentation techniques combined with X-ray microdiffractometry and transmission electron microscopy analysis associated to selected area diffraction and bright-field imaging combined methodologies aimed to analyze dentin substrate submitted to TDg-NPs treatment. In line with the distinct applied experimental procedures, it should be taken into account that measurements were done in biological *ex-vivo* samples. Similar magnitude of differences were reported previously [16]. Distinct new techniques, to advance in innovation, should be implemented. Sealing ability through the fluid filtration system, Z potential, Fourier-transform infrared spectroscopy (FTIR), microtensile bond strength (MTBS), field emission scanning electron microscopy (FESEM) and chemical characterization with Raman analysis, would contribute to achieve this goal. A limitation of our methodology could be the absence of these techniques into the present investigation. For nanoindentation analysis, the number of teeth in each group was four, and it may be considered a limitation for being a low number, not able to overcome the biological variability. But it has been previously published for similar techniques in which specimens from teeth (and not teeth) are used as statistical unit that a minimum of three teeth per experimental group (with appropriate analysis of tooth dependency) are enough to account for reliable results [68].

5. Conclusions

The presence of TDg at the resin-dentin interface has promoted the precipitation of HAp, as major crystalline phase, at the intrafibrillar compartment of the collagen fibrils, enabling functional mineralization. TDg-NPs facilitated specific organization of nanocrystals, randomly oriented, showing less structural variation in both angles and distances that improved crystallographic relative order of atoms and maturity. Nanocrystals inducted by TDg-NPs, which showed the highest crystallite and grain size, followed a well-defined lineation pattern based on hexagonal prisms morphology of submicron size. New minerals produced by TDg-NPs application exhibited less spaced nanocrystals, growing and settling compactly with much smaller co-alignment angles, if compared to those produced after the undoped NPs dentin treatment, that exhibited a relative amorphization. Thermal challenging of dentin treated with TDg-NPs have provoked a decrease of functional mineralization and crystallinity, associated to immature hydroxyapatite formation.

CRediT authorship contribution statement

Manuel Toledano: Writing – review & editing, Writing – original draft, Visualization, Validation, Supervision, Project administration, Methodology, Investigation, Funding acquisition, Formal analysis, Conceptualization. **Enrique Fernández-Romero:** Writing – review & editing, Visualization, Methodology, Investigation, Data curation. **María T. Osorio:** Writing – review & editing, Investigation, Data curation. **Estrella Osorio:** Writing – review & editing, Writing – original draft, Visualization, Methodology, Investigation, Data curation. **Fátima S. Aguilera:** Writing – review & editing, Writing – original draft, Visualization, Software, Resources, Methodology, Investigation, Data curation. **Raquel Toledano:** Writing – review & editing, Investigation, Data curation. **Raquel Osorio:** Writing – review & editing, Writing – original draft, Visualization, Supervision, Project administration, Methodology,

Investigation, Funding acquisition, Formal analysis, Conceptualization.

Declaration of competing interest

The authors declare that they have no known competing financial interests or personal relationships that could have appeared to influence the work reported in this paper.

Acknowledgements

The present study was supported by Grant PID2020–114694RB-I00 funded by MCIN/AEI 10.13039/501100011033. This research is part of E. F-R.'s Ph.D. research study. Funding for open access charge: Universidad de Granada / CBUA.

Glossary

ACP: amorphous components
BF: bright field
EDS: energy-dispersive X-ray spectroscopy
EDX: energy dispersive X-ray
Ei: modulus of Young
ELR: elastin-like recombinamer
FESEM: Field emission scanning electron microscopy
FFT: fast fourier transform
FTIR: Fourier-transform infrared spectroscopy
FWHM: full width at half maximum
GSK-3: glycogen-synthase-kinase 3
HAADF: high angle annular dark field detector
HAp: hydroxylapatite
HRTEM: high resolution transmission electron microscopy
MTBS: microtensile bond strength
NPs: nanoparticles
SAED: selected area electron diffraction
SB: single bond
SBFS: simulated body fluid solution
STEM: scanning transmission electron microscopy
TDg: tideglusib
TEM: transmission electron microscopy
XRD: X-ray diffraction
μXRD^2:X-ray micro-diffractometer

Supplementary materials

Supplementary material associated with this article can be found, in the online version, at doi:10.1016/j.jdent.2024.105334.

References

[1] M. Toledano-Osorio, E. Osorio, F.S. Aguilera, A. Luis Medina-Castillo, M. Toledano, R. Osorio, Improved reactive nanoparticles to treat dentin hypersensitivity, Acta Biomater. 72 (2018) 371–380, https://doi.org/10.1016/j.actbio.2018.03.033.
[2] M. Hashimoto, H. Ohno, H. Sano, M. Kaga, H. Oguchi, In vitro degradation of resin-dentin bonds analyzed by microtensile bond test, scanning and transmission electron microscopy, Biomaterials 24 (2003) 3795–3803, https://doi.org/10.1016/s0142-9612(03)00262-x.
[3] J. Hebling, D.H. Pashley, L. Tjäderhane, F.R. Tay, Chlorhexidine arrests subclinical degradation of dentin hybrid layers in vivo, J. Dent. Res. 84 (2005) 741–746, https://doi.org/10.1177/154405910508400811.
[4] D.H. Pashley, F.R. Tay, C. Yiu, M. Hashimoto, L. Breschi, R.M. Carvalho, S. Ito, Collagen degradation by host-derived enzymes during aging, J. Dent. Res. 83 (2004) 216–221, https://doi.org/10.1177/154405910408300306.
[5] L. Breschi, A. Mazzoni, F. Nato, M. Carrilho, E. Visintini, L. Tjäderhane, A. Ruggeri, F.R. Tay, E.D.S. Dorigo, D.H. Pashley, Chlorhexidine stabilizes the adhesive interface: a 2-year in vitro study, Dent. Mater. 26 (2010) 320–325, https://doi.org/10.1016/j.dental.2009.11.153.
[6] M.R. Carrilho, F.R. Tay, A.M. Donnelly, K.A. Agee, L. Tjäderhane, A. Mazzoni, L. Breschi, S. Foulger, D.H. Pashley, Host-derived loss of dentin matrix stiffness associated with solubilization of collagen, J. Biomed. Mater. Res. B Appl. Biomater. 90 (2009) 373–380, https://doi.org/10.1002/jbm.b.31295.
[7] A.C. Profeta, F. Mannocci, R. Foxton, T.F. Watson, V.P. Feitosa, B. De Carlo, R. Mongiorgi, G. Valdré, S. Sauro, Experimental etch-and-rinse adhesives doped with bioactive calcium silicate-based micro-fillers to generate therapeutic resin–dentin interfaces, Dent. Mater. 29 (2013) 729–741, https://doi.org/10.1016/j.dental.2013.04.001.
[8] J. Thadathil Varghese, F. Islam, P. Farrar, L. Prentice, B.G. Prusty, Multi-response optimisation analysis of material properties in dental restorative composites under the influence of thermal and thermomechanical stimuli - A 3D finite element study, J. Mech. Behav. Biomed. Mater. 150 (2024) 106363, https://doi.org/10.1016/j.jmbbm.2023.106363.
[9] A. Bigi, E. Boanini, M. Gazzano, M.A. Kojdecki, K. Rubini, Microstructural investigation of hydroxyapatite–polyelectrolyte composites, J. Mater. Chem. 14 (2004) 274–279, https://doi.org/10.1039/B308687A.
[10] R. Osorio, E. Osorio, A.L. Medina-Castillo, M. Toledano, Polymer nanocarriers for dentin adhesion, J. Dent. Res. 93 (2014) 1258–1263, https://doi.org/10.1177/0022034514551608.
[11] X. Deng, A. Hasan, S. Elsharkawy, E. Tejeda-Montes, N.V. Tarakina, G. Greco, E. Nikulina, J.M. Stormonth-Darling, N. Convery, J.C. Rodriguez-Cabello, A. Boyde, N. Gadegaard, N.M. Pugno, M. Al-Jawad, A. Mata, Topographically guided hierarchical mineralization, Mater. Today Bio 11 (2021) 100119, https://doi.org/10.1016/j.mtbio.2021.100119.
[12] C. Sfeir, P.-A. Fang, T. Jayaraman, A. Raman, Z. Xiaoyuan, E. Beniash, Synthesis of bone-like nanocomposites using multiphosphorylated peptides, Acta Biomater. 10 (2014) 2241–2249, https://doi.org/10.1016/j.actbio.2014.01.007.
[13] Y. Li, J.C. Rodriguez-Cabello, C. Aparicio, Intrafibrillar mineralization of self-assembled elastin-like recombinamer fibrils, ACS Appl. Mater. Interfaces 9 (2017) 5838–5846, https://doi.org/10.1021/acsami.6b15285.
[14] J.C. Rodríguez-Cabello, L. Martín, M. Alonso, F.J. Arias, A.M. Testera, Recombinamers" as advanced materials for the post-oil age, Polymer 50 (2009) 5159–5169, https://doi.org/10.1016/j.polymer.2009.08.032.
[15] M. Toledano, E. Osorio, M.T. Osorio, F.S. Aguilera, R. Toledano, E.F.- Romero, R. Osorio, Dexamethasone-doped nanoparticles improve mineralization, crystallinity and collagen structure of human dentin, J. Dent. 130 (2023) 104447, https://doi.org/10.1016/j.jdent.2023.104447.
[16] M. Toledano-Osorio, F.S. Aguilera, E. Muñoz-Soto, E. Osorio, M. Toledano, G. Escames, A.L. Medina-Castillo, M.T. Osorio, M.T. López-López, M. Vallecillo-Rivas, R. Osorio, Melatonin-doped polymeric nanoparticles induce high crystalline apatite formation in root dentin, Dent. Mater. 37 (2021) 1698–1713, https://doi.org/10.1016/j.dental.2021.09.001.
[17] P. Spencer, Q. Ye, N.J.B. Kamathewatta, S.K. Woolfolk, B.S. Bohaty, A. Misra, C. Tamerler, Chemometrics-assisted Raman Spectroscopy characterization of tunable polymer-peptide hybrids for dental tissue repair, Front. Mater. 8 (2021) 681415, https://doi.org/10.3389/fmats.2021.681415.
[18] V.C.M. Neves, R. Babb, D. Chandrasekaran, P.T. Sharpe, Promotion of natural tooth repair by small molecule GSK3 antagonists, Sci. Rep. 7 (2017) 39654, https://doi.org/10.1038/srep39654.
[19] M. Toledano, F.S. Aguilera, E. Fernández-Romero, A.J. Lagos, M. Bonilla, C. D. Lynch, R. Osorio, Dentin remineralization using a stimuli-responsive engineered small molecule GSK3 antagonists-functionalized adhesive, Dent. Mater. Off. Publ. Acad. Dent. Mater. 40 (2024) 393–406, https://doi.org/10.1016/j.dental.2023.12.010.
[20] A. Alaohali, C. Salzlechner, L.K. Zaugg, F. Suzano, A. Martinez, E. Gentleman, P. T. Sharpe, GSK3 Inhibitor-induced dentinogenesis using a hydrogel, J. Dent. Res. 101 (2022) 46–53, https://doi.org/10.1177/00220345211020652.
[21] M. Toledano-Osorio, E. de Luna-Bertos, M. Toledano, F.J. Manzano-Moreno, C. Ruiz, M. Sanz, R. Osorio, NP-12 peptide functionalized nanoparticles counteract the effect of bacterial lipopolysaccharide on cultured osteoblasts, Dent. Mater. (2024), https://doi.org/10.1016/j.dental.2024.06.017.
[22] L.E. Bertassoni, S. Habelitz, M. Pugach, P.C. Soares, S.J. Marshall, G.W. Marshall, Evaluation of surface structural and mechanical changes following remineralization of dentin, Scanning 32 (2010) 312–319, https://doi.org/10.1002/sca.20199.
[23] F. Wang, E. Guo, E. Song, P. Zhao, J. Liu, Structure and properties of bone-like-nanohydroxyapatite/gelatin/polyvinyl alcohol composites, Adv. Biosci. Biotechnol. 1 (2010) 185–189, https://doi.org/10.4236/abb.2010.13026.
[24] J. Xue, A.V. Zavgorodniy, B.J. Kennedy, M.V. Swain, W. Li, X-ray microdiffraction, TEM characterization and texture analysis of human dentin and enamel, J. Microsc. 251 (2013) 144–153, https://doi.org/10.1111/jmi.12053.
[25] T. Sui, M.A. Sandholzer, N. Baimpas, I.P. Dolbnya, A. Walmsley, P.J. Lumley, G. Landini, A.M. Korsunsky, Multiscale modelling and diffraction-based characterization of elastic behaviour of human dentine, Acta Biomater 9 (2013) 7937–7947, https://doi.org/10.1016/j.actbio.2013.04.020.
[26] K. Fujisaki, M. Todoh, A. Niida, R. Shibuya, S. Kitami, S. Tadano, Orientation and deformation of mineral crystals in tooth surfaces, J. Mech. Behav. Biomed. Mater. 10 (2012) 176–182, https://doi.org/10.1016/j.jmbbm.2012.02.025.
[27] M. Toledano, F.S. Aguilera, E. Osorio, M. Toledano-Osorio, G. Escames, A. L. Medina-Castillo, R. Toledano, C.D. Lynch, R. Osorio, Melatonin-doped polymeric nanoparticles reinforce and remineralize radicular dentin: morpho-histological, chemical and biomechanical studies, Dent. Mater. 37 (2021) 1107–1120, https://doi.org/10.1016/j.dental.2021.03.007.
[28] A.L. Medina-Castillo, Thermodynamic principles of precipitation polymerization and role of fractal nanostructures in the particle size control, Macromolecules 53 (2020) 5687–5700, https://doi.org/10.1021/acs.macromol.0c00973.
[29] S. Sauro, F. Mannocci, M. Toledano, R. Osorio, D.H. Pashley, T.F. Watson, EDTA or H3PO4/NaOCl dentine treatments may increase hybrid layers' resistance to

degradation: a microtensile bond strength and confocal-micropermeability study, J. Dent. 37 (2009) 279–288, https://doi.org/10.1016/j.jdent.2008.12.002.
[30] H. Ryou, L.-N. Niu, L. Dai, C.R. Pucci, D.D. Arola, D.H. Pashley, F.R. Tay, Effect of biomimetic remineralization on the dynamic nanomechanical properties of dentin hybrid layers, J. Dent. Res. 90 (2011) 1122–1128, https://doi.org/10.1177/0022034511414059.
[31] A.B. Rodriguez-Navarro, Registering pole figures using an X-ray single-crystal diffractometer equipped with an area detector, J. Appl. Crystallogr. 40 (2007) 631–634, https://doi.org/10.1107/S0021889807014574.
[32] F. Perales, F. Agulló-Rueda, J. Lamela, C. de las Heras, Optical and structural properties of Sb2S3/MgF2 multilayers for laser applications, J. Phys. Appl. Phys. 41 (2008) 045403, https://doi.org/10.1088/0022-3727/41/4/045403.
[33] I.-M. Low, Depth-Profiling of crystal structure, texture, and microhardness in a functionally graded tooth enamel, J. Am. Ceram. Soc. 87 (2004) 2125–2131, https://doi.org/10.1111/j.1151-2916.2004.tb06369.x.
[34] F. Martinez-Ruiz, A. Paytan, M.T. Gonzalez-Muñoz, F. Jroundi, M.M. Abad, P. J. Lam, J.K.B. Bishop, T.J. Horner, P.L. Morton, M. Kastner, Barite formation in the ocean: origin of amorphous and crystalline precipitates, Chem. Geol. 511 (2019) 441–451, https://doi.org/10.1016/j.chemgeo.2018.09.011.
[35] A.A. Dawasaz, R.A. Togoo, Z. Mahmood, A. Azlina, K.Thirumulu Ponnuraj, Effectiveness of self-assembling peptide (P11-4) in dental hard tissue conditions: a comprehensive review, Polymers 14 (2022) 792, https://doi.org/10.3390/polym14040792.
[36] L.K. Zaugg, A. Banu, A.R. Walther, D. Chandrasekaran, R.C. Babb, C. Salzlechner, M.a.B. Hedegaard, E. Gentleman, P.T. Sharpe, Translation approach for dentine regeneration using GSK-3 antagonists, J. Dent. Res. 99 (2020) 544–551, https://doi.org/10.1177/0022034520908593.
[37] Y. Li, T.T. Thula, S. Jee, S.L. Perkins, C. Aparicio, E.P. Douglas, L.B. Gower, Biomimetic mineralization of woven bone-like nanocomposites: role of collagen cross-links, Biomacromolecules 13 (2012) 49–59, https://doi.org/10.1021/bm201070g.
[38] M. Balooch, S. Habelitz, J.H. Kinney, S.J. Marshall, G.W. Marshall, Mechanical properties of mineralized collagen fibrils as influenced by demineralization, J. Struct. Biol. 162 (2008) 404–410, https://doi.org/10.1016/j.jsb.2008.02.010.
[39] L.E. Bertassoni, S. Habelitz, J.H. Kinney, S.J. Marshall, G.W. Marshall Jr., Biomechanical perspective on the remineralization of dentin, Caries Res. 43 (2009) 70–77, https://doi.org/10.1159/000201593.
[40] M. Toledano, E. Fernández-Romero, F.S. Aguilera, E. Osorio, J.A. Rodríguez-Santana, M. Garrido, P.A. Solís, F. García-Godoy, R. Osorio, Tunable polymer-peptide hybrids for dentin tissue repair, J. Dent. (2024) 105027, https://doi.org/10.1016/j.jdent.2024.105027.
[41] A.G. Schwartz, J.D. Pasteris, G.M. Genin, T.L. Daulton, S. Thomopoulos, Mineral distributions at the developing tendon enthesis, PLoS ONE 7 (2012) e48630, https://doi.org/10.1371/journal.pone.0048630.
[42] X. Niu, Y. Du, J. He, X. Li, G. Wen, Hydrothermal synthesis of co-exposed-faceted WO3 nanocrystals with enhanced photocatalytic performance, Nanomater. Basel Switz. 12 (2022) 2879, https://doi.org/10.3390/nano12162879.
[43] K.M. Zurick, C. Qin, M.T. Bernards, Mineralization induction effects of osteopontin, bone sialoprotein, and dentin phosphoprotein on a biomimetic collagen substrate, J. Biomed. Mater. Res. A 101 (2013) 1571–1581, https://doi.org/10.1002/jbm.a.34462.
[44] Y. Liu, S. Mai, N. Li, C.K.Y. Yiu, J. Mao, D.H. Pashley, F.R. Tay, Differences between top-down and bottom-up approaches in mineralizing thick, partially demineralized collagen scaffolds, Acta Biomater. 7 (2011) 1742–1751, https://doi.org/10.1016/j.actbio.2010.11.028.
[45] M. Gungormus, F. Tulumbaci, Peptide-assisted pre-bonding remineralization of dentin to improve bonding, J. Mech. Behav. Biomed. Mater. 113 (2021) 104119, https://doi.org/10.1016/j.jmbbm.2020.104119.
[46] J.H. Kinney, J. Oliveira, D.L. Haupt, G.W. Marshall, S.J. Marshall, The spatial arrangement of tubules in human dentin, J. Mater. Sci. Mater. Med. 12 (2001) 743–751, https://doi.org/10.1023/A:1011232912734.
[47] M. Toledano, M. Toledano-Osorio, A.L. Medina-Castillo, M.T. López-López, F. S. Aguilera, R. Osorio, Ion-modified nanoparticles induce different apatite formation in cervical dentine, Int. Endod. J. 51 (2018) 1019–1029, https://doi.org/10.1111/iej.12918.
[48] Y. Liu, J. Huang, H. Li, Synthesis of hydroxyapatite–reduced graphite oxide nanocomposites for biomedical applications: oriented nucleation and epitaxial growth of hydroxyapatite, J. Mater. Chem. B 1 (2013) 1826–1834, https://doi.org/10.1039/C3TB00531C.
[49] M.J. Olszta, X. Cheng, S.S. Jee, R. Kumar, Y.-Y. Kim, M.J. Kaufman, E.P. Douglas, L. B. Gower, Bone structure and formation: a new perspective, Mater. Sci. Eng. R Rep. 58 (2007) 77–116, https://doi.org/10.1016/j.mser.2007.05.001.
[50] R.G. Handschin, W.B. Stern, X-ray diffraction studies on the lattice perfection of human bone apatite (Crista Iliaca), Bone 16 (1995) S355–S363, https://doi.org/10.1016/S8756-3282(95)80385-8.
[51] M. Toledano, R. Osorio, E. Osorio, A.L. Medina-Castillo, M. Toledano-Osorio, F. S. Aguilera, Ions-modified nanoparticles affect functional remineralization and energy dissipation through the resin-dentin interface, J. Mech. Behav. Biomed. Mater. 68 (2017) 62–79, https://doi.org/10.1016/j.jmbbm.2017.01.026.
[52] T. Karakida, K. Onuma, M.M. Saito, R. Yamamoto, T. Chiba, R. Chiba, Y. Hidaka, K. Fujii-Abe, H. Kawahara, Y. Yamakoshi, Potential for Drug Repositioning of Midazolam for Dentin Regeneration, Int. J. Mol. Sci. 20 (2019) 670, https://doi.org/10.3390/ijms20030670.
[53] K. Yoshihara, N. Nagaoka, A. Nakamura, T. Hara, S. Hayakawa, Y. Yoshida, B. Van Meerbeek, Three-dimensional observation and analysis of remineralization in dentinal caries lesions, Sci. Rep. 10 (2020) 4387, https://doi.org/10.1038/s41598-020-61111-1.
[54] A. Kiesow, M. Morawietz, J. Gruner, S. Gierth, L. Berthold, E. Schneiderman, S. St John, High-Resolution characterization of enamel remineralization using time-of-flight secondary ion mass spectrometry and electron microscopy, Caries Res. (2024), https://doi.org/10.1159/000535979.
[55] M.J. Balart, X. Hao, C.L. Davis, Automated SEM/EDS analysis for assessment of trace cross-contamination in 316l stainless steel powders, Metall. Mater. Trans. A 53 (2022) 345–358, https://doi.org/10.1007/s11661-021-06474-4.
[56] A.E. Porter, R.K. Nalla, A. Minor, J.R. Jinschek, C. Kisielowski, V. Radmilovic, J. H. Kinney, A.P. Tomsia, R.O. Ritchie, A transmission electron microscopy study of mineralization in age-induced transparent dentin, Biomaterials 26 (2005) 7650–7660, https://doi.org/10.1016/j.biomaterials.2005.05.059.
[57] P. Bodier-Houllé, P. Steuer, J.-C. Voegel, F.J.G. Cuisinier, First experimental evidence for human dentine crystal formation involving conversion of octacalcium phosphate to hydroxyapatite, Acta Crystallogr. Sect. D 54 (1998) 1377–1381, https://doi.org/10.1107/S0907444998005769.
[58] R.G. Carvalho, L.F. Patekoski, R.M. Puppin-Rontani, C.R. Nakaie, F.D. Nascimento, I.L.S. Tersariol, Self-assembled peptide P11-4 interacts with the type I collagen C-terminal telopeptide domain and calcium ions, Dent. Mater. 39 (2023) 708–717, https://doi.org/10.1016/j.dental.2023.06.004.
[59] M. Toledano, F.S. Aguilera, E. Osorio, I. Cabello, M. Toledano-Osorio, R. Osorio, Functional and molecular structural analysis of dentine interfaces promoted by a Zn-doped self-etching adhesive and an in vitro load cycling model, J. Mech. Behav. Biomed. Mater. 50 (2015) 131–149, https://doi.org/10.1016/j.jmbbm.2015.05.026.
[60] Z. Zhang, F. Zhou, E.J. Lavernia, On the analysis of grain size in bulk nanocrystalline materials via x-ray diffraction, Metall. Mater. Trans. A 34 (2003) 1349–1355, https://doi.org/10.1007/s11661-003-0246-2.
[61] Th. Leventouri, A. Antonakos, A. Kyriacou, R. Venturelli, E. Liarokapis, V. Perdikatsis, Crystal structure studies of human dental apatite as a function of age, Int. J. Biomater. 2009 (2009) 698547, https://doi.org/10.1155/2009/698547.
[62] S. Marković, L. Veselinović, M.J. Lukić, L. Karanović, I. Bračko, N. Ignjatović, D. Uskoković, Synthetical bone-like and biological hydroxyapatites: a comparative study of crystal structure and morphology, Biomed. Mater. Bristol Engl. 6 (2011) 045005, https://doi.org/10.1088/1748-6041/6/4/045005.
[63] K.-D. Liss, A. Bartels, A. Schreyer, H. Clemens, High-Energy X-Rays: a tool for advanced bulk investigations in materials science and physics, Textures Microstruct. 35 (2003) 219–252, https://doi.org/10.1080/07303300310001634952.
[64] A. Moshaverinia, S. Ansari, M. Moshaverinia, N. Roohpour, J.A. Darr, I. Rehman, Effects of incorporation of hydroxyapatite and fluoroapatite nanobioceramics into conventional glass ionomer cements (GIC), Acta Biomater. 4 (2008) 432–440, https://doi.org/10.1016/j.actbio.2007.07.011.
[65] A.V. Zavgorodniy, R. Rohanizadeh, M.V. Swain, Ultrastructure of dentine carious lesions, Arch. Oral Biol. 53 (2008) 124–132, https://doi.org/10.1016/j.archoralbio.2007.08.007.
[66] L.D. Landau, E.M. Lifshitz, Statistical Physics: Volume 5, Elsevier, 2013.
[67] S. Ucar, S.H. Bjørnøy, D.C. Bassett, B.L. Strand, P. Sikorski, J.-P. Andreassen, Formation of hydroxyapatite via transformation of amorphous calcium phosphate in the presence of alginate additives, Cryst. Growth Des. 19 (2019) 7077–7087, https://doi.org/10.1021/acs.cgd.9b00887.
[68] S. Armstrong, L. Breschi, M. Özcan, F. Pfefferkorn, M. Ferrari, B. Van Meerbeek, Academy of dental materials guidance on in vitro testing of dental composite bonding effectiveness to dentin/enamel using micro-tensile bond strength (μTBS) approach, Dent. Mater. 33 (2017) 133–143, https://doi.org/10.1016/j.dental.2016.11.015.

SUPPLEMENTARY MATERIAL

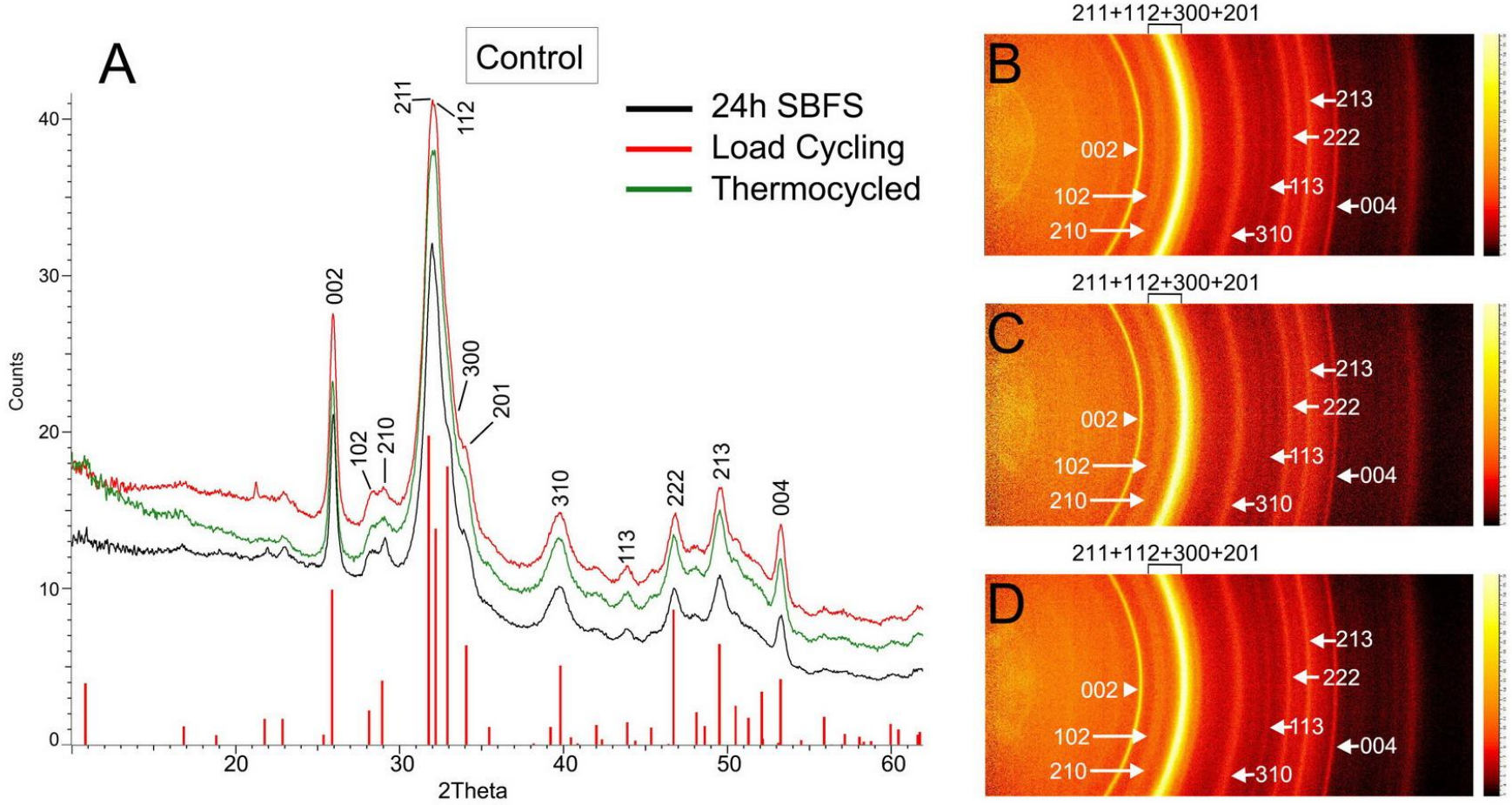

Figure S1. Refined μXRD[2] profiles of the control group, after load cycling and after thermo-cycling (**A**). Vertical bars represent hydroxyapatite (HAp) peaks derived 2-theta *versus* diffraction-intensity relationships in the correspondence JCPDS cards. FWHM: Full Width at Half Maximum. Debye-Scherrer rings of the control group at 24 h storage (**B**), after load cycling (**C**) and after thermo-cycling (**D**) are shown.

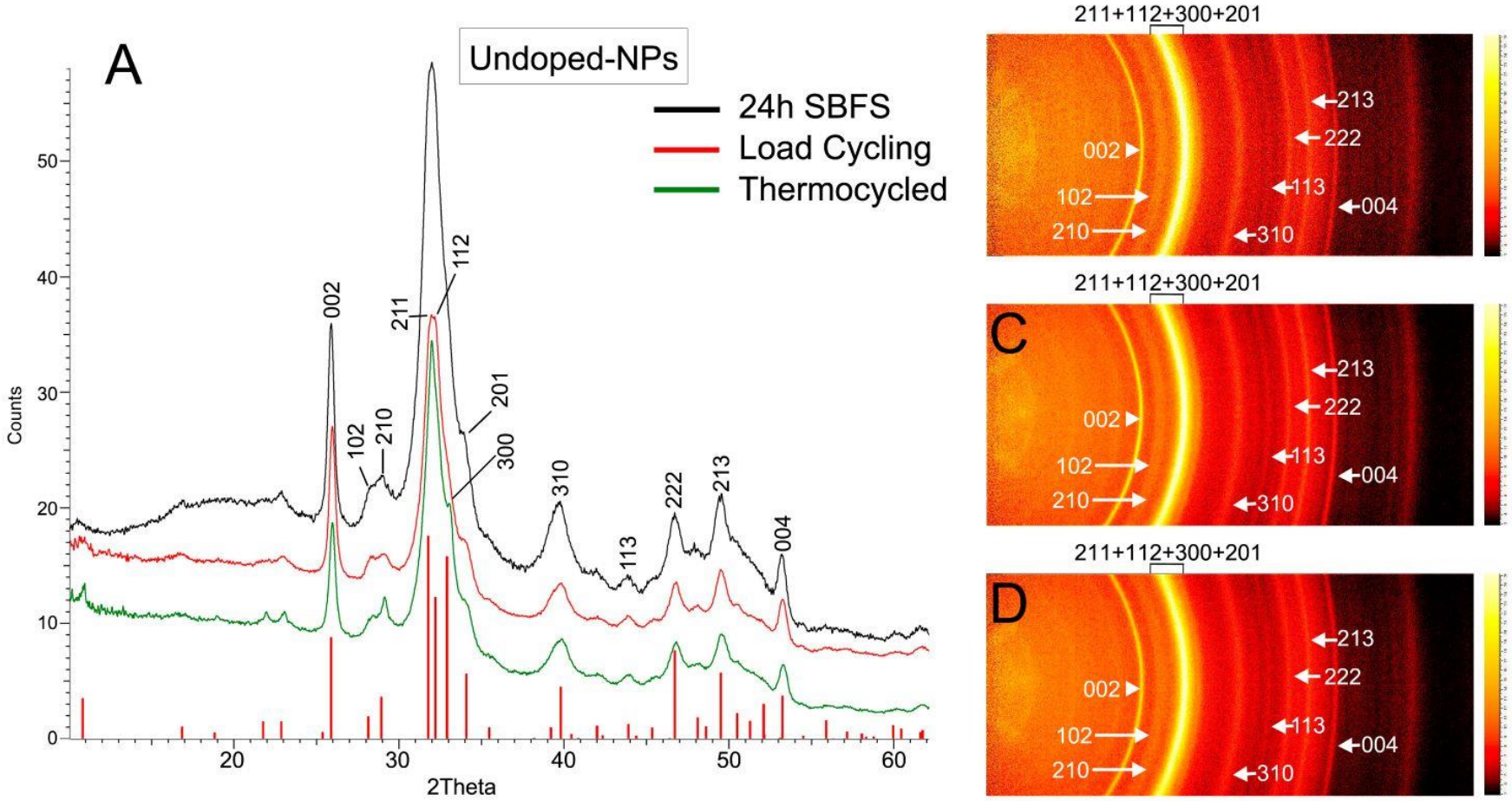

Figure S2. Refined μXRD[2] profiles of specimens treated with undoped NPs, after load cycling and after thermo-cycling (**A**). Vertical bars represent hydroxyapatite (HAp) peaks derived 2-theta *versus* diffraction-intensity relationships in the correspondence JCPDS cards. FWHM: Full Width at Half Maximum. Debye-Scherrer rings of the undoped NPs group at 24 h storage (**B**), after load cycling (**C**) and after thermo-cycling (**D**) are shown.

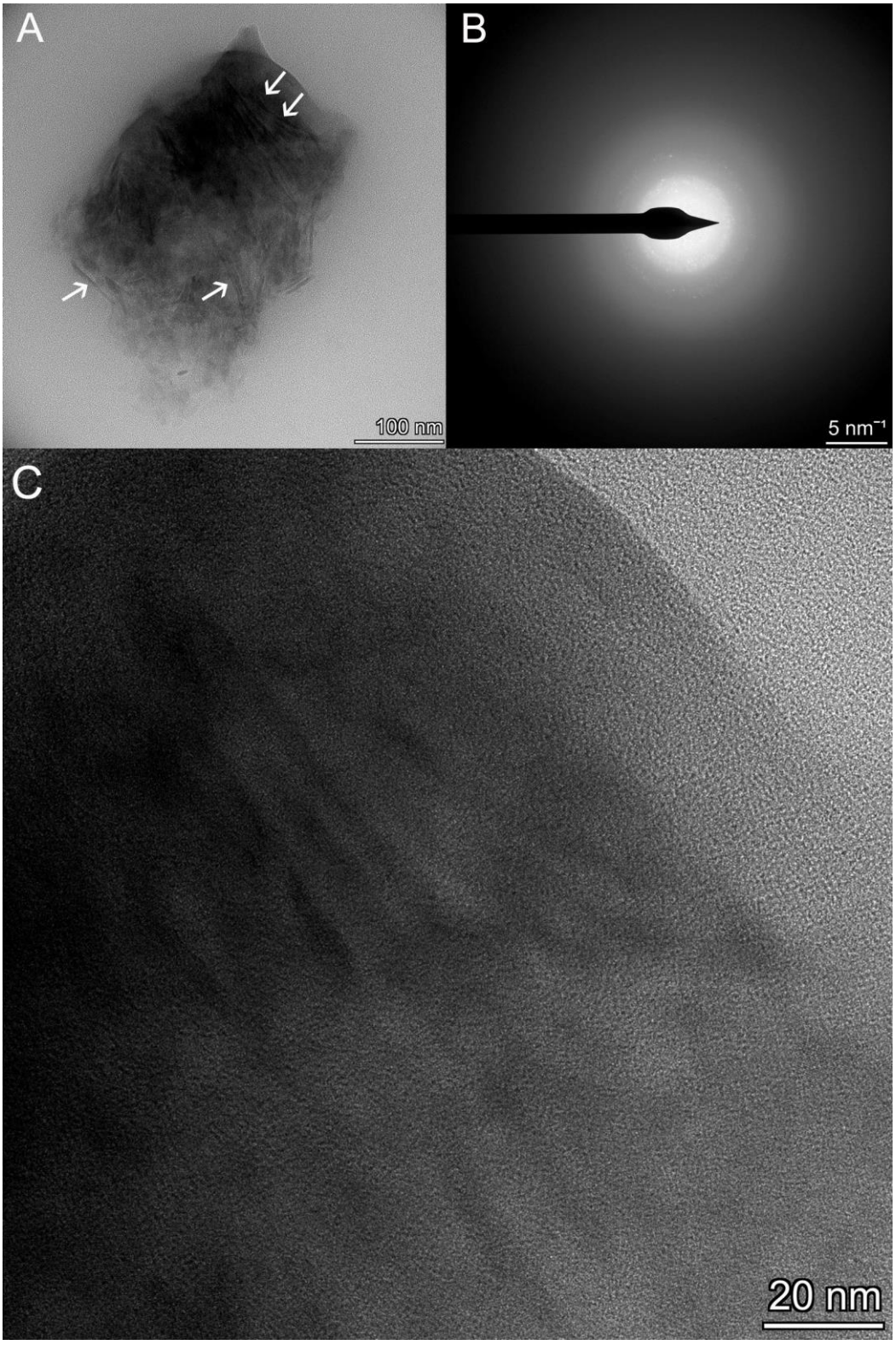

Figure S3. **A**, Bright-field of an assembly of polyhedral apatite crystals formed by plate-like overlapped crystals (pointers) of dentin treated with TDg-NPs and load cycled. It may be observed the in detailed polyhedral apatite appearance of crystallites. Aligned crystal arrays may be shown (arrows) (scale bars: 100 nm). **B**, Corresponding Fast Fourier Transform (FFT) diffraction pattern of hydroxyapatite nanocrystals from A. **C**, High Resolution TEM (HRTEM) image of a single hydroxyapatite nanocrystal showing the growth orientation and crystallite lattice, from a dentin sample treated with TDg-NPs and load cycled. The image highlights topography of the mineralized structures showing the parallel co-alignment of multiple apatite nanocrystals growing in star-shaped, showing partial randomly orientation.

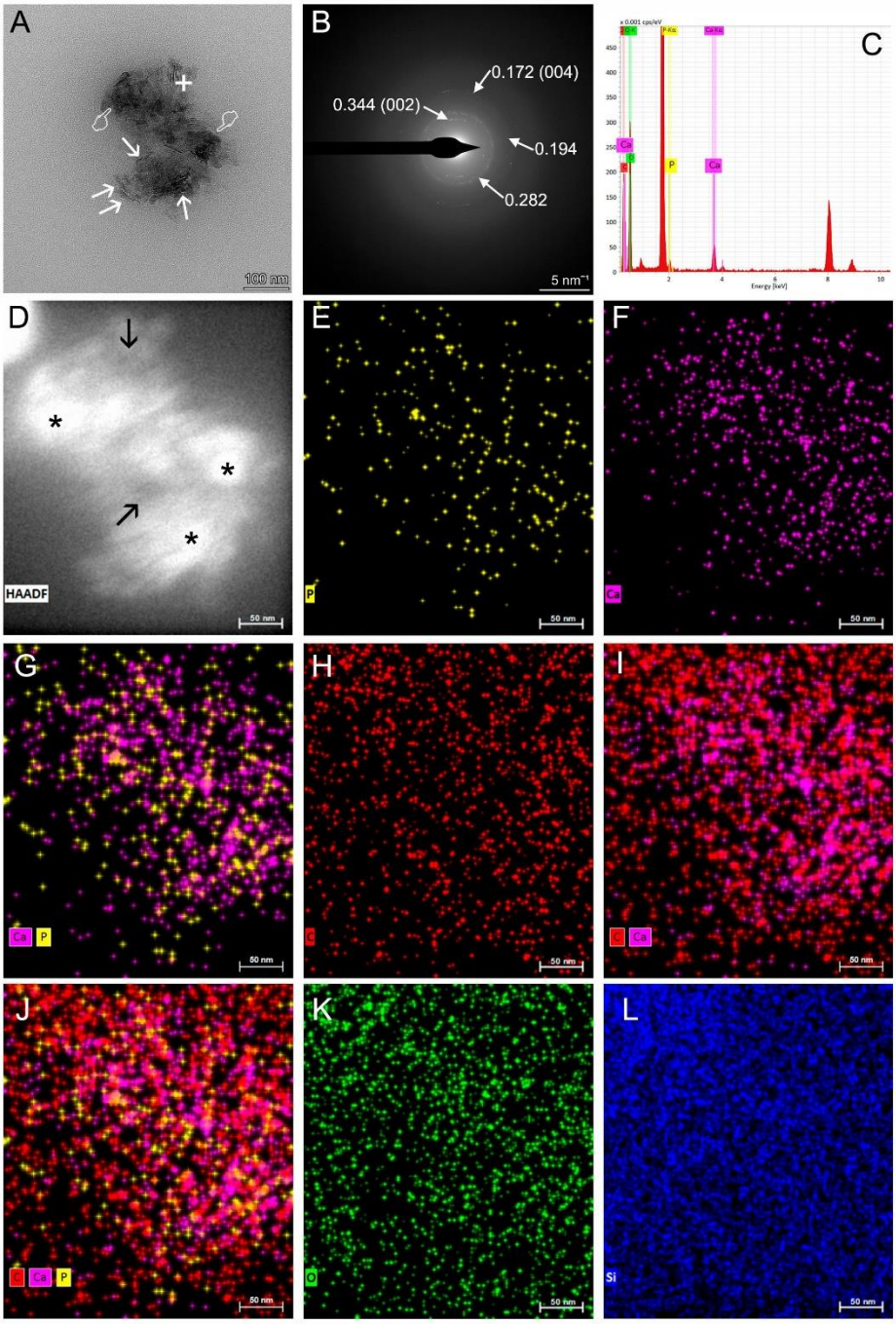

Figure S4. **A**, Bright-field of multiple irregular nanocrystals rods and platforms-like overlapped deposits (pointers) of dentin treated with TDg-NPs and thermo cycled. The detailed polyhedral apatite appearance of crystallites may be observed. Aligned crystal arrays may be shown (arrows) (scale bars: 100 nm). **B**, It shows a specific area electron diffraction (SAED) of the crystals (+) shown in (A), at nanoscale, unveiling a highly polycrystalline structure. Four Debye rings and interplanar distances (d spacing) ranging from 0.172 nm to 0.344 nm were identified. Measurements were done at 10 μm ϕ. **C**, Representative Energy-dispersive X-ray spectroscopy (EDS) of the crystal (+) observed in (A) showing the nanometer-sized apatite composition of calcium and phosphate as part of the elemental analysis. **D**, *High-angle annular dark-field* scanning transmission electron microscopy (HAADF and S-TEM image or Z-contrast imaging) reflecting the collection of the electrons scattered through very large angles, within the nanocrystals. This resulted image shows mass- (or Z-) contrast with higher atomic number regions of the sample appearing brighter (asterisks) than light element regions (arrows). Two dimensional elemental mapping of phosphate [P] (**E**), calcium [Ca] (**F**), calcium phosphate [CaP] (**G**), carbon [C] (**H**), calcium carbonate [CaC] (**I**), carbonated calcium phosphate [CaPC] (**J**), oxygen [O] (**K**) and silica [Si] (**L**).

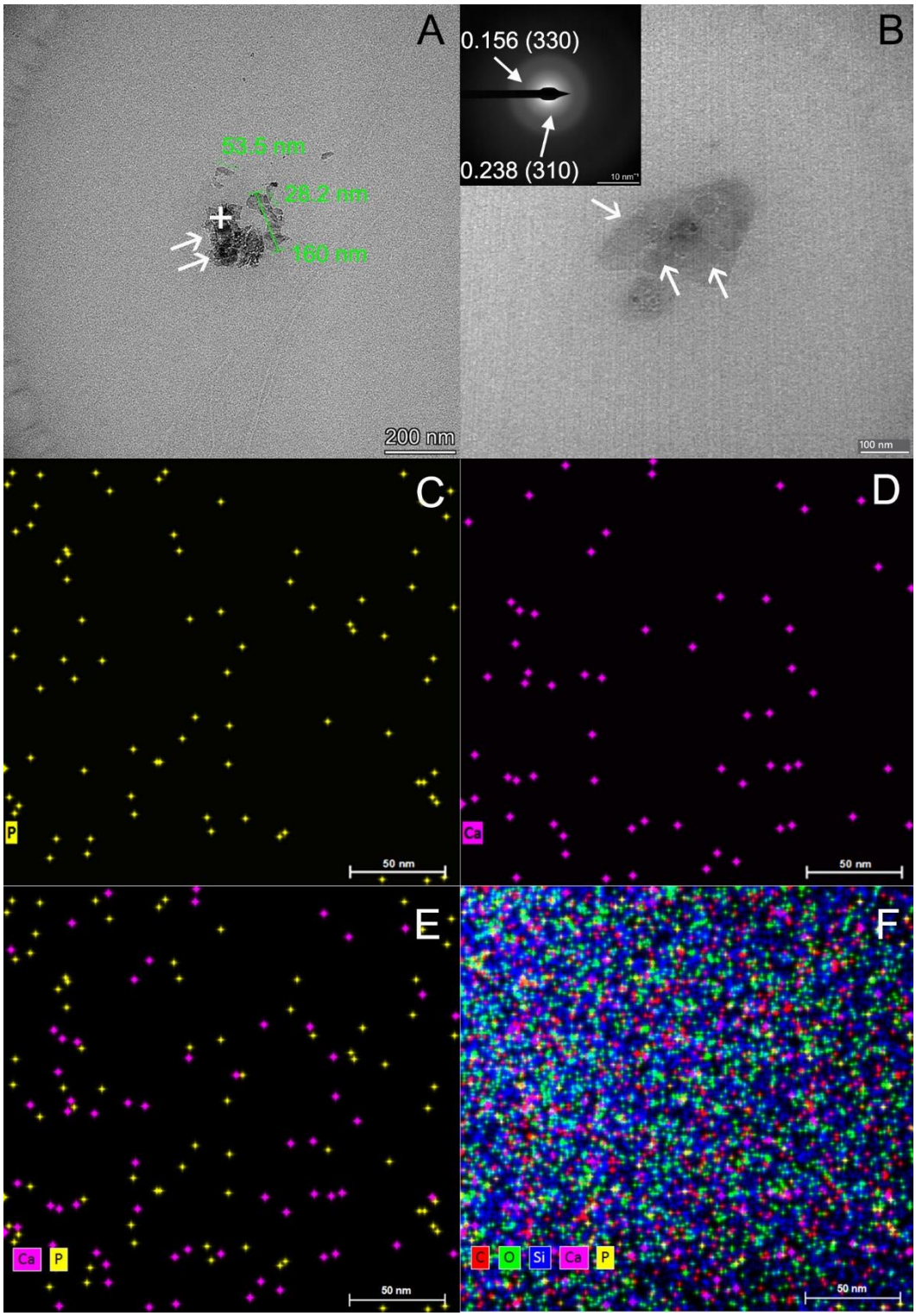

Figure S5. **A**, Bright-field of an assembly of irregular polyhedral and starry block-like apatite crystals of dentin used as control, and assessed after load cycling. It is observed that the particles have a domain of locally aligned crystal arrays, showing the staggered order of polygon crystallites (arrows) (scale bar: 200 nm). **B,** Control specimen after load cycling showing a bright-field of an assembly of polymorph/polyhedral apatite crystals shaped by juxtaposed plate-like polygons (arrows), amorphous in nature. The inset is showing a specific area electron diffraction (SAED) of crystal (+) shown in A, at nanoscale, unveiling a highly amorphous structure. Two Debye rings and interplanar distances ranging from 0.156 nm to 0.238 were identified. **C,** Two dimensional elemental mapping of phosphate [P], calcium [Ca] (**D**), calcium phosphate [CaP] (**E**), and integrated mapping with phosphate [P], calcium [Ca], carbon [C], oxygen [O] and silica [Si] (**F**).

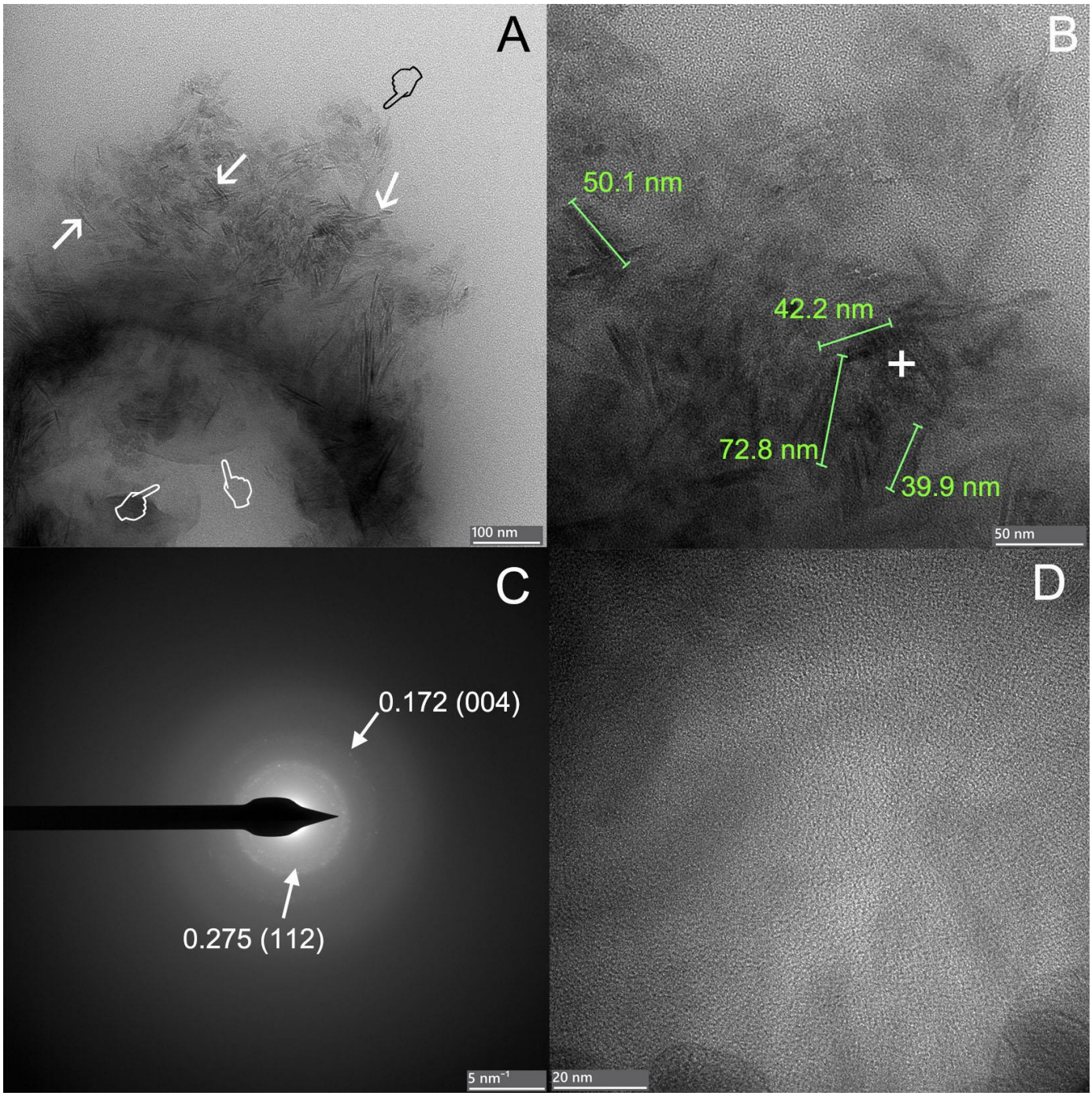

Figure S6. **A**, Bright-field of an assembly of polyhedral plate-like overlapped crystals (pointers) and needle-like crystals (arrows) of dentin treated with TDg-NPs at 24 h storage. **B**, Observation of the same section showing the in detailed polyhedral apatite appearance of crystallites on the upper side. Aligned crystal arrays may be shown (scale bars: 50 nm). **C**, A crystal (+) shown in (B), at nanoscale, displaying a selected area electron diffraction pattern (SAED), containing two differentiated halo rings and clear d spacing values. **D**, High resolution TEM (HRTEM) image of a single hydroxyapatite nanocrystal showing its growth orientation and crystallite lattice.

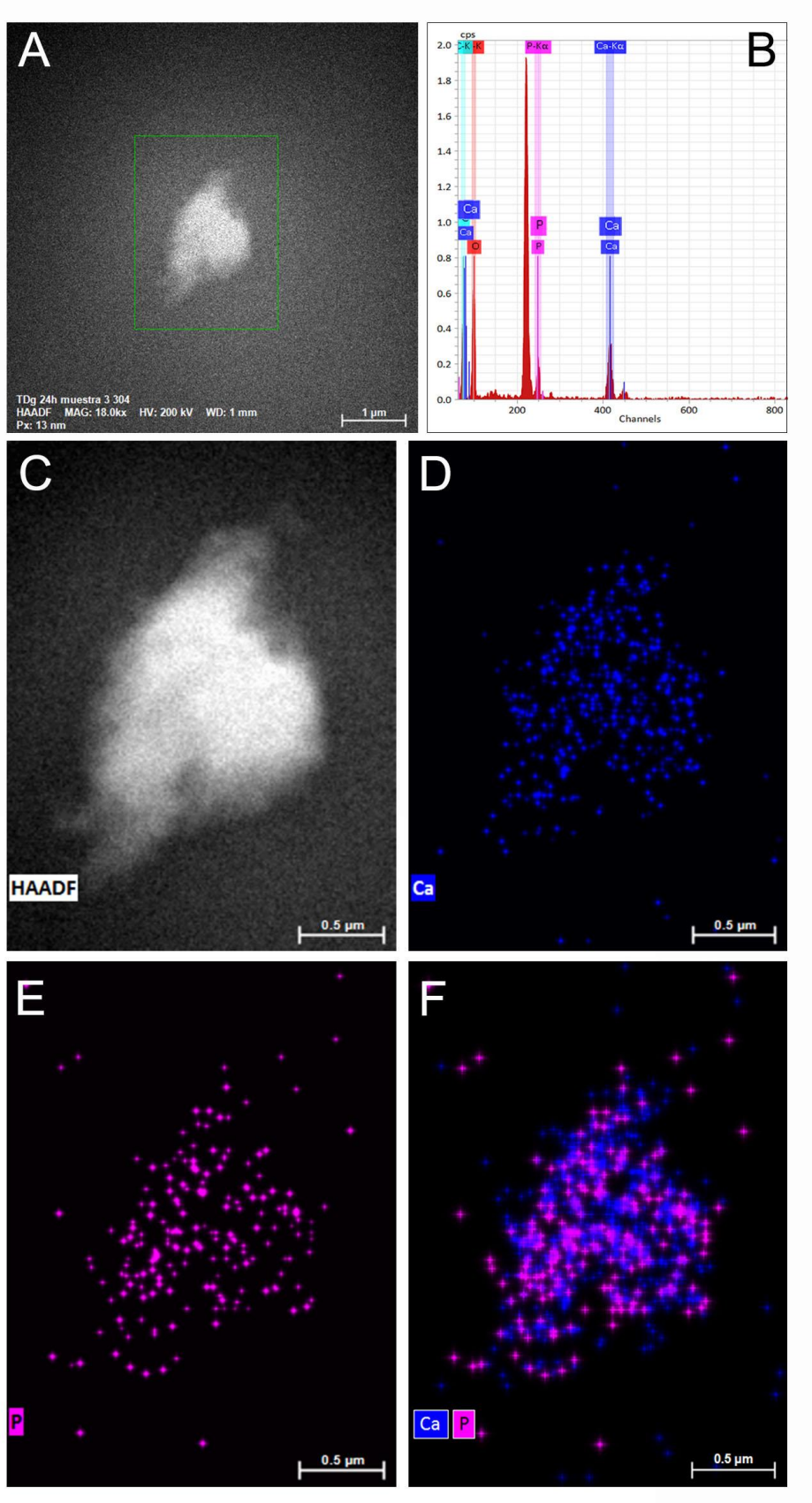

Figure S7. **A**, Crystal capture for Energy-dispersive X-ray spectroscopy (EDX) analysis, in a sample of dentin infiltrated with TDg-NPs at 24 h storage. **B**, Representative EDX of the crystals (+) observed in Figure S4B, showing the nanometer-sized apatite composition of calcium and phosphate as part of the elemental analysis. **C,** Scanning TEM (STEM) bright-field image and EDS-STEM mapping of the crystal observed in (A). **D,** Two dimensional elemental mappings of calcium [Ca], phosphate [P] (**E**), and calcium phosphate [PCa] (**F**).

Table S1. Relative intensity (%) of the Hydroxyapatite characteristic diffraction planes obtained in each study group (with a margin of error 1.5%).

Groups		Diffraction planes		
		(002)	(112)	(310)
Control	24h SBFS	45	90	14
	24h Load	46	96	16
	Thermocycled	41	96	14
Undopeds- NPs	24h SBFS	41	93	16
	24h Load	53	97	14
	Thermocycled	36	84	13
TDg-NPs	24h SBFS	45	97	14
	24h Load	31	74	19
	Thermocycled	44	95	16

For all the diffraction patterns, the peaks values had been normalized at maximum to the intensity of the 211 peak basis near 31.90 2Theta.